Design of a Carbon Neutral Aircraft

Final Report
Group 13

Technische Universiteit Delft

TU Delft

ALBATROSS EMBRACER

EMBRACE THE FUTURE

This page is intentionally left blank

Design of a Carbon Neutral Aircraft

Final Report

Group 13

Y. Farah - 4651510
K. Kaneko - 4657314
A. Van Meenen - 4674030
B. Saify - 4669428
S. Shrestha - 4677846
S. Singh - 4660951
M. Swart - 4677129
F. Vassen - 4667557
M. van Vliet - 4538838
S. Vermani - 4657764

Version nr.	Receivers	Changes made
1	Dr.ir. John-Alan Pascoe Biagio della Corte Christopher Teruna María Seoane Álvarez Ganesh Gebhard	—-
2	Dr.ir. John-Alan Pascoe Biagio della Corte Christopher Teruna María Seoane Álvarez Ganesh Gebhard	Feedback Implemented

TU Delft

Preface

This is the Final Report, which is the natural continuation of the Project Plan, the Baseline Report and Midterm Report for the DSE Project: Carbon Neutral Ready Airliner. The report was compiled and written by a team of 10 students who dedicated all their time and energy to present this report.

The group would like to thank the principal tutor Dr.ir. John-Alan Pascoe, along with the tutor coaches Biagio della Corte MSc and Cristopher Teruna MSc, for their mentoring during the project, and the teaching assistant Marìa Seoane Alvarez BSc for all the feedback given in this report. We would also like to thank the Delft University of Technology, Ir. J.A. Melkert and all other people involved with the Design Synthesis Exercise for their time and giving us the opportunity to make this project a reality.

Abstract

Sustainability has become an increasingly important issue, and several different governments around the world have been working towards more environmentally friendly approaches throughout different industries. This has led to measures such as the European Green Deal, which aims to make Europe climate neutral by 2050. For the aircraft industry, however, this goal creates a so-called circular causality problem. This is because there may be limited investment in increasing production of alternative energy sources due to the limited availability of aircraft that use them. On the other hand airlines may hesitate due to the limited availability of fuel to buy such aircraft. In order to solve this problem, the carbon neutral ready aircraft has been proposed.

The carbon neutral ready aircraft is designed such that it initially is powered by fossil fuels and can then be converted to be powered by a carbon neutral energy source. The carbon neutral energy source that is chosen for this aircraft design is synthetic kerosene. The carbon neutral aircraft has a high wing configuration with a high aspect ratio wing. To cope with the large span of the aircraft it was decided to give the aircraft the ability of the wing tips to be folded up. Furthermore, the wing has support struts which connect the wing to the lower part of the fuselage. The propulsion system of the aircraft has two novel features: two wing mounted ultra high bypass ratio turbofan engines and an electrically powered ducted fan, which ingests the boundary layer at the aft of the fuselage. An additional five-gear configuration was chosen for the landing gear to provide the aircraft with stable ground operations while not creating a need for a fairing which interferes with the boundary layer being ingested by the aft ducted fan.

Carrying out the design of this aircraft shows that the aircraft is financially feasible and performs as well as the baseline A320 aircraft in terms of payload and range, while allowing sustainability goals such as the European Grean Deal to be met. The aircraft has a 17 % emission reduction compared to the A320neo, while still employing fossil fuel based kerosene. Furthermore, at least 90% by mass of the primary structure of the aircraft is recyclable. From the recommendations however, it is clear that a lot still needs to be done before the carbon neutral aircraft can enter into service in 2030.

Executive Overview

Project Objective

The European Green Deal aims at making Europe climate neutral by 2050. To achieve this it is also important for aircraft to become carbon neutral by converting from fossil fuels to carbon neutral sources. There are multiple such carbon neutral sources under development, however since there are no major aircraft that can make use of these carbon neutral sources there is limited investment towards developing these carbon neutral sources. On the other hand, due to the lack of alternative energy sources, airlines are reluctant to replace aircraft in their fleet with aircraft that use these alternative energy sources. This leads to a so called "chicken-and-egg" scenario and the following Mission need statement (MNS) :

Mission Need Statement

New strict environmental legislation, but the lack of current sustainable energy infrastructure necessitates the development of a new aircraft which can be converted to be carbon neutral when infrastructure becomes available, within the next ten years.

The aim of this project is to develop an aircraft that initially flies on Kerosene, but when the infrastructure becomes available, can be converted to a carbon neutral energy source. Furthermore, this aircraft is required to have similar performance as the Airbus A320 and Boeing 737, while also having a similar cost performance. Additionally, the aircraft is required to be able to convert from fossil fuels to the carbon neutral energy source within a month. This leads to the following Project Objective Statement (POS):

Project Objective Statement

Design an Airbus A320 (or Boeing 737) replacement aircraft that initially uses kerosene but can be converted to be carbon neutral within one month, using a design team of 10 students with a time limit of 10 weeks.

Top-Level Requirements

The design of the carbon neutral aircraft was carried out to meet the different stakeholders' top-level requirements which are shown in Table 1. These requirements were given by Stakeholders such as the Customer and Airports. These were deemed to be crucial to the design of the aircraft and were thus also given the highest importance throughout the design process, as not meeting these requirements could kill the design.

Table 1: Top-Level Requirements for the CNA

Identifier	Description
REQ-CN-PERF-1	The CNA shall have a cruise speed of Mach 0.78.
REQ-CN-PERF-2	The CNA shall have a maximum range of at least 3400 NM.
REQ-CN-PERF-3	The CNA shall carry a payload of 20 tons.
REQ-CN-PERF-4	The CNA shall have a range at max payload of 2150 NM.
REQ-CN-PERF-5	The CNA shall be able to carry 194 pax in a high density lay-out and 7 LD3 containers underfloor at max payload.
REQ-CN-PERF-17	The CNA shall be able to convert to carbon neutral within one month.
REQ-CN-SAFE-4	The CNA shall have a 10^{-9} /flight hour risk of catastrophic failure.
REQ-CN-ECON-5	The CNA shall enter into service in 2030.
REQ-CN-ECON-6	The list price of the CNA shall be $110 million.
REQ-CN-SYS-SUS-1	The CNA's primary structure shall be recyclable for 75% of its mass.
REQ-CN-SYS-SUS-2	The CNA shall have a 10% emission reduction per passenger kilometre with repect to A320/ 737 baseline whilst using fossil fuel.
REQ-CN-ECON-7	The CNA shall be capable of serving all airports currently served by the Airbus A320 or Boeing 737.

Market Analysis

A market analysis was performed to see whether the need of a carbon neutral aircraft (CNA) is present. During this market analysis it was determined that one of the largest challenges in the aircraft industry is reducing the environmental impact of aviation. The increasing annual traffic leads to an increasing contribution towards emissions of greenhouse gases, leading to a need for an aircraft powered by renewable energy sources. However, none of the renewable energy sources currently have the potential to replace fossil fuels especially for medium to long range transport aircraft. This means that the CNA needs to offer a solution to the increasing emissions due to the increasing aviation traffic, by providing an aircraft that can cover long distances with a large amount of passengers.

Due to the initiatives of governments to reduce the environmental impact, the whole aircraft industry aims to improve their designs, allowing a reduction in aviation's environmental impact. Therefore it is very important to make sure that the CNA is not only competitive to current aircraft, but can also be a worthy competitor to future aircraft that Airbus and Boeing introduce to the market. However, since it is difficult to predict the performance of aircraft in the future, it is first necessary to make sure that the CNA can perform on the same level as or better than the current A320 baseline. Looking at the CNA's top level requirements it can be seen that in terms of range and payload, the CNA caters to the increasing world traffic demand. This can be seen from the fact that the CNA has a higher range than most narrow body aircraft and is capable of carrying a larger payload. Furthermore, the fact that that the CNA is has fewer emissions before conversion and has a primary structure of which at least 90% by mass is recyclable means that the CNA can provide a competitive aircraft in terms of sustainability.

The financial environment at entry into service, will greatly affect the list price of the aircraft, leading to a constraint on the cost of the aircraft. This constraint can kill the design if the aircraft costs too much, while customers in the case of the carbon neutral aircraft could just buy a normal A320 aircraft. The main strengths of the aircraft are its usage of the carbon neutral synthetic kerosene and its 17 % increased fuel efficiency, which will reduce operating costs, while the carbon neutral status can play a major role in company branding. Furthermore, the overall cost stemming from synthetic Kerosene is currently higher than that of fossil fuel based kerosene, however by 2030, the cost of the synthetic kerosene will drop significantly, while that of the regular jet fuel will stagnate. The shift towards the sustainable fuel, will also be accompanied by government subsidies and positive market sentiment, which has been shown to be an increasing trend over the course of the last decade. The current airline industry is already heavily reliant on subsidies and tax breaks, meaning that airlines cannot afford losing government support, meaning that they do have to reach their emission target. Thus, becoming carbon neutral is a must for any airline.

Just competitiveness in terms of performance and sustainability is not enough to determine whether the CNA will be successful financially. For this it is also important to make sure that the aircraft has a feasible and profitable market share. Analysis of the market led to the identification of two possible scenarios for the market share of the CNA. The CNA can either be a direct competitor to Airbus and Boeing and thus obtains a market share of 30% or the rights of the CNA are bought by either Boeing or Airbus and used to replace their current fleet of the A320 or B737 baseline aircraft, meaning that the CNA has a market share of around 45%. Since the entry into service is 2030 and it is forecasted that all aircraft will be carbon neutral by 2050, a period of 20 years is given to achieve the total production quantity. For the first of the two previously mentioned options, the total production quantity is 6940 aircraft which leads to a 347 aircraft a year. In the latter case the production quantity would be 10400 aircraft, which leads to 520 aircraft a year. Using the previously mentioned market shares and production quantities, preliminary cost estimations can be carried out, which lead to an estimated cost of 54.5 M$ and 51.75 M$ per aircraft, for production quantities of 6940 and 10400 aircraft respectively. However, it is important to note that the final price of the aircraft heavily relies on the development of the novel aspects, which will significantly increase costs. However, as previously mentioned, government subsidies will relieve costs on all fronts of the aircraft industry, with the increasing carbon neutrality. For this it can be estimated that the costs mentioned above can have cost reductions between 10 to 50 % from the accumulation of financial benefits, making the carbon neutral aircraft, financially competitive.

Final Design

The aircraft consists of a conventional tube-and-wing body. This makes manufacturing cheaper, because manufacturers do not have to restructure their manufacturing and assembly floors. Most of the aircraft is made out of aluminium, which reduces the cost of manufacturing because no hard to manufacture metals are used and no composites are used. The conventional tube-and-wing body also makes the design less complicated and more familiar to passengers.

The wing is mounted on top of the cabin instead of under the cabin. The wings also have a very high aspect ratio. This high aspect ratio increases the efficiency of lift generation. This means that less drag is generated for the same amount of lift compared to other aircraft. The reduction in drag also reduces the thrust required. This reduction in

thrust means that less fuel has to be burnt, which results in lower emissions and a lower fuel costs. However, the high aspect ratio means that the wings will be thinner relative to their span and, therefore, weaker. This is mitigated by introducing a strut in the structure. This strut will support the wing and makes the high aspect ratio possible.

The high aspect ratio introduces a problem with the wingspan. The wingspan increased to 50.4 metres. Normally this would not fit in the same gates as competitors like the Airbus A320 and Boeing 737. However, the CNA can fold the outer part of the wing inwards, such that it will fit in the smaller gates. This results in access to more airports and lower airport fees, since the larger gates do not have to be used.

The CNA has two ultra high bypass ratio engines and a BLI system. The BLI also helps in reducing the drag of the aircraft and therefore fuel consumption. In addition, the BLI produces 24% of the thrust during cruise. The BLI does stick out further than the tail cone does normally. This meant that the landing gear had to move backwards, such that the aircraft could still take-off without scraping the ground. This resulted in extra landing gear in the struts, for a total of 5 landing gears. Two below the fuselage, one under each strut and one nose landing gear.

To reduce fuel consumption even more, ultra high bypass ratio engines are used. Conventional aircraft have a bypass ratio of around 11, this engine has a bypass ratio of 15. These engines are more efficient for the same amount of thrust. They burn less fuel and therefore also have lower emissions. The reduced fuel burn also reduces operational costs.

The CNA can be converted to a carbon neutral energy source. This is done by replacing the fossil-fuel kerosene in the tanks with synthetic kerosene. This has a couple of advantages. First of all, it is carbon neutral. Synthetic kerosene is produced by capturing CO_2 in the air and converting it into kerosene. The second advantage is that the aircraft does not have to convert. Since the properties of synthetic kerosene and fossil-fuel kerosene are the same, no conversion of the engines or other parts of the aircraft has to take place. This reduces the cost of the aircraft and it reduces the time it is not in service. Another advantage of synthetic kerosene is that it is much purer compared to fossil fuel derived kerosene. Almost no soot is produced due to the purity of the fuel. The last advantage to point out is, that airports do not have to make large investments into the carbon-neutral fuel. Due to the similarities between the two fuels, no new infrastructure is required at the airports. All of the infrastructure is ready for synthetic kerosene. The total production cost of the aircraft is estimated at 58.4 M$. The maximum take-off mass is estimated at 70 tons and the operational empty weight is estimated at 41 tons.

The CNA has reduced its fuel consumption compared to the latest Airbus A320, the A320neo. It is 17% more fuel efficient than the A320neo. This reduction in fuel consumption reduces the operational costs of the aircraft a lot. Next to that the emissions reduce at the same time, because less fuel is being burnt. Due to the synthetic kerosene, there will be no soot in the emissions. There is also a 38% reduction in NOx emissions. All of this is achieved with the same maximum payload and the same range as Airbus A320's and Boeing 737's. The compatible airports did not reduce, due to the folding outer wing. The Albatross Embracer is presented in Figure 1.

Figure 1: The Albatross Embracer

Requirement Compliance

Table 2 is the requirement compliance matrix of the most important requirements. As can be seen, the CNA complies with most of them. The complied requirements are marked with ✓, partial compliance is marked with ~and requirements which have not been complied are marked with X.

REQ-CN-PERF-1 through REQ-CN-PERF-5 are performance requirements that the aircraft is designed for. Every part of the aircraft works together to make these requirements possible. Like the supercritical airfoils, the high lift over drag number and the efficient ultra high bypass ratio engines. REQ-CN-PERF-17 is achieved by using a carbon neutral fuel that is very similar to the current aircraft fuel, kerosene. Due to the high similarity in the fuel, almost no conversion is necessary and can therefore easily be performed in one month. By making sure that all departments pay extra attention to safety and redundancy of flight critical systems, is REQ-CN-SAFE-4 achieved.

REQ-CN-ECON-5 is achieved by using technologies and concept that are very close to being introduced on the market. That means the technology readiness level of this aircraft is fairly high. This makes it possible to have this aircraft enter service in 2030. The price to produce the aircraft is 58.4 M$, which means a list price of 110 M$ is achievable. Therefore is REQ-CN-ECON-6 complied with. Through the use of a close to conventional design and a folding outer wing, REQ-CN-ECON-7 is achieved. The close to conventional shape makes sure that there will be no difficulties in using current airport infrastructure, like taxiways and gates. The folding outer wing helps achieve the use of the same type of gates as the Airbus and Boeing. The aircraft can, therefore, serve the same airports as competitors.

At least 90% by mass of the primary sturcture is recyclable and, therefore, is REQ-CN-SYS-SUS-1 complied with. REQ-CN-SYS-SUS-2 is achieved by using a high aspect ratio wing, ultra high bypass ratio engines, and boundary layer ingestion engines. These concepts help reduce fuel consumption, either directly or indirectly through drag or weight reduction. And a reduction in fuel consumption means a reduction in emissions.

Table 2: Requirement compliance matrix

Requirement ID	Description	Source	Compliance
REQ-CN-PERF-1	The CNA shall have a cruise speed of Mach 0.78.	Customer	✓
REQ-CN-PERF-2	The CNA shall have a maximum range of 3400 NM.	Customer	✓
REQ-CN-PERF-3	The CNA shall carry a payload of 20 tons.	Customer	✓
REQ-CN-PERF-4	The CNA shall have a range at max payload of 2150 NM.	Customer	✓
REQ-CN-PERF-5	The CNA shall be able to carry 194 pax in a high density lay-out and 7 LD3 containers underfloor at max payload.	Customer	✓
REQ-CN-PERF-17	The CNA shall be able to convert to carbon neutral within one month.	Customer	✓
REQ-CN-SAFE-4	The CNA shall have a 10e-9 /flight hour risk of catastrophic failure.	Customer	✓
REQ-CN-ECON-5	The CNA shall enter into service in 2030.	Customer	✓
REQ-CN-ECON-6	The list price of the CNA shall be $110 million.	Customer	✓
REQ-CN-ECON-7	The CNA shall be capable of serving all airports currently served by the Airbus A320 or Boeing 737.	Customer	✓
REQ-CN-SYS-SUS-1	The CNA's primary structure shall be recyclable for 75% of its mass.	Customer	✓
REQ-CN-SYS-SUS-2	The CNA shall have a 10% emission reduction per passenger kilometre with repect to A320/ 737 baseline whilst using fossil fuel.	Customer	✓

Financial Analysis

A preliminary cost estimation shows that for production quantities of 6940 and 10400 aircraft, the total costs of the aircraft are 62.8 M$ and 59.7 M$ per aircraft respectively. Furthermore the direct operational cost is estimated to be 0.03414 $/km/pax. Carrying out an analysis on the return on investment of the aircraft, it can be seen that the return on the investment is -8% for the case where Airbus/Boeing buy the rights to the CNA and -13% for the case where the CNA becomes a direct competitor of Airbus and Boeing aircraft. This leads to the conclusion that the development and production of the aircraft cannot be profitable. However, as derived from the market analysis it is highly likely that financial benefits from government subsidies will reduce the overall costs by upto to 50%. This means that in the most optimum case the return on investment could be as high as 84%. Thus, it can be concluded that the financial benefits of carbon neutral flying are essential to making the design of the CNA financially feasible and profitable.

Nomenclature

α	Angle of Attack
α_0	Zero Lift Angle of Attack
ΔP	Difference in pressure
λ	Taper Ratio
Λ_{LE}	Leading Edge Sweep Angle
Λ_{TE}	Trailing Edge Sweep Angle
σ_y	Yield stress of material
$\sigma_{fatigue}$	Fatigue strength of material
σ_{ult}	Ultimate Strength
τ_{ult}	Shear strength of material
C_D	3D Total Drag Coefficient
C_d	2D Drag Coefficient
C_f	Skin Friction Coefficient
C_L	3D Lift Coefficient
C_l	2D Lift Coefficient
C_{D_0}	Zero Lift Drag Coefficient
C_{D_i}	Induced Drag Coefficient
C_{L_α}	3D Lift Curve Gradient
C_{l_α}	2D Lift Curve Gradient
C_{L_α}	Lift Curve Slope
$C_{L_{max}}$	3D Maximum Lift Coefficient
$C_{l_{max}}$	2D Maximum Lift Coefficient
C_{root}	Root Chord
C_{tip}	Tip Chord
Cm	Pitching Moment Coefficient
Cm_α	Pitching Moment Gradient
CO_2	Carbon dioxide
E	Youngs Modulus
G	Shear Modulus
H_V	Vickers Hardness
I	Moment of inertia
K_{1C}	Fracture Toughness
$M_{D_{\text{div}}}$	Drag Divergence Mach Number
$M_{fatigue}$	Average highest bending moment during one cycle
M_y	Bending Moment
Q	First moment of area
q	Dynamic Pressure
r_{fus}	Fuselage outer radius
S_h	Surface area of the horizontal tail
V_∞	Freestream Velocity
V_{fus}	Shear force
AR	Aspect Ratio
BLI	Boundary Layer Ingestion
BPR	Bypass Ratio
CC	Combustion Chamber
CFD	Computational Fluid Dynamics
CG	Centre of gravity
CNA	Carbon Neutral Aircraft
DDTF	Direct Drive Turbofan
EW	Empty Weight
GTF	Geared Turbofan
HLD	High Lift Device
HPC	High Pressure Compressor
HPT	High Pressure Turbine
HWFAP	HardWall Forward Acoustic Panel
LE	Leading Edge
LPC	Low Pressure Compressor
LPT	Low Pressure Turbine
MAC	Mean Aerodynamic Chord
MLW	Maximum Landing Weight
MTOW	Maximum Take-off Weight
NADP	Noise Abatement Departure Procedure
NOx	Nitrogen Oxides
OEW	Operational Empty Weight
OPR	Overall pressure ratio
QFD	Quality function deployment
RBF	Radial Basis Function
t	Thickness
TE	Trailing Edge
TIT	Turbine Inlet Temperature
TSFC	Thrust specific fuel consumption
UHBR	Ultra High Bypass Ratio
VLM	Vortex Lattice Method

Contents

1 Introduction

The European Green Deal aims to make Europe climate neutral by 2050. To achieve this aim it is important for all the carbon emitting industries across Europe to make changes to the way that they operate. One such industry is the aviation industry. For Europe to meet its goal of climate neutrality it is important that aircraft transition from fossil fuel based kerosene to alternative sources which are carbon neutral. Many new developments are currently being made in the search for alternative energy sources for the aircraft industry. However, there may be limited investment in scaling up production for these carbon neutral energy sources, since there may not be any aircraft that can use them. At the same time airlines may be reluctant to replace their current fleet with aircraft that can use these alternative energy sources. This leads to a so called "chicken-and-egg" scenario. The Solution? An aircraft that can use multiple energy sources.

The aim of this project is to design an aircraft which is initially powered by fossil fuels, but can easily convert to a carbon neutral energy source, when these energy sources become available on a large scale. This aircraft is required to perform comparably to the A320 and similar aircraft, while also having a similar cost. This gives airlines the incentive of investing in aircraft that can meet sustainability goals set by the European Union. The aim of this report is to present the preliminary design of the Carbon Neutral Airliner along with the design choices, their justifications and the consequential results, while showing that the aircraft meets its requirements and can help Europe become climate neutral. Furthermore, this report also presents a plan for the next steps of the design of the Carbon Neutral Aircraft, after this preliminary design phase.

The report starts off with an overview of the Project in Chapter 2. Then the report describes the need for the aircraft from a financial perspective in the Market Analysis in Chapter 3. Chapter 4 describes the general methodology that was adopted for the whole design process of the aircraft. An analysis of the mission carried out by the aircraft is presented in Chapter 5. Chapter 6 shows the steps taken in the design process of the fuselage of the aircraft and Chapter 7 and Chapter 8 describe the aerodynamic and structural wing design respectively. Chapter 9 describes the design of the Powerplant systems of the aircraft and its novel aspects. Chapter 10 and Chapter 11 describe the design process of the empennage and landing gear of the aircraft. Chapter 12 looks at the aerodynamic modelling of the whole aircraft and carries out a noise analysis of the design. Chapter 13 describes the analysis of the flight performance of the aircraft. Chapter 14 gives a plan for the manufacturing, assembly and integration plan of the aircraft in its production phase, while Chapter 15 describes the logistics and operations plan of the aircraft. Chapter 16 discusses the reliability, maintainability, availability and safety of the aircraft. Chapter 17 gives a finally summary of the design of the carbon neutral aircraft. Chapter 18 carries out the financial analysis and shows that the carbon neutral aircraft can be financially feasible and profitable and finally Chapter 19 gives a plan for how the further design of the aircraft can be carried out. Then a risk assessment of the project is described in Chapter 20 finally moving on to the Conclusion in Chapter 21.

2
Project Overview

This chapter gives a high level overview of the project. Starting with the project objectives in Section 2.1, the project objective statement and the need statement are described. The main stakeholder requirements are described in Section 2.2, followed by a brief summary of all the previous design stages and a description of the final concept chosen for the detailed design phase, in Section 2.3. Finally, the chapter is concluded with a functional analysis of the aircraft subsystems in Section 2.4.

2.1. Project Objective

The legal and environmental authorities around the world have started raising concerns on the environmental impact of current current living standards and industrial operations, resulting in an increased demand for emission reductions. One such action taken by authorities in Europe is the European Green Deal, aiming to make Europe climate neutral by 2050 [1]. Since the aviation industry forms a significant part (2 % of total human-induced CO_2) of total emissions, an innovative approach towards carbon neutrality is needed. [1]

In order for aviation to become carbon neutral, new aircraft designs are needed which consume less fuel and can use carbon neutral energy sources. A lot of promising research into alternative energy sources has been carried out and many improvements are currently being made as well. However, the amount of investments made for the full scale development of these innovative improvements is significantly low. There are two main reasons behind this, firstly the sparse infrastructure available for these innovative designs and second is the low demand from the airlines due to limited infrastructure development. This results in a so called "chicken-and-egg" scenario where neither side wishes to make the first commitment due to uncertainties. This is where the current project comes into play, to serve as a mediator solution to this problem. Thus, the mission need statement of the project can be summarised as follows.

Mission Need Statement

New strict environmental legislation, but the lack of current sustainable energy infrastructure necessitates the development of a new aircraft which can be converted to be carbon neutral when infrastructure becomes available, within the next ten years.

Thus, based on the above mentioned need statement, the objective of the project is set to design a baseline aircraft which can enter into service by 2030. This aircraft will serve as a solution for the "chicken-and-egg" scenario in the carbon neutral energy field. This will increase certainty for customers and will allow airlines to make initial steps towards a sustainable change. The main target area for the project is the Airbus A320 and Boeing 737 class aircraft. This class of aircraft incorporates a substantial share of the total market and will thus have a large impact on the problem mentioned earlier. To conclude, the objective statement of the project can be summarised as follows:

Project Objective Statement

Design an Airbus A320 (or Boeing 737) replacement aircraft that initially uses kerosene but can be converted to be carbon neutral within one month, using a design team of 10 students with a time limit of 10 weeks.

2.2. Stakeholder Requirements

The carbon neutral aircraft (CNA) was designed based on a few top level requirements from various stakeholders. These stakeholders were divided into categories; the stakeholders are the customers (airlines), legal aviation authorities (EASA), airports and the passengers (or the general population). Each of these stakeholders provide a set of requirements however some are more critical than the others, these are the key stakeholders. The key stakeholders are the customer, aviation authorities and airports. These stakeholders are given equal priority because requirements not being met by them would kill the design. The reason that the passengers aren't considered 'key' stakeholders is that requirements stemming from them are also included within the requirements from aviation authorities. For ex-

[1] URL `https://www.atag.org/facts-figures.html` cited [19. June 2020]

ample, there are requirements for noise and emissions that must be met from both the authorities and passengers. It must be noted however that the CNA tries to improve on these requirements rather than just meeting them exactly, in-line with the overall goal of sustainability. The top level requirements from each key stakeholder are summarised in Table 2.1.

Table 2.1: Stakeholder Requirements

Identifier	Description
Customer	
REQ-CN-PERF-1	The CNA shall have a cruise speed of Mach 0.78.
REQ-CN-PERF-2	The CNA shall have a maximum range of at least 3400 nm.
REQ-CN-PERF-3	The CNA shall carry a payload of 20 tons.
REQ-CN-PERF-4	The CNA shall have a range at max payload of 2150 nm.
REQ-CN-PERF-5	The CNA shall be able to carry 194 pax in a high density lay-out and 7 LD3 containers underfloor at max payload.
REQ-CN-PERF-17	The CNA shall be able to convert to carbon neutral within one month.
REQ-CN-SAFE-4	The CNA shall have a 10^{-9} /flight hour risk of catastrophic failure
REQ-CN-ECON-5	The CNA shall enter into service in 2030
REQ-CN-ECON-6	The list price of the CNA shall be $110 million
REQ-CN-SYS-SUS-1	The CNA's primary structure shall be recyclable for 75% of its mass
REQ-CN-SYS-SUS-2	The CNA shall have a 10% emission reduction per passenger kilometre with repect to A320neo/ 737max whilst using fossil fuel
REQ-CN-ECON-7	The CNA shall be capable of serving all airports currently served by the Airbus A320 or Boeing 737
Airport	
REQ-CN-PERF-19	The CNA shall be able to take-off within a runway length of 1800m at sea level
REQ-CN-PERF-31	The CNA shall have a wingspan of less than 36 m while on ground.
Legal	
REQ-CN-SYS-SUS-3	The CNA shall produce no more than 96.5 EPNdB at the lateral full-power reference noise measurement point as described by ICAO annex 16
REQ-CN-SYS-SUS-4	The CNA shall produce no more than 91.3 EPNdB at the flyover reference noise measurement point as described by ICAO annex 16.

2.3. The Design

In previous reports, an extensive exploration of potential solutions for the objective has been done [2][3]. After an elaborate trade-off, three concepts were selected [4]. The first concept was a braced high wing convertible to use synthetic kerosene. The second concept was a high wing cryogenic hydrogen aircraft with extra fuel storage pods mounted under the wings, that used fossil kerosene without the wing mounted pods before conversion. The third concept was a low wing aircraft with ultra high bypass ratio (UHBR) turbofans and an aft boundary layer ingestion (BLI) propulsor, convertible to use synthetic kerosene. These concepts were worked out in more detail, after which the best concept was chosen. In this final trade-off, the main criteria were operational cost, safety, sustainability and certainty. The conclusion of this trade-off was that concept one was the best concept, performing better at all criteria except safety. Furthermore, concept two was the designated loser, performing significantly worse in all criteria.

The winning concept was, therefore, a high aspect ratio braced wing aircraft initially operating on fossil fuel, with the possibility to switch to carbon-neutral synthetic kerosene. Certain aspects from the detailed concepts, however, showed great potential and were therefore added. The carbon neutral airliner design that is described in this report has the following unique aspects:

- High Wing
- High Aspect Ratio Wing
- Strut-braced Wing
- Foldable Wingtips to increase Wing Span whilst remaining under ICAO Type C
- A Boundary Layer Ingestion Ducted Fan at the Aft Fuselage
- T-Tail
- Eventual Compatibility with Synthetic Kerosene
- Ultra High Bypass Ratio Turbofans
- Novel Slim Landing Gear System with Supporting Gears

The carbon neutral airliner, ALBATROSS EMBRACER, will be referred to in this report as CNA (Carbon Neutral Aircraft). A visual representation of the CNA is shown in Figure 2.1.

Figure 2.1: Isometric view of the CNA

2.4. Functional Analysis

In order to describe the functions that the aircraft has to perform, a Functional Breakdown Structure (FBS) was generated and is depicted in Figure 2.2. Initially, several key phases for the aircraft were identified. These phases are illustrated as red boxes and they include the development phase, maintenance phase, operation, conversion to carbon neutral and lastly retire. The main focus of this diagram is on the Operation, Conversion and Retire phases that the aircraft undergoes.

The operation phase in the FBS consists of several higher level functions that the aircraft must perform during the lifetime. The functions are detailed up to two levels and various aspects related to nominal missions and emergency situations are explored. The higher level functions are represented in blue and are designated the number after the first decimal point, whereas the lower level functions are shaded in grey and the function number appears after the second decimal point.

The conversion phase is considerably one of the most important phases for this aircraft as it closely reflects the goal of this aircraft. However, given the design choices made for the carbon neutral energy source, the conversion procedure is not too sophisticated thus this phase is less extensive.

With the FBS in place, a Functional Flow Diagram (FFD) was formulated. The FFD in Figure 2.3 illustrates the chronological order of all the functions executed during the operation phase. The order of the highest level functions are shown on top section of Figure 2.2. These top level functions are very similar to a conventional aircraft, where the aircraft is developed and manufactured, operated and retired. One major difference is that the CNA has a conversion process within it's lifetime (hence, two operation phases are shown in the diagram). Within this diagram, the "AND" logic gates are used to describe the functions being executed in parallel and the "OR" logic gates are used to describe decisions/choices that might be made at certain times.

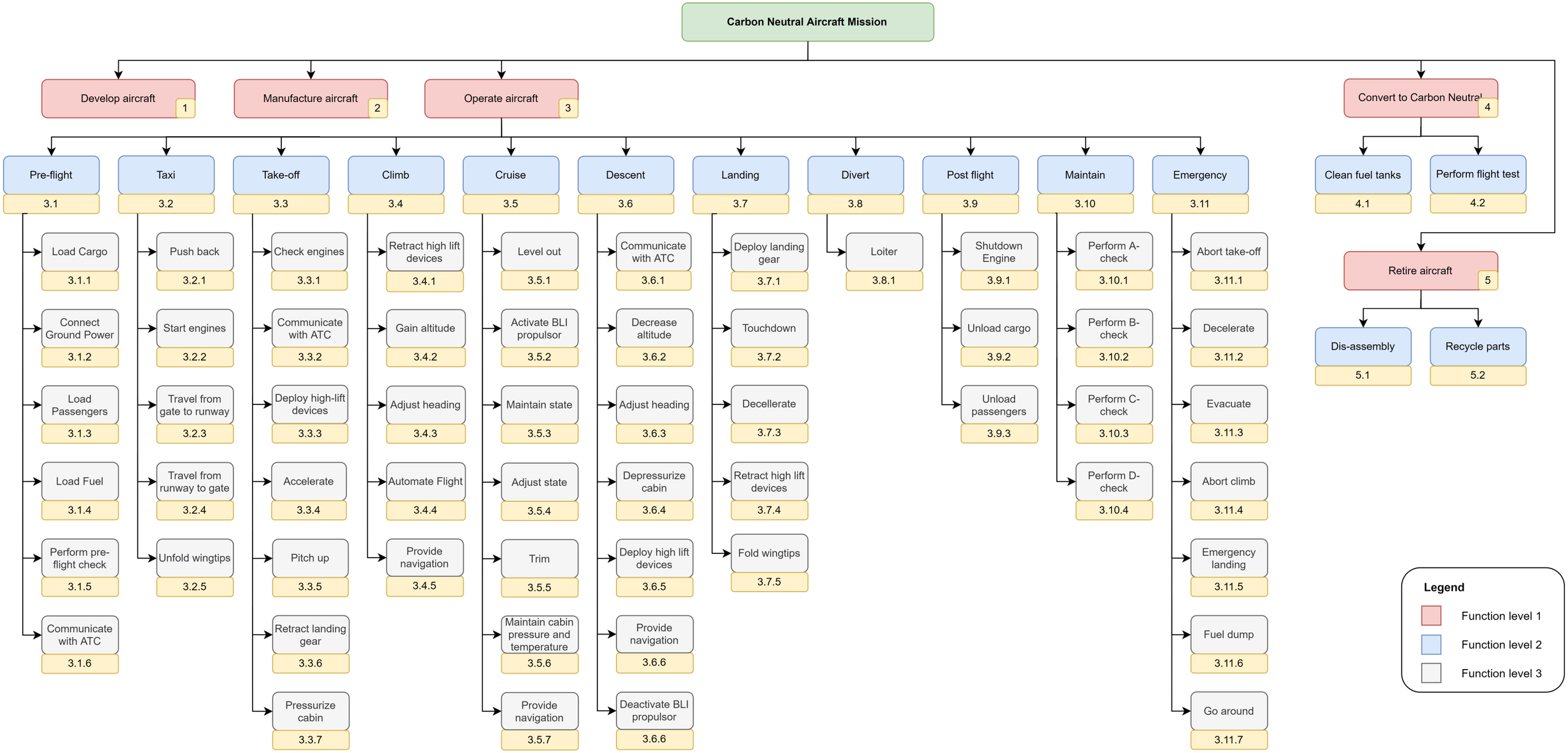

Figure 2.2: Functional Breakdown Structure

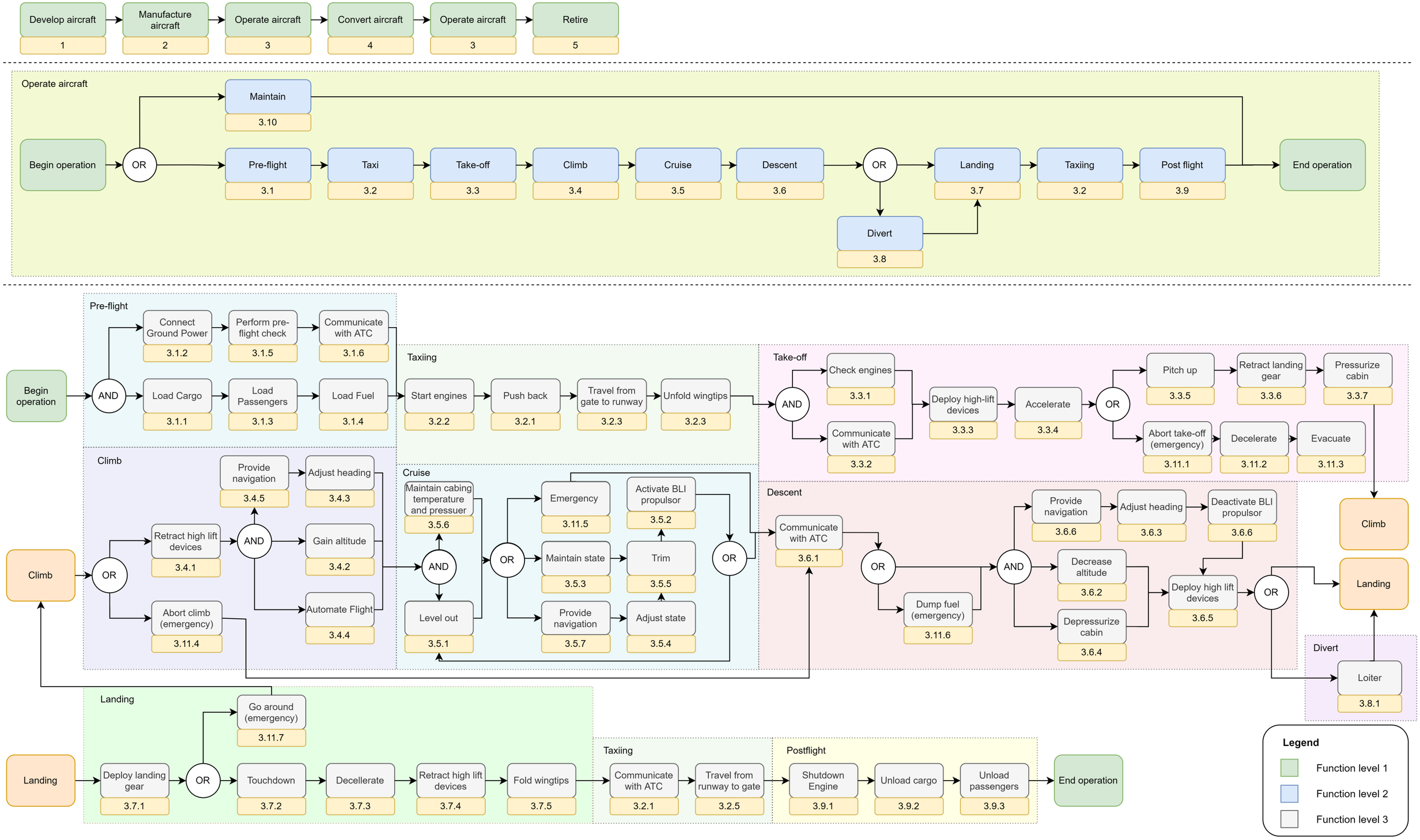

Figure 2.3: Functional Flow Diagram

3
Market Analysis

The aim of this chapter is to assess the competitiveness of the CNA, by comparing it with the market trends and the competitor aircraft. The top level requirements are compared with competitor aircraft, where they were verified that the CNA is a viable aircraft to be in the market. The general trends of the industry are reported in Section 3.1, the customer needs are critically analysed in Section 3.2, the financial environment of the CNA is discussed in Section 3.3, and the market positioning of the CNA is established in Section 3.4. Finally, the requirements that were formed through the market analysis, as well as the SWOT analysis of the CNA are reported in Section 3.5.

3.1. Trends in Aviation Industry

From as early as the 1980s, the aviation industry has been growing due to the exponential growth in world traffic. This can be seen in Section 3.1, with about 4.3% growth every year [5]. By the entry into service of the CNA in 2030, world annual traffic is estimated to have almost doubled from today. Furthermore, the average seating offered by single aisle aircraft has been increasing over the past few decades, seen in Figure 3.2. 169 seats are offered on average nowadays, which is expected to grow to approximately 189 by 2030, assuming a linear growth since 1998. These forecasts were made before the ongoing COVID-19 outbreak, which may cause them to significantly differ from reality. The number of flights have dropped and aircraft manufacturers are facing a large amount of unemployment [1]. However, for the duration of this DSE project, it is assumed that world traffic will recover latest by the time the CNA enters into service.

One of the largest challenges faced by the industry is to reduce the environmental impact of aviation, which is currently responsible for a large portion of total global CO_2 emission. Combined with the increasing annual traffic, aircraft will be responsible for an even larger portion of total CO_2 emissions. One way of reducing the CO_2 emissions is to improve the efficiency of the aircraft and their operations. However this is not a valid option to reach a carbon neutral aircraft, since even the most efficient aircraft will still emit CO_2 as long as the aircraft are making use of fossil fuel. This gives rise to a need for a new energy source that has a neutral environmental impact. There have been multiple projects and concepts for aircraft with renewable energy sources, such as solar energy [2], electric energy by means of batteries [3] [4] and liquid hydrogen [5]. However, none of them have the potential to completely replace fossil fuels to this date, especially in medium to long range aircraft. Hence, the CNA needs to offer a solution to this dilemma of increasing world traffic and the increase in emissions that comes along with it, by means of a carbon neutral aircraft.

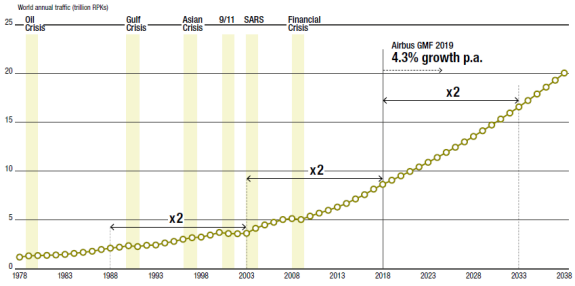

Figure 3.1: World annual traffic in Revenue Passenger Kilometre and forecast until 2038 [5]

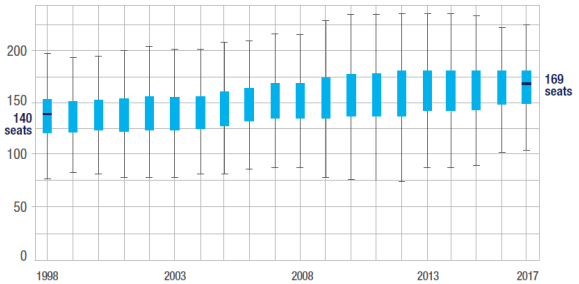

Figure 3.2: Annual trend in seat offered by single-aisle aircraft [6]

[1] URL https://www.seattletimes.com/business/boeing-aerospace/boeing-indefinitely-extends-production-shutdown-at-washington-state-plants-due-to-coronavirus/ cited [17. June 2020]
[2] URL https://aroundtheworld.solarimpulse.com/leg-15-from-New_York-to-Seville cited [17. June 2020]
[3] URL https://www.nasa.gov/press-release/nasa-electric-research-plane-gets-x-number-new-name cited [17. June 2020]
[4] URL https://www.theguardian.com/business/2017/sep/27/easyjet-electric-planes-wright-electric-flights cited [17. June 2020]
[5] URL https://www.aerospace-technology.com/projects/hy4-aircraft/ cited [19. June 2020]

3.2. Customer Needs

There are series of customer needs, in the form of stakeholder requirements that the CNA is designed to fulfil. These are namely, REQ-CN-PERF-1, REQ-CN-PERF-3, REQ-CN-PERF-4, REQ-CN-PERF-5, REQ-CN-SYS-SUS-1, and REQ-CN-SYS-2 described in Section 2.2. These were compared with the capabilities of competitor aircraft of the CNA to assess its competitiveness in the market.

The specified Mach number directly translates to the travel time the customer wants for a given flight path. It is possible to fly an aircraft at its most optimum altitude and velocity to minimise its fuel consumption, but that is often times slower. For airlines, it is beneficial to have an aircraft that is designed to fly fast while being fuel efficient, which can be operated many more times in a given time frame. The competitors of the CNA, such as the Boeing 737 and A320, have the cruise Mach numbers of 0.78 and 0.79 respectively, which are very similar to the customer needs[7] [6]. The combination of a harmonic range of 2150 nm and a payload mass of 20 t is compared with competitors' payload and range combinations. It was seen that the CNA has a relatively larger range than most single aisle aircraft, such as MD-83 and the 737 series, while having a larger payload mass than the A320 [**?**]. As seen from Section 3.1, the demand for world traffic is increasing as well as the average seating of the single aisle aircraft. It can be speculated that by 2030, approximately 189 seats are offered on average by potential competitors, while the CNA will offer more seats than that.

The production and the disposition of aircraft are highly energy intensive processes, which rely heavily on energy sources based on fossil fuel. In 2011, Airbus has demonstrated the capability of recycling 70-75% of aircraft mass, and their current goal is to reach 90% recyclability [8]. This means that 75% is about the minimum required for the CNA to keep up with its recyclability. Although the CNA is designed to be carbon neutral after conversion to its new energy source, it will emit CO_2 before that. Additionally, the exact conversion time is not known at this stage of the project. Furthermore the carbon neutral energy source of the CNA, synthetic kerosene, is a drop-in fuel. Meaning any aircraft that currently operates with fossil fuel based kerosene can operate with it. This is why in order for the CNA to be competitive throughout its lifetime, lower emission than competitors is essential.

The validity of these requirements in 2030, which is the entry in to service of the CNA, is extremely difficult to predict. For example, Airbus has developed the A320neo family which was able to improve fuel efficiency by at least 15% compared to the A320ceo [9]. This suggests that the competitors of the CNA will perform better to some extent than current aircraft in the market of 2020. This means that competitiveness of the CNA cannot be achieved by just being slightly better than current competitors. This is why it is crucial for the CNA to meet its ambitious requirements, such as the 10% emission reduction compared to A320neo.

3.3. Financial Environment

Effective market penetration is not only a matter of delivering the desired aircraft to clients, it also heavily relies on the aircraft's market positioning. This environment, through a variety of elements, will greatly affect the aircraft's desired list price and, through this, constrain the entire design process with cost limitations. With a clear push for sustainable and fuel efficient flight, companies are searching for an effective solution in an environment full of uncertainties. A variety of innovative designs are constantly presented but their overall costs are often the bottleneck for a deal to be made, the Carbon Neutral Aircraft's costs thus have to be competitive.

The main strengths of the aircraft are its carbon neutral fuel usage and its fuel efficiency. The fuel efficiency increase over conventional aircraft will reduce operating costs while the carbon neutral status can play a major part in company branding. Furthermore, despite the currently higher prices of synthetic fuel compared to regular jet fuel, with the aircraft entering service in 2030 and being operational for the decades to follow, the overall costs stemming from the synthetic fuel use will decrease over time [3]. All this will be taking place while regular jet fuel's associated costs stagnate.

The shift to sustainable fuel will further be strengthened through financial stimuli in the form of government subsidies and positive market sentiment. Indeed, over the course of the last decade, the trend clearly shows a growth in both government and population's involvement and interest in a carbon neutral future. Companies are now given incentives to invest in this future and are pushed to profitability despite the increased costs of carbon neutrality. Furthermore, with the current airline industry heavily reliant on subsidies and tax breaks to even stay solvent, they can not afford losing government support and have to reach their emission targets. From a financial perspective, becoming

[6] URL `https://web.archive.org/web/20160403132507/http://www.airbus.com/aircraftfamilies/passengeraircraft/a320family/technology-and-innovation/` cited [17. June 2020]

carbon neutral is thus a must for any airline.

Breaking down the financial incentives of a carbon neutral aircraft reveals a list of promising benefits. These are listed in Table 3.1 with their probability of occurrence and their financial impact rated from low to high. As expected, governments are expected to be involved in this push for a green future. With them setting aside money to promote innovation and sustainability, they incentivize the industry through tax breaks; low interest loans and grants for research and development purposes.[7] This push for green energy is furthermore reflected through the increase in carbon taxes effectively making regular kerosene increasingly expensive. With airline customers having an ever growing vocal opinion and preference for carbon neutral flying, it is forecasted that they will increasingly opt for such flights. This increase in demand will allow airlines to charge a premium on ticket prices for carbon neutral flights and thus increase profitability. It is also to be noted that airports also have their own sustainability and emissions goals and regulations. With their required push towards carbon neutrality they are forecasted to further give incentives to airlines through discounts on landing and docking fees. Finally, by flying carbon neutral, airlines will be exempted from the fines planned after 2050 for carbon emissions both eliminating this financial burden and avoiding negative publicity.

Table 3.1: Probability and impact analysis of forecasted financial benefits

Financial benefits	**Probability**	**Impact**
Government subsidies - tax breaks	High	High
Government subsidies - initial cost	High	High
Carbon taxes	High	High
More passengers due to market sentiment	Medium	Medium
Premium on ticket prices	Low	Medium
Discount on airport fees	Medium	Medium
Reduced risk of fines after 2050	High	Medium

3.4. Competitive Market Positioning

With a clear necessity of being financially attractive to the operating airline and financially feasible and profitable to the client airline producer, these parties have to be met with a competitive value proposition. The first step in assessing a competitive market positioning is to evaluate and determine a targeted market share for the aircraft. Through plans of designing an aircraft similar in size and range to the Airbus A320 and Boeing 737 the total size of the market can safely be assumed as being equal to the amount of those aircraft in service. This can be expanded and simplified to the worldwide narrow-body fleet in service expected around 2030 which is forecasted to equal 23,128 aircraft by 2027 [8]. Assuming the two mentioned manufacturers have similar market shares across their fleet, a respective market share of 45 and 43 percent of the narrow-body market is noted for the A320 and the B737 [9].

These observations lead to two possible scenarios for the market penetration of the design. The first scenario is that the client is a direct competitor to Airbus and Boeing and positions the aircraft as such. It will thus target to obtain a similar market share of $88 \cdot \frac{2}{6} = 30\%$ by the year 2050 which is forecasted as the tipping point towards a 100 % renewable energy airline industry [10]. This leads to a targeted aircraft market of $0.3 \cdot 23128 = 6938$ aircraft by 2050. With the first aircraft entering into service in 2030, a period of 20 years is given to achieve this production quantity. In order to achieve the client's production demands, the process aims at a production volume of 347 aircraft a year.

The other possible scenario is that either Airbus or Boeing become the client by buying the rights to this design. This design would then be forecasted to replace the client's fleet by 2050 and thus obtain a market share of around 45 %. The targeted market would thus be equal to 10,407 aircraft by 2050 and would, using the same calculation as before, lead to a production volume of 520 aircraft a year.

With a design process heavily impacted by possible cost restrictions, it is crucial to determine a target cost per aircraft before starting this process. This can be achieved through the initial cost budgeting method of the DAPCA IV cost model using the production volumes determined above [3]. The total production output case of 6938 aircraft leads to

[7] URL https://www.government.nl/latest/news/2019/06/28/climate-deal-makes-halving-carbon-emissions-feasible-and-affordable cited [18. June 2020]

[8] URL https://www.oliverwyman.com/our-expertise/insights/2017/feb/2017-2027-fleet-mro-forecast.html cited [18. June 2020]

[9] URL https://www.forbes.com/sites/greatspeculations/2020/01/06/how-airbus-has-grown-over-the-years-to-dethrone-boeing-as-the-largest-commercial-aircraft-maker/586afb5a3a59 cited [18. June 2020]

[10] URL https://www.icao.int/environmental-protection/Documents/EnvironmentalReports/2016/ENVReport2016_pg16-22.pdf cited [18. June 2020]

an estimated cost of 54.5M$ per aircraft while the 10407 aircraft case leads to an estimated 51.7M$ per aircraft, both given in 2030$s [3]. With this estimation method based on regular kerosene aircraft, it has to be noted that the final price is affected by the design's carbon neutral fuel type and further innovations increasing fuel efficiency. The usage of synthetic kerosene and the production and development of the novel brace and BLI elements will significantly increase cost. However, as discussed in Section 3.3, the carbon neutrality of the aircraft allows the forecasted financial benefits to relieve cost on all fronts through subsidies. With governments actively trying to minimise any additional costs stemming from the transition to and usage of carbon neutral fuel types, it can be estimated that the increase in cost mentioned above will be compensated by active government support. With this support forecasted to lead to anywhere from 10 to 50% cost reduction from the accumulation of financial benefits, the subsidies ultimately keep the expected costs around the prices mentioned.

With the design's profitability being key to successful production while the design's list price dictates its successful market penetration, a healthy balance must be found. The targeted production costs can be compared to the current list prices of similar aircraft to determine which profit margins are reasonable. The list price for the A320neo is found to be 110M in 2018$s [11] but, through major deals and big volume sales, most Airbus' customers receive discounts of up to 50% when sold [12]. The usual sale price thus lies around 55M in 2018 $s which leaves little room for the Carbon Neutral Aircraft to be profitable for manufacturers. Projecting these prices onto the two possible manufacturing client cases mentioned earlier, it becomes clear that if the client positions the CNA as a competitor to the existing fleet, the list price inevitably has to surpass that of the competition in order to be profitable. But, with the knowledge of Section 3.3, it can be concluded that this higher price would not necessarily be a problem due to the range of financial benefits incurred down the line from the aircraft's carbon neutrality. In this case, the production volume of 347 aircraft per year at 54.5M $ would serve as an effective target. Looking at the other possible scenario of either Airbus or Boeing being the client and replacing their fleet with this design, the production cost of 51.7M $ leaves significantly more room for profit on a 55M$ list price. At a yearly production of 520 aircraft at 51.7M$ per aircraft, the client could list their fleet replacing aircraft at the same price as its predecessor and remain profitable throughout its push towards carbon neutrality.

3.5. Top Level Requirements and SWOT Analysis

With the market analysis performed, the customer needs were critically compared with the market environment and the financial environment of the aviation industry. Once the competitiveness of the new design is confirmed with its specified level of performance and the price, these were formulated into top level requirements. These include the customer needs verified in Section 3.2, the list price and the production cost per aircraft discussed in Section 3.4.

Given that the CNA complies with all these requirements, its strengths, weaknesses, opportunities and threats (SWOT) were analysed and summarised in Table 3.2. The main strengths of the CNA are that it flies with a carbon neutral energy source, and improved efficiency while operating with traditional fossil fuel. This means that the CNA is always more environmentally sustainable than competitors without depending on the nature of its energy source. The opportunities the CNA expects are the subsidies to promote the use of a carbon neutral energy source and the improved performance over competitors with the use of novel configurations. This also makes it more attractive to investors. On the other hand, this may result in a more expensive and longer development as there is no baseline model the CNA can be developed upon. One of the threats are the emerging competitors, as all aircraft manufacturers are shifting towards more sustainable aviation. Another threat is not particularly towards the CNA, but the aviation industry is facing an extremely difficult time with the COVID-19 outbreak, which may negatively impact the market over an extended period of time.

Table 3.2: SWOT analysis of the CNA

	Helpful	**Harmful**
Internal Factor	**Strengths** - Can operate carbon neutral - Improved fuel efficiency	**Weaknesses** - Higher estimated price - Longer development time
External Factor	**Opportunities** - Attractive to investors - Potential subsidies	**Threats** - Emerging competitors - Decline in aviation industry due to COVID-19 outbreak

[11] URL `https://www.airbus.com/newsroom/press-releases/en/2018/01/airbus-2018-price-list-press-release.html` cited [18. June 2020]

[12] URL `https://simpleflying.com/airbus-reveals-on-average-airlines-get-50-off-airline-list-prices/` cited [18. June 2020]

4
Design Methodology

This chapter details how the design of the aircraft is approached. Section 4.1 and Section 4.2 discuss the sustainable development strategy and the iteration methodology respectively. The verification, validation and sensitivity analysis methodologies are discussed in Section 4.3, Section 4.4 and Section 4.5 respectively. The budgeting and weight estimation methodologies are in Section 4.6 and Section 4.7 respectively.

4.1. Designing Towards Sustainability

One of the key aspects to be considered during the design of the aircraft is the sustainability. The importance of sustainability in the aircraft design is explained in Section 4.1.1 and the strategies adopted towards a sustainable design are explained in Section 4.1.2. Lastly, the sustainability of the final design of the CNA is discussed in Section 4.1.3.

4.1.1. Motivation for Sustainable Design

The current global pollution is a central topic in the future development of the airline industry. As of 2020, the global emissions from aviation are 70% higher than in 2005, and projections show that by 2050 the increase is going to be 300% with respect to 2005 [1]. To reduce the emissions and face this global issue, the European Commission has set the European Green Deal, an agenda for sustainable development in the EU which resulted in the Circular Economy Action Plan[2]. According to the Plan, the solution for a sustainable development is the transition from a linear economy to a circular economy, which is shown in Figure 4.1.

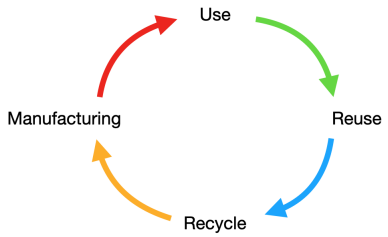

Figure 4.1: Circular Economy

The philosophy in the circular economy is that a product has to be designed in such a way that it can either be reused or recycled after its end-of-life. In case the product is recycled, the materials of the product will become an input material for other products, so the need of raw materials is minimised. On the contrary, the linear economy continuously requires raw material and the products become unused waste after their operational life. It is therefore of utmost importance to design an aircraft that can best fit into the circular economy and be sustainable under the social, environmental and economical aspects.

4.1.2. Sustainable Development Strategy

Multiple strategies were established to make the designing of the CNA sustainable at the initial stage of the project. These can be categorised into two, the strategies to make the designing process more sustainable, and the strategies that make the final product more sustainable.

Three strategies were established to ensure sustainability of the working environment of the design. The social sustainability of the design process was mainly assured by two strategies. One is to establish rules for the well being of the workplace, such as strict rulings against discrimination of other team members. Another is that all team members have agreed to strictly follow measures against the COVID-19 outbreak, to minimise negative social impact by all

[1] URL https://ec.europa.eu/clima/policies/transport/aviation_en cited [18. June 2020]
[2] URL https://ec.europa.eu/commission/presscorner/detail/en/ip_20_420 cited [1. May 2020]

group members. Environmental sustainability of the design process was ensured by encouraging all team members to perform their tasks digitally as much as possible to produce minimal paper waste.

High emphasis was put on designing a more environmentally sustainable aircraft in the design process. This was mainly driven by the system requirements, such as REQ-CA-SUS-1 and REQ-CA-SUS-2, which are requirements on the recyclability and the emission levels of the aircraft respectively. However, these requirements were deemed not enough to design a sustainable enough aircraft. Hence, five objectives were established during the baseline phase to clarify how the design must be shaped so that it is sustainable. These were: the reduction of fuel consumption before conversion, the minimisation of noise emission, the minimisation of material usage, the usage of recyclable materials to the greatest extent possible, and the selection of a carbon neutral source that has the least environmental impact. All the team members were aware of these objectives, which led to design choices that comply the with the defined objectives as much as possible.

The effect of establishing these objectives can be seen in various design choices, as well as from the nature of the final design of the CNA. For example during the concept selection phase, when three different concepts were compared to select the design to proceed further with, the sustainability of the concept was one of the criteria used for scoring. This made sure that the chosen concept has the best performance, and is also environmentally sustainable at the same time. Later when a more technical design was performed, each department was allocated more specific objectives that were derived from the five objectives explained above. For example, the propulsion department was responsible for maximising the fuel efficiency by optimising for the minimal thrust specific fuel consumption and the structures department was responsible for selecting recyclable material as much as possible.

4.1.3. Sustainability of the Final Design

Given that the aircraft accomplishes the mission need and project objective stated in Section 2.1, the aircraft will have the capabilities to make a positive impact in the field of sustainable aviation. The first and most important impact of the CNA pertains to the environmental side of sustainability. As the aircraft will be able to shift to a carbon neutral energy source by 2030, the aircraft has the potential of reducing the net CO_2 emissions of the aviation industry, as its carbon emissions will be zero after conversion.

On the social side, the aircraft will increase the demand of carbon neutral energy sources, which will subsequently increase the production and availability of such sources for other aircraft. Furthermore, the aircraft will pioneer the world of sustainable flying, and will encourage the airlines and aircraft manufacturers to shift towards designing carbon neutral aircraft. The social impact of the aircraft will go beyond the aviation sector: by demonstrating that a propulsion system conversion is possible whilst keeping the same structure, the CNA will be a concrete example of energy source transition for other transportation industries such as the automotive and maritime sectors. Furthermore, the noise level of the aircraft is in line with the limits stated in the Annex 16 "Environmental Protection" and set by ICAO (International Civil Aviation Organisation). This means that the aircraft will not generate more noise than current airliners, implying that inhabitants in the surroundings of the airports will not be negatively affected by the operational procedures of the CNA.

The last aspect is the economical aspect. 75% Of the aircraft's primary structure mass has to be recyclable, which makes the aircraft fit well inside the circular economy, therefore accomplishing the objectives stated by the Circular Economy Action Plan. Furthermore, a proper manufacturing approach for this aircraft will further decrease the unit cost, therefore increasing the demand and circulation of the CNA around the world.

4.2. Iteration Methodology

The design of an aircraft is a complex process, as there is no correct solution from the start. Hence, the design has to be iterated as much as possible, with the constraints being the available human resources and time. Design iterations also require the effective flow of data, design choices, and interfaces across the design departments. This was achieved by keeping track of inputs, outputs and interfaces of each department via systematic management. These inputs, outputs and interfaces were given identifiers, and updated and checked frequently to keep track of all design processes.

The iteration process is visualised in Figure 4.2. The baseline values of the lift to drag ratio (L/D) and thrust specific fuel consumption (TSFC) are obtained from the previous design phase. These values were used to obtain initial (Class I) estimates for the operational empty weight (OEW) and maximum takeoff weight (MTOW) based on reference aircraft. The MTOW, preliminary aerodynamic parameters and legal requirements (on take-off, climb and landing performance) were used to determine the thrust to weight ratio (T/W) and the wing loading (W/S) using a loading di-

agram. Then the required thrust and the wing surface area were sent to the propulsion and the aerodynamics groups. During Phase I, the aircraft was designed in detail with many interfaces between the departments, shown by the horizontal arrows in Figure 4.2. After this, in Phase II, the class II weight estimation was performed and then the aircraft was designed for stability and controllability both in the air and on the ground. Then finally the class II weight estimation was compared with class I. If the difference between the OEWs was higher than 1%, the design was re-iterated but this time the new class I weight estimation was found using the new class II OEW and updated L/D and TSFC values. The iteration procedure was halted when the two OEW converged to within 1% of each other.

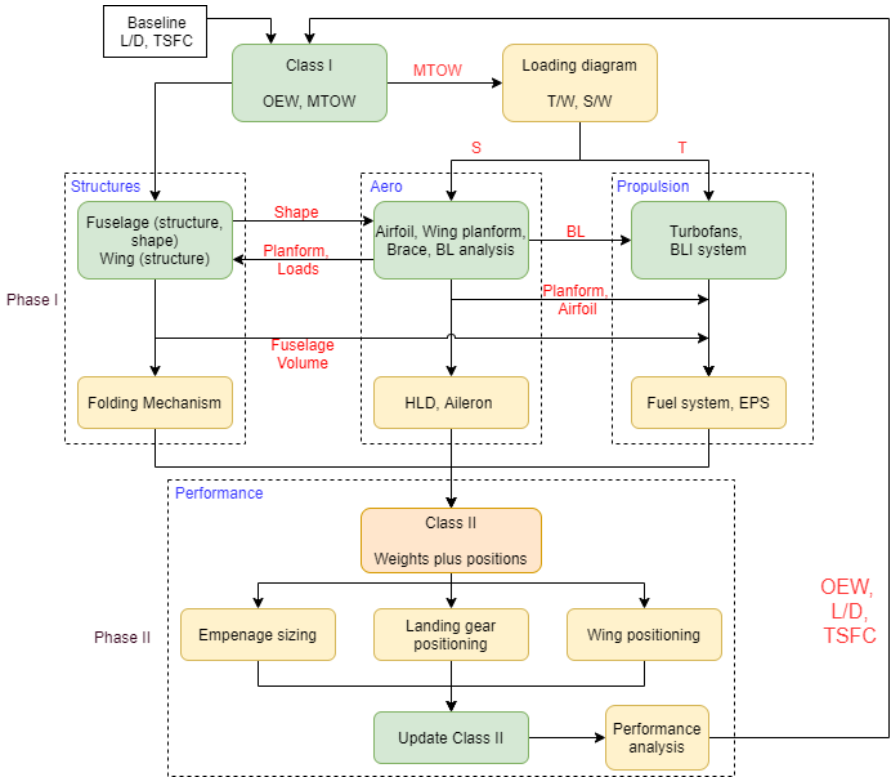

Figure 4.2: Iteration flow diagram [3]

4.3. Verification Methodology

The process of designing an aircraft requires complicated calculations to be performed so as to support the design choices and to demonstrate the feasibility of the design. Thus, several design tools capable of carrying out the necessary calculations were developed. If for any case an error was present in the calculations, the results would be invalid, and could have the potential to jeopardise the whole design process. In order to avoid this, it is thus necessary to have a rigorous verification process. The purpose of having a verification process is to check if the developed model is accurately representing the chosen physical model [10]. This verification process was carried out by conducting a series of tests on the developed programs at namely two different levels, unit level (Unit Tests) and system level (System Tests).

For the case of the unit tests, the developed design tools were tested at the lowest (unit) level. These tests involved testing individual functions either by varying the input and assessing if the behaviour of the output is as expected, or by comparing the output against an analytical solution. This therefore verifies that each function was in itself correctly formulated.

In contrast with the unit tests, the system tests involved testing the program as a whole. The system tests essentially ensured that the program, as a whole, was functioning as it should by testing if each of the functions were assembled correctly. These tests came after the successful completion of the unit tests, so as to ensure that, if an error was to be found, it wouldn't be because of a fault in a function, but rather that they are combined incorrectly.

[3] The different colours only show distinction for better readability

4.4. Validation Methodology

All numerical computations are validated to ensure the tools used correctly model reality as well as to prove that the assumptions that were used are valid. Three validation methods are applied throughout the design process. The first method is 'comparison'. The outcome is compared with the range of values typically found in aircraft of similar mission. A database of 9 reference aircraft is utilised, each aircraft having over 80 recorded parameters on multiple subsystems such as fuselage dimensions, high lift devices, performance and many more. Comparison is especially applicable on parts of the aircraft that closely resemble conventional designs. The second method is 'statistical relationships'. When the range of typical values in reference aircraft is large, a regression is used to link two parameters in the database together. For example, the tail surface area is highly dependent on the tail arm, so the statistical relationships method is very suitable. Finally, the third method is 'run code with reference inputs'. Python scripts are ran with inputs from real aircraft, which should yield values within a certain predetermined margin from the actual true value (usually 5% is used, but this depends on the certainty of the assumptions). If the outcome lays outside this range, two causes are possible. The assumptions used have a larger effect than initially accounted for and are thus need to be re-evaluated, or there might be a bug in the code which remained undetected after verification.

4.5. Sensitivity Analysis Methodology

The sensitivity analysis is performed to determine the effect certain assumptions can have on the final product. Not all assumptions underwent a sensitivity analysis, only assumptions which have the greatest uncertainties. It is also important to differentiate between uncertain assumptions. Assuming that an efficiency is 90%, but it could actually be 89%, is an uncertain assumption.

A sensitivity analyses helps discover assumptions that have large effects on the final aircraft design. Which in turn helps to discover what can be done to mitigate the effects of these assumptions. In the recommendations, it can be specified what further steps have to be taken to check if the sensitive assumptions are incorrect. And if they are incorrect what could be done to improve the aircrafts design. The sensitivity analysis also helps discover design cancelling assumptions. If these assumptions turn out to be incorrect, it would remove the whole possibility of the design. These incorrect assumptions would result in major design requirements not being met, for example, the 10% reduction in fuel consumption.

4.6. Budgeting Methodology

The variety of resources available to a design team must be carefully managed and monitored to allow efficient resource allocation while minimising the tendency for resource usage to snowball. In this design's case, the crucial resources affecting both technical and financial feasibility are the weight and the cost. For these, an initial maximum value is set as baseline for all design departments to follow. A contingency is added onto this value to account for the significant uncertainty at this stage in the design process. These limits are then updated as design iterations are performed to better represent the final product and, through this, the contingencies decrease. The resources can furthermore be shuffled between departments to locations that can make better use of them. In the end, the resource budgeting makes sure each department stays up to date on the latest weight and cost targets and uses those across the design. The budget thus allows for a well integrated and connected design team that strives for optimum resource usage.

4.7. Weight Estimation Methods

The design process is characterised by classes of weight estimations. In this design, the Class I and Class II weight estimations are performed. For the Class I estimation, the procedure is taken from literature [**?**]. For the Class II, several weight estimation methods exist, where the accuracy depends on the type of aircraft that has to be designed and on the aircraft features such as struts. The choice of a weight estimation method is not trivial, as the use of an inappropriate method could lead to results that are not representative. By comparing several methods such as Roskam, Raymer and Torenbeek, the latter method was chosen, as this method shows the highest weight accuracy for jet transport aircraft [11][12][13][14]. However, the Torenbeek estimation for the furnishing weight shows significant deviations from the real weight, and by noticing that the method underestimates the weight by 50%, it has been decided to multiply the furnishing weight by 1.5 for an accurate result [14]. As in Section 9.11, other weight estimation methods have been used wherever the ones from Torenbeek have significant deviations. These deviations are due to the fact that data on novel technologies are not taken into account in the empirical estimation methods of Torenbeek.

5
Mission Analysis

Before the detailed design phase can be started, the mission analysis of the CNA has to be performed in order to have a clear definition of the required performance from the aircraft. In this chapter, Section 5.1 explains the mission profile, whereas Section 5.2, Section 5.3 and Section 5.4 explain the thrust and wing loading diagram, the payload-range diagram and the flight envelope respectively.

5.1. Mission Profile

A complete mission profile for the CNA is shown in Figure 5.1. The engines are started and taxiing to the runway is performed, where the take-off takes place. After the take-off, the climb phase is initiated, and it ends at the TOC (Top Of Climb) at 36,000 ft (FL360). At the TOC, the BLI is turned on, and the cruise phase is carried on until the TOD (Top Of Descent). From here, the BLI is turned off and the descent procedure is initiated. The aircraft eventually finishes the descent with the approach and landing phase to the airport, or it will divert to an alternate airport. In that case, a short climb is performed to a low cruise altitude where the CNA cruises to the alternate airport. After the alternate cruise, the necessary loiter is performed, followed by the descent, the landing and the engines shutdown at the gate.

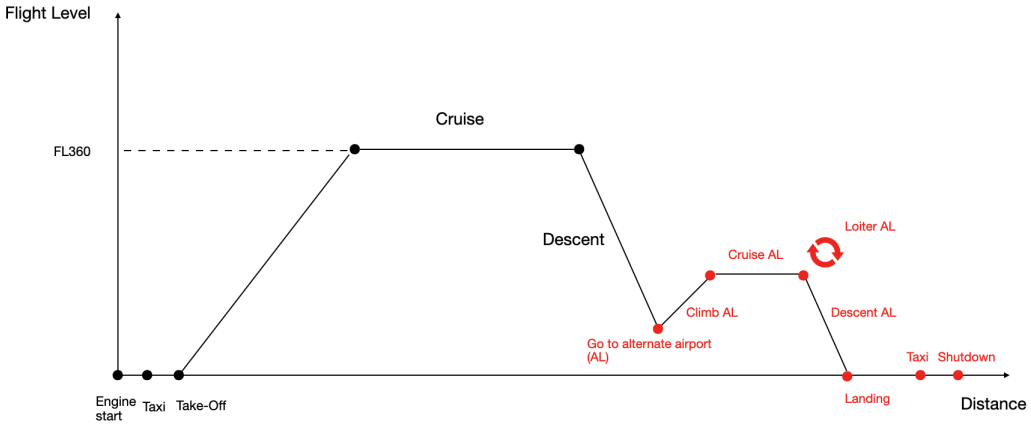

Figure 5.1: Mission profile of the CNA

5.2. Thrust Loading and Wing Loading

The wing loading (W/S) and the thrust loading (T/W) of the aircraft were chosen with the help of the plot shown in Figure 5.3. The methods of plotting the curves are identical to the method explained in the midterm report [3]. These lines were drawn according to the critical boundaries regarding stall speed in the landing condition, ensuring take-off performance, cruise speed and climb gradient. The selected W/S and T/W are 4570 N/m^2 and 0.239 respectively, indicated by the red dot in Figure 5.3. This design point was chosen primarily to obtain a favourable wing surface area and thus the favourable planform. With this planform a high L/D of the entire aircraft could be achieved, while ensuring the wings were still foldable in order to be compatible with the airport gates. The corresponding wing area was found to be approximately 151 m^2. Then the minimum T/W was selected so that the thrust required is the lowest, which often results in lighter engines and therefore a lighter aircraft. With this T/W, the critical thrust was found to be about 165 kN. These were two of the primary inputs for designing the aircraft. As shown in Figure 5.3, the limiting case case of the CNA for this design point is the take-off performance.

5.3. Payload-Range Diagram

The requirements state that the CNA shall have a range with maximum payload of 2150 NM and a maximum design range of 3400 NM. In order to calculate these ranges for the CNA, a payload-range diagram is generated. The payload-range diagram is an important tool to assess the performance of the aircraft. It allows the airline companies and the designers to know the maximum possible range with a given amount of payload, and vice versa. The diagram

is constructed by first loading the aircraft with the maximum payload [**?**]. The fuel is then added until the MTOW is reached, and the resulting range is the harmonic range. If a higher range is desired, the payload weight must be lowered in order to accommodate more fuel. When the tanks are completely filled, the maximum range is reached, which is the longest range of commercial interest. Since the payload-range diagram calculates only the cruise range, the ground distances for climb and descent of 200 km each are added. These are estimated during Class I. The payload range diagram is shown in Figure 5.2. From the figure, the range with maximum payload (harmonic range) is 3591 km (2155 NM), and the maximum design range is 6330 km (3418 NM), which means that the range requirements are met.

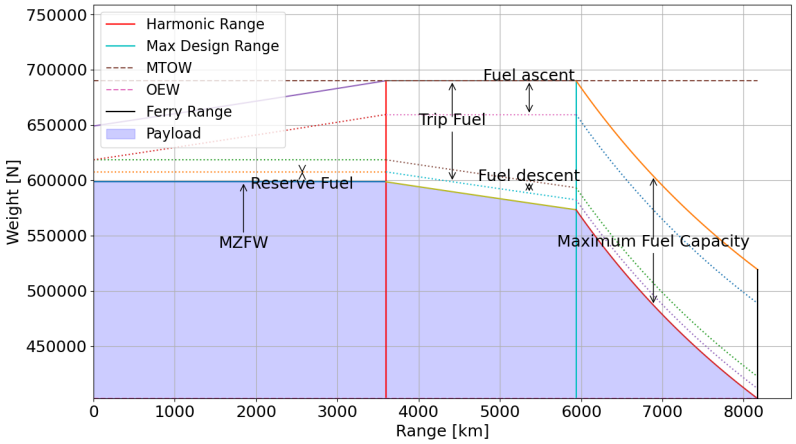

Figure 5.2: Payload-range diagram of the CNA

5.4. Flight Envelope

The flight envelope was established according to the guidelines set by the CS-25 regulations, the diagram is shown in Figure 5.4. From the CS-25 regulations, the maximum positive load factor with high lift devices (HLDs) retracted and the maximum negative load factor were determined to be 2.5 and -1 respectively for the CNA. The maximum C_L in the clean configuration was extrapolated, with the stall angle of about 20° and was found to be 1.74. With this value, the stall speed (V_{S1}), the cruise speed (V_C), the manoeuvre speed (V_A), and the dive speed (V_D) at an altitude of 11000 m were calculated to be 65.6 m/s, 125.4 m/s, 103.7 m/s and 156.7 m/s respectively. The velocities are denoted in equivalent airspeed (EAS). The gust velocities at high angles of attack, during cruise and at dive speed were determined with statistical gust velocities at different altitudes [**?**]. For the CNA at 11000 m altitude, these were found as 13.3 m/s, 9.5 m/s, and 4.8 m/s respectively. These gust velocities were used to draw the gust envelope, shown in red in Figure 5.4. From Figure 5.4, the highest load case the CNA experiences was found to be 2.5. On top of this, a safety factor of 1.5 was applied. The ultimate load factor that the aircraft needs to be designed for was determined to be 3.75. This was one of the primary inputs for the structural designs.

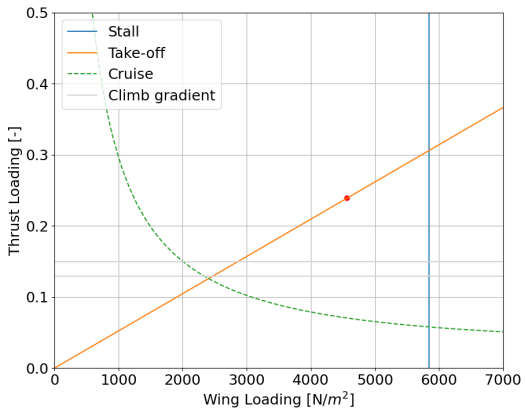

Figure 5.3: Thrust and wing loading diagram of the CNA, the design point shown with a red dot

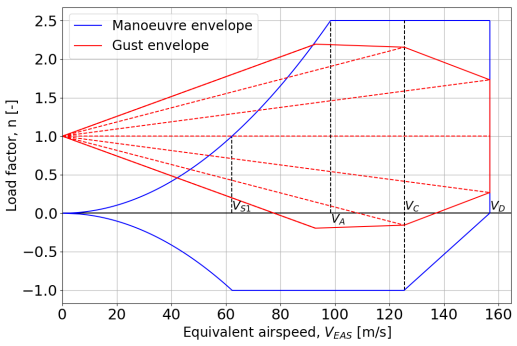

Figure 5.4: Flight envelope of the CNA at an altitude of 11000 m

6
Fuselage Design

This chapter describes the fuselage design on a structural level and discusses the internal and cabin design. It first discusses the main objective and requirements of the design process in Section 6.1. The methodology and assumptions are then described in Section 6.2, and an initial fuselage sizing performed in Section 6.3. The structural design is described in Section 6.4, which is then followed by the environmental control of the cabin in Section 6.5. The fuselage weight is estimated in Section 6.6. Finally, the qualitative analysis and recommendations are explored in Section 6.7

6.1. Objectives and Requirements

With a main purpose of transporting passengers and cargo from one place to another, an aircraft requires a comfortable and safe cabin section. Furthermore, with wings, propulsion systems and other elements producing the required forces for flight, this central element of the aircraft has to carry and distribute the loads through the entire structure. In the CNA's case this fuselage section is required to be able to carry 194 passengers and 7 LD3 containers in the underfloor compartment in a high density passenger lay-out and cargo at max payload.

In order to fulfil these needs, the fuselage is sized according to a set of more specific requirements from the CS-25 regulations. These are requirements such as specific aisle widths and a maximum number of seats abreast which have to be taken into account when sizing the interior. Further regulation concerning passenger comfort has to be followed such as specific pressures inside the cabin, and comfortable temperature and air humidity. These are taken into account through the structural analysis and environmental control designs. Finally, with clear requirements surrounding sustainability from both the customer and overall market, the structure's material recyclablility requirement is taken into account. The leading requirements for the design of this fuselage can be summarised in Table 6.1.

Table 6.1: Driving requirements for the fuselage

Identifier	Requirement	Source
REQ-CN-PERF-5	The CNA shall be able to carry 194 pax in a high density lay-out and 7 LD3 containers underfloor at max payload.	Customer
REQ-CN-CABIN-1	The CNA shall have emergency exits which comply with CS 25.807.	CS 25.807
REQ-CN-CABIN-2	The CNA shall have aisle width that complies with CS 25.815.	CS 25.815
REQ-CN-CABIN-3	The cabin shall have at most 3 seats abreast at every side of the aisle.	CS 25.817
REQ-CN-CABIN-7	Pressurised cabins and compartments to be occupied shall be equipped to provide a cabin pressure altitude of not more than 2438 m (8000 ft) at the maximum operating altitude of the aeroplane under normal operating conditions.	CS 25.841
REQ-CN-CABIN-8	The cabin environmental control shall provide a comfortable temperature, pressure and humidity during the whole flight.	Design
REQ-CN-SYS-SUS-1	The CNA's primary structure shall be recyclable for 75% of its mass.	Customer
REQ-CN-STRUCT-3	The limit loads shall be determined over the flight envelope by means of a gust loading and manoevre diagram.	CS 25.341
REQ-CN-STRUCT-5	The structure must be able to support limit loads without detrimental permanent deformation. At any load up to limit loads, the deformation may not interfere with safe operation.	CS 25.305

REQ-CN-PERF-5 leads to a transport class aircraft for which a layout of passengers and cargo comparable to reference aircraft is suitable. The different REQ-CN-CABIN requirements lead the interior design and the sizing while REQ-CN-SYS-SUS-1 plays a major role in material selection. Finally REQ-CN-CABIN-7 and the 2 REQ-CN-STRUCT play a major role in the load carrying and distributing abilities of the fuselage. With a focus on safe and efficient transport, the objective is to design a light and aerodynamically efficient fuselage which can handle all loads applied and fulfil passenger needs.

6.2. Methodology and Assumptions

First looking back at the requirements in Table 6.1, some initial choices were made. Indeed a pressurised cabin was required which was going to both affect the internal loads through pressure differences and required a pressure bearing structure. This, together with the cabin requirements on passenger seating, safety and comfort, led to the choice of designing the well tested and efficient standard cylindrical (double bubble) fuselage shape of reference aircraft. The cylindrical shape furthermore reaches the discussed desired outcomes by effectively carrying the pressurisation loads while minimising structural weight. It also minimises the wetted area to reduce friction drag and avoids corners causing flow separation [**?**].

With these first design choices allowing an initial fuselage sizing to occur, it was then possible to evaluate the critical load types and cases, and from there analyse and design the fuselage for these. Due to the nature of the design process where all departments designed side by side and required inputs from each other, it was important to start by estimating the major fuselage characteristics without too many inputs and outside factors and evaluate how it performs with respect to the objectives. The more in depth design was then performed using the previous one as baseline. In order to achieve this, an iterative design process was chosen within the fuselage design process.

This iterative process starts by modelling the fuselage as a constant thickness cylinder over its entire length. On this, the different load types and cases were applied giving an overview of their effects on the fuselage. This allowed the critical cases to be defined and a first approximation of the required skin thickness to be made. The fuselage was then modelled as a cylinder with skin; stringers and frames. This was done such that the fuselage can withstand the different loads while minimising weight. This gave a better approximation of overall sizes and weight. As the full scale aircraft iteration was performed, new required fuselage sizes came to light whilst the fuselage shape got more detail. At this point the major design choices affecting weight and other departments were made and quantitatively justified. This allowed for a final qualitative iteration to be performed and designed for aspects such as cutouts and discuss their effects on the overall fuselage design. With these steps exploring the structural aspects of the fuselage, it was then important to design the cabin itself and to make sure this will achieve the required passenger safety and comfort. A final estimation of the weight and cost of the entire fuselage was performed, and completed the overall picture of the characteristics of the CNA's fuselage. Through this it showcased how the fuselage fulfils the variety of customer requirements and the design objectives.

To successfully design the fuselage in such an iterative manner, assumptions had to be made during the design process. The main assumptions were made during the structural design such as that the fuselage was modelled as a thin walled, constant thickness cylinder; the fuselage was simplified to a constant radius cylinder over its length and the weight of the aircraft was assumed as a constant distributed load over its length. This simplified the calculations and allowed for a first estimation of the results to be made without introducing too much complexity and uncertainty in the process.

6.3. Initial Fuselage Sizing

With the choice in Section 6.2 of sizing the fuselage according to standard cylindrical fuselage shapes, it was possible to size the fuselage according to statistical methods of reference aircraft. These methods successfully take into account the variety of safety requirements and are proven effective from their vast track record in aviation. While using these methods, it was important to take into account the effects of design choices on other departments throughout the process. Indeed, from an aerodynamic perspective, a lower radius decreases fuselage drag. The sizing was thus performed in such a way as to stay on the lower end of acceptable sizes.

Looking back at the cabin requirements in Table 6.1, a number of 194 passengers in high density lay-out and 7 LD3 containers under-floors are noted. These, together with the requirement of a maximum of 3 seats abreast at every side of the aisle, led the initial design. According to market demand of a single aisle carbon neutral aircraft as discussed in Chapter 3, a single aisle; 6 seat per row lay-out was chosen. To accommodate the required 194 passengers, 33 rows are thus necessary. It is further known that, in order to remain both safe and comfortable, the seat width, the seat pitch, the aisle width and the aisle height have to range between 43 and 71 cm; 80 and 101 cm; 51 and 71 cm and be above 193 cm respectively [**?**]. Staying on the lower end of the possible sizing in order to reach the aerodynamic goals the values specified in Figure 6.1 and a seat pitch of 812.8 mm were chosen. These chosen widths and the associated clearances lead to a cabin diameter of 3.66 m. Furthermore, the number of lavatories and emergency exits were chosen in compliance with regulations as again shown in Figure 6.2. Finally, two galleys were deemed sufficient and passenger luggage can be stored in overhead compartments in the cabin.

Moving to the cargo compartment, the customer requirement from Table 6.1 requires room for 7 LD3 containers under-floors. These containers having a combined length of 10.7 m and a maximum width of 2 m [**?**]. The containers were found to not be a limiting factor to the interior fuselage design in both length and width. These sizes allowed for a required cabin length of 32 m to be derived by adding the seat pitches with number of rows; emergency exits; lavatories and galleys. With the clear wish for minimal width in mind, the excess space in the cargo compartment's width left from the usage of LD3 containers showed clear possible benefits by altering the fuselage shape. In order to minimise the perimeter length, a double bubble design was chosen allowing for two smaller circles to make up the fuselage cross section. The top circle allows for the required passenger safety and comfort both in height and width and has an inner radius of 1.91 m, while the bottom circle allows for efficient container storage by having an inner radius of 1.83 m. This thus reduces both the fuselage wetted area and the fuselage width at its widest. In terms of fuselage height, the top circle joins the bottom circle at the point where they both reach a width of 3.66 m, this led to a top circle that continues on until reaching this diameter with an offset of 531 mm while the bottom stops at its widest point. The total height of the fuselage, with the outer linings thus came at 4.37 m. The aisle height was set at 1.9 m under the wingbox and 2.34 m for the rest of the aisle.

The outer dimensions of the fuselage could now be designed. It used average inner lining - outer contour distances of 50 to 100 mm per side for fuselage width; an average cockpit length of 4.4 m and tail length of 6.6 m for similar aircraft [**?**]. In order to encourage minimal material usage and keep a small width for aerodynamic drag benefits, the total added width was chosen as 0.1 m. This led to a fuselage width of 3.76 m at the cabin floor and 3.92 m at its widest point in the upper bubble part. The fuselage length on the other hand could be computed to equal 42.6 m by adding up the cockpit, the cabin and the tail parts. This gives the fuselage a slenderness ratio of 10.9 which is typical for transport aircraft. An overview of this design can be seen as a top view in Figure 6.2 and as a cross section in Figure 6.1.

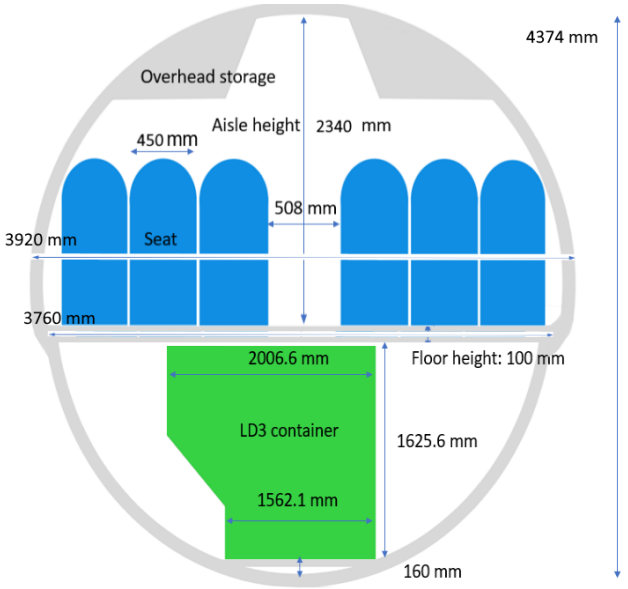

Figure 6.1: Schematic drawing of the cabin layout, cross sectional view

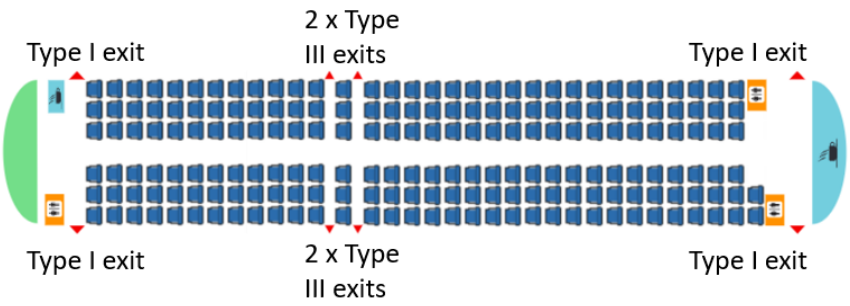

Figure 6.2: Schematic drawing of the cabin layout, top view [3]

6.4. Structural Design

With the objectives of a light and safe transport in mind, the fuselage structure has to withstand all loads it might encounter while minimising its structural weight. This structure was designed by evaluating the different load types and cases and selecting an adequate material to fulfil its needs. It then designed an optimised load bearing structure for the found critical load type and case with minimal weight through a structural design process. Through this, the optimum stringer amount and skin thickness for specific reference stringers and frame spacing were found, allowing a clear overview of the required fuselage structure.

6.4.1. Internal Loads

Given the initial fuselage sizes found in Section 6.3, it was possible to size the structure necessary to carry the variety of loads the fuselage gets exposed to over its lifetime. To accomplish this, the critical load types and cases that the CNA might encounter first had to be evaluated. During flight the fuselage structure is exposed to bending moments, shear, torsion and pressure differences. The different elements of the structure thus have to cope with one or more of these loads. Due to the great similarity of the fuselage sizing and loading with respect to reference aircraft, the structure was chosen to implement the same elements as reference aircraft. Imagining the fuselage as a beam, there are longitudinal elements in the form of longerons and stringers that carry the biggest part of the bending moment. Then there are transverse elements in the form of frames that generally serve to maintain the shape of the fuselage. Finally there is the external skin that carries the shear from transverse and torsional loads, and cabin pressure differences [15].

From the flight envelope in Section 5.4 and statistical data, the critical load cases of the aircraft were found to be during landing and manoeuvre where the load factors are 2 and 3.75 respectively [16]. Furthermore, for manoeuvre, there is also a pressure difference component when at high altitudes. At landing a 2g load is applied through the main landing gears while during manoeuvre the 3.75g load comes from the wings. Furthermore, in both cases, the tail acts as a support. The weight of the aircraft itself was, on the other hand, assumed to act as a constant distributed load along the fuselage. Finally, the force itself that gets multiplied by the load factors is the aircraft MTOW times g where the MTOW equals 70459 kg.

In order to compute the different loads mentioned earlier using these load cases it was first required to set up a free body diagram for each case and visualise the situation. For the landing case a load of $n \cdot m \cdot g = 1561.4$ kN is applied at the main landing gear positioned at 24.71 m from the nose and where n is the load case factor. A distributed load of $n \cdot m \cdot g/l = 36.6$ kN/m is furthermore applied along the length of the fuselage and the tail acts as a support at 37.1 m from the nose. On the other hand, for the critical manoeuvre load case, a load of 2927.7 kN is applied at the wing positioned at 14.47 m from the nose. A distributed load of 68.7 kN/m is applied along the length in a similar fashion to the landing case while the tail again acts as a support. The free body diagram of this case (found critical in Section 6.4.3) is shown in Figure 6.3. During this load case, a pressure difference will furthermore affect the fuselage. With a required cabin pressure of 75266 Pa and a pressure at flight ceiling of 16235 Pa, a pressure difference of 59030 Pa has to be taken into account.

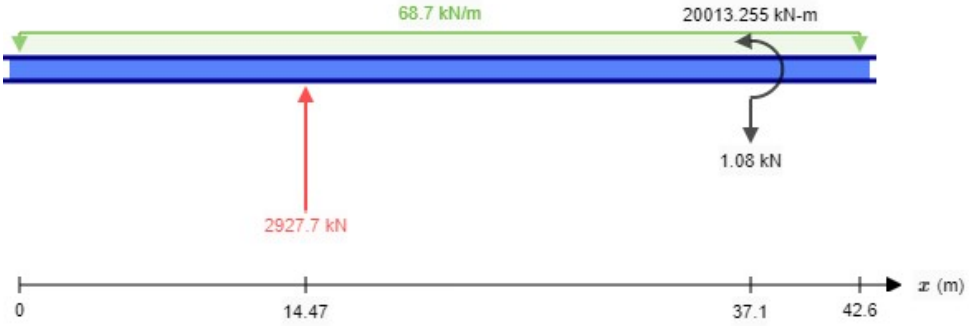

Figure 6.3: Free body diagram of the fuselage at critical manoeuvre loads

6.4.2. Material Selection

Before being able to determine the critical load type and case for the fuselage, its material had to be selected. With the variety of different materials used throughout the airline industry and with each material having its own unique strengths and weaknesses, it was important to evaluate which material best suits the aircraft's loads and characteris-

tics. Different materials ranging from aluminium types and glare to natural fibres were considered. Despite promising characteristics, the natural fibres were discarded for structural usage due to high uncertainties and flammability risks [17]. On the other hand, the aluminium and glare types, and quasi-isotropic composite were all promising on several aspects. A Quality Function Deployment (QFD) was set up in order to objectively compare the materials and scores them on factors such as "Sustainable and Recyclable", "Low cost", "Low density", "Safety" and "Easy maintenance". On the other axis an array of factors were scored, most notably their different mechanical properties, such as "Material Cost" and "Recyclability and Production Sustainability". Applying weights to each factor according to the QFD's approach and scoring all materials using their properties[1], the most efficient material for the given case was found to be Al 2014-T6. This material was thus used during the remainder of the fuselage's design.

6.4.3. Design

With the loads determined and the material chosen, the fuselage structure was then designed. In order to achieve this, a first model of the fuselage structure was set on which further iterations were to be applied later. As explained in Section 6.2, the fuselage was modelled as a cylinder with constant thickness from the tip of the nose until the end of the tail cone. Furthermore, it only had a skin element and no other reinforcements. With the different load cases applying forces as shown in the free body diagram in Figure 6.3 and load types in the form of critical shear load, critical moment load and regular fatigue affecting the structure, it was possible to size the elements for these loads and determine the critical one. With the fuselage structure sized for this critical load, it is able to withstand all other loads as well.

Sizing for critical shear and moment required these values to be found for both load cases from their respective free body diagrams. The shear force diagram derived from the free body diagram of the critical manoeuvre load case as later found in this subsection can be seen in Figure 6.4. Critical shear loads of -904 kN and 1933 kN were found for the landing and critical manoeuvre cases respectively. The bending moment diagram can be seen in Figure 6.5 for the critical manoeuvre case. From this, critical moment loads of -11172 and 18974 kN·m were found for the manoeuvre and landing cases respectively.

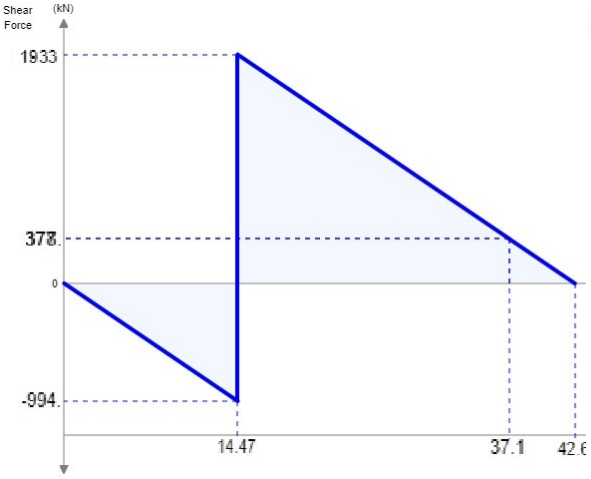

Figure 6.4: Shear force diagram of the fuselage at critical manoeuvre loads

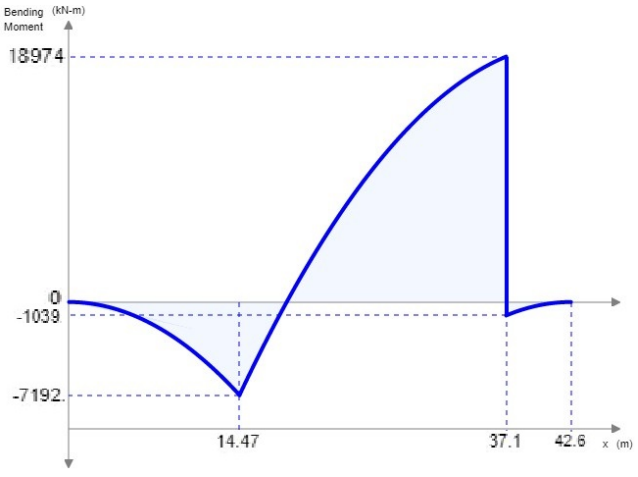

Figure 6.5: Bending moment diagram of the fuselage at critical manoeuvre loads

With only the skin element, the required fuselage skin thickness for each load could be computed. Starting off with comparing the two load cases, the required thickness was derived from the moment loading for the landing case according to Equation (6.1a) and from the moment loading and pressure difference for the manoeuvre case according to Equation (6.1b). In these equations, t is the skin thickness required to take on the loads, M_y is the critical moment from the bending moment diagrams, y is the point of highest stress (here it is equal to R), $\sigma y/SF$ is the material's yield stress divided by a safety factor of 1.5 chosen for this structural design, r_{fus} is the fuselage outer radius found in Section 6.3, and ΔP is the pressure difference of the cabin and the exterior.

$$t = \frac{M_y \cdot y}{\frac{\sigma_y}{SF} \cdot \pi \cdot r_{fus}^3} \qquad t = \frac{M_y \cdot y + \Delta P \cdot r_{fus}^4 \cdot \pi}{\frac{\sigma_y}{SF} \cdot \pi \cdot r_{fus}^3} \tag{6.1a,6.1b}$$

[1] URL `https://www.aerospacemetals.com/index.html` cited [18. June 2020]

Plugging in the numbers found above for the moments and the pressure difference, using the fuselage radius of 1.96 m used in this approximation and an Al 2014-T6 yield stress of 414 MPa [2], a fuselage skin thickness of 3.35 mm was found for the landing case and a skin thickness of 6.11 mm was found for the high altitude manoeuvre case. This revealed the high altitude manoeuvre case to be the critical load case for the CNA and gave a first estimate of the required skin thickness.

Now that the critical load case was determined, it was possible to evaluate which load type was critical for the fuselage structure (here again simplified as a skin) for this load case. As previously discussed, the significant load types are bending moment, shear and fatigue. Again, if sized for the critical load type, the structure can take on all other load types. The skin thickness required for the bending moment was already determined above. The thickness for the shear loads could be computed using Equation (6.2a) where τ is the shear strength, V_{fus} the critical shear from the shear moment diagram of Figure 6.4, Q is equal to $Q_{fus} = A_{ext_{fus}} \cdot r_{fus} - A_{intfus} \cdot (r_{fus} - t)$ and is the first moment of area of the fuselage, I_{fus} is the moment of inertia and t again the thickness of the skin. Using this critical shear found above, a shear strength of 290 MPa, and solving for thickness gave a thickness of 4.25 mm. Finally, the skin thickness required for fatigue could be found using Equation (6.2b) where all variables are the same as Equation (6.1b) except the M_{fatigue} that evaluates the highest bending moment of a typical life cycle and $\sigma_{fatigue}$ that equals the fatigue strength of the material. For $M_{fatigue}$, a 30° bank angle load was taken as average highest manoeuvre load with a load factor of 1.15 and allowed for a new free body diagram and bending moment diagram to be made. σ_{fatigue} was furthermore given as 124 MPa. These values allowed for a skin thickness of 5.4 mm to be found for the fatigue load type. Comparing the 3 skin thickness for the load types revealed the bending moment load type as critical for the fuselage structure with a thickness of 6.11 mm. This skin thickness thus allowed the structure to withstand all load types and cases of the CNA under the current assumptions.

$$\tau = \frac{V_{fus} \cdot Q_{fus}}{I_{fus} \cdot t} \qquad t = \frac{M_{fatigue} \cdot y + \Delta P \cdot r_{fus}^4 \cdot \pi}{\frac{\sigma_{fatigue}}{SF} \cdot \pi \cdot r_{fus}^3} \tag{6.2a,6.2b}$$

At this point the fuselage structure was able to withstand all loads, but using only a skin element requires both a high thickness leading to high mass and creates buckling problems. As discussed in Section 6.4.1, stringers are very effective at carrying bending moment loads and are significantly lighter than the skin while carrying this load. This led the design to apply its first iteration as explored in Section 6.2 where stringers (and later on frames) were added to the structure to better reach the objectives of mass minimisation. Purely looking at bending moment, the lightest option would be to only use stringers in the fuselage structure, however, with pressure differences and other load types also acting on the structure a skin is necessary. This skin will furthermore be impacted by buckling which will lead to a minimum thickness required to withstand those loads. With the objective of mass minimisation in mind, it was thus beneficial to find this optimum skin thickness and stringer amount leading to the lowest total mass while still being capable of carrying all loads.

First off, purely looking at the bending moment stress and ignoring buckling, finding the minimum mass thickness and stringer amount led to an optimisation problem where the skin thickness, stringer amount and stringer characteristics acted as variables and where their total mass had to be minimised. Furthermore, for this problem, the material yield strength was the constant factor that limited the variables. In order to limit the complexity of the optimisation the properties of the stringers had to be set. With the CNA's fuselage closely resembling that of the Airbus A320, the stringers used within that aircraft were chosen for this design. These stringers are Z stringers with an area of 112 mm^2 [18]. This allowed Equation (6.3a) to be set up with, as variables, both the skin thickness and the amount of stringers. This equation originates from the same equation as Equation (6.1b), but here the moment of inertia contains the stringer elements as shown by Equation (6.3b) where A_{stringer} is the area of the chosen stringers and z_{skin} is the z location of each stringer on the skin to the centre line of the cylindrical approximated fuselage.

The two variables of the skin thickness and the amount of stringers were then linked to structural mass through Equation (6.4), where the masses of the skin and total stringers were added up. Here m_{fus1} represents the mass of skin and stringers, r_{ext} the external radius of the fuselage and r_{int} the internal radius (where $r_{int} = r_{ext} - t$), l is the length of the element (here taken as 1), ρ_{material} is the density of the material, $n_{\text{stringers}}$ is the number of stringers and $A_{\text{stringers}}$ is the area of the chosen stringer. With these two equations the skin thickness and the amount of stringers were linked through Equation (6.3a) and could be tweaked to obtain the lowest mass in Equation (6.4). Through an Excel sheet a list of amount of stringers were plugged into a rearranged version of Equation (6.3a) outputting a skin thickness and these two were then plugged into Equation (6.4), where the mass of this setup was then given as output. It was then possible to find the lowest mass and its associated amount of stringers and skin thickness. Due to the exclusion of buckling, the lowest mass was achieved at a skin thickness of near 0 and with 136 stringers. For this case the mass was

[2] URL `https://www.aerospacemetals.com/index.html` cited [18. June 2020]

found to equal 65 kg/m (or 2770 kg for the simplified fuselage).

$$\frac{\sigma_y}{SF} = \frac{M_y \cdot y}{I_{yy}} + \frac{\Delta P \cdot r_{fus}^4}{t \cdot r^3} \qquad I_{yy} = t \cdot \pi \cdot r^3 + \sum A_{stringer} \cdot z_{skin}^2 \tag{6.3a,6.3b}$$

$$m_{fus1} = (\pi \cdot r_{ext}^2 \cdot l - \pi \cdot r_{int}^2 \cdot l) \cdot l \cdot \rho_{\text{material}} + \text{n}_{\text{stringers}} \cdot A_{\text{stringer}} \cdot l \cdot \rho_{\text{material}} \tag{6.4}$$

As previously discussed, the exclusion of buckling led to a mass minimisation at 0 skin thickness, however, this would lead to a multitude of problems surrounding the other loads. In order to find a minimum skin thickness (after which the rest of the bending loads can be carried by the stringers) buckling had to be taken into account. This thickness was found using Equation (6.5) where $\sigma_{cr_{\text{plate}}}$ is the critical stress after which buckling starts to occur, this value was found to equal $1/3\sigma_y$ [19], C is a value from literature and in this case equal to 7.2 [13], E is the material's modulus of elasticity, ν is the material's poisson ratio, t again the skin thickness and b is the frame spacing. This frame spacing thus has an impact on skin thickness and ultimately on the structure's mass. By evaluating the effect of different values on mass and taking into account its use as discussed in Section 6.4.1, the spacing was chosen as 0.5 m. This led to a minimum thickness to carry buckling loads of 1.91 mm.

$$\sigma_{cr_{plate}} = C \cdot \frac{\pi^2 \cdot E}{12 \cdot (1 - \nu^2)} \cdot \left(\frac{t}{b}\right)^2 \tag{6.5}$$

This minimum thickness could be plotted on the mass optimisation sheet resulting in a required amount of stringers for this skin thickness and its associated optimum mass. Taking a skin thickness of 2.05 mm, an amount of 64 stringers was found to lead to the lowest mass. In this case the total mass of the skin and the stringers equals 134 kg/m (or 5709 kg for the simplified fuselage).

6.4.4. Verification, Validation and Sensitivity

The verification of the used methods was essential to judge the method's reliability. The software used to model the fuselage's free body diagram and generate the required shear force and bending moment diagrams was verified by comparing its results for a relatively simple free body diagram with results achieved through hand calculations. Performing this test using a beam affected by a point load and distributed load similar to the fuselage load case and performing the analysis by hand gave the same results and thus verified the software used. The different load case and type calculations followed by the initial skin thickness calculations were performed using governing physics equations and were performed by hand, thus not needing specific verification. Finally, the Excel sheet used during the mass optimisation had to be verified. A first test was performed by setting the stringer area to zero, when doing this all rows outputted a required skin thickness equal to that of the calculations without stringers, as expected. A second test was performed by multiplying the material density by two, when performed it could be see that the mass was also multiplied by two, again as expected. Finally, increasing the material's yield stress close to infinity yielded a result where the required amount of material (stringers + skin) was reduced close to zero, thus as the material gets infinitely effective, nearly no material is needed, this was also as expected.

The final outcomes of this design process could be validated by comparing results to that of reference aircraft. This comparison was appropriate given the resemblance of the fuselage to that of reference aircraft. From reference data the skin thickness of the Boeing B737 was found to be around 0.94 mm thick and its stringer count around 88 stringers [20]. The results of the above design process were thus relatively close to those found of reference aircraft in their order of magnitude, the skin thickness is however twice as large than on reference aircraft. This difference can be assumed to result from further optimisation and research and due to the higher aspect ratio of this design leading to higher bending moment and thus more required material.

It finally has to be noted that, despite the fuselage's similarities resulting to overall low impact on the design's sensitivity, a few differences ultimately lead to uncertainty. Indeed the strut's attachment points on the fuselage and the assumptions made on how their loads are transferred will add a level of uncertainty. These effects will later be taken into account through reinforcements in the fuselage to reduce the sensitivity of the system to their uncertainty.

6.5. Environmental Control System

Looking back at REQ-CN-CABIN-8 in Table 6.1, significant attention had to be paid to passenger comfort during flight with critical aspects being cabin temperature; pressure and humidity. Again, with the fuselage and cabin sizing being relatively similar to that of reference aircraft, the cabin was equipped with similar designs for passenger accommodation and comfort. The cabin temperature is regulated by a commercial air-conditioning system that manages to keep the passengers at a comfortable temperature inside the cabin. This system is capable of performing while outside temperatures span from -50 to +50 ° C and uses airport equipment while at the gate and bleed air from the engines during flight.

The cabin furthermore has to be pressurised at a pressure altitude of not more than 2438 m according to REQ-CN-CABIN-7 of Table 6.1. This allows passengers to comfortably breathe sufficient oxygen. In the case of emergency or depressurisation, chemical oxygen generators are present to supply pilots and passengers of oxygen until a safe altitude is reached. It is to be noted that the aircraft was designed to withstand these pressurisation loads in Section 6.4. Finally, the cabin humidity is regulated by a humidifier in the bleed air intake systems.

6.6. Weight Estimate

With a fuselage closely resembling that of reference aircraft, it was possible to relatively effectively estimate the fuselage group's weight using statistical methods based on these reference aircraft. These statistical methods furthermore allowed for the estimation of the variety of elements that were left out in Section 6.4 by incorporating all elements through their formulas. This gives a better weight estimate to be used by other departments and allowed for effective mass budgeting. The fuselage structure mass (W_f) could be estimated using Equation (6.6) from the weight estimation methods of Torenbeek, using the factor of proportionality (k_f), the dive speed in EAS (V_D), the tail moment arm (l_t), the width and the height of the fuselage (b_f and h_f) and the gross shell area (S_G) [13]. Furthermore, k_f is 0.2645 for a fuselage with a pressurised cabin and the main landing gear mounted on it [13], S_G is the area of the entire outer surface of the fuselage, while all holes and windows are assumed to be faired over. Next, l_t, b_f, h_f and S_G were designed to be 19.4 m, 3.9 m, 4.37 m, and 512 m^2 respectively. This led to an estimated mass of the fuselage to be 9042 kg, with a CG that was assumed to be located at the middle of the total fuselage length.

$$W_f = k_f \cdot \sqrt{V_D \cdot \frac{l_t}{b_f + h_f}} \cdot S_G^{1.2} \tag{6.6}$$

6.7. Qualitative Analysis and Recommendations

Building upon the results of Section 6.4 allowed for a final internal iteration to be performed as discussed in Section 6.2 where detailed elements were updated and added in a qualitative manner. This section further acts as future recommendations where the mentioned qualitative elements are to be computed and integrated within the structure.

First off, attention had to be paid to the cockpit and tail-cone sections. These sections were sized based on the required scrape angle, which was derived from the landing gear positioning discussed in Chapter 11. In order to avoid scraping the tail section at the highest lift off angle using the landing gear setup discussed in Chapter 11, the bottom part of the fuselage had to curve upwards from 32 meters from the nose onward at an angle of 14°.The top part of the fuselage curves downwards for more efficient boundary layer usage by the BLI propulsor as will be explored in Chapter 9. Furthermore, the nose bottom section was flattened from 2 meters from the nose onward allowing more usable area. These two sections curving together and progressively reducing their outer diameter, reduced the number of stringers needed to carry their loads. Indeed lowering the radius parameter in Section 6.4 lowered the number of stringers needed and these sections thus have to be designed for an evolving amount of stringers along the fuselage length as the radius progressively reduces, this in order to save mass.

Another main addition to the structural design stemmed from passenger requirements and the compromises that have to be made to accommodate them. Passengers require doors to board, load their food and load their luggage and doors to evacuate in case of emergency. They furthermore require windows to look outside [15]. This led to cutouts throughout the fuselage structure causing stress concentrations that need reinforcements. Next to this, the braces transfer loads into the fuselage at their connection points and the BLI, through its weights, generates a load in the aft section. The load integration points and load paths of these thus need further reinforcements.

7
Aerodynamic Wing Design

This chapter describes the wing design from an aerodynamic perspective. First, the objective and requirements are listed in Section 7.1. In Section 7.2 the methodology used with the corresponding general assumptions is described. Section 7.3 and Section 7.4 describe the design of the main wing, Section 7.5 explains the design of the strut, and Section 7.6 sets out the design of the high lift devices and control surfaces. Finally Section 7.7 lists the recommendations.

7.1. Objective and Requirements

The top level objective of the aerodynamic wing design is to design a wing that has a lift over drag (L/D) ratio greater than 31. This L/D ratio is determined from the requirement to have a 10% emission reduction per passenger kilometre with respect to competitor aircraft whilst using fossil fuel. In the concept selection phase the objective was set to design a high aspect rtio (AR) wing in order to obtain this high L/D ratio. To enable this high AR wing, a strut must be designed without lowering the aerodynamic performance of the main wing. The two top level objectives are therefore the aerodynamic design of a high AR wing, and the aerodynamic design of the supporting strut. Lower level objectives are to design high lift devices (HLDs), control surfaces, winglets, interfaces and to design for low airframe noise emission.

The main driving requirements are displayed in Table 7.1. These requirements are closely related with all other departments and changed multiple times due to the iterative characteristic of the design. The values in Table 7.1 are of the last converged iteration.

Table 7.1: Driving requirements for the aerodynamic wing design process

Identifier	Requirement	Source
REQ-CN-LIFT-2	The lifting surfaces shall produce $6.73 \cdot 10^5$ N of lift at Mach 0.78 with clean configuration at altitude of 11000 m.	Design
REQ-CN-LIFT-3	The lifting surfaces shall produce $7.05 \cdot 10^5$ N of lift at take off speed.	Design
REQ-CN-LIFT-4	The lifting surfaces shall produce $6.27 \cdot 10^5$ N of lift at approach speed.	Design

7.2. Methodology and Assumptions

The design methodology provided different levels of detail for all elements. This level of detail was determined by the element, its novelty, the available resources, and the scope of this project with the aim of a convincing and feasible design. Furthermore, the design methodology provided a framework for recommendations and future referencing.

The first method that started the design methodology was the design of the initial wing characteristic based on the infinite wing principle. This effectively let the design become two dimensional, enabling the focus to be on the design of the airfoil. Afterwards, more accurate wing characteristics were obtained based on the finite wing principle and the design of the geometrical wing. The finite wing principle takes the geometry of the wing into account and determines the overall wing characteristics with more accuracy than the infinite wing principle. The geometrical wing design determines the severity of the effect of the finite wing principle, and closely relates to structural design and flight performance & control. After having designed the finite wing geometry and its aerodynamic characteristics, the control surfaces were designed according to empirical methods from Raymer and Torenbeek [12][13]. The strut was designed with the same methodology as the wing, however, with a different goal as described in Section 7.5.

The design methodology used is based on methods and principles which have underlying assumptions. Furthermore, as the design was limited by resources and the scope of this project, more assumptions were made throughout the design process. All general assumptions are listed below. Case specific assumptions are mentioned and explained in the corresponding sections.

1. **Initial Oswald Efficiency Factor:** It was initially assumed that the Oswald efficiency factor only depends on aspect ratio (AR) [21]. The relation used was determined on flight test data of a broad range of reference aircraft. Included were low, medium and very high ARs. This makes the assumption approximate the Oswald efficiency factor in a conservative manner, justifying its use for initial approximation. As this value was only needed for initial computations, it changed during the design. This removed the error from this initial assumption.
2. **Initial Skin Friction Coefficient:** According to Raymer, C_{fe} = 0.003 for civil transport aircraft [12]. This is the initial assumption made, but the Cfe changed during the design due to computations in openVSP. This removed the error from this initial assumption.
3. **Incompressible Flow for Mach<0.3:** For a Mach number smaller than 0.3, it is generally assumed that the flow behaves like an incompressible fluid. This assumption is used in general aerodynamic literature due to the low error margin, and therefore deemed justified [12][13][22].
4. **Increase in C_{D_0} During Landing and Take-off:** It was assumed that C_{D_0} increases during landing and take-off by 0.03 and 0.09 respectively [22]. These values were chosen from a typical range, where the influence from the undercarriage is conservatively approximated and the influence from flaps was taken as a mean. This is justified by the fact that due to the high wing, the undercarriage was designed to be bigger than reference low-wing aircraft. Furthermore, the flaps were not designed to be small nor big; hence an average value could be used.
5. **Increase in Oswald Efficiency Factor During Landing and Take-off:** It was assumed that e increases during landing and take-off by 0.05 and 0.1 respectively [22]. These values are dictated by Roskam, and therefore deemed justified for initial estimation.
6. **Steady Flow:** As the design is performed for steady flight condition, use is made of the steady flow assumption.
7. **Ratio Laminar Flow and Turbulent Flow:** Most aircraft have 10 to 20 % of laminar flow over the lifting surfaces, with the other 80 to 90 % being turbulent flow [12]. For drag calculations, it was assumed that the laminar flow takes up 10% of the flow over the lifting surfaces. This is a conservative approach, as it results in the highest skin drag.
8. **Smooth Paint Surface:** For computations on the skin friction coefficient, it was assumed that the aircraft would have a smooth paint surface. This is justified as all aircraft have a major percentage of their surface painted to prevent corrosion.

7.3. Design for Wing Characteristics

This section describes the design of the wing characteristics. First, the infinite wing design is described in Section 7.3.1. Second, the finite wing design is explained in Section 7.3.2.

7.3.1. Infinite Wing Design

The infinite wing design entails the selection of the airfoil based on a desired lift coefficient. This lift coefficient was derived from the required aircraft performance during cruise. The total wing lift coefficient C_L was overestimated by 10% to include the negative lift contribution from the horizontal tail. The design C_L obtained, however, is for the three dimensional wing and needs to be related to the two dimensional lift coefficient C_l. This can be done with Equation (7.1a).

$$L = q \cdot S \cdot C_L \cong q_{\text{eff}} \cdot S \cdot C_l \qquad q_{eff} = \frac{1}{2} \cdot \rho \cdot V_{eff}^2 \qquad V_{\text{eff}} = V_\infty \cdot \cos \Lambda_{LE} \tag{7.1a, 7.1b, 7.1c}$$

In these equations, q and q_{eff} are the dynamic pressure and effective dynamic pressure respectively, V_{eff} the effective velocity and Λ the wing sweep angle. Equation (7.1a) is an assumption, and generally does not hold. The finite wing effect reduces the lift slope of the airfoil (C_{l_α}). This effect is approximated by the DATCOM method, and states that the C_L is generally lower then the C_l. However, the lift curve slope C_{L_α} scales directly with the AR. Since the wing design has a excessively larger AR than conventional wings, the lift curve slope is excessively higher than conventional lift curve slopes. It is therefore assumed that Equation (7.1a) holds. Rewriting Equation (7.1a) with Equation (7.1b) and Equation (7.1c) gives:

$$C_{l_{\text{design}}} = \frac{C_{L_{\text{design}_{\text{wing}}}}}{(\cos \Lambda)^2} \tag{7.2}$$

In Equation (7.2), a 30° wing sweep was chosen. This number is slightly higher than that of competitor airliners, since the airfoil was selected out of a dated series that might have lower overall performance than later once. Consequently, the larger sweep angle increases the critical Mach number. The use of this dated series is due to the fact that later series with modern airfoils are company-sensitive information and not generally available. The decision to not assume a lower sweep as the airfoil can be improved in later design was taken to be able to simulate the aerodynamic performance. If the sweep was lowered, shock waves would have occurred and the data would not have been valid.

As two dimensional design only takes into account steady, incompressible flow, the lift coefficient obtained in Equation (7.2) needs to be corrected for compressibility. For this purpose the Prandtl-Glauert compressibility correction, valid from Mach 0.8 to 1.2, was used. The reason for using this method is that it is one of the most simple, yet very accurate methods for conceptual designs.

With $C_{L_{\text{design}}} = 0.489$ obtained from the design point and weight estimations, and $\Lambda = 30°$, the corrected design lift coefficient for the two dimensional wing is $C_{l_{\text{design}}} = 0.448$. With the design lift coefficient in mind, a selection of airfoils was made to start the trade-off.

Due to the high Mach number, two databases were selected to choose airfoils from; the NACA-6 series and the NASA SC(2) series [23][24]. Both series have been reported to perform well at transonic speeds. Initially the decision was taken to use only the NACA-6 series airfoils, as NACA performed extensive windtunnel tests on these airfoils. Not very far in the design process, however, it was found that the sweep angle would become too big due to its low drag divergence Mach number ($M_{D_{\text{div}}}$). Therefore, a final selection was chosen from supercritical airfoils instead. Since there is no available test data available, XFLR5 [1] was used to model the aerodynamic characteristics of the airfoils.

The final airfoil trade-off is summarised in Table 7.2. The NASA SC(2) airfoils were chosen to achieve a design lift coefficient of 0.4. This was based on the assumption that further aircraft mass reduction can be obtained as the aircraft design is refined. To minimise the risk of delay in schedule, however, in parallel a conservative design was done with airfoil design lift coefficients higher than 0.4. During the design it was found that the mass did not increase drastically, justifying the use of the nonconservative approach.

Table 7.2: Final airfoil trade-off

ID	Parameter	Airfoil 1	Airfoil 2	Airfoil 3	Airfoil 4	Airfoil 5	Score				
1	Name	SC(2)-0406	SC(2)-0410	SC(2)-0412	SC(2)-0414	LG10SC	1	2	3	4	5
2	Thickness ratio (high is best)	0.06	0.1	0.12	0.14	0.1				1	
3	Sensitive to surface quality (Y/N)	Y	Y	Y	Y	Y					
4	Re for Data below	9.00E+06	9.00E+06	9.00E+06	9.00E+06	9.00E+06					
5	Cl @ AOA =0 (close to Cl_des is best)	0.164	0.241	0.277	0.314	0.11					
6	AOA @ Cl =0 [deg]	-1.4	-1.99	-2.24	-2.49	-1.0				1	
7	Cl_max (highest is best)	1.67	2.09	2.17	2.26	1.87				1	
8	AOA for Cl_max [deg] (highest is best)	15	18	21.1	22.5	19.2				1	
9	Stall Characteristics	Smooth	Steep	Smooth	Smooth	Smooth	1		1	1	1
10	Cd_min (lowest is best)	0.006	0.006	0.006	0.006	0.0047					1
11	Cl of Cd_min	0.45	0.45	0.45	0.45	0.45					
12	(Cl/Cd)max (highest is best)	112.5	114	129.2	131.3	144.2					1
13	Cl of (Cl/Cd)max (low Cl is best)	1.07	1	1.3	1.54	0.95					1
14	Cruise Cm	-0.044	-0.074	-0.083	-0.093	-0.01					1
15	Start Substantial Drag Increase (larger is better)	1	1	1	1	1	1	1	1	1	1
16	Is Cl cruise inside drag bucket (Y/N)	Y	Y	Y	Y	Y					
17	M critical (@ Cruise Cl equivalent AOA)	0.4292338	0.568292	0.5875397	0.5956992	0.5811973				1	
18	M drag divergence	0.806	0.757	0.733	0.709	0.757	1				
							3	**1**	**2**	**7**	**6**

In the trade-off in Table 7.2 it can be see that there are two clear winners. Since the wing has a great AR, SC(2)-0414 was chosen due to its higher thickness over chord ratio. This was done for better integration of the wingbox, strut and wing design, making the overall design lighter.

7.3.2. Finite Wing Design

After the selection of the airfoil, the characteristics of the finite 3D wing were determined. This section describes the methodology applied for the design of main wing aerodynamic characteristics. The lifting characteristics of the main wing were determined in terms of lift curve slope (C_{L_α}), maximum lift coefficient ($C_{L_{max}}$) and stall angle (α_s). These

[1] URL `http://www.xflr5.tech/xflr5.htm` cited [2. June 2020]

parameters were evaluated at two conditions namely takeoff/landing phase (high lift), and cruise phase (low drag). The lift curve was evaluated using the DATCOM method [25]. This analytical method is based on the numerical and experimental investigation of the wing characteristics compared to the airfoil characteristics. This method is valid for all subsonic speed conditions and all AR values of the wing, which makes it applicable to the wing design of the CNA [25]. However, this method assumes that there are no shock waves present over the surface of the airfoil. As this assumption can have a significant effect on the results, it is validated later using advanced computations as described in Chapter 12. Using this method, C_{L_α} can be written as shown in Equation (7.3).

$$C_{L_\alpha} = \frac{2 \cdot \pi \cdot \mathrm{AR}}{2 + \sqrt{\frac{\mathrm{AR}^2 \cdot (1 - M_\infty^2)}{k^2} \cdot \left[1 + \frac{\tan^2 \Lambda_{0.5}}{(1 - M_\infty^2)}\right] + 4}} \tag{7.3}$$

In Equation (7.3), M_∞ is the freestream Mach number, $\Lambda_{0.5}$ is the sweep angle with respect to half chord line and k is the factor related to the wing's airfoil, calculated in terms of airfoil lift slope (C_{l_α}) as $k = C_{l_\alpha}/2\pi$. Further, using the lift curve slope of the wing, the required trim angle at cruise can be determined, using the Equation (7.4), where, α_{trim} is the required angle of attack at cruise and α_0 is the zero lift angle of attack. Based on the results from Equation (7.4), the incidence angle of the wing (i_w) is adjusted with respect to fuselage, to ensure passenger comfort during cruise.

$$\alpha_{\text{trim}} = \frac{C_{L_{\text{design}_{\text{wing}}}}}{C_{L_a}} + \alpha_{0L} \tag{7.4}$$

The maximum lift coefficient ($C_{L_{\max}}$) is another important parameter to ensure a good aerodynamic design of the wing. In order to incorporate this into the design, the $C_{L_{\max}}$ is calculated in terms of airfoil maximum lift coefficient ($C_{l_{\max}}$) using Equation (7.5a) [22]. In Equation (7.5a), the values for $\frac{C_{L_{\max}}}{C_{l_{\max}}}$ and $\Delta C_{L_{\max}}$ are also derived from [22], based on the airfoil design characteristics.

$$C_{L_{\max}} = \left[\frac{C_{L_{\max}}}{C_{l_{\max}}}\right] \cdot C_{l_{\max}} + \Delta C_{L_{\max}} \tag{7.5a}$$

$$\alpha_{stall} = \frac{C_{L_{max}}}{C_{L_a}} + \alpha_{0L} + \Delta\alpha_{C_{Lmax}} \tag{7.5b}$$

Now, using this obtained $C_{L_{\max}}$, the stall characteristics of the wing can also be analysed. The stall angle for the wing α_{stall} was computed using Equation (7.5b). It was derived simply using the fact that at α_{stall}, the lift coefficient is $C_{L_{\max}}$. Additionally, it takes into account the non linear part of the lift curve slope which is not represented by C_{L_α} alone, by using an additional term $\Delta\alpha_{C_{L_{\max}}}$.

The stall angle presented here is an estimate due to the complex flow behaviour during stall. A high-fidelity prediction method would allow for a better estimate but it was omitted due to the schedule constraint of this project. Also, other pilot assistance systems will be added, such as stick shakers and audio warnings, to avoid the aircraft to reach near stall attitudes, as also governed by regulations.

This concludes the description of the important tools developed to analyse the most important lifting characteristics of the wing. These tools were used to assess the design performance at every different iteration stage, leading to an efficient final wing design. However, since many of the methods rely on analytical approximations, and the interference effects between components are neglected, a more robust simulation was also performed to verify the results of these tools. These simulations are described in detail in Chapter 12.

The drag acting on the wing is also an important consideration for the wing design as it directly affects the fuel consumption of the aircraft and hence the sustainability of the complete aircraft. The total drag can be decomposed into two main sources namely, C_{D_0}, the zero lift drag , and C_{D_i}, the lift induced drag. Since the empirical method available from reference literature are inaccurate for high-aspect-ratio wing, the aerodynamic drag prediction was carried out using a different method, namely OpenVSP. The detailed descriptions of the methodology and the results are presented in Section 12.1.

7.4. Planform Design

The aerodynamic performance of the 3D finite wing is significantly affected by the design of the wing planform geometry. Several parameters such as the AR, taper ratio (λ) and the leading edge sweep angle (Λ_{LE}) are geometric parameters which can be altered in order to achieve the desired performance.

The AR is defined as $AR = \frac{b^2}{S}$. As seen through Equation (7.3), from an aerodynamic perspective, a high AR is desirable for improving performance as it increases the lift slope and decreases induced drag. The design of a braced wing aircraft as the one being designed in this report originates from the desire to make the aircraft more aerodynamically

efficient. The AR for the CNA was chosen to be 17 based on a literature study on the braced wing design concept [26] [27] [28] [29]. This design choice for the AR was made as having a lower AR would not provide significant improvements and defy the purpose of the braced wing design, whereas a higher value would result in the wing being too slender to be structurally feasible.

The other geometric parameter is the taper ratio, λ ($\lambda = \frac{C_{tip}}{C_{root}}$). The value of λ ultimately has an influence on the span-wise lift distribution. The value of λ was selected using an iterative process in which the span-wise lift distribution was altered to closely resemble an elliptical lift distribution. Following this process, the value of λ was set to equal 0.44 with a root chord of 4.135m.

The last parameter is the wing sweep angle, Λ_{LE}. Having a swept wing increases the Mach number at which drag divergence occurs. The performance of an airfoil can be significantly degraded (in terms of drag) when flying at high Mach numbers due to the formation of strong normal shock waves on the surface. Applying a sweep to a wing essentially alters the apparent freestream Mach number experienced by the airfoil (given by Equation (7.6)) and thus delays drag divergence. The sweep angle for the wing was computed using Equation (7.6) such that the apparent Mach number (M_{apparent}) is lower than the drag divergence number of the airfoil given that the cruise Mach number M_∞ is 0.78.

$$M_{\text{apparent}} = M_\infty \cdot cos(\Lambda_{LE}) \tag{7.6}$$

Through the obtained Mach drag divergence number for the selected airfoil, the minimum required sweep angle was found to be approximately 25°. However, this way of finding the required sweep angle is quite coarse, as it does not account for various nuances in the flow, for instance the shocks being present in the flow over the wing. Therefore, in order to allow for some margin in the design, a sweep angle of 30° was chosen.

In order to further enhance the performance of the wing, the addition of winglets were also considered. Due to limited time resources, the exact geometry of the winglet was not fully optimised and a simple trapezoidal winglet with a span of 1m was considered. This winglet was tested within OpenVSP and by tweaking certain parameters (the dihedral angle and taper ratio) and assessing its effect on the induced drag, the geometry of the winglet was finalised. Thus the final dihedral angle is 60° and a taper ratio of 0.29. The final planform design is depicted in Figure 7.1. In terms

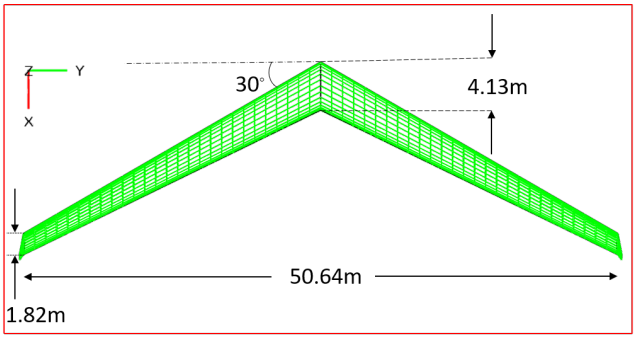

Figure 7.1: Final Wing Planform design

of the verification, several unit tests were carried out to test whether the equations in Section 7.3.2 were implemented correctly in the program. These unit tests involved tweaking certain parameters in the input and comparing the output to the expected results. For instance, one of the test for Equation (7.3) was to test the effect of AR. Increasing the AR should result in a higher value of C_{L_α}, this was thus confirmed through the test. Apart from these unit tests, the final planform geometry was tested within OpenVSP to finalise the aerodynamic parameters of the wing. The exact validation of OpenVSP is done using experimental data and a numerical simulation in Chapter 12.

7.5. Strut Design

The strut is an important component of the CNA, as it supports the high AR main wing. As its objective is solely to provide structural support, the strut was designed to minimise its drag. Furthermore, since the strut needs to provide a force opposite to the lift force, the strut was designed to produce no lift during standard cruise conditions. The design was performed with the same methodology as the design of the main wing; that is, first infinite wing design was completed, after which finite wing and wing planform design were carried out.

With the design lift coefficient of the strut set to zero, a selection of airfoils was made. To design for zero lift whilst optimising for structural performance, the selection existed solely of symmetric airfoils. A trade-off was performed in

the same manner as illustrated in Table 7.2. As all symmetric airfoils have very similar characteristics, the full trade-off is not shown. During the trade-off, two airfoils were very closely scored. These were the NASA SC(2)-0010 and the NACA 0012. In Figure 7.2 and Figure 7.3 the C_l and C_d versus angle of attack of these two winners from the trade-off are shown. Both graphs show the similarity in their aerodynamic performances. The decision to design the strut with the SC(2)-0010 airfoil was made in order to have favourable drag divergence conditions. This is important to keep the sweep to a minimum, which reduces the structural mass of the strut. Furthermore, it can be noted that the SC(2)-0010 has a slightly higher $C_{l_{max}}$ than NACA 0012, increasing performance during take-off and landing.

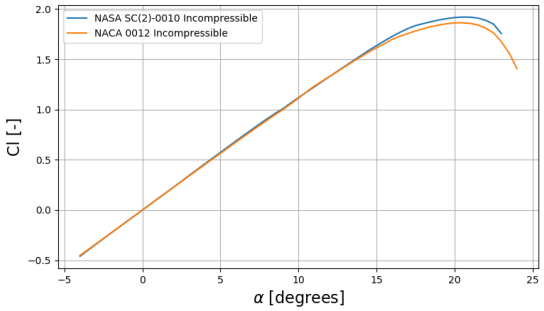

Figure 7.2: Cl-alpha curve for the airfoils NASA SC(2)-0010 and NACA 0012

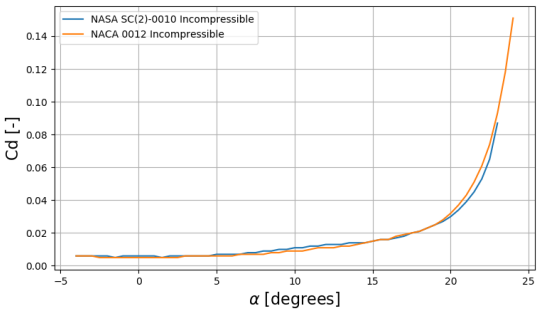

Figure 7.3: Cd-alpha curve for the airfoils NASA SC(2)-0010 and NACA 0012

The finite strut design was performed as described in Section 7.3.2. The design of the planform, however, differed mainly in two aspects; design for the planform of the strut-wing connection and the strut-fuselage connection. The final design can be seen in Figure 7.4. An intersection point as far as possible from the fuselage was chosen to give room to the engine placement close to the fuselage to cope with one engine inoperative requirements. From research carried out on subsonic high Mach number braced wing transport aircraft it was decided to stay within the range presented by reference aircraft, which is 70% of the span [30]. As the hinge is located at 71% of the span, the location of the strut-wing connection is indeed the outer most possible. Furthermore, by previous research done it has been shown that for the lowest structural wing mass, the sweep of the strut needs to be in a range of ±5°of the main wing [30]. For the initial design, it was chosen for the sweep of the strut to equal the sweep of the wing. Furthermore, in order to cope with resource constraints on the structural design, a strut-braced design without juries was adapted. To cope with aeroelastic effects, a study is performed in Section 8.4 to show that the strut can cope with these effects without juries.

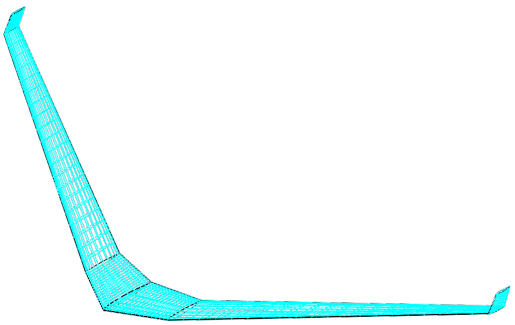

Figure 7.4: Isometric view of the strut in OpenVSP

The design of the strut-wing connection was dominated by a two dimensional nozzle effect. This means that a strong shock occurs at the strut and at the wing, making them prone to an adverse aeroelasitc behaviour and a high drag. As found by Ko et al., in the vicinity of the wing-strut connection the upper surface of the strut and the lower surface of the wing act as a two dimensional nozzle [31]. To examine this effect, Ko et al. make use of CFD simulations. To examine the nozzle effect in case of the CNA, the Mach-area relations of quasi one-directional flow are used. The flow at the connection point, however, is three directional. To justify the assumption of quasi one-directional flow, the research performed by Ko et al. is referred to. It is explained that the presence of a wall, in the case of the article a pylon, does not effect the shock strength significantly as proven by CFD. As such, the flow with or without walls experiences the same nozzle effect and shock conditions. For modelling of this nozzle effect, it is therefore chosen to include walls to satisfy the quasi one-directional flow assumption. The Mach-area relation can be written as Equation (7.7). With a sweep angle of 30°, it can be shown that the Mach number experienced by the strut is M = 0.68. It was found that $\left(\frac{A}{A^*}\right) = 1.11$ [32].

$$\left(\frac{A}{A^*}\right)^2 = \frac{1}{M^2} \cdot \left[\frac{1}{\gamma+1} \cdot \left(1 + \frac{\gamma-1}{2} \cdot M^2\right)\right]^{(\gamma+1)/(\gamma-1)} \tag{7.7}$$

The strut is designed to have the same chord as the wingbox for easy attachment, which is between 15-60% of the chord at any spanwise location. Knowing the chords of both the wing and the strut, Equation (7.7) can be used to determine the throat area [2]. If the distance between the strut and wing is greater than this throat area, no shock waves occur. Having the exact location and shape of the airfoils of the wing and the strut, it was calculated that the throat area is A^* = 0.747 m. This throat is situated at 0.87 m from the wing leading edge. To account for the thickness of the airfoils at the throat location, the vertical section of the strut was designed to be 0.98 m. Furthermore, the diagonal section of the strut has the same twist angle to cope with the throat area requirement whilst not generating any lift at cruise conditions. The calculation tool used was verified using several unit tests. For example, the equation to obtain the chord length at the spanwise location of the connection was verified by comparing the outcomes with known values, such as the mean aerodynamic chord, root chord and tip chord.

The design of the strut-fuselage connection was dominated by the structural performance, the clearance of the engines and the possibility to store the landing gears. The storage possibility for the landing gears was hereby leading, resulting in the design of the strut root section to be horizontal, with the half span, the root chord and the taper ratio of 3 m, 3.54 m and 0.7 respectively. Furthermore, the root section was designed to have no twist in order not to generate any lift at cruise conditions. The design of the strut was an iterative process, where use was made of OpenVSP as explained in Section 12.1.

7.6. High Lift Devices and Control Surfaces

Following the design of the wing planform, the design of the movable surfaces on the wing were carried out. The exact design procedure for the movable surfaces are discussed in this section. Firstly in Section 7.6.1 the high lift devices sizing is discussed, followed by the aileron sizing in Section 7.6.2.

7.6.1. High Lift Devices

In the previous subsections, the wing design was focused on making the wing optimal for cruise. By doing so however, the wings are underdesigned for the take-off and the landing phases. If the wings were instead optimised for take-off and landing, the wings would be overdesigned for cruise and would most likely lead to an inefficient flight. A solution to this problem is the use of High Lift Devices (HLDs) that are deployed during take-off and landing, and are capable of improving the aerodynamics of the wing so as to favour these conditions.

All types of HLDs are designed to either increase the $C_{L_{\max}}$ of the wing, delay the stall or both. In order to size the HLDs for the CNA, the approach described by Torenbeek was used [13]. Equation (7.8a) and Equation (7.8b) are the two equations described by Torenbeek in order to estimate the change in wing lift coefficient $\Delta C_{L_{max}}$ and the zero lift angle of attack $\Delta\alpha_{0L}$, given the $\Delta C_{l_{max}}$ and $(\Delta\alpha_{0L})_{\text{airfoil}}$ which are dependant on the type of HLD, the flapped area ratio $\frac{Swf}{S}$ and the angle of the hinge line $\Lambda_{\text{hinge-line}}$.

$$\Delta C_{L\max} = 0.9 \cdot \Delta C_{l\max} \cdot \frac{Swf}{S} \cdot \cos\Lambda_{\text{hinge-line}} \qquad \Delta\alpha_{0L} = (\Delta\alpha_{0L})_{\text{airfoil}} \cdot \frac{Swf}{S} \cdot \cos\Lambda_{\text{hinge-line}} \tag{7.8a,7.8b}$$

The exact sizing procedure went as follows, initially the required $\Delta C_{L_{max}}$ was evaluated by taking the difference between the maximum C_L of the wing in its clean configuration and the required maximum C_L for take-off and landing. These maximum required C_Ls for take-off and landing were increased by 10% in order to account for the down force generated by the horizontal stabiliser. With the estimation of the stall characteristics carried out in Section 7.3.1 and the aircraft performance analysis carried out in Chapter 13, the required $\Delta C_{L_{max}}$ for both take off and landing were then computed. Before diving into the sizing however, some physical interfaces and constraints for the HLDs had to be noted. Since the CNA has a folding wing tip 18m away from the fuselage centreline, adding HLDs or control surfaces on the folding part would immensely increase the complexity of the structure. Therefore, a design constraint was set which implied that neither the HLDs nor the ailerons could be positioned in the folding section. Adhering to this meant that the leading edge (LE) HLDs could span up to a maximum of 18m, and 15m for the trailing edge (TE) HLDs (giving a clearance of 3m for the ailerons). Furthermore, given the fact that the wings are very slender, the internal volume of the wing is limited. Thus, accounting for the structural considerations (wingbox size) and the fuel

[2] Note: the two dimensional throat 'area' translates to a distance when seen in a three dimensional view.

tank size, yet another constraint was set on the maximum chord fraction that could be used to place the HLD.

With these constraints and considerations, the required flapped area ($\frac{Swf}{S}$) was computed for various types of HLDs at various deflection angles using Equation (7.8a) in an iterative manner. For all the computations the value of $\Lambda_{\text{hinge -line}}$ was assumed to the value of the sweep angle at the respective edge ($\Lambda_{\text{hinge-line}} = \Lambda_{LE}$ for LE HLD and $\Lambda_{hinge-line} = \Lambda_{TE}$ for TE HLD). Out of all the outcomes from this iterative process, only a handful of solutions complied with the aforementioned constraints and were thus the feasible set of options. In order to select a solution from this list of feasible solutions, a qualitative trade-off of the HLDs was carried out. This qualitative trade off comprised of three criteria, the weight, the complexity and the drag. A simple example of such a trade-off is a case when choosing between a plain flap or a split flap. If both types of systems show that they can provide the required $\Delta C_{L_{\max}}$, it would be better to opt for a plain flap as it would generate less drag. Another example considering the weight and the complexity is choosing between a triple slotted flap and a double slotted flap, which in this case it is better to opt for the latter since the complexity and the weight of the triple slotted flap are considerably higher. The reason for this trade-off being qualitative is due to the fact that a detailed trade-off would otherwise require a far more in depth analysis of the systems, which would go beyond the time frame of this project. Nevertheless, by using this method, a design for the HLDs could be finalised which could meet the take-off and the landing requirements.

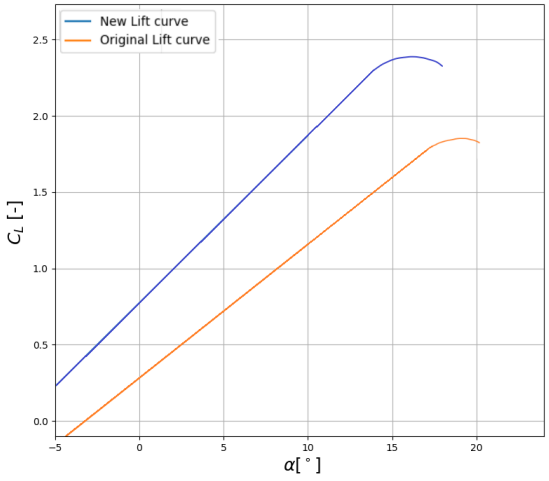

Figure 7.5: Lift curve in take off configuration

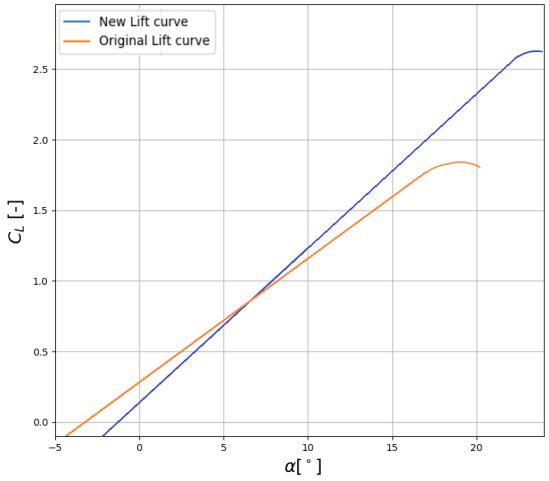

Figure 7.6: Lift curve in landing configuration

Table 7.3: Final HLD sizes and parameters

Parameters	**LE HLD**	**TE HLD**
Type	Kruger Flap	Double Slotted Fowler Flap
$\frac{Swf}{S}$ [-]	0.62	0.50
Swf [m^2]	93.48	75.39
Chord fraction [-]	0.15	0.25
Starting position from fuselage centreline [m]	2.60	3.60
End position from fuselage centreline [m]	17.03	15.08
$\delta_{f_{take-off}}$ [°]	0	10
$\delta_{f_{land}}$ [°]	-	50
$\Delta C_{L_{max_{take-off}}}$ [-]	0	0.72
$\Delta\alpha_{L_{max_{take-off}}}$ [°]	0	-5.36
$\Delta C_{L_{max_{land}}}$ [-]	0.14	0.79
$\Delta\alpha_{L_{max_{land}}}$ [°]	8.05	-6.74

Following this sizing method, the chosen HLDs along with their sizes and configurations during take-off and landing are depicted in Table 7.3. The final choices for the LE HLD and the TE HLD were the Kruger Flap and the Double Slotted Fowler Flap respectively. During take-off, only the Double Slotted Fowler Flap would be used with a deflection of 10° and during landing, both sets of HLDs would be used with a TE flap deflection of 50°. Figure 7.5 and Figure 7.6 show how the lift curve for the wing changes when in the take-off and in the landing configurations calculated with Equation (7.8b).

7.6.2. Aileron Sizing

REQ-CN-CTRL-14 (CS 25.147(d)) states that the aircraft must be able to make a 60° roll ϕ in less than 11 s at speed V_2. This is the requirement that drives the sizing of the aileron, which is the device responsible for the roll of the aircraft. In addition, the aileron is hinged to the back spar of the wing, which is located at 60% of the wing chord from the leading edge (Section 8.2). The TE HLDs finish at 15 m from the wing root, whereas the folding mechanism starts at 18 m. Therefore the aileron has 3 m space constrained by the envelopes of the folding mechanism and HLDs. The required roll rate is calculated using Equation (7.9a) by assuming that roll happens in a steady state condition. To calculate the actual roll rate generated by the aileron, Equation (7.9b) is used. Here the roll rate depends on velocity V, wing span b and aileron deflection angle δ_a, whereas $C_{l_{\delta a}}$ and C_{l_p} are the control and roll damping derivatives respectively.

$$P = \frac{\phi}{t} \qquad P = -\frac{C_{l_{\delta a}}}{C_{l_p}} \cdot \delta_a \cdot \left(\frac{2 \cdot V}{b}\right) \tag{7.9a,7.9b}$$

The deflection angle is the average between the absolute values of the maximum upward deflection $\delta_{a_{up}}$ and the downward $\delta_{a_{down}}$, as shown in Equation (7.10)

$$\delta_a = \frac{1}{2} \cdot \left(\delta_{a_{up}} + \delta_{a_{down}}\right) \tag{7.10}$$

The difference among these two values is set in order to minimise the effects of the adverse yaw. This phenomenon happens because during the turn one aileron goes up and the other goes down, so the wing side with the upward deflected aileron produces less lift, whereas the wing with the downward aileron deflection produces more lift. This moment couple produces the roll in the direction of the wing with less lift. However, the wing with more lift has the downside of increasing its induced drag, hence the aircraft has the tendency of yawing in the opposite direction of the turn, requiring the pilot to use the rudder to counteract. Typically the downward deflection is 75% of the upward deflection [**?**].

The equations for roll control and damping derivatives are shown in Equation (7.11a) and Equation (7.11b). They are both dependent on reference wing surface area S_{ref}, wing span b and aileron airfoil lift curve slope c_{l_α}. The airfoil used for the aileron is the same airfoil used for the wing (SC(2)-041). $C_{l_{\delta a}}$ is eventually dependent on the aileron effectiveness τ, which is derived thanks to Figure 7.7. The aileron effectiveness depends on the ratio between aileron chord and wing chord c_a/c_w. There is also an integral of the chord as a function of the spanwise location y, and the boundaries b_1 and b_2 are referring to the distance from the fuselage centerline of the inboard and outboard aileron span respectively. On the other hand, C_{l_P} depends also on the aileron airfoil zero-lift drag coefficient c_{d0}.

$$C_{l_{\delta a}} = \frac{2 \cdot c_{l\alpha} \cdot \tau}{S_{ref} \cdot b} \int_{b_1}^{b_2} c(y) \cdot y dy \qquad C_{l_P} = -\frac{4 \cdot \left(c_{l\alpha} + c_{d_0}\right)}{S_{ref} \cdot b^2} \int_0^{b/2} y^2 \cdot c(y) dy \tag{7.11a,7.11b}$$

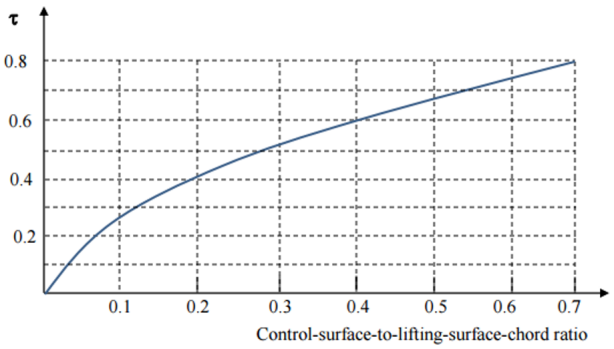

Figure 7.7: Aileron effectiveness [**?**]

The design procedure consists in choosing preliminary values for b_1, b_2, $\delta_{a_{up}}$ and $\delta_{a_{down}}$ from the aircraft database [**?**]. Since the aileron is hinged at the aft spar, $c_a/c_w = 0.4$. Iterations are performed to get a roll rate higher than the required from CS-25 with reasonable aileron dimensions. The final geometry of the aileron is shown in Table 7.4. Using Equation (7.9b), the roll rate is 0.132 rad/s, whereas the required is 0.095 rad/s, which means REQ-CN-CTRL-14 is satisfied. The program used to size the aileron was verified with a unit test. An increase in aileron surface area should provide a higher roll rate, so the outer span was enlarged. The increase in roll rate shown by the program

corresponded was proven with hand calculations, hence the program was verified.

Table 7.4: Aileron geometry

Parameter	Symbol	Value	Unit
Inboard Span	b_1	15.5	[m]
Outboard Span	b_2	17.5	[m]
Chord Ratio	c_a/c_w	0.4	[-]
Effectiveness	τ	0.6	[-]
Upward Deflection	$\delta_{a_{up}}$	25	[deg]
Downward Deflection	$\delta_{a_{down}}$	20	[deg]

For validation, the aileron geometry was compared with ailerons of other jet airliners to check whether the dimensions are reasonable. From Table 7.5, it is evident that the aileron is located closer to the fuselage with respect to other aircraft, and also the chord ratio is bigger. These values make sense because the aileron is constrained by the folding part of the wing, and an inner location of the aileron requires a bigger surface to produce the same couple moment which results in the roll rate, hence the aileron chord is also relatively bigger.

Table 7.5: Comparison of aileron geometries

No.	Aircraft	c_a/c_w	Span Ratio		δ_{Amax} (deg)	
			$b_1/(b/2)$	$b_2/(b/2)$	Up	Down
1	CNA	0.4	0.61	0.69	25	20
2	Fokker 100A	0.24	0.6	0.94	25	20
3	Airbus 340-600	0.22	0.64	0.92	25	20

7.7. Recommendations

The aerodynamic design of the wing was carried out with a limited time at hand and with limited resources. The design could therefore not be optimised to full extent. Throughout the design process, certain assumptions were made to simplify the process. These assumptions can be removed in the future detailed design steps and certain additional recommended steps can be included, which are presented here.

First, it is recommended that a detailed CFD analysis of the whole wing and strut is done. This can further validate the obtained results, such as lift and drag values, absence of shock waves, and the downwash generated by the high wing to size the Boundary Layer Ingestion propulsor (see Section 9.2) with more accuracy.

Due to the time constraint, not much focus was given to winglets design. As is known, winglets are able to improve the effective AR of the wing. Designing winglets could therefore increase the surface area, whilst keeping the span and effective AR constant. This allows for greater L/D values, lowering the fuel consumption and operational cost of the aircraft. Furthermore, an anhidral driven by dynamic stability requirements could lower the projected wingspan. This would allow for an increase in span and therefore an increase in surface area, whilst keeping the AR constant.

The airfoils that were used to design the CNA wing and strut were off-the-shelf airfoils, designed by NASA in the 1960's and 1970's. In order to increase low and high speed performance, and to decrease sweep and weight, it is recommended that an airfoil is designed specifically for the CNA wing and strut. Furthermore, it was researched whether the use of two or more airfoils could decrease geometrical washout. Due to the superb performance of the current airfoils, it was not considered in the final design. It is therefore recommended that this option is explored further with the CNA-specific designed airfoils.

Lastly, it is recommended that an optimum lift distribution for the strut is found. Currently, the strut is not generating lift during standard cruise conditions. In further design, however, it might show benefits to have the strut generate some amount of lift. This can increase the L/D and other performance parameters, but will decrease the structural performance of the strut. It is therefore recommended that with extensive iterations and optimum lift distribution is found.

8
Structural Wing Design

The CNA has a wing aspect ratio of 17.0, which is far beyond the range found in typical commercial airliners [**?** , p 54]. Due to the high slenderness of the wing, the wing structure needs a thorough structural analysis to prove that this novel wing configuration is safe to use on a commercial aircraft. The objective and requirements for the wing structural design are found in Section 8.1. Then the methodology, assumptions and their effects are explained in Section 8.2. The structural analysis is then reported in Section 8.3. The aeroelasticity analysis of the main wing is explained in Section 8.4. The strut structure is then reported in Section 8.5. Customers wish the new aircraft to be compatible with the same gates and taxiways as the A320/737 class aircraft it replaces. The aircraft is therefore fitted with folding wingtips. These were designed with high safety and reliability in mind and its design is documented in Section 8.6. Next, the wing mass and fuel volume estimation, verification and validation and recommendations are presented in Section 8.7, Section 8.8 and Section 8.9.

8.1. Objective and Requirements

The top level objective is to design a wing and strut structure that is as light as possible, while being able to carry all loads to be expected during its lifetime without catastrophic failure. The wing and the strut are subjected to many possible load cases. Besides to the aerodynamic lift and drag forces, the wing is also subjected to forces originating from the fuel weight and pressure, the engine weight and thrust, its own structural weight, the fatigue due to its cyclic loading and finally damage tolerance aspects. The wing structure thus needs to meet an extensive list of requirements. Apart from the load cases, requirements also arise from regulations set by airworthiness authorities and requirements related to the interconnection with other aircraft systems. The main driving requirements for the wing and strut structural design are listed in Table 8.1.

Table 8.1: Driving requirements for the wing and strut structure

Identifier	Requirement	Source
REQ-CN-WING-1	The wing and strut structure shall sustain an ultimate load factor of 3.75 for 3 seconds without catastrophic failure.	CS 25.305
REQ-CN-WING-2	The wing structure shall not plastically deform at any point at limit load.	CS 25.307
REQ-CN-WING-3	The wing structure shall have sufficient torsional stiffness to prevent undamped flutter at speeds below the design dive speed V_D.	CS 25.629
REQ-CN-WING-4	The wing structural mass shall be below 9800 kg.	Budget
REQ-CN-WING-5	The wing shall have sufficient volume to store at least 14.7 m^3 of fuel.	Propulsion

For the folding wingtip, the top level objective is to design a folding mechanism that is safe and reliable, while keeping its weight low. Since this is a novel feature, many questions arise concerning its safety. Can the aircraft fly safely without wingtips? How is it ensured that the mechanism does not unlock in flight? How is the mechanism controlled and what if there is a malfunction within this system? Those questions will be answered. Furthermore, an extensive list of regulatory and mechanism-related requirements are formulated. The driving requirements are summarised in Table 8.2.

Table 8.2: Driving requirements for the folding wingtip

Identifier	Requirement	Source
REQ-CN-FWT-01	The wingtip shall transition from the folded position to the extended position (or vice-versa) within 6 seconds.	Design
REQ-CN-FWT-05	The Folding wingtips and its operating mechanism must be designed for 65 knot horizontal ground gust conditions in any direction.	CS-25 Special Condition D-21-9
REQ-CN-FWT-08	The wingtip fold operating mechanism shall ensure that the wingtips are properly secured during ground operations.	CS-25 Special Condition D-21-9
REQ-CN-FWT-11	The wingtips must have means to safeguard against unlocking in flight as a result of failures, including failure of any single structural element.	CS-25 Special Condition D-21-9

8.2. Methodology and Assumptions

The internal wing structure is modelled as a box beam. The box beam is the main load-bearing structure inside the wing and carries most of the shear, bending and torsional loads imposed on it. The box beam model used in this analysis is a rectangular box that consists of two spars, top and bottom skins, stiffeners and four spar caps as shown in Figure 8.1. These structural elements need to be sized so that the structure can safely bear all the loads imposed on it as well as meeting the requirements in Section 8.1.

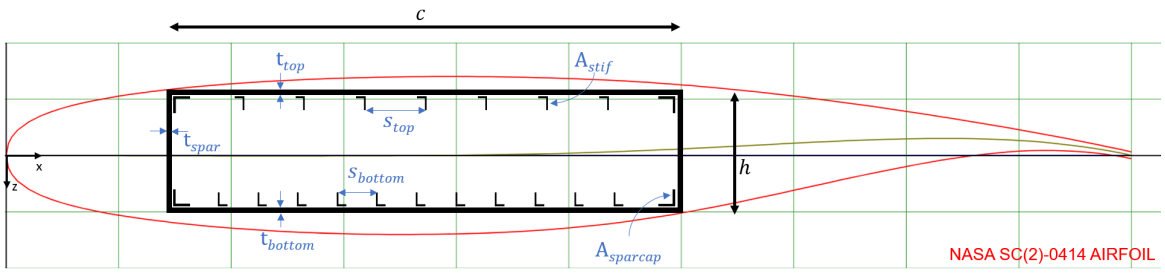

Figure 8.1: The wingbox as fitted in the airfoil, with structural design parameters indicated

The box beam has a central position in the airfoil. The goal is to maximise the wingbox area within the cross-section. This is constrained by other systems. Before the front spar, space is necessary for the leading edge, slats and the anti-ice system. Behind the aft spar, the flaps and ailerons are positioned. The wingbox runs from 15% until 60% of the chord as found in typical commercial transports [**?** , p 24]. This can be used because the CNA has similar HLD. The wingbox height is then maximised within the airfoil and uses 79% of the maximum thickness. In conclusion, the wingbox cross-section is well-defined within the airfoil.

The wingbox needs to cope with numerous load cases, so the critical load case needs to be defined. The load to which the wing is subjected originate from cruise flight, hard landings, taxi, manoeuvre at maximum limit load (positive and negative limit load factor), fatigue, vibrations, flutter and design for damage tolerance. The structural design was performed for the manoeuvre at maximum load factor because this is the most critical load case, and later other failure modes and requirements were checked (in fact, buckling and flutter). The design was iterated until all requirements were met.

Now this load case is defined more clearly. The wingbox is subjected to multiple forces of different magnitudes. This is outlined in the free body diagrams given in Figure 8.2 and Figure 8.3 for the rear view and top view of the right wing respectively. First and foremost, the wing's aerodynamic loading is decomposed in a lift force (perpendicular to the chord line) and a drag force (parallel to the chord line). It causes normal stress and shear stress in the material due to it generating a bending moment (around the x and z axes), internal shear force (in the x-z plane) and torque (around the y axis). Secondly, the engine mass, wing structural mass and fuel mass result in a weight force (point load or distributed load) applied to the wing structure. The fuel weight was set to zero as that was the most critical case for the manoeuvre load. Finally, the engine thrust was added.

The reaction forces and the boundary conditions for the structure need to be defined. They are indicated in orange in the free body diagrams. The wingbox is connected to the fuselage via the wing root and via the struts. This results in a problem that is statically indeterminate. In order to simplify the initial approach, certain assumptions were made as listed below.

1. **Pin Supports at Root and Strut:** The wing was assumed to be pin supported at the wing root and the strut. This simplified the problem to a statically determinate problem. However, the deflections of the wing are overestimated because certain reaction forces (constraints) are lacking. Thus, this leads to a conservative estimate of the deflections. Furthermore, the internal moment near the root is underestimated, underestimating the amount of structural elements needed, especially near the root. This assumption is thus valid for a preliminary analysis, but needs review when further developing the wing root structure.
2. **Thin-walled Structure:** The wingbox was assumed to be a thin-walled structure. All thickness terms of order two or higher were discarded in stiffness calculations because their contributions to the overall stiffness were very small. This assumption is valid if the thickness is smaller than 10 times the smallest overall dimension (the wingbox height in this case). Therefore this assumption needs validation later. By using the thin-walled assumption, the stiffness is underestimated.

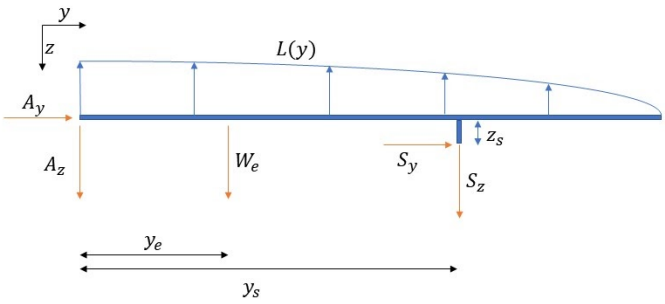

Figure 8.2: Free body diagram, right wing as viewed from behind

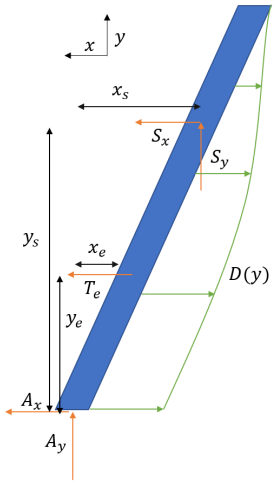

Figure 8.3: Free body diagram, right wing as viewed from above

3. **Rectangular Cross-section:** The wingbox was simplified to a rectangular cross-section. In all computations, the wingbox did not follow the airfoil shape. This assumption is acceptable because the structural stiffness (inertia) is underestimated using this simplification, so it is conservative.

4. **2-Dimensional Model:** A two dimensional structural model was used. Consequently, the effect of the wing sweep on the internal torque was neglected. This means the torsional loads imposed on the wingbox are underestimated. This assumption is acceptable because the strut provides a load path and will consequently reduce the internal torque in the inboard wing (if correctly placed) compared to a wing without a strut. This assumption however needs further review when further developing the wing structure.

5. **Small Structural Weight:** The effect of the structural weight on the bending moment and the shear force was neglected. The structural weight is of an order of magnitude smaller than the aerodynamic loading. The effect of the assumption is conservative since the bending moment will be overestimated in this case.

6. **Small Drag Force:** The effect of the drag force on the bending moment and the shear force was neglected. Since the drag force is an order of magnitude smaller than the lift force and it causes bending about the z-axis of the wingbox, which has a larger moment of inertia, this is acceptable. By making this assumption, the internal stresses are underestimated.

7. **Small Fuel Pressurisation Loads:** The loads imposed on the structure due to the fuel pressurisation were neglected. The fuel pressure improves the buckling performance of the wing skin, so neglecting this is conservative. Furthermore, the pressurisation bends the spars outwards slightly, but these deformations were assumed to be small and therefore this assumption is valid.

8. **No Torsional Loads Carried By Open Sections:** The stiffeners were assumed to not take up any torsional loads. Stiffeners are open sections and therefore have very small contributions to the torsional stiffness compared to the box structure defined by the skins and spars. By making this assumption, the torsional stiffness is underestimated.

8.3. Structural Analysis

The sizing of the design parameters of the wingbox as defined in Figure 8.1 is an iterative process in which the design is checked for three failure modes and constantly updated. This is done using a numerical tool developed in Python. The tool layout as well as the design flow is given in Figure 8.4. Within this section, the internal loading is determined, then the material will be selected followed by the analysis of three failure modes. Finally, the spanwise wingbox properties and internal stress results will be explained.

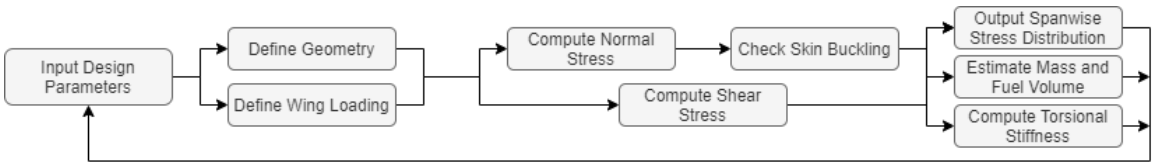

Figure 8.4: Flow of the design process of the wingbox structure

8.3.1. Internal Loading

In order to design the wing structure for the aircraft, first and foremost, the most critical load case had to be identified. Following the flight envelope calculation done in Section 5.4, three critical load cases resulting in a load factor of 2.5 were found. For the design, this load-factor was scaled by a factor of 1.5 which determined the ultimate load factor of 3.75. The critical case was taken to be at the cruise speed with a C_L of 1.62. Since all of the three scenarios produce same load factor, any of the three cases could be chosen as the critical case to carry out the design.

With the simulations carried out by the aerodynamics department, the exact loading distributions for this critical load case was generated. Figure 8.5 shows the distributed lift load interpolated using 1D Radial Basis Functions (RBF) over the span. It is however worth noting that this critical load case occurs at conditions that the aerodynamic simulations are not able to accurately model (due to possible shock waves and flow separation). Therefore, it can be expected that the obtained results are actually an underestimate of the actual loads experienced by the wing. Nonetheless, this loading data provides sufficient amount of insight in order to carry out the structural design.

With the distributed load and the free body diagram in Figure 8.2, the (statically determinant) system was solved in order to compute the reaction forces at the wing root and at the wing-strut connection. Given these computed loads, the internal moment and the shear force distribution were computed. Figure 8.7 shows how the internal moment and the shear force vary along the span of the wing at the critical load case. The sign convention of the positive moment and shear is depicted in Figure 8.6. The two kinks in the shear force diagram are due to the engine weight and the z-component of the force provided by the strut.

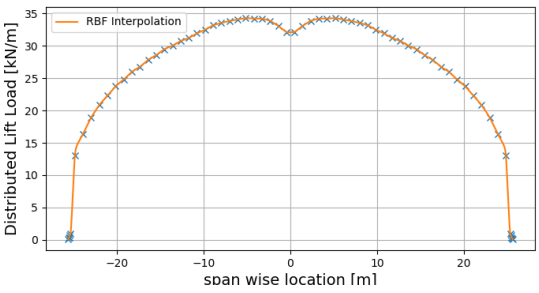

Figure 8.5: Distributed lift load at limiting condition

Figure 8.6: Sign Convention for positive bending moment and shear forces

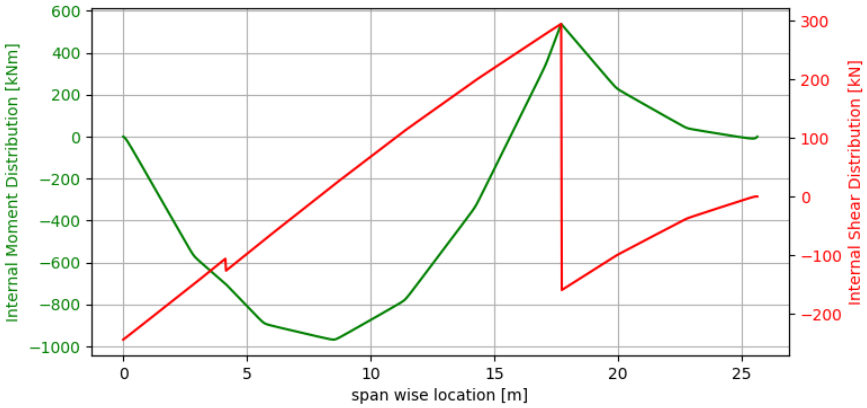

Figure 8.7: Distributed moment and shear force diagram

The exact manner through which this internal loading was computed relates to the relation between the distributed load, the shear force and the moment.

$$V(y) = \int_{\frac{b}{2}}^{y} L(\xi)d\xi \qquad M(y) = \int_{\frac{b}{2}}^{y} V(\eta)d\eta = \int_{\frac{b}{2}}^{y}\int_{\frac{b}{2}}^{\eta} L(\xi)d\xi d\eta \tag{8.1a, 8.1b}$$

Equation (8.1a) and Equation (8.1b) are the integral form of the definitions of the shear force V and the moment M as a function of the distributed lift load, L. In the case that there are discrete point loads as opposite to distributed load, the equations still hold, and are rather simpler as the double integral becomes a single integral. These general formulations were used in order to compute the internal loads in the wing. These integrals were all evaluated numerically via a numerical quadrature rule. Using this method, the two major loads, namely the moment and the shear were determined. However, there is still another load acting on the wing coming from the fact that the lift force is not acting at the shear centre of the wingbox. The exact chord-wise location of the centre of pressure at each span-wise location was obtained from the aerodynamic simulation data. Furthermore, given the fact that the wingbox was considered as a simple rectangular cross-section with at least one symmetry axis, the shear centre was at the centroid. With the location of the load, and the location of the shear centre known, the internal torque distribution was then computed.

With the internal loading determined, the internal bending and shear stresses were then computed using Equation (8.2a) - Equation (8.2c). These equations are valid for symmetric sections (product moment of inertia is zero, $I_{xz} = 0$) which incorporates the bending moment M, the shear force V and the torque T.

$$\sigma_{bending} = \frac{M \cdot z}{I_{xx}} \qquad \tau_{shear} = -\frac{V}{I_{xx} \cdot t} \cdot \int_0^s t \cdot y ds \qquad \tau_{torque} = \frac{T}{2 \cdot t \cdot A_m} \tag{8.2a, 8.2b, 8.2c}$$

8.3.2. Material Selection

Having obtained the internal loading, a suitable material was chosen. The material should have an acceptable performance on different criteria, not only stiffness and strength. The wing is subjected to cyclic loading, so a high fatigue strength is desirable. The aircraft is designed for a lifetime of 25 years and it will have to cope with harsh conditions such as the environment and damage by ground handling, so a high hardness is desirable. In terms of damage tolerance, a high fracture toughness is desirable such that the aircraft can see longer service intervals which results in a large benefit in terms of its operational cost. Speaking of cost, the material cost and machine-ability are other important properties. These and many more aspects were taken into account, and as will be explained one is more important than the other. A qualitative function deployment (QFD) was used for this.

Before a trade-off was made, a suitable "pool" of materials was chosen and its mechanical properties documented. The materials that were considered consist of both conventional (such as different types of aluminium and titanium) and novel materials (such as natural fibres, carbon fibre reinforced polymers and glass reinforced aluminium). A summary of the materials considered and their most important properties are tabulated in Table 8.3 where G is the shear modulus, K_{Ic} is the fracture toughness and H_V is the Vickers Hardness. Some materials have been filtered out because they are "obvious losers" (steel, titanium and natural fibres). They are respectively too heavy, costly and weak.

The QFD ranked eight different material properties by linking them to top level customer wishes. The top level wishes considered were low weight, sustainability, low cost, safety and easy maintenance, in this order of importance. Next, the material properties were linked to customer wishes by means of a correlation factor, which resulted in relative weights. The most important properties are the specific stiffness (E/ρ) and specific torsional stiffness (G/ρ) each accounting for a weight of 19%. The least important property considered is the hardness, only weighing for 4%. Using all relative weights, the different materials were scored. The results are displayed in Table 8.3 where the materials are ranked by score and their percentage difference is given.

The aluminium alloys scored the highest and the composite scored the lowest, the latter mainly due to its poor recyclability and cost. Aluminium 2024-T4 and 2014-T6 were the two best materials and scored well overall. The 7000 series aluminium alloys came in second mainly due to their lower torsional stiffness and lower recyclability. They scored worse on recyclability due to higher hardness and more difficult and environmentally demanding machining processes. Since these criteria were given high weights, the 7000 series alloys ended up with a lower score despite showing better mechanical properties. Finally, glare was found to be performing the best in fatigue and damage tolerance, but because those criteria were given low weights (each accounting for only 8%) the material cannot make up for its worse specific stiffnesses (E/ρ and G/ρ) and higher cost.

[1] URL `http://matweb.com/index.aspx` cited [18. June 2020]

Table 8.3: Main material properties of the feasible materials. The fatigue strength is given for 500 000 cycles. The CFRP chosen is a quasi-isotropic carbon fibre reinforced polymer with a 0°/90°/±45° layup with an urethane resin matrix. [33]

	σ_y **[MPa]**	σ_{ult} **[MPa]**	ρ $[\frac{kg}{m^3}]$	E **[GPa]**	G **[GPa]**	$\sigma_{fatigue}$ **[MPa]**	K_{Ic} **[MPa$\sqrt{m}$]**	H_V	**Score**	**Relative Difference [%]**
Al 2024-T4 [1]	324	469	2780	73.1	28	138	26	137	1.85	\
Al 2014-T6 [1]	414	483	2800	72.4	28	155	26.4	155	1.84	0
Al 7178-T6 [1]	538	607	2830	71.7	27	150	18	189	1.69	9
Al 7075-T6 [1]	503	572	2810	71.7	26.9	159	20	175	1.63	12
Glare 4 4/3 [34]	270	880	2300	57	17.5	156	45	137	1.58	15
CFRP [33]	474	474	1609	109	2.96	\	\	\	1.41	24

A final choice was made. To simplify the design process only one material was used in the wingbox. However, if more resources would be available, it is recommended to choose a different material for example for the top and bottom skin because they experience different loads. It was found that a 7000 series aluminium would be ideal for the skins loaded in compression, and a 2000 series alloy for the parts loaded in tension and shear. But since only one material was chosen, the 2000 series was selected as it ranked highest in the QFD. Aluminium 2014-T6 was chosen over Aluminium 2024-T4 because of a much higher yield stress. This concludes the material selection.

8.3.3. Analysis of Failure Modes

Each wing was initially divided in ten equally sized sections. The design process began with setting equal properties in all ten sections. Then, three failure modes were checked. The three failure modes considered were: exceeding the ultimate strength at ultimate load, exceeding the maximum allowable shear stress at ultimate load and skin buckling. The cross-sectional parameters were iterated until the wingbox does not fail in any sections, while keeping the stresses as high as possible for a most weight-optimal design.

The wingbox was designed such that the internal normal stress does not exceed the ultimate strength of the aluminium 2014-T6 (483 MPa) [2]. This was done by altering the design parameters shown in Figure 8.1 to increase or decrease the moment of inertia. The moment of inertia can be increased most effectively by a combination of increasing the skin thickness, the number of stiffeners and the areas of the stiffeners and spar caps. However, not all solutions converge to a lower weight. This was an iterative process, in which the weight was immediately estimated within the tool, and the designer can get a feeling for what decisions lead to a lower weight.

Since the wingbox has a simple cross-sectional shape, and the drag force was neglected, all forces cause bending around the x-axis. The maximum normal stress due to bending occurs at the top or the bottom skin, depending on the number of stiffeners fitted to each skin. If the number of stiffeners between the top and bottom skin are different, the centroid will shift towards the skin with more stiffeners. Consequently, the other skin will see the highest normal stress for that section.

From the internal bending moment in Figure 8.7 one identifies that the moment changes its sign. Along most of the inboard wing, the internal moment is negative. The top skin is loaded in tension and the bottom skin is loaded in compression. However, in the outboard wing (between strut and wingtip) the opposite holds. This has consequences on the cross-sectional configuration. In the inboard wing the bottom skin needs more stiffeners to counter buckling, while in the outboard wing the top skin needs more stiffeners. This was found inherent to the braced wing configuration.

A number of constraints arise when designing the wingbox parameters. The skin thickness cannot be lower than 2 mm in order not to be sensitive to external damage in regular daily operations [35]. The stiffeners must be inspected for cracks and corrosion, so an L-stiffener is selected. The spar and skin thickness is chosen to increase or decrease incrementally. The thickness is increased or decreased in steps of 0.5 mm. This is because the skin plates need to be manufactured and the accuracy of the tools is limited.

Next, the shear was analysed. The wingbox was designed such that the internal shear stress remains below the maximum allowable shear stress. The shear strength of aluminum is 290 MPa [3]. The highest shear stress occurs in the

[2] It should be noted that for the limit load the normal stress should be below the yield stress so that no permanent deformation occurs as per REQ-CN-WING-2. For the ultimate load, the internal stress may exceed the yield stress but should stay below the ultimate strength of the material as defined by REQ-CN-WING-1.

[3] URL `http://asm.matweb.com/search/SpecificMaterial.asp?bassnum=MA2014T6` cited [19. June 2020]

spars. This is certain because the drag force was not taken into account. Since the highest normal stress and the highest shear stress occur at different places in the cross-section, they are analysed separately. In a further design iteration, the stresses should be evaluated simultaneously along the cross-section and superimposed using the von Mises failure criterion, for example. This was however not performed due to time constraints.

Again the same design approach was used. All ten spanwise stations start with the same configuration. The tool outputs the maximum shear stress in the spars. When the shear stress was above the shear strength, the skin thickness or the spar thickness were increased. If the stress is below the allowable, the thicknesses were reduced in order to save weight, while keeping in mind the constraints already mentioned (such as the minimum skin and spar thicknesses for damage tolerance). The iterations were performed until the shear stress was near but below the material shear strength, and this while aiming for a low weight solution.

Finally, the wingbox structure was checked for skin buckling. Equation (6.5) was reformed to Equation (8.3) to obtain the minimum required stiffener spacing (b) in terms of the applied stress (σ), material properties, the skin thickness and the clamping condition (C = 4 when the skin is assumed to be simply supported). When the design tool detects buckling in a skin panel, it displays the number of stiffeners necessary to resolve the buckling.

$$b = \sqrt{\frac{C \cdot \pi^2 \cdot E \cdot t_{\text{skin}}^2}{12 \cdot (1 - \nu^2) \cdot |\sigma|}} \tag{8.3}$$

A number of simplifications were made. First and foremost, when the skin buckles it can no longer carry any additional loads. Therefore, it was chosen to prevent buckling below the ultimate load. In order to save more weight, one could allow the skin to buckle after the limit load, given that the remaining load-bearing components (mainly stiffeners and spars at that point) can carry the remaining loads up until the ultimate load without failure (such as crippling of stiffeners). This needs further analysis. The second simplification is that the stiffener spacing was chosen to be constant. If drag was not neglected, the wing bends upwards and backwards, meaning the normal stress would be higher in the top right and bottom left corners of the cross-section, which consequently means the stiffeners could be closer together there and further apart in the other quadrants. This demands a variable spacing along the skin, for a more optimal design in terms of weight.

Finally ribs were added to the wing to transfer the loads between the skins and the spars as well as providing local strengthening where point loads are applied (such as the engine pylon and strut attachment). The rib spacing is limited by panel buckling and in-plane shear loads originating from the pressurisation of the fuel tanks. The rib spacing was determined using literature, and was found to be optimal for a spacing between 28 in and 32 in for a Boeing 737 class aircraft [35]. This is also applicable to this aircraft, because the fuel pressurisation and panel buckling are similar as well as the mission profile and consequently the load cases. On the other hand, the torque and the bending are not similar due to the braced wing configuration, but these do not have the largest influence on the rib spacing. Taking the larger spacing to lower the weight and the cost, the wing has at least 63 ribs.

8.3.4. Results

After numerous design iterations, the final design was determined. All wingbox cross-sectional parameters are given in Figure 8.8-a and Figure 8.8-b. They show the material thickness and stiffener distribution over the span. There are ten spanwise stations, and the thickness increases in steps. A thicker skin is used in the bottom skin of the inboard wing and the top skin of the outboard wing because these skins are loaded in compression. The spar thickness is continuous at the minimum value of 2 mm for a large portion of the span. It is increased to 3 mm in the last spanwise station in order to keep the shear stress below the maximum allowable within the spar.

The stiffeners follow a similar pattern. More material is added where parts are loaded in compression in order to prevent buckling. A maximum of 25 stiffeners is required where the internal moment is largest as found in Section 8.3.1. This is halfway the inboard wing in the bottom skin. Special attention is payed to the continuity of load paths. The number of stiffeners should be kept constant for as long as possible to prevent stress concentrations at ribs and to keep the manufacturing cost down.

The third plot (Figure 8.8-c) shows the internal normal stress over the span. In the ideal case, all stations should fail simultaneously, so all stations should have the same stress at ultimate load (preferably just below 489 MPa which is the ultimate strength of the material). However, the skin thickness and spar thickness is already minimal at sections where the stress could be higher. The thickness there was defined by damage tolerance, not by loading. The change

in sign of the normal stress occurs at the attachment with the strut. Finally, the fourth plot (Figure 8.8-d) shows the internal shear stress along the span. This should always remain below 290 MPa and is indeed the case. The highest shear stress occurs at the attachment point with the strut due to the sudden application of the large point force. The stress is also high near the tip, but below the ultimate shear strength.

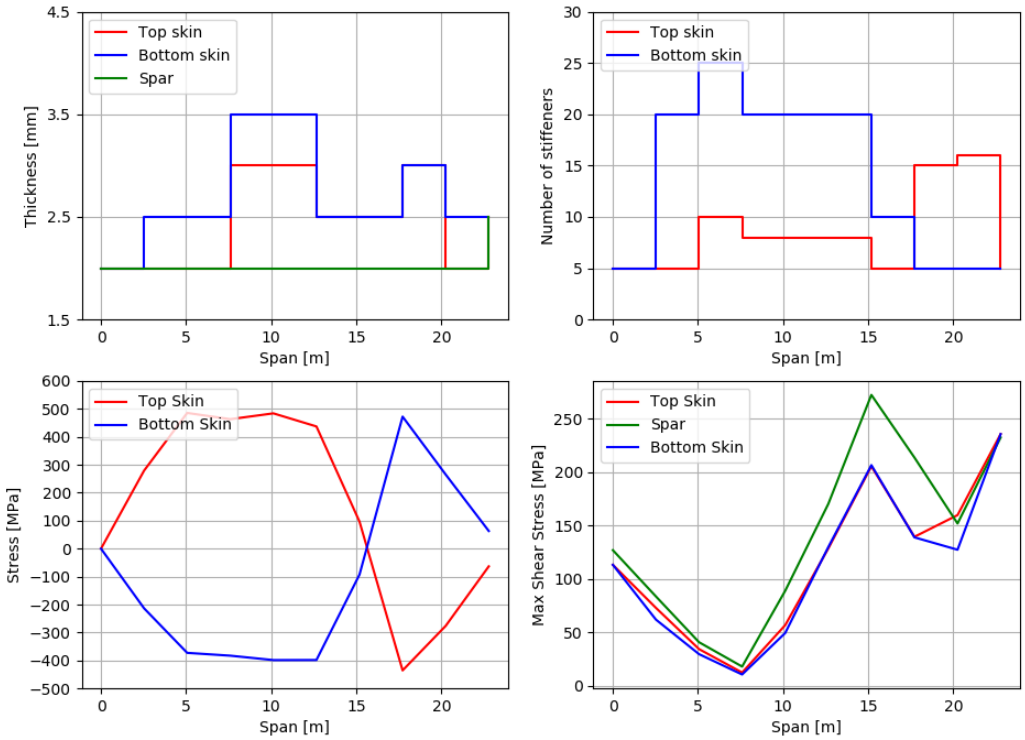

Figure 8.8: Wingbox properties and internal loading for the ultimate flight load of 3.75g: material thickness distribution (a), stiffener distribution (b), normal stress distribution (c) and shear force distribution (d)

As a final check, the wing structure was checked for flutter as explained in Section 8.4. The torsional stiffness of the wing structure was however found to be insufficient. This means that the wingbox design is in fact not limited by REQ-CN-WING-1 but it is limited by REQ-CN-WING-3. The torsional stiffness was increased by 58% to prevent undamped oscillations. This was achieved by increasing the skin thickness with 150% and the spar thickness by 200%. This however made the wing 47% heavier. A thorough analysis on the wings aeroelastic characteristics is found in Section 8.4.

8.4. Aeroelasticity Study

Aeroelasticity is defined as the interaction between the aerodynamic forces and the elastic forces acting on a structure. These aerodynamic forces in return are also dependent upon the deflection caused by them [36]. This interaction between the two types of forces can mainly be categorised into two different cases - static and dynamic. Both of these cases are important for most of the aerospace applications. For the CNA, these effects are even more prominent since it has slender wings with a very high aspect ratio. Therefore, it is important to ensure that these phenomena do not hinder with the aircraft performance throughout its flight envelope.

In order to verify the aircraft's nominal performance with respect to the critical aeroelastic phenomena, both static and dynamic aeroelasticity analyses were performed. For these analyses, only the main wing was considered. In real life, the contribution from the complete aircraft needs to be assessed. However, based on the time constraint and project resources, only the wing analysis was considered. The aeroleastic phenomena associated with the wing are also the ones which are prominent for most of the critical scenarios [36]. Therefore, this restricted analysis will nevertheless be sufficient to prove the aircraft's response with respect to potentially dangerous aeroelastic phenomena.

8.4.1. Static Aeroelasticity

Static aeroelasticity deals with the analysis of deflection of the structures due to aerodynamic loads, where both the loads and the motion are considered to be independent of time. The aerodynamic forces acting on the structure cause the deformation of the structure, which in return change the form of aerodynamic forces acting on the structure, and

this phenomenon continues until equilibrium is achieved. This interaction between the structure and the fluid (air in the case of aircraft) is crucial for a wing's stability and performance. There are two main phenomena associated with the static aeroelasticity namely "control reversal" and "divergence". Both of these phenomena and the associated results for the CNA design are described in further detail in this section.

In order to assess the wing design of the CNA for static aeroelasticity related aspects, it is important to accurately model the wing. For the static analysis, a semi rigid wing model is chosen for the wing. This model is chosen over other 2-DOF(degree of freedom) models, as it allows the finite wing parameters to be incorporated in the model, which are crucial for a finite wing analysis. In order to implement the model, a number of assumptions are made which were explained as follows along with their justifications.

1. **Taper Ratio Neglected:** The taper ratio of the wing was neglected in the model and a constant chord was assumed. This assumption can have a significant effect on the overall structural stiffness of the wing, which can lead to under estimation of the static aeroelastic aspects. Therefore, in order to account for this, the structural stiffness (bending and torsion) of the wing was corrected to reflect the actual taper ratio. These corrections were introduced by changing the stiffness values (GJ,EI) to effective stiffness values (taking average over entire length), obtained from Section 8.3, to ($\overline{GJ}, \overline{EI}$), which were then assumed to be constant throughout the length.
2. **2D System:** The model is a 2- DOF system. Therefore, only bending and torsion modes are considered. These two are the most critical modes, with respect to the aeroelasticity aspects [37]. Thus, the application of the model is well suited for the CNA wing analysis.
3. **Fixed Wing Root:** The wing root incidence angle was assumed to be fixed. The rest of the wing structure was assumed to be flexible with respect to the fixed root. This assumption can be considered valid as it clearly depicts the real wing structure arrangement.
4. **Linear System:** The variations of deflection over the wing was assumed to be depicted by an idealised linear relation. Thus, the non-linear terms were neglected. This assumption can simplify the system to a great extent without having much effect on the analysis results, especially since it is related to static behaviour of the wing [37].
5. **No Compressibility Effects:** The compressibility effects were ignored for the aeroelastic analysis. The analysis including the compressibility is rather complex and requires numerical simulation techniques [36]. Thus, respecting the project time constraint, these effects were not considered. However, the effect of this assumption will not be significant for low angles of attack, as there are no shock waves present over the airfoil surface as shown later in Section 12.1. Hence, this assumption will not have a significant influence on the results for CNA wing design.

Using the above mentioned assumptions, the CNA wing can be modelled as shown in Figure 8.9. In the Figure 8.9, $b_{1/2}$ is the half span of the wing, c is constant chord length (assumed to be equal to MAC), $\Lambda_{0.5}$ is the half chord sweep, e_{ac} is the distance between the elastic axis and the aerodynamic centre line and x_f is the distance of the elastic axis from the wing leading edge. Now, using this model, the critical static aeroelasticity related phenomenon can be assessed, which are explained as follows.

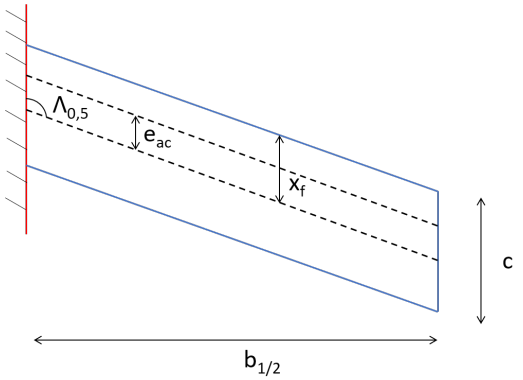

Figure 8.9: Semi rigid wing model used for divergence study on wing design

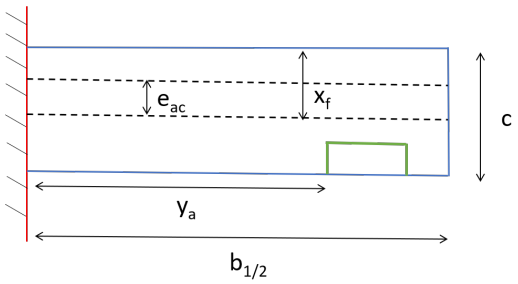

Figure 8.10: Semi rigid wing model used for control reversal study on wing design

The most critical phenomenon is the divergence, which occurs when the aerodynamic moments acting over the structure take over the restoring moments caused by the structural stiffness. This results in the structural failure, which can

result in a catastrophic failure. In order to find divergence, the total deflection due to bending and torsion had to be found initially. Using the equilibrium conditions, the resulting deflection can be found using Equation (8.4).

$$\begin{aligned} \frac{d}{d\bar{y}}\left(\overline{GJ}\frac{d\bar{\theta}}{d\bar{y}}\right) &= -q\cdot e_{ac}\cdot c\cdot a_{\text{airfoil}}\cdot\alpha - q\cdot c^2\cdot c_{m_{\text{airfoil}}} + N\cdot m_l\cdot g\cdot d_{cg} \\ \frac{d^2}{d\bar{y}^2}\left(\overline{EI}\frac{d^2w}{d\bar{y}^2}\right) &= q\cdot c\cdot a_{\text{airfoil}}\cdot\alpha - N\cdot m_l\cdot g \end{aligned} \tag{8.4}$$

In Equation (8.4), q represents the dynamic pressure, a_{airfoil} is the 2D lift slope, α is the angle of attack, $c_{m_{\text{airfoil}}}$ is the 2D moment coefficient, N is the load factor (L/W), m_l is the mass per unit length, d_{cg} is the distance between the CG and the elastic axis and rest of the parameters are same as for the standard model explained initially. Using the boundary conditions of the model (fixed root and flexible wing) along with these equilibrium equations, the solution can be obtained for both deflections. The analytical equation for these equations was obtained using the Ritz method [37]. Furthermore, the divergence condition can then be calculated using the fact that at divergence, theoretically, the deflections become infinite. Thus, the divergence dynamic pressure (q_{Divg}) is found to be as shown in Equation (8.5), where all the variables are as explained earlier.

$$q_{Divg} = \frac{\overline{GJ}\cdot\pi^2}{4\cdot e_{ac}\cdot c\cdot a_{\text{airfoil}}\cdot b_{1/2}^2\cdot\cos^2(\Lambda_{0.5})\cdot\left[1-\frac{3\cdot\pi^2}{76}\cdot\frac{b_{1/2}}{e_{ac}}\cdot\frac{\overline{GJ}}{\overline{EI}}\cdot\tan(\Lambda_{0.5})\right]} \tag{8.5}$$

The backward sweep of the wing effects positively towards the divergence speed. In fact, there is a critical sweep angle after which the divergence does not occur for a given wing geometry [37] [36]. This angle is known as the isoclinic sweep angle (Λ_∞). Further, this sweep angle can be computed using Equation (8.6).

$$\tan(\Lambda_\infty) = \frac{76\cdot\overline{EI}\cdot e_{ac}}{3\cdot\pi^2\cdot\overline{GJ}\cdot b_{1/2}} \tag{8.6}$$

Using Equation (8.6), Λ_∞ was found for the wing design, using values from Section 8.3. It resulted in a value for half chord sweep angle of 2.1°. For the wing design of the CNA, the half chord sweep is 28°. Thus, it can be concluded that the divergence phenomenon will not occur for the wing, throughout the entire flight envelope. This was further verified using the dynamic pressure obtained using Equation (8.5). This result is in line with the findings from the experimental data, regarding divergence of swept back wings. As it is stated that divergence is generally not a critical scenario for aircrafts with swept back wings [36].

The second main phenomenon is the aileron (control) reversal. This condition occurs when the ailerons act in the opposite direction with respect to the expected direction, due to the wing deformation. The flexibility in the wing allows a torsional deflection of the wing due to interaction between the airflow and the structure. As the dynamic pressure increases, this deformation tends to increase, making the ailerons less effective. This is often measured in terms in aileron effectiveness, which is defined as the wing tip helix angle per unit aileron displacement (Equation (8.7)), where the wing tip helix angle is defined in terms of roll rate (p), half span ($b_{1/2}$) and freestream velocity (V) and aileron displacement (β) as $pb_{1/2}/V\beta$. In order to analyse the aileron effectiveness, the aileron is added to the initially defined wing model. The position of the aileron is same for the actual wing. The new model is shown in Figure 8.10, where the aileron is shown in green. In this figure all the parameters are similarly defined as for the wing model without aileron, except y_a, which is the lateral distance of the aileron from the wing root. In order to analyse the aileron effectiveness, a particular element of width dy is considered over the wing and the equilibrium equations are found for this element after the aileron is deflected. Taking into account the rolling moment and the change in lift forces due to the aileron deflection, the equilibrium equations were rewritten further. Using these equations and the boundary conditions for the model, the aileron effectiveness can be written as shown in Equation (8.7) [37]. Further, at the critical speed when control reversal will happen, the aileron effectiveness will cease to zero.

$$\frac{p\cdot b_{1/2}}{V\cdot\beta} = \frac{\lambda\cdot b_{1/2}\left\{c\cdot c_{m_\beta}\cdot\left[(\lambda\cdot b_{1/2})^2 - 2\cdot\sec(\lambda\cdot b_{1/2}) + 2\right] - 2\cdot e_{ac}\cdot c_{\ell_\beta}[\sec(\lambda\cdot b_{1/2}) - 1]\right\}}{2\cdot a_w\cdot e_{ac}\cdot[\lambda\cdot b_{1/2} - \tan(\lambda\cdot b_{1/2})]} \tag{8.7}$$

In Equation (8.7), c_{m_β} is the moment coefficient due to aileron deflection, c_{l_β} is the lift coefficient due to aileron deflection, a_w is the wing lift slope and λ is defined as shown in Equation (8.8).

$$\lambda^2 = \frac{0.5 \cdot \rho \cdot V^2 \cdot a_{\text{airfoil}} \cdot e_{ac}}{\overline{GJ}} \tag{8.8}$$

Using Equation (8.7) and Equation (8.8), the aileron effectiveness can be plotted against the freestream velocity at cruise altitude. The results are shown in Figure 8.11. As can be seen from the figure, the aileron effectiveness is always larger than 0.5 throughout the whole flight envelope. Thus, it can be concluded that the aircraft will not be affected by control reversals due to aeroelastic effects throughout the entire flight envelope. However, this method is overestimating the effectiveness, since the effect of wing sweep is not included. Therefore, it is recommended to use advanced computational methods in order to account for the wing sweep effect, for the next design steps, which are outside the current project scope. However, it is expected that the design will not suffer major limitation due to this assumption, as high margins are available even at very high speeds.

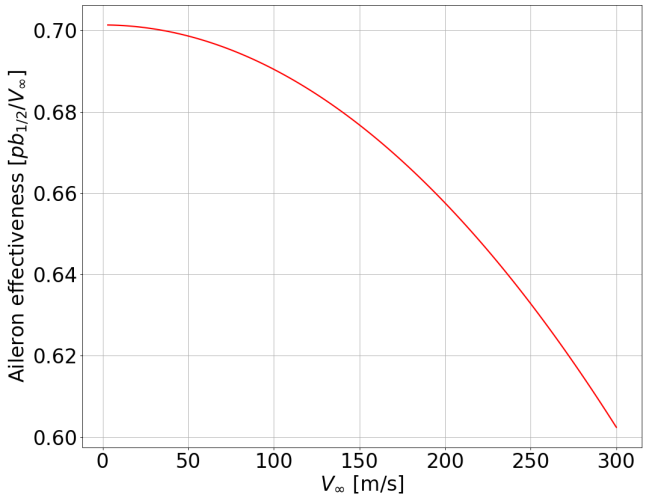

Figure 8.11: Results for aileron effectiveness at different freestream speeds

8.4.2. Dynamic Aeroelasticity

The dynamic aeroelasticity deals with the study of oscillatory effects of the interactions between aerodynamic, elastic and inertial forces. The most important phenomenon dealt under dynamic aeroelasticity is the flutter. The flutter is described as an unstable self exciting vibration, that allows the structure to extract the energy from the airflow. In order to assess the design for the flutter, the critical flutter speed criterion used by the certification authorities is considered. Below this critical speed, the oscillations are damped whereas above this speed, one of the vibration modes become negatively damped, leading to unstable oscillations. For the CNA wing design, this flutter is critical aspect because of its high aspect ratio and slenderness. In order to assess the design for the flutter, a binary flutter model is considered. This model is widely used in the literature for initial flutter assessment. However, in order to use this model, certain assumptions need to be made. All the assumptions made and their effects on the design are listed as follows.

1. **Rectangular Wing Planform:** The effect of the wing taper and sweep were neglected for this model. The effect of this assumption leads to an overestimation of flutter speed, due to the coupling effects which are present due to the wing sweep being ignored. The resulting model is shown in Figure 8.12.

2. **Binary Modes:** The flutter instability can involve two or more modes of vibration, arising from coupling effects. However, for this model only two modes of vibration were assumed. It was found from the literature that considering the two critical modes is sufficient to assess the design in the conceptual design phases and for higher modes, more complex analysis and wind tunnel tests are done [36]. The two critical modes are shown in Figure 8.13 and Figure 8.14 respectively.

3. **Simplified Unsteady Aerodynamics:** The inclusion of unsteady aerodynamic terms in the model makes it very complex and difficult to predict. However, completely ignoring this effect could lead to an inaccurate model [37]. A solution to this is, introducing a factor $M_{\dot{\theta}}$ to account for unsteady aerodynamics [36]. Therefore, this factor was included to the model while calculating equilibrium equations, accounting for simplified unsteady characteristics.

4. **No Structural Damping:** The structural damping was ignored in the aeroelastic model. Since the real damping values related to structure are often measured experimentally. Also, for aeroelastic modelling these values are typically ignored [36]. However, this implies that the flutter prediction results are conservative. Thus, the applicability of this assumption is justified for the wing design of the CNA.

Using the above mentioned assumptions, the model for the wing can be created. This binary flutter model, along with the two vibration modes, are shown in Figure 8.12, Figure 8.13, and Figure 8.14 respectively. In the Figure 8.12, all the parameters are defined in the same way as for the semi rigid wing.

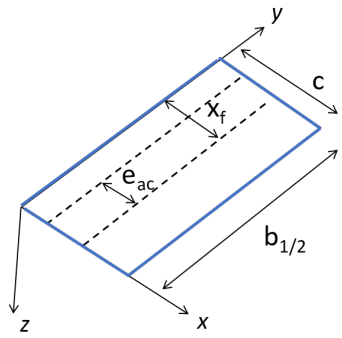

Figure 8.12: Binary flutter model used for flutter study on CNA wing design

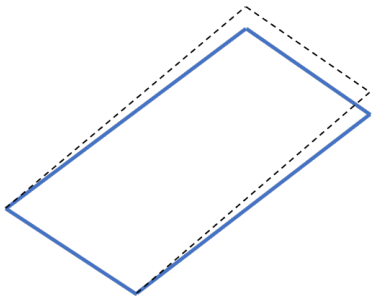

Figure 8.13: First vibrational mode considered for flutter study (bending mode)

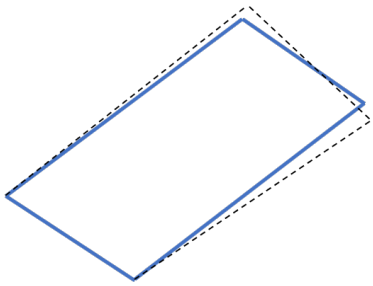

Figure 8.14: Second vibrational mode considered for flutter study (torsion mode)

Furthermore, in order to assess the flutter characteristics of the design, firstly equations of motion were derived [36]. In order to derive such a system, the generalised coordinates q_b and q_t were used. These generalised coordinates are defined in terms of local coordinates x,y and z (defined in Figure 8.12), as shown in Equation (8.9a) and Equation (8.9b).

$$z_b(x,y,t) = \left(\frac{y}{b_{1/2}}\right)^2 \cdot q_b(t) + \left(\frac{y}{b_{1/2}}\right) \cdot (x - x_{ec}) \cdot q_t(t) \qquad \theta_T = \left(\frac{y}{b_{1/2}}\right) \cdot q_t \tag{8.9a,8.9b}$$

In Equation (8.9a) and Equation (8.9b), z_b is the displacement in z direction due to the bending, θ_T is the deflection due to torsion, x and y are the local coordinates. The full system of equations using this model is shown in Equation (8.10).

$$\overline{m}\begin{bmatrix} \frac{b_{1/2}\cdot c}{5} & \frac{b_{1/2}}{4}\cdot\left(\frac{c^2}{2} - c\cdot x_{ec}\right) \\ \frac{b_{1/2}}{4}\cdot\left(\frac{c^2}{2} - c\cdot x_{ec}\right) & \frac{b_{1/2}}{3}\cdot\left(\frac{c^3}{3} - c^2\cdot x_{ec} + c\cdot x_{ec}^2\right) \end{bmatrix}\begin{Bmatrix} \ddot{q}_b \\ \ddot{q}_t \end{Bmatrix} + \rho V \begin{bmatrix} \frac{c\cdot b_{1/2}}{10}\cdot a_{\text{wing}} & 0 \\ -\frac{c^2\cdot b_{1/2}}{8}\cdot e_{ac}\cdot a_{\text{wing}} & -\frac{c^3\cdot b_{1/2}}{24}\cdot M_{\dot{\theta}} \end{bmatrix}\begin{Bmatrix} \dot{q}_b \\ \dot{q}_t \end{Bmatrix}$$
$$+\left\{\rho V^2 \begin{bmatrix} 0 & \frac{c\cdot b_{1/2}}{8}\cdot a_{\text{wing}} \\ 0 & -\frac{c^2\cdot b_{1/2}}{6}\cdot e_{ac}\cdot a_{\text{wing}} \end{bmatrix} + \begin{bmatrix} \frac{4\cdot E\cdot I}{b_{1/2}^3} & 0 \\ 0 & \frac{G\cdot J}{b_{1/2}} \end{bmatrix}\right\}\begin{Bmatrix} q_b \\ q_t \end{Bmatrix} = \begin{Bmatrix} 0 \\ 0 \end{Bmatrix} \tag{8.10}$$

In Equation (8.10), $\overline{m}$ is the mass per unit area of the wing, a_{wing} is the wing lift coefficient, ρ is the freestream density, V is the freestream velocity and $M_{\dot{\theta}}$ is the factor accounting for unsteady aerodynamics forces mentioned earlier. The value for $M_{\dot{\theta}}$ is found to be -1.2 [36]. Equation (8.10) shows that the mass matrix and the stiffness matrix are symmetric. However, the matrices correlating to the aerodynamic forces are non-symmetric. Thus, it can be identified that the two modes are coupled and this coupling will be the root cause of the flutter in the system. In order to identify the flutter conditions for the design, the frequencies and the damping ratios of the modes need to be identified. This was done by converting the derived set of equations to an eigenvalue problem. Firstly, the system of equations shown in Equation (8.10) can be written in a generalised matrix notation, which can then be written in the form of eigenvalue problem as shown in Equation (8.11) and Equation (8.12).

$$\mathbf{A_1}\ddot{\boldsymbol{q}} + (\rho V \mathbf{B_1})\dot{\boldsymbol{q}} + \left(\rho V^2 \mathbf{C_1} + \mathbf{E_1}\right)\boldsymbol{q} = \boldsymbol{\theta} \tag{8.11}$$

$$\begin{Bmatrix} \dot{\boldsymbol{q}} \\ \ddot{\boldsymbol{q}} \end{Bmatrix} - \begin{bmatrix} 0 & \mathbf{I} \\ -\mathbf{A_1}^{-1}\left(\rho V^2 \mathbf{C_1} + \mathbf{E_1}\right) & -\mathbf{A_1}^{-1}(\rho V \mathbf{B_1}) \end{bmatrix}\begin{Bmatrix} \boldsymbol{q} \\ \dot{\boldsymbol{q}} \end{Bmatrix} = 0 \tag{8.12}$$

Now using Equation (8.12), the eigenvalues of the system can be found. Consequently, the frequencies and the damping ratios of the two modes at different airspeed can be evaluated. Thus, the flutter critical speed was then found, when the damping of one of the modes becomes negative. The values obtained from structural design of the wing (Section 8.3) were used to compute the critical flutter speed. For the initial design, it was found out that the flutter speed is around 227 m/s which is less than the cruise speed and hence the flutter would hinder the aircraft's safe operation. Thus, in order to meet the requirement, the torsional rigidity of the wing was increased, as explained in Section 8.3. The new obtained results are shown in Figure 8.15. As can be seen from the figure, for the final design, the flutter speed has increased to 290 m/s. Thus, the CNA wing will not suffer from flutter throughout its entire flight envelope. However, this method did not consider the wing sweep and is also limited to the two vibration modes. This simplification can have negative effects on the critical flutter speed, but at the same time, the wing box structure is also underestimated, as the cross section is restricted to a rectangular form, leading to an underestimation of its torsional stiffness, which directly affects the critical flutter speed. In order to quantitatively assess this effect, advanced numerical simulation tools are needed, which are not feasible within the current project scope and are recommended for the upcoming design phases of the CNA.

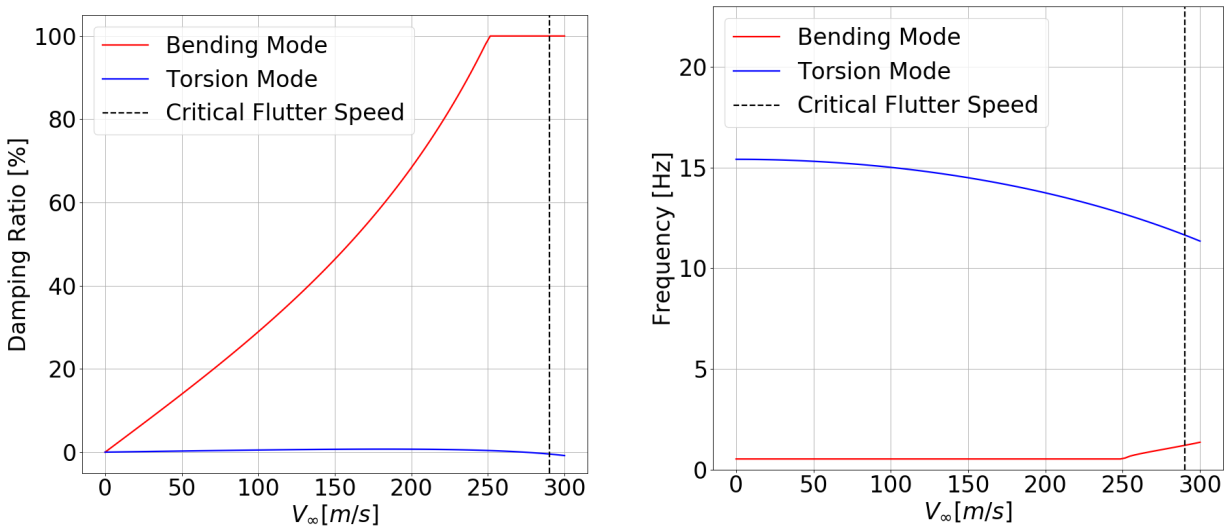

Figure 8.15: Flutter results for final design (after modifying for flutter constraint)

8.4.3. Validation

The aeroelastic phenomenon can have a serious impact on the aircraft's performance and safety. This is even more important for the current design, due to the high aspect ratio and the slenderness of the wings. Thus, it is important to validate the model used to assess these effects for the current design. Since any inaccurate findings can lead towards major drawback of the design. In order to validate the model, a test case involving similar high aspect ratio wing was chosen. This was chosen because it will ensure that there are no limitations on the model due to the high aspect ratio of the wings. This test case was the high span wing of HALE aircraft [38]. This wing had an aspect ratio of 32 and had no sweep. This fact of having no sweep was accepted, since no other test case involving high aspect ratio was found. And choosing a conventional wing with sweep would not have been a fair comparison, as the effect of the large span will not be involved and the associated vibrational modes will differ. Which leads to significant coupling effects which were neglected in the model, due to the large span of CNA wing design. For this test case, the data from the advanced numerical simulations and comparison with experimental results was obtained [38]. Using the wing planform parameters, the flutter and divergence analysis was done using the model. The results obtained from the model used for the CNA and the reference data available are summarised in Table 8.4.

Table 8.4: Comparison of flutter and divergence model results with numerical data from the literature

Parameter	Current Model	Available Data	Difference (%)
Critical Flutter Speed [m/s]	31.5	32.21	-2.2
Flutter Frequency [rad/s]	23.36	22.61	+3.3
Divergence Speed [m/s]	37.15	37.29	-0.4

As observed from Table 8.4, it can be concluded that the model is able to predict both the flutter speed and the diver-

gence speed rather accurately (within ±5% margin) for high aspect ratio wings. This implies that the results presented earlier in this section are valid for the current design stage and as the next design phases are initiated, the neglected effects mentioned earlier in the assumptions, should be considered by the means of advanced numerical simulations and wind tunnel experiments.

8.5. Strut Sizing

With the objective of a light strut structure that is capable of carrying all applied loads, the strut sizing was performed in a similar manner as the wingbox following a similar design methodology as described in Section 8.2. Furthermore it took into account the critical load types and cases affecting the aircraft and used the same material as the wingbox as discussed in Section 8.3. The strut structure was thus modelled as a box beam that fits inside the strut airfoil shape while maximising the structure's area. With the strut using the SC(2)-0010 airfoil as discussed in Section 7.5, a box shaped structure of width 440 mm and height 88 mm located from around 20% to 60% of the chord was found to optimise the available space. This box was assumed to have a constant thickness over all sides.

During operation, the wing structure transmits forces to the strut mostly as axial forces and bending moments. Furthermore, despite the during cruise assumed non-lifting properties of the strut, the strut creates a lifting forces over its length during climb and descent. These forces allowed for the free body diagram of Figure 8.16 to be drawn. The length of the strut was design to be 18.25 m at an angle of 13.84°. Using the critical load data and the angle, a bending moment of 1700 kN was found to be applied to the strut. A distributed lift force of 5.53 kN was furthermore found using the max manoeuvre speed of 108.7 m/s.

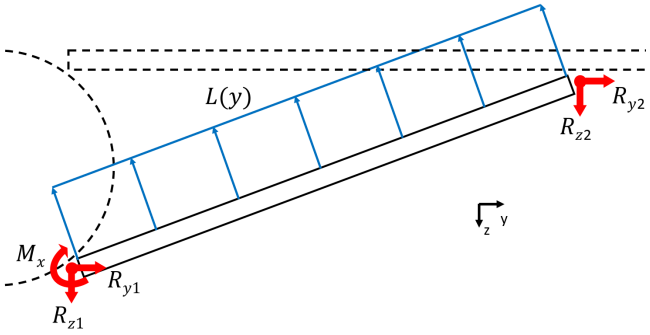

Figure 8.16: Free body diagram of the strut structure

The free body diagram allowed for both the maximum moment and shear forces affecting the structure to be found. Designing for a constant thickness box that is able to cope with both these forces, using the yield and shear strengths of the used material, and its first and second moment of area, revealed the bending moment as being critical for thickness. A thickness of 2.23 mm was found to be the thickness required to withstand all loads.

8.6. Folding Wingtip Feature

The folding wingtip was introduced as a design solution to limit the wingspan during ground movement. The aircraft should fit within a Code D gate as defined by the ICAO, having a ground wingspan of 36 m or less (REQ-CN-PERF-31). Folding wings have been employed on numerous aircraft, especially military aircraft that need to be stored below the decks of aircraft carriers. The Boeing 777X is also fitted with folding wingtips, but it has never been done on commercial aircraft with a wingtip larger than 3.5 m [4]. Therefore this new feature demands research and analysis on areas such as safety, hinge design, structural loading and reliability, all of which are carried out in this section.

Requirements presented in Section 8.1 allow for the determination of the hinge design and its critical load cases. According to CS-25 regulations, a folding wingtip is not a control surface but part of the primary airframe structure. The mechanism was designed with great attention to safety whilst aiming to keep the weight down. The hinge is powered by two hydraulic actuators which rotate the wingtip from the horizontal (extended) position by 120° to the nearly vertical (folded) position using two bevel gears. A set of four locking pins is used to secure the wingtip in place for both positions. These are mechanically driven and electrically powered. The hinge design is presented in Figure 8.17 and Figure 8.18 with the hinge in the extended and the folded positions respectively.

[4] URL `https://airwaysmag.com/industry/the-faa-approves-boeings-777-x-folding-wingtips/` cited [20. June 2020]

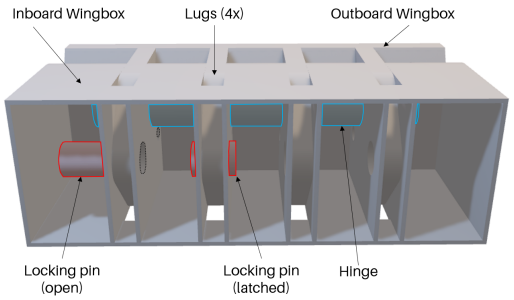

Figure 8.17: CAD model of the folding wingtip in its extended state highlighting the main parts. The left two lugs show the locking pins in the open and latched positions

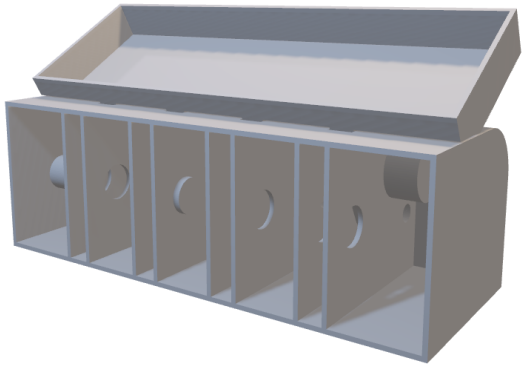

Figure 8.18: CAD model of the folding wingtip rotated by 120° to its fully folded state

8.6.1. Load Cases and Mechanism Design

Three load cases were considered: the extended, folded and transient cases. Figure 8.19 and Figure 8.20 visualise the first two load cases respectively. They were used to size the hinge structural components. The third transient load case was used to size the folding actuators that provide the torque to rotate the wingtip.

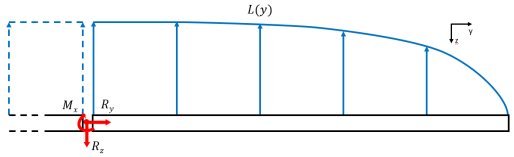

Figure 8.19: Free body diagram of the folding wingtip in the extended position

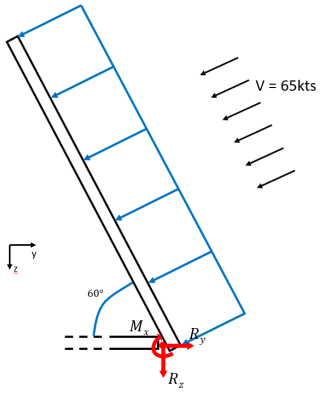

Figure 8.20: Free body diagram of the folding wingtip in the folded position

In the extended position, the loads on the hinge are caused by the bending moment and shear force loads from the wing's aerodynamic loading. In this report, the structural weight, drag and vibration loads were assumed small (see Section 8.2). During flight, the wingtip is held in place by four locking pins. The structure was designed such that the wingtip remains secured after up to two locking pins or lugs fail. In this report a preliminary structural sizing was performed using the methodology shown in Section 8.2. These results are summarised in Table 8.5.

In the folded position, the limit load is defined by REQ-CN-FWT-05. The folded wingtip was designed such that it can withstand 1.5 times the load imposed by a 65 kts (120 km/h) crosswind. The crosswind has the biggest effect when it hits the wingtip perpendicularly and was sized accordingly. The wingtip locks in place during ground movement as defined by REQ-CN-FWT-08. The results of the preliminary sizing are presented in Table 8.6. Finally, in the transient case, the same loading as in the folded position applies to the folding actuators. Those provide the torque to move the wingtip from one position to the other in under 6 seconds as per REQ-CN-FWT-01.

Table 8.5: Results of structural sizing for the ultimate load in flight

Parameter	Value
Ultimate Moment	402 kNm
Distance Between Lugs and Shaft	200 mm
Number of Lugs and Pins	4
Number of Failed Lugs per Pins	2
Ultimate Shear Force per Lug	1005 kN

Table 8.6: Results of structural sizing for the ultimate load on ground

Parameter	Value
Horizontal Gust Force	40 kN
Ultimate Moment	83 kNm
Bevel Gear Reduction Ratio	50
Number of Actuators	2
Torque per Actuator	828 Nm

8.6.2. Control System Design

When the aircraft is preparing for take-off, the wingtip is extended by flight crew command. This happens when the aircraft is first in line for take-off, before the hold-short markings. The wingtips extend within 6 seconds. In the same way spoilers are armed/disarmed by the flight crew before landing, the wingtip folding is armed/disarmed. When armed, the wingtips will automatically extend when the groundspeed drops below 20 kts. The flight crew can monitor the status as displayed on the Engine Indication and Crew Alerting System (EICAS) display.

Commands from the pilots and avionics need to be passed onto the wingtip actuators, and this sequence of actions is monitored and executed by the Folding Wingtip Control System (FWCS). The FWCS's main objective is a safe operation of the wingtips, especially in case of abnormal conditions. The system is heavily interlinked with other aircraft systems such as the Take-off Configuration Warning System (TOCWS) and the Engine Indication and Crew Alerting System (EICAS) which are present in each aircraft as per regulatory requirements. An overview of the Control System Design is given in Figure 8.21.

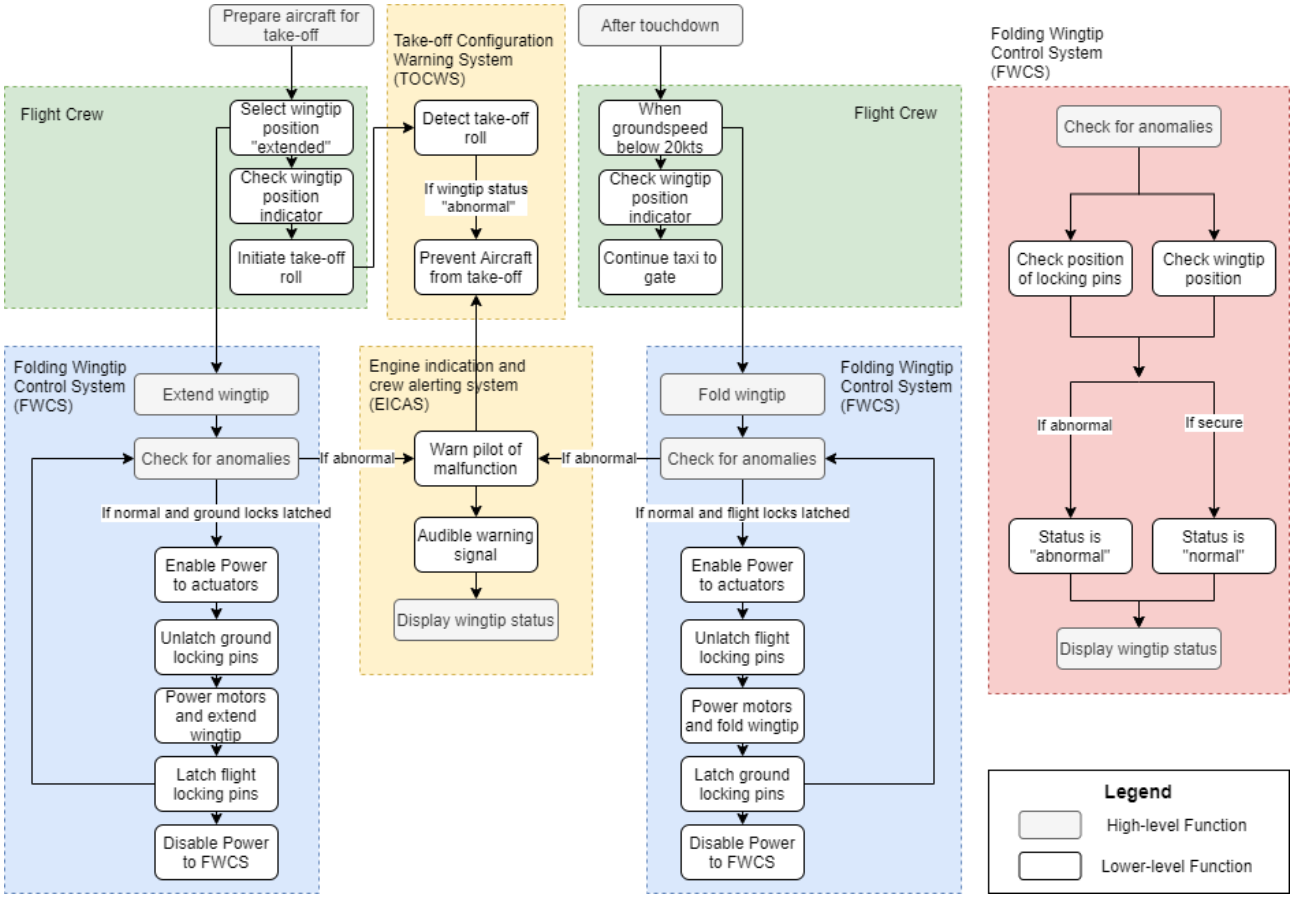

Figure 8.21: Control System block diagram

8.6.3. Design for Safety and Reliability

Before entering the runway for take-off, the flight crew runs through the checklists which include the "Wingtip Extended" status check. The FWCS cannot be activated in flight. The system is completely disengaged (by disconnecting power supply to the FWCS) and cannot be turned on by the flight crew or any other system as soon as the aircraft's ground speed exceeds 20 kts or the aircraft is airborne. This means that during flight, the wingtip is locked in place and forms a part of the primary airframe structure. However, the system can fail or transmit incorrect data to the FWCS. Many risks have been identified and the main risks and their mitigation actions are summarised in Table 8.7.

A robust system is also ready to take the consequences of failed sensors. The FWCS relies heavily on position sensors. Each pin uses two sensors for redundancy, but they might fail simultaneously leaving the pins in an unknown state. Two options arise: the pin can be locked but the sensor transmits the "unlocked" status or the pin is unlocked but the sensor transmits "latched". The first option does not cause any danger, since this will result in a notification to the flight crew and eventually repair. The second option causes a safety risk. In this case the flight crew is unaware that one

or more pins are not latched. This only causes a severe safety hazard when at least two pins are malfunctioning and on top of that four or more sensors are malfunctioning. This is extremely unlikely and therefore this risk is acceptable.

Table 8.7: Overview of main risks and actions to be undertaken

Safety Risk	Mitigation
The flight crew initates the take-off roll with folded wingtips.	The take-off roll is detected by the TOCWS. If the wingtip status is not "extended", the system will automatically apply the brakes and prevent a take-off. The flight crew is notified by visual and audible signals by the EICAS.
One or more lugs/pins shear-out after incorrect maintainance checks.	The mechanism is designed to withstand the ultimate flight load (3.75g) with up to one lug/pin broken. In limit flight load conditions (2.5g), the wingtip is secure with up to two lugs/pins broken.
One or more locking pin position sensors fail or transmit incorrect data.	Each locking pin has two sensors. If data differs between sensors on the same pin, the anomaly is detected and the wingtip can not fold or extend. The flight crew is notified by visual and audible signals. If both sensors on the same pin fail, then incorrect data is used. The consequences are explained further down the text.
The wingtip actuators are heavily damaged after a birdstrike.	The malfunction is detected by the FWCS and the flight crew is notified by visual and audible signals. Upon touchdown the wingtip can not be folded. With the wingtips extended, the aircraft cannot continue taxi and the passengers must be transported to the terminal by other means. Procedures will be outlined in a recovery manual as per regulatory requirements.
The flight crew initiates a go-around while the wingtip is folding.	The go-around is detected by the TOCWS and the FWCS will extend the wingtips again. This way a safe configuration is guaranteed before reaching the minimum unstick speed V_{mu}.
The horizontal gust loads exceed 65kts while on ground (heavy storm).	Ground crew must lock the wingtip with straps. If done incorrectly, the locking pins are designed to tolerate 1.5 times this limit load.

In terms of reliability, the system is equipped with two folding actuators. Both are capable of folding the wingtip individually if the other fails, although the motion will not be finished within 6 seconds. The benefit is that the aircraft maintains its operational capabilities and the repair can be planned in advance. If the folding wingtip malfunctions and consequently the aircraft cannot taxi to the designated terminal, the aircraft may use Code E taxiways and gates. If the airport does not accommodate Code E aircraft, passengers have to be transported to the terminal by other means. The aircraft has to be towed for repair possibly impacting airport flight scheduling. This would be a very costly operation. Secondly, there is no fuel stored in the wingtip, such that the structure becomes more reliable, lighter and folding actuators needed to be less powerful.

8.7. Weight and Fuel Volume Estimate

Two weights are estimated. The first weight is the material weight only, of all structural wingbox components. This was obtained by multiplying the material volume with the material density of 2800 kg/m^3 and gives 1886kg. However, the wing weight is more than just material weight. More wing elements such as structural reinforcements around cutouts, HLD and spoilers must be added. In order to estimate the total wing mass (W_W), a Class II method by Torenbeek is used, given by Equation (8.13)[13]. It uses the gross weight (W_G), factor of proportionality (k_W), ultimate load factor (n_{ult}), maximum thickness of the root chord (t_r) and wing surface (S). For a transport aircraft with spoilers and wing mounted engines, k_W is $6.47 \cdot 10^{-3}$, W_G is equivalent to zero fuel weight and b_{ref} is 1.905 m. b_s can be computed with $b/cos\Lambda_{1/2}$ where $\Lambda_{1/2}$ is the half chord sweep. The factor 0.7 accounts for a braced wing mass, which the weight of the struts represents 10% of the W_W[13]. S, b, n_{ult}, $\Lambda_{1/2}$ of the aircraft are 150.9 m^2, 50.64 m, 3.75, and 28° respectively. This resulted in the wing mass of 9740 kg, with its centre of gravity estimated to be at the quarter chord of the MAC. Finally, the fuel volume available is estimated by summing all wingbox volumes within all inboard wing sections (no fuel is stored in the wingtip). This gives a usable fuel volume of 22.6m^3.

$$\frac{W_W}{W_G} = 0.7 \cdot k_W \cdot b_s^{0.75} \left(1 + \sqrt{\frac{b_{\text{ref}}}{b_s}}\right) \cdot (n_{\text{ult}})^{0.55} \cdot \left(\frac{b_s / t_r}{W_G / S}\right)^{0.30} \tag{8.13}$$

8.8. Verification and Validation

The design tool used to determine the internal loading and failure modes of the structural design needed verification and validation to ensure its results are representative. Verification is done using a series of unit tests and system tests, whereas validation is performed by comparing the wingbox parameters with those typically found in aerospace products. For this the reference wing structure from a Boeing 737 is used.

8.8.1. Verification

The verification process was stared by carrying out the unit tests. When generating the internal loading distribution, a numerical quadrature integral was used. The following unit tests were carried out to verify the implementation of the quadrature rule.

The quadrature rule approximates an integral of a function by taking some weighted sum of the function values at discrete nodes. Thus, if N number of quadrature weights are generated for an integral between 0 and 1, then the sum of all the quadrature weights must equal to 1. By testing with $N = 1, 2, 3$, it was verified that the quadrature weights were correctly generated. The values for N tested in the previous test were just arbitrary as it was only testing if the formulation of the weights was done correctly. However, this value of N is related to the degree of precision of the quadrature rule. Where if N nodes are taken for the integral, then the degree of precision is equal to $N-1$. Meaning that the quadrature can exactly integrate a $N-1$ order polynomial. The next unit test was thus designed to test the degree of precision. For this test, the quadrature integral of a fourth order polynomial was compared to an analytical solution. The test was carried out by setting $N = 5$, which would ensure a degree of precision of 4. The considered function was $f(x) = 5 \cdot x^4 - 3 \cdot x^3 + x^2 - 3 \cdot x + 4$, which was integrated between -1 and 1 giving an analytically solution of 10.67. For the quadrature integral, five equidistant nodes between -1 and 1 were taken. These nodes resulted in the quadrature weights being: $w_i = [0.15, 0.71, 0.26, 0.71, 0.15]$. By taking the weighted sum of the function values at the nodes ($f(x_i)$) with the weights (w_i), resulted in the quadrature solution converging to the exact analytical solution.

With the successful verification of the quadrature function, the verification of the calculation tool for the bending and shear stresses were carried out. The shear stresses are caused primarily due to the shear force and the torque. The governing equations are given in Equation (8.2b) and Equation (8.2c).

In order to verify that Equation (8.2c) had been correctly incorporated into the program, a unit test was done. Equation (8.2c) suggests that for a given torque (T) and the wingbox geometry, (thickness t and enclosed area A) the shear flow should be constant through the whole cross section. This was tested for various torques and wingbox geometries, and was confirmed to be true.

The following unit tests were carried out to test Equation (8.2b) in the program. The nature of the equation is such that it will always produce the maximum shear flow ($\tau \cdot t$) at the position of the neutral line in the case of a pure shear force. Thus, by altering the values such as V and wingbox dimensions, it was confirmed that the maximum shear flow will always occur at the neutral line regardless of the load or wingbox dimensions. Additionally, a second unit test was carried out simultaneously. This test involved checking if the integrated shear flow in the structure added up to the applied shear force. The integral of the shear flow was done using the aforementioned verified quadrature rule. This test was also successfully completed and that thus concluded the unit tests for the program.

The last steps of the verification process was to carry out the system tests. For all the system tests, a clamped beam was considered. The first test involved checking if the internal moment and shear is equal to zero at the end of the beam for any given loading. This was tested and confirmed for three different load cases, one case with a single point load, another with a uniform distributed load and the last one with a linearly varying (over the span) distributed load.

Lastly, the verification process was concluded by comparing the moment and shear force diagrams generated by the program, to the analytically computed diagrams. For this comparison, the same three load cases (as for the previous system test) were used. The comparison of the generated diagrams for the linearly distributed load shown in Figure 8.22, are presented in Figure 8.23 and Figure 8.24.

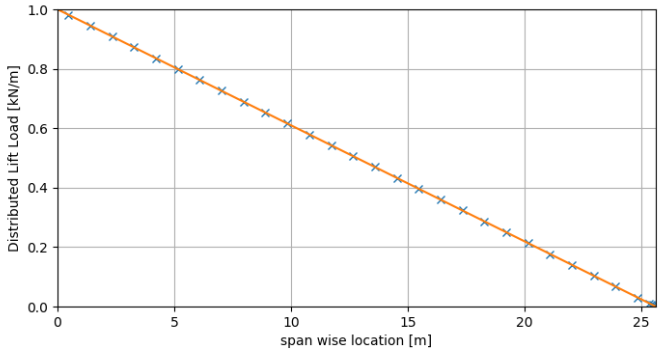

Figure 8.22: Linearly distributed load case used for verification

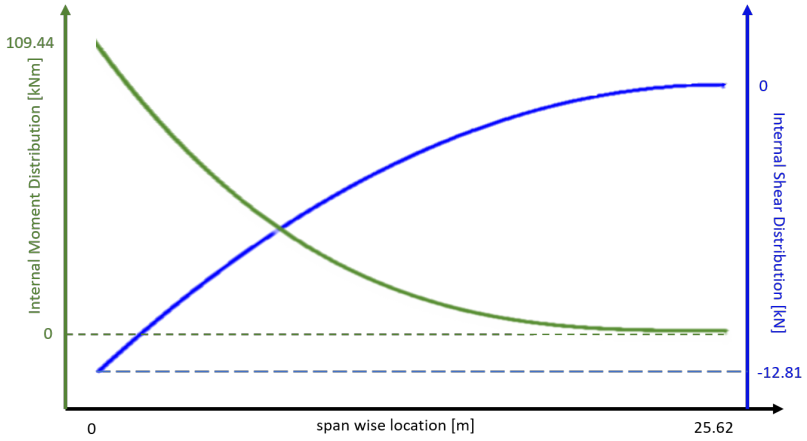

Figure 8.23: Analytically computed moment and shear force diagram

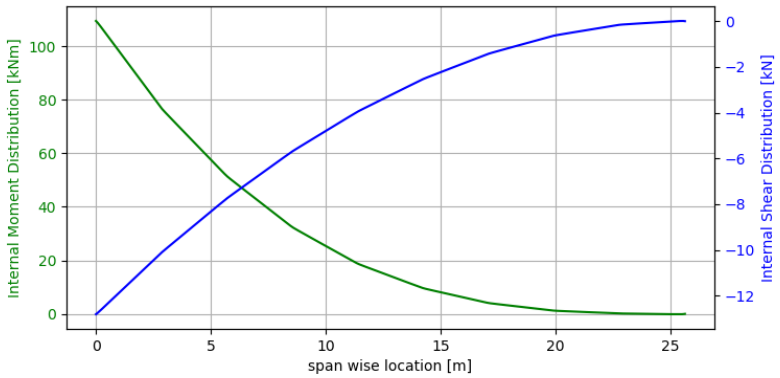

Figure 8.24: Moment and shear force diagram generated by the program

As shown through Figure 8.23 and Figure 8.24, the results of the numerical and analytical computation are almost indistinguishable. Upon closer inspection of the two graphs, it was found that the values for the analytical and numerical case differed by a maximum of 0.05%. Similar results were obtained for the other two load cases. This clearly showed that the program was working as intended, and this concluded the verification process.

8.8.2. Validation

The cross-sectional wingbox properties were compared with values typically found in aircraft of similar mission. This is the "comparison" method (section 4.4). However, before applying this method, one must take into account its

implications. Reference data was found for the wing of a Boeing 737 with a MTOW of 77100kg using aluminium 2219 for the top skin and Aluminium 7075 for all other parts[35]. However, this data must be used with care. The wing is loaded differently due to not having any struts and the wing is not nearly as slender. Furthermore, some severe assumptions were used while designing the wingbox (such as a rectangular wingbox cross-section), making the use of the comparison method not very accurate. Therefore, the comparison was used to check if the structural dimensions were of the same order of magnitude. In Table 8.8, typical values found in literature are compared with the used values. No other validation methods were applied (such as "run code with reference inputs") because the output of the code (stress distribution) cannot be checked with any real stress distribution. Instead, stress calculations were verified by hand for one simple spanwise station (as stated in verification).

Table 8.8: Validation of wingbox part dimensions

Wingbox Part	Reference Value [mm]	Used Value [mm]	Same order of magnitude	Reasoning
Spar Caps flange thickness	5.08	15	✓	
Top skin thickness	2.54 - 6.10	3.0 - 5.3	✓	
Spar web thickness	2.54 - 12.4	4.0 - 6.0	✓	On the lower side, probably because sweep is neglected (2D assumption)
Stiffener height	40.6 - 71.1	70.0	✓	
Stiffener spacing (top skin)	127 - 203	63.5 - 310	✓	Exceeds range most likely because the top skin sees a different load case for most of its span, in fact the full inboard wing
Stiffener thickness	1.27 - 2.79	10.0	✓	Z-stiffeners vs L-stiffeners are used

8.9. Recommendations

To assist further design on the wing and strut structure, a series of recommendations are made. Firstly, research into the longitudinal positioning of the strut structure is recommended. This was not done due to the 2D simplification. An optimal placing can be found such that the torsional loads are relieved and such that the strut can contribute to improving the torsional stiffness. Especially since flutter was found to be critical, this recommendation could have a large effect on reducing the structural mass.

Secondly, a more detailed structural analysis is recommended. This can happen in three areas: more accurate load cases, an improved wingbox model and more representative failure criteria. In terms of load cases, sizing for touch-down at MLW should be performed, which is critical to prevent buckling in the strut at touchdown. Some forces which have been neglected initially (most notably drag and structural weight) should be incorporated. The wingbox model could be improved by carrying out the analysis in 3D using a wingbox that follows the airfoil shape. This could be extended with using variable stiffener and rib spacings and different materials for parts that see a different dominant loading. Finally, more representative failure criteria such as the von Mises criterion should be applied. Fatigue should also be investigated. This concludes the wing structural design recommendations.

9
Aircraft Propulsion and Electrical Systems

This chapter discusses the power and propulsion of the CNA. It describes how the power required for the subsystems is achieved and distributed. It also describes the propulsion system of the CNA and how the requirements of thrust and emissions are reached. Section 9.1 discusses the requirements and objectives of the power and propulsion system. Section 9.2 discusses the design of the boundary layer ingestion (BLI) propulsor and Section 9.3 discusses the design of the turbofan. Section 9.4 show the results and how those results were achieved. Section 9.5, Section 9.6 and Section 9.7 discuss the design and material of the turbofan and BLI nacelle. Section 9.8 and Section 9.9 discuss the fuel system and fuel emissions respectively. Section 9.11 and Section 9.12 discuss the weight of the propulsion system and electrical power system respectively. Section 9.13 discusses how the power for the BLI is provided. The verification and validation, and the sensitivity analysis are discussed in Section 9.14 and Section 9.15 respectively. Lastly are the future recommendations discussed in Section 9.16.

9.1. Objectives and Requirements

The powerplant system provides the aircraft with the required thrust and the electrical power to complete its mission. The propulsion system needs to be very efficient in order to meet the requirement of 10% emissions reductions compared to existing aircraft (REQ-CN-SUS 2). In addition to this, the propulsion system shall be reliable, safe and have limited noise emissions.

The propulsion system used on the aircraft is novel; ultra high bypass ratio engines are utilised as primary thrust providers along with an extra boundary layer ingesting propulsor to improve the fuel efficiency of the aircraft. The BLI propulsor is powered via a high power electrical system which distributes power from the turbofans to the propulsor. Since these technologies have not been tested on aircraft of this class yet, they were designed to an extent sufficient to prove their feasibility on the CNA. Considerations were made regarding the impact of these new technologies on the safety and reliability of the aircraft. It must be proved that these systems can in fact match current aircraft in these areas and surpass them in overall efficiency, in order to justify their use.

In conclusion, the top level objectives of the power plant design, which includes the turbofans, the BLI system, and other electrical power systems, were to assure sustainability in terms of fuel efficiency of the aircraft, noise, and recyclability. . Requirements were set on target thrust specific fuel consumption, emissions, and noise for the propulsion system. In addition to these, the technical requirements imposed on the propulsion system were also to be met. The top level requirements imposed on the propulsion and electrical system are mentioned in Table 9.1.

Table 9.1: Propulsion and Power system requirements

Identifier	Description	Source
REQ-AE-PROP-1	The propulsion system shall operate at least upto a cruise speed of Mach 0.78 at an altitude 11000 m.	Customer
REQ-AE-PROP-4	The propulsion system shall deliver 165 kN static thrust at sea level maximum thrust.	Design
REQ-AE-PROP-20	The propulsion system shall deliver 24 kN thrust at cruise altitude at mach 0.78.	Design
REQ-AE-PROP-14	The propulsion system shall have a specific fuel consumption during cruise of at most 13 g/kN/s.	Design
REQ-AE-PROP-15	The propulsion system shall produce no more than 96.5 EPNdB at the lateral full-power reference noise measurement point as described by ICAO annex 16.	ICAO
REQ-CN-PROP-MG-2	The power shall be transferred efficiently (>0.85) between the generators and motors powering the BLI propulsor.	Design
REQ-CN-EPS-1	The electrical power system (EPS) shall be able to provide a maximum power of 400 kW of power.	Design

9.2. BLI Propulsor Design

The boundary layer analysis, model assumptions and the model itself are discussed in this chapter. Section 9.2.1 discusses the boundary layer and its analysis. Section 9.2.2 and Section 9.2.3 discuss the assumptions and model of the BLI propulsor respectively.

9.2.1. Boundary Layer Analysis

In order to have an effective design of the propulsor, it is important to understand the boundary layer characteristics near the tail section of the fuselage, namely, the boundary layer thickness (δ), displacement thickness (δ^*) and the velocity profile. The δ is defined as the vertical distance from the surface where velocity in the boundary layer becomes equal to the freestream velocity (V_∞) or $U = 0.99 \cdot V_\infty$. Whereas the velocity profile depicts the trend of the change in the flow velocity throughout the boundary layer.

Predicting the behaviour of turbulent boundary layer at compressible regime is relatively complex, with no analytical method being available [32]. A CFD analysis could overcome this challenge although there is a risk of high inaccuracies involved due to schedule constraint. Hence, a different methodology is proposed.

The methodology involved the exploration of the experimental data for similar configurations as that of the CNA aircraft. It was found out that the ESDU (Engineering Sciences Data Unit) engineering database contains many of such experimental data [1]. This database is widely used in the aerospace industry for such design applications, making it suitable for the current design case. The database provides the boundary layer data for certain standard bodies at the turbulent compressible flow conditions [39]. Therefore, in order to fit this data for the design case at hand, certain assumptions were needed. The assumptions used and their justifications are listed as follows.

1. **No Interference Effect:** The boundary layer on the fuselage can be easily influenced by the wings, struts, and vertical tail. However, these effects could be challenging to predict without a high-fidelity simulation. Hence they are neglected in this analysis and the boundary layer profile over the fuselage alone was taken as leading for the design.
2. **Axisymmetric Body:** The fuselage is assumed to be axisymmetric, following the CNA design which has curved upper and lower surfaces, unlike that of conventional airliners . This assumption allows the use of ESDU database for boundary layer data.
3. **Uniform Thickness of the Boundary Layer:** The boundary layer is assumed to have a uniform thickness all around the fuselage at the inlet of the BLI propulsor. However, in reality this is not the case at all. Firstly, this is due to the fact that the angle of the tailcone on the upper surface and the bottom surface vary a little, meaning that the upper half of the fuselage is a different surface than the bottom half of the fuselage. Furthermore, since the interference effects are neglected for the boundary layer analysis, the uniform distribution will not occur in reality. Thus, for the first estimation of design this will be considered as acceptable, due to the project constraints. But, during the later design stages, the use of high fidelity simulations can help overcome this effect. The effect of this assumption is that the thrust and power values of the BLI propulsor calculated in Section 9.2.3 will have some inaccuracies when compared to reality. It can either lead to a conservative design or an overestimation, but at this design stage there is not enough information available to actually know which effect will be prominent.

Using the assumptions listed above, the boundary layer data was obtained from the database. In order to use the data for the CNA fuselage, the body with the most similar geometrical characteristics was used. This standard body is shown in Figure 9.1 [40]. Using this body, and using actual geometrical values of the fuselage, the boundary layer data was obtained from [39]. The results of the δ and δ^* at 1 m before the end of the fuselage, for both top and bottom surface, are shown in Table 9.2.

[1] URL `https://www.esdu.com/cgi-bin/ps.pl?sess=unlicensed_1200618084351ygb&t=gen&p=home` cited [8. June 2020]

Figure 9.1: Axisymmetric Standard body used for data from ESDU

Surface	δ [m]	δ^* [m]
Top	0.383	0.0554
Bottom	0.383	0.0554

Table 9.2: Boundary layer parameters at 1m before the fuselage end (x = 41.6m)

Further, in order to estimate the velocity profile for the boundary layer, no analytical methods were found for the case at hand. This was mainly because the velocity profile is significantly affected by the presence of the wall effects (especially related to temperature variations) which are very case dependent. But for the propulsor design, the velocity profile is a major factor, as it directly affects the propulsor's performance. Therefore, in order to facilitate the design, additional assumptions were made. It was assumed that the fuselage surface can be approximated as a flat plate for the velocity profile calculations. This assumption can be considered valid for the velocity calculations, since from the flow perspective, the fuselage surface acts as a flat plate. In order to have an accurate prediction, it is recommended to conduct a CFD simulation, which is not feasible within the current project scope. As a result, these assumptions allow a simple estimation for the velocity profile of the boundary layer, and using this, the design of the propulsor was carried out. The resulting velocity in the boundary layer (V_{BL}) can be written using the power law, in terms of freestream velocity (V_∞), distance from the surface (y) and boundary layer thickness (δ) [39] [32].

$$\frac{V_{BL}}{V_\infty} = \left(\frac{y}{\delta}\right)^{\frac{1}{7}} \tag{9.1}$$

All the required boundary layer parameters are now analysed for the different locations over the fuselage, based on the fuselage design. These parameters are further used for the detailed design of the propulsor, as explained in the following sections.

9.2.2. Model Assumptions

The BLI propulsor is a ducted fan which ingests the boundary layer of the aircraft and uses this to provide additional thrust. The propulsor is powered electrically by a Motor-Generator system which is described in more detail in Section 9.13. The design of the BLI propulsor requires a model, which can use the aerodynamic properties of the Boundary Layer to predict how it behaves thermodynamically. To be able to do this it is important to first make assumptions regarding the behaviour of the boundary layer at the inlet of the BLI Propulsor. The assumptions that were made for the design of the BLI Propulsor are as follows:

1. **Uniform Boundary Layer Velocity Profile**: The velocity profile upstream of the BLI Propulsor is assumed to be uniform. In reality, the flow velocity varies inside the boundary layer, however to simplify the calculation process, the flow in the boundary layer is represented by the average velocity of the flow in the boundary layer. This assumption thus also leads to the total temperature and total pressure, which are dependent on the velocity of the air, to be assumed to be uniform as well. This is a valid assumption, because thermodynamically, the increase in the kinetic energy of the flow across the fan, is the same for both the uniform and the non-uniform velocity profile, meaning that there is no difference in thrust produced by the BLI propulsor. Furthermore, in reality the fan also acts as a fluid mixer making the flow after the fan uniform to a high degree. The main drawback of this assumption is that it does not account for the effect of the varying velocity on the structure of the fan and the fatigue inducing loading this leads to, which is further described in Section 9.6.

2. **Static Temperature and Pressure Values**: For the boundary layer it was assumed that the static pressure value is equal to the freestream pressure. In reality the variation in static pressure is very small and thus it is neglected in the design of the BLI Propulsor. The static temperature in the boundary layer is assumed to be 220 K on average compared to the freestream temperature of 216.65 K. In reality, the temperature varies throughout the boundary layer and increases towards the surface. However, since it was not possible to estimate the static temperature in the boundary layer at this stage of the design, this assumption was made. This underestimation of the average static temperature means that the total temperature at the inlet is most likely higher in reality, which means that the thrust produced by the BLI propulsor is higher due to a higher exhaust velocity. Furthermore, the power required to drive the fan is also higher.

3. **Efficiencies**: The isentropic and polytropic efficiencies of the different parts of the BLI propulsor are assumed to have the following values. The inlet efficiency is assumed to be 99%, the isentropic efficiency of the fan is assumed to be 90% and the isentropic efficiency of the nozzle of the BLI propulsor is assumed to be 98%. The values are in the ranges of typical values of these efficiencies [41]. However, in reality it is possible that there are some variations in these efficiencies, which will have the effect that the thrust and power values calculated in Section 9.2.3 will have some inaccuracies when compared to reality. If all of the efficiencies are overestimated, then the thrust value will also be an overestimate and the power value will also be inaccurate. However, if all of the efficiencies are underestimated, then the opposite is true for the thrust value.

9.2.3. Model and Design

The BLI propulsor is an electric ducted fan that ingests a part of the boundary layer of the aircraft. The BLI propulsor ingests the slow moving boundary layer and by doing so, also reduces the necessary power required to generate the same amount of thrust when compared to a normal ducted fan that ingests the freestream air. For the preliminary design the BLI propulsor is designed such that it only actively produces thrust during cruise. This was done, as a boundary layer analysis for the flow during the climb and descent phases of the flight would be too complicated for the current preliminary stage of the design. The overall architecture of the BLI consists of a motor-generator system which powers the BLI propulsor, a fan that compresses the airflow and a nozzle. The exact stations of the BLI propulsor that were analysed are presented in Table 9.3.

Table 9.3: BLI propulsor station names

Station Name	Station Number
BLI Freestream	0,BLI
BLI Intake	2,BLI

Station Name	Station Number
BLI Fan	13,BLI
BLI Exhaust	19,BLI

To be able to use the results of the analysis from Section 9.2.1, it was important to first calculate the average velocity of the boundary layer profile. This was done using Equation (9.2a), which gives the average velocity as a function of the boundary layer thickness (δ) and the velocity profile of the flow in the boundary layer as a function of the distance from the surface ($V(y)$). This was then used to calculate the mass flow of the boundary layer that is ingested by the inlet of the BLI propulsor, using Equation (9.2b). The mass flow is given by the product of the freestream density (ρ_∞), the average velocity of the boundary layer ($V_{average}$) and the inlet area of the BLI propulsor (A_{inlet}), which is determined by the diameter of the tail at the inlet location and the thickness of the boundary layer that is ingested by the propulsor.

$$V_{average} = \int_0^\delta \frac{V(y)}{\delta} \cdot dy \qquad \dot{m}_{inlet} = \rho_\infty \cdot V_{average} \cdot A_{inlet} \tag{9.2a,9.2b}$$

Since the BLI propulsor simply consists of an inlet, a fan and a nozzle, thermodynamic relations can be used to carry out any performance calculation for the BLI propulsor. The boundary layer analysis and the model assumptions from Section 9.2.1 and Section 9.2.3 respectively can be used to generate the total temperature and pressure conditions of the flow in the boundary layer before the inlet (Station 0,BLI). Across the inlet (Station 2,BLI), there is a decrease in the total pressure of the flow due to the frictional effects which occur between the flow and walls of the inlet. The total pressure of the flow after the inlet can be calculated by incorporating the inlet efficiency given in Section 9.2.2. The total temperature however stays constant across the inlet. After the inlet, air flows into the fan (Station 13,BLI), which in this case is just a compressor with a pressure ratio ($\Pi_{\text{compressor}}$). This pressure ratio can be used to calculate the total pressure after the fan and it can also be used to calculate the total temperature after the fan using the polytropic efficiency of the fan.

After the fan provides the flow with additional energy, it has to be converted into thrust, which is done by the nozzle of the BLI propulsor. However for the nozzle there are two things that can happen. Either the flow becomes choked and the exhaust velocity of the BLI propulsor has a mach number of 1, or the flow is not choked and the exhaust mach number is smaller than 1. Whether the flow is choked or not depends on the critical pressure ratio, which is a function of the isentropic efficiency of the nozzle. The power required for the fan of the BLI propulsor is a function of the difference in total temperature across the fan as shown in Equation (9.3) where κ_a is the ratio of specific heats.

$$P_{\text{req}} = \dot{m} \cdot \kappa_a \cdot (T_{\text{t,13,BLI}} - T_{\text{t,2,BLI}}) \tag{9.3}$$

This description of the model of the BLI propulsor shows that the main inputs for the sizing of the BLI propulsor are the proportion of the boundary layer which is ingested and the fan pressure ratio. Using the total thrust requirement for cruise and the link between the BLI propulsor and the turbofan which is further described in Section 9.4.1, an optimisation process can be carried out to determine the best combination of the fan pressure ratio and the proportion of the boundary layer which is ingested. The process of this optimisation and the final results of the BLI propulsor sizing are described in Section 9.4.

9.3. Turbofan Design

This section discusses the methodology, assumptions and model of the turbofan design. Section 9.3.1 and Section 9.3.2 discuss the methodology and assumptions, and the turbofan model respectively.

9.3.1. Methodology and Assumptions

The general approach followed to design the ultra high bypass (UHBR) turbofan engines was to build a simplified thermodynamic model of the engine using ideal cycle analysis. The model was then made more accurate by accounting for losses in the various components such as the compressors and turbines based on (polytropic and isentropic) efficiencies. This was the highest level of detail delved into; the rotational velocity and blade design for the rotor stages was not looked into as this was not required to prove the feasibility of achieving a low thrust specific fuel consumption (TSFC) value for the engine. Instead, this design presents the overall values for the pressure ratios of various turbofan stages and their temperatures.

The model was used to optimise the engine for fuel consumption based on the thrust required at different flight conditions. Due to the large number of variables, the optimisation was performed based on qualitative reasoning rather than a programmed brute force algorithm. Several assumptions were made regarding the design in order to simplify the process. The assumptions made are listed as follows:

1. **Constant Specific Heats:**Specific heats are assumed to be 1000 [J/(kg·K)] for air and 1150 [J/(kg·K)] for the gas exiting the combustion chamber [41]. It is true that the value of specific heat changes significantly with temperature, however this does not have a large impact on the analysis. A detailed explanation of this is given in Section 9.15.

2. **Constant Specific Heat Ratios:** Specific heat ratios were assumed to be 1.4 for air and 1.33 for the gas exiting the combustion chamber based on literature. These values are sufficient to perform a preliminary analysis [41].

3. **Efficiencies:** Component efficiencies are determined based on existing engines or trends [42]. They are summarised in Table 9.4. The reason the low pressure spool has a lower mechanical efficiency than the high pressure spool is because it transmits power via gearing to the fan, as well as the BLI generator. The high pressure spool simply directly connects the LPT to the HPT leading to fewer losses.

4. **Maximum turbine inlet temperature:** The maximum turbine inlet temperature (TIT) is limited to 1750 K based on trends in modern turbofan technology. A higher TIT is better for efficiency but is limited by material properties. [42].

5. **Fuel Properties:**The lower heating value of the fuel is assumed to be 43 MJ/kg for both kerosene and synthetic kerosene because these fuels have nearly the same chemical formulation.

6. **Steady state:** No transient analysis is performed on the engine. This is performing a transient flow analysis was not possible with the available time and resources.

7. **Volumetric Flow:** The volumetric air flow (product of velocity and area) through the engine is assumed constant for a specific throttle setting. The mass flow entering the engine is defined as the product of the volumetric flow and air density. The area in this case is the area of the stream tube captured by the engine. When the engine is stationary, the stream tube captured is very large, while at higher speeds the area of the stream tube decreases. This is because of spillage of air around the inlet nozzle. Hence, even though the inlet velocity is increasing, the decrease in effective area results in the mass flow remaining approximately constant at a given throttle setting at a certain altitude.

8. **Constant Potential Energy:** There is no change in potential energy of the fluid passing through the engine. This is applicable because the gasses flow, on average, along the central axis of the engine without any change in height when in level flight.

Table 9.4: Assumed component efficiencies

Component	Efficiency	Component	Efficiency
Inlet (pressure loss)	0.99	Combustion chamber	0.99
Fan (isentropic)	0.9	Combustion chamber (pressure loss)	0.99
Core and fan nozzles (isentropic)	0.98	High pressure spool (mechanical)	0.995
Turbines and compressors (polytropic)	0.94	Low pressure spool (mechanical)	0.985

9.3.2. Model and Design

The configuration of the turbofan is an important part of its performance. It has a twin-spool design, this means that there are two co-axial shafts. The advantage of this design is that different components can rotate at different velocities and that higher pressure ratios can be achieved. Different rotational velocities make larger diameter fans, compressors, and turbines possible while keeping the tips of the blades below Mach 1. The turbofan consists of one fan, two compressors, the LPC and HPC, and two turbines, the LPT and HPT. Two compressors are used such that higher overall pressure ratios can be achieved. Each compressor needs it's own turbine and, therefore, there are two turbines. The BLI system, which was explained in more detail in Section 9.2, receives power from the turbofans. Turbofans also accommodate generators, which provide the most weight and power-efficient option to deliver power to the BLI and other electrical systems in the aircraft. The fan, LPC and generator are connected to the LPT and the HPC is connected to the HPT. Most turbofans with twin spools have these connections because this results in a more even power split between the two turbines and their shafts. A gearbox is added between the shaft of the LPC and the fan to reduce rotational velocity because the blades of the large fan could otherwise reach Mach 1.

The different components are called stations. Each station has its own specific number. These numbers are used in equations to keep track of the changes. The stations of the turbofan and their equivalent number are shown in Figure 9.2. The station numbers of the BLI were discussed in Table 9.3.

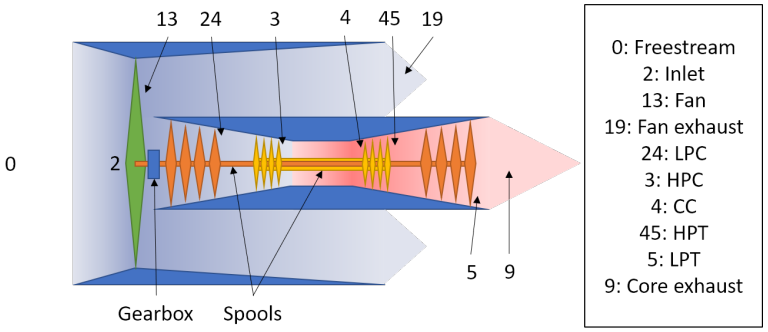

Figure 9.2: Turbofan configuration and station names (not to scale)

The turbofan is modelled by going through the stations from left to right in Figure 9.2. The path splits at the fan where the bypass air goes around the core and the rest through the core. A change in bypass ratio changes how much air goes around the core and how much goes through the core. If the bypass ratio is 10. It means that for every kg of air in the core, there is 10 kg of air going around the core. For each station the total pressures and temperatures from the previous station are used to determine the values at the new station. The amount of compression of the fan and compressors changes with the pressure ratio. A higher pressure ratio results in a higher power requirement. This power is produced by the two turbines. Therefore, changing the pressure ratios of the fan and compressors, changes the conditions all throughout the engine. There are efficiency losses throughout the engine, they result in a loss of energy to noise or heat. The turbine inlet temperature, or TIT, is chosen and specifies until what temperature the flow is heated inside the combustion chamber, a higher TIT means higher fuel flow. A certain TIT is required however, because the turbines need to extract energy from the flow to compress the flow. If this energy is not there it means that the turbines can not extract enough power, which means the pressure ratios can not be achieved.

A certain number of inputs are necessary to estimate the performance of the turbofan. These inputs are listed in Table 9.5. M_0 is the freestream Mach number, p_0 is the freestream pressure, and T_0 is the freestream temperature. The same atmospheric values are required for BLI, but due to the boundary layer are not all equal to the freestream values. These BLI conditions are calculated as explained in Section 9.2.1.

There are also engine specific inputs. These are listed in Table 9.5. BPR is the bypass ratio of the turbofan, $\dot{m}_{BLI}$ is the mass flow of the BLI, Π_{BLI} is the pressure ratio of the BLI, Π_{fan} is the pressure ratio of the fan with the same designation for the LPC and HPC. $\dot{m}_{core}$ is the mass flow through the core, TIT is the turbine inlet temperature, and $P_{electrical}$ is the power required for the electrical systems of the plane.

Table 9.5: Inputs for turbofan model

Input	Unit	Input	Unit	Input	Unit
M_0	-	$T_{0,BLI}$	K	Π_{LPC}	-
p_0	Pa	BPR	-	Π_{HPC}	-
T_0	K	$\dot{m}_{BLI}$	kg/s	$\dot{m}_{core}$	kg/s
$M_{0,BLI}$	-	Π_{BLI}	-	TIT	K
$p_{0.BLI}$	Pa	Π_{fan}	-	$P_{electrical}$	W

In this model the total temperature and total pressure are calculated at each station. They are influenced by efficiencies, pressure ratios, massflow, power requirements, gas and air constants, and fuel burn. The combustion chamber uses Equation (9.4) to calculate the ratio between fuel mass flow and air mass flow. Combustion chambers are not 100% efficient, therefore there is a decrease in pressure and more fuel has to be added for the same increase in temperature. $c_{p,g}$ is the constant pressure heat capacity in hot conditions, η_{cc} is the efficiency of the combustion chamber, and LHV_f is the lower heating value of the fuel used. The amount of fuel burnt depends on the change in temperature and the combustion chamber efficiency. A higher efficiency and a smaller temperature difference decreases the amount of fuel burnt.

$$f = \frac{c_{p,g} \cdot T_{t,4} - c_{p,g} \cdot T_{t,3}}{\eta_{cc} \cdot LHV_f} \tag{9.4}$$

The first turbine is the HPT. Equation (9.5a) and Equation (9.5b) show how to get the total temperature and pressure after the turbine respectively. $c_{p,a}$ is the constant pressure heat capacity in cold conditions, η_{eff} is the mechanical efficiency of the shaft, and κ_g is the heat capacity ratio in hot conditions. To make sure all of the mass flow is accounted for is the fuel to air ratio added with the $(1+f)$ term in Equation (9.5a). The total temperature after the HPT depends mostly on the power required by the HPC, this is what the numerator of Equation (9.5a) is. The total pressure only changes if the temperature ratio changes and, therefore, changes with power required by the HPC.

$$T_{t,45} = T_{t,4} - \frac{c_{p,a} \cdot (T_{t,3} - T_{t,24})}{c_{p,g} \cdot \eta_{mech} \cdot (1+f)} \qquad p_{t,45} = p_{t,4} \cdot \frac{T_{t,45}}{T_{t,4}}^{\frac{\kappa_g - 1}{\kappa_g \cdot \eta_{po,HPT}}} \tag{9.5a,9.5b}$$

The BLI is integrated in such a way that if the mass flow of the engine is changed it will not result in a change of TSFC. TSFC is a measure in the amount of fuel that needs to be burnt to achieve one kilo-newton of thrust. This is achieved by handling the BLI as another bypass ratio. Instead of using the massflow of the BLI directly is an effective bypass ratio with the core massflow used, to simplify equations. The BLI is powered by the LPT. The LPT powers a lot more than just one compressor and the BLI, it also powers the fan and electric system of the aircraft. Equation (9.6) shows the total temperature after the LPT. The numerator shows the power consumers, which are the fan, LPC, BLI, and electrical power. All of which are divided by the core mass flow. The power of the BLI is divided by two, because both engines will be providing power for the BLI therefore only half has to be delivered by one engine. $\eta_{BLI,conversion}$ is the conversion efficiency that the BLI system encounters when it converts the energy from the engine into electricity to turn it into rotational motion at the BLI. The BPR_{BLI} can be determined with: $BPR_{BLI} = \frac{\dot{m}_{BLI}}{\dot{m}_{core}}$. The power required is dependent on the temperature ratios these stations experience, this is reflected in Equation (9.6).

$$T_{t,5} = T_{t,45} - \frac{c_{p,a} \cdot \left((T_{t,13} \cdot BPR - T_{t,2} \cdot (BPR+1) + T_{t,24}) + \frac{BPR_{BLI} \cdot (T_{t,13,BLI} - T_{t,2,BLI})}{2 \cdot \eta_{BLI,conversion}} \right) + \frac{P_{electrical}}{\dot{m}_{core}}}{c_{p,g} \cdot \eta_{mech} \cdot (1+f)} \tag{9.6}$$

The energy that was added to the flow by the fan and compressors, and removed from the flow by turbines, now has to be converted into thrust. This is done with the nozzles. The fan and the core have their own nozzles. The nozzle can be in two scenarios, choked and not choked. The BLI uses the same theory as the turbofan tool for exhaust nozzles. The critical pressure ratio tests are performed on the fan exhaust, core exhaust, and the BLI exhaust separately. That is because it is a possibility for any of them to be choked. There are two different equations to determine the exhaust velocity. A choked exhaust changes the exhaust velocity. The static temperature of the exhaust flow changes, if the exhaust is choked.

Pressure differences between the exhaust and inlet also add to the thrust force. The effective velocity takes this pressure difference into account and gives a new velocity that can be used in the thrust equation explained later. Equation (9.7) shows the effective exit velocity for the core, where a is the speed of sound.

$$V_{e,9,eff} = V_{e,9} + \frac{a^2}{\kappa \cdot V_{e,9}} \cdot \left(1 - \frac{p_0}{p_9}\right) \tag{9.7}$$

Once the exhaust velocities and pressures are determined, can the thrust and TSFC be calculated. The mass flow $\dot{m}$ changes for every exhaust; for the core it is equal to "$\dot{m}_{core} \cdot (1+f)$", for the fan it is equal to "$\dot{m}_{core} \cdot BPR$", and for the BLI it is equal to "$\dot{m}_{core} \cdot BPR_{BLI}$". This model only gives two outputs: TSFC and total thrust. The TSFC has to stay as low as possible while the required thrust is still met. Equation (9.8a) is the amount of thrust generated by the core, bypass, or BLI flow. The sum of which is used to determine TSFC. The results of the turbofan are shown and discussed in Section 9.4.

$$F_T = \dot{m} \cdot (V_{e,eff} - V_0) \qquad TSFC = \frac{f \cdot \dot{m}_{core}}{\sum F_T} \tag{9.8a,9.8b}$$

9.4. Optimisation and Results

Now that the model has been created, the process of optimising the design variables can be performed as explained in Section 9.4.1 and the results are presented in Section 9.4.2.

9.4.1. Optimisation Procedure

Once the model was setup and verified, it was used to find the ideal combination of various input design variables in order to minimise the TSFC for a given value of cruise thrust. The propulsion system also had to meet the static maximum thrust requirements at sea level. The engine was optimised for cruise flight as this is the flight phase where most of the fuel is burnt, but the requirement for take-off thrust had to also be accounted for. The flight cruise altitude flown at is 11000 m at a speed of M 0.78, with ambient pressures and temperatures of 22632.6 Pa and 216.65 K respectively.

The thrust delivered by the propulsion system in cruise is a combination of three components; the turbofan bypass flow, the turbofan core flow and the thrust due to the BLI propulsor. The total thrust is found by summing up these components.

It can be seen from Equation (9.7) and Equation (9.8a) that the thrust is a function of several variables. The mass flow through the engine is dependent on the altitude and engine setting, and is hence an adjustable variable. The consequence of changing the cruise mass flow is that the mass flow at sea level is also affected as explained in Section 9.3.1. The other variables contributing to the thrust are exhaust velocities and the exhaust static pressures of the core, fan, and BLI propulsor nozzles. These variables can be controlled one at a time, however there are many interdependencies between these variables and other design inputs such as fan pressure and compressor pressure ratios, which makes it difficult to set all these variables together to a particular set of values. In essence, it is challenging to work backwards from the thrust requirement, such that the required pressure ratios, turbine inlet temperature, and mass flow can be determined to meet a certain TSFC. Instead, the input variables must changed iteratively in order to converge to the required thrust with the lowest possible TSFC.

In order to have a high thermal efficiency, some design variables can benefit the engine greatly, such as the overall pressure ratio. However, there are physical and technological limits to these, and hence some design inputs must be constrained. The physical limits to some of the design variables are summarised in Table 9.6. These limits are set based on values from existing turbofan engines and values projected by upcoming UHBR turbofan engine manufacturers. The engine with one of the highest overall pressure ratios (OPR) is the GE9x with an OPR of 60:1 [2].

Table 9.6: Turbofan constraints

Parameter	Fan pressure ratio	HPC pressure ratio	Overall pressure ratio	Turbine inlet temperature
Range	1.1 to 1.7	<22	<65	<1750 K

Given these limits, the problem becomes a constrained optimisation problem. This problem could be solved by programming the whole model and iterating the design variables until the most optimum solution is found. However,

[2] URL `https://www.geaviation.com/commercial/engines/ge9x-commercial-aircraft-engine` cited [20. June 2020]

the number of design variables and their inter-dependencies made it more appropriate to use trial and error, rather than using a brute force algorithm trying various pressure ratios, turbine inlet temperatures and BLI bypass ratios. The design tool was made using a spreadsheet, which had the benefit of visualising all the numbers in one place and the effects of changes could be seen instantly. This allowed for a better understanding of the system by giving insights into how certain variables affect others. It is true that a more rigorous approach would be a parametric design optimisation via an optimisation algorithm, but this was not possible with the available resources. It is recommended to follow a more detailed optimisation approach for future analysis.

For the optimisation, the BPR of the turbofan was kept constant at 15. The reason for this is that a BPR of 15 is expected to be feasible within the given EIS time and it has been shown that higher BPRs improve TSFC [43]. Hence, it had to be proved that a BPR of 15 does indeed have benefits in fuel consumption and is a possible target for the required EIS time. It is still true however, that the higher BPR does increase the engine weight, and this impacts the performance of the aircraft. It is possible that a BPR of 14 is more compatible with the CNA, however exploring various BPRs would not be possible with the available time. Hence, a BPR of 15 was adhered to for turbofan design.

The list of variables being iterated to meet the required thrust at both cruise and take-off were then the fan pressure ratio, LPC pressure ratio, HPC pressure ratio, BLI bypass ratio, turbine inlet temperature and the mass flow through the engines core.

9.4.2. Final Propulsion System Parameters and Configuration

The primary takeaways at the end of design iteration and the values obtained are now discussed. The numerical results are summarised in Table 9.7.

The fan pressure ratio has a large impact on engine performance. Due to the high bypass ratio of 15, the power required by the fan becomes enormous if the fan pressure ratio is increased which means that the TIT needs to be increased beyond what is capable (>1800 K) in order to provide enough power to the fan. This resulted in a fan pressure ratio of around 1.4, which is still within the normal range.

The optimum pressure ratio for cruise would be 65, staying at the limit of what is possible. However, to meet the take-off thrust requirement, such a high pressure ratio is not optimal. The reason for this is the very different atmospheric conditions for the two flight phases. At sea level, if an overall pressure ratio of 65 was used, the TIT would again increase beyond what is capable. Hence, a compromise was made between the cruise and take-off performance of the engine. The final OPR was found to be 61.74.

The BLI propulsor also had an optimal bypass ratio. It was found that a lower inlet velocity for the BLI propulsor increases the system TSFC. If the BLI propulsor inlet area was increased, then the average inlet velocity would go up and the BLI propulsor would also be ingesting more of the boundary layer. Ideally, increasing BPR_{BLI} improves fuel efficiency, however, it means that the propulsor needs more power. There are inefficiencies in converting the mechanical power from the turbofans to electrical power at the BLI motor and at some point these inefficiencies make the power loss increase to the point that the whole system ends up becoming inefficient. In addition to this, the weight of the electronic components also increases with power. This would be manageable if the mass of the turbofans would decrease proportionally. However since the turbofans are assumed to be the only thrust providers during take-off, they do not decrease in size. In conclusion, the BLI propulsor improves the fuel efficiency without adding excessive amounts of weight, as this would nullify the lowered TSFC. Due to all the above reasons, the BPR_{BLI} was set based on a constant mass flow through the propulsor, which is explained in Section 9.2.

Once the designed engine met all it's input requirements, a thrust and TSFC map was created for varying altitudes and mach numbers as shown in Figure 9.3 and Figure 9.4 respectively. These maps were used to analyse the various performance aspects of the aircraft such as take-off, climb and cruise. It can be observed that the thrust scales as expected with both speed and altitude, however the TSFC is more interesting. The TSFC is more or less independent of altitude except for at high mach numbers. The engine requires higher TIT when flying very fast at low altitudes resulting in higher TSFC.

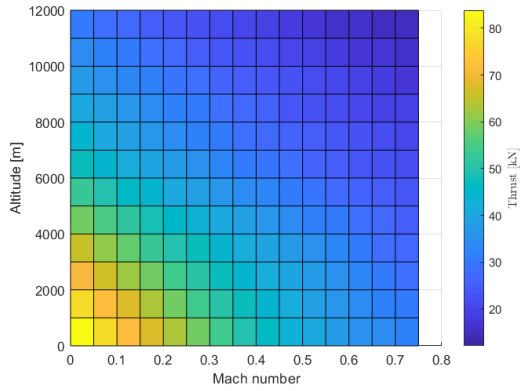

Figure 9.3: Engine thrust map

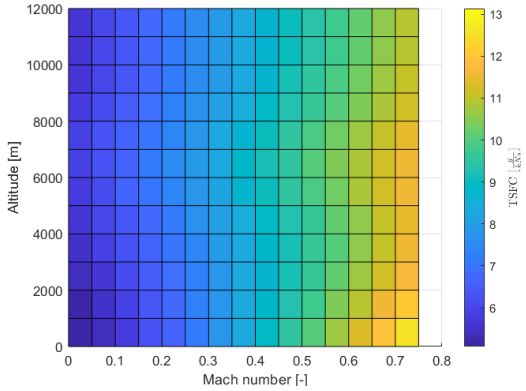

Figure 9.4: Engine TSFC map

Table 9.7: Propulsion system final design parameters

	Cruise	Take-off (static)	Units
Fan PR	1.4	1.4	[-]
LPC PR	2.1	2.1	[-]
HPC PR	21	21	[-]
BLI PR	1.6	-	[-]
TIT	1720	1730	[K]
BLI_ mass flow	42	0	[kg/s]
Core Mass Flow	5.9	22	[kg/s]
Thrust	12.1	82.8	[kN]

9.5. BLI Propulsor Duct Design and Tail Integration

The duct of the BLI propulsor is similar to a duct for any other ducted fan. The only difference is that the inlet of the BLI propulsor starts 1m before the fuselage ends. The BLI propulsor is designed such that, at the inlet, the propulsor ingests approximately 18.2 cm of the boundary layer as a result of the optimisation that is further described in Section 9.4. As already mentioned the boundary layer is assumed to have a constant thickness at the inlet of the BLI propulsor, which gives a certain mass flow of the boundary layer at the inlet of the BLI propulsor. The design of the duct after the inlet was carried taking the mass flow into consideration, such that the flow would not speed up, but rather stay at the same velocity as at the inlet, as this would otherwise negatively impact the thrust produced by the BLI propulsor. The size of the duct is such that it always has a thickness of 10 cm. This design choice was made as a preliminary estimate, as it was assumed that a 10cm thickness would be enough to have a functional shroud for the BLI Propulsor.

Furthermore, the fan diameter of the BLI propulsor is derived to be approximately 1 m. Of this 1 m, the spinner to which the fan blades are connected has a diameter of approximately 20 cm, meaning that the fan blades have a length of approximately of 40 cm. Comparing the size of the BLI propulsor of the CNA to that of the NASA STARC-ABL concept, it can be seen that the sizing of the fan diameter can be validated. The BLI propulsor of NASA STARC-ABL concepts, produces approximately 25 kN of thrust and requires 2.6 MW [44]. Comparing this to the BLI propulsor of the CNA it can be seen that the NASA STARC-ABL concept produces around five times the thrust of the aircraft and requires around 60% more power. Using this and the fact that the fan diameter of the BLI propulsor of the STARC-ABL concept is 2 m, an initial sanity check can be provided and it can be said that the fan diameter of the BLI propulsor of the CNA has the right order of magnitude. However, it is important to note that many other factors such as the exact shape of the fan blades and the rotational velocity of the fan also play a very important role and that a more accurate validation of the fan design of the BLI propulsor can only be carried out at later stages of design when these parameters are known.

The BLI propulsor is located behind the empennage of the aircraft as shown in Figure 9.5. The fan of the propulsor itself is behind the fuselage and connects to a shaft, which is connected to the power source as will be discussed in Section 9.13. The fan is located behind the fuselage so that there is no interference between the fan and any other structure of the fuselage and the tail. Furthermore, placing the fan of the propulsor behind the fuselage also has some benefits in terms of safety, because if the fan blades break or burst, any loose parts are more likely to not hit any other parts of the aircraft and thus, there is a smaller chance that the bursting of the fan blades leads to any serious structural damage on the rest of the aircraft. Furthermore, the duct of the BLI propulsor needs to be connected to the tail cone

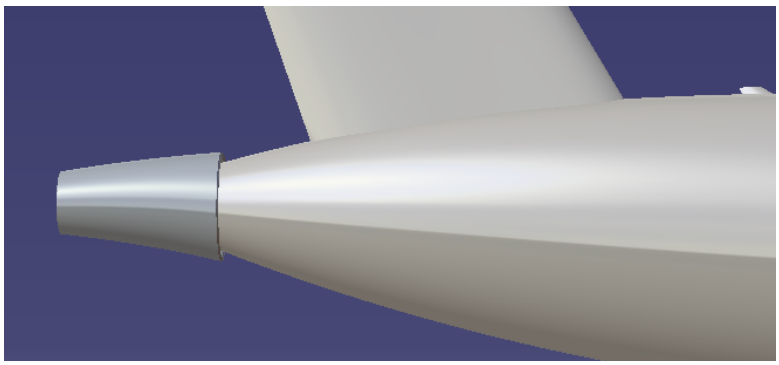

Figure 9.5: Integration of the BLI propulsor and Fuselage of the CNA

of the fuselage by struts. A more in depth aerodynamic and structural analysis of this is necessary to determine the number of struts needed and their dimensions and shape, which was not carried out for this preliminary stage of the design.

9.6. Material for the Fan of the BLI Propulsor

The fan of the BLI propulsor is its main component which accelerates the incoming boundary layer and thus it is also the main component of the BLI propulsor which generates thrust. Due to its importance, the fan of the propulsor needs to be designed carefully and a major part of this design is the material choice.

The fan blades of the propulsor are mainly loaded in bending which comes from the varying flow velocity of the boundary layer along the radius of the fan blades and in axial tension which comes from centrifugal loads which arise due to the high rotational speeds of the blades. However, due to the differences in the velocity profiles of the boundary layer at the different positions along the perimeter of the fuselage cross section at the tail, the loading experienced by the fan blades has a highly cyclic nature. This is due to the fan's high rotational speed. This cyclic stress can lead to localised structural damage and thus lead to the initiation of cracks which can grow and lead to fracture and failure of the material. This means that the material of the fan blades must be resistant to cracks and the blades must be resistant to fatigue. Next to all of this, the material also needs to be as lightweight as possible.

The fan blades were modelled as cantilever beams that are free on one end and fixed on the other end. Furthermore, the loading on the blades was approximated as a non-uniform distributed load for the static analysis. For the dynamic analysis it was assumed that the fixed end of the beam is attached to the mounting hub which constantly rotates at a fixed rotational velocity. Using this model and the previously discussed requirements of the properties of the material of the fan blades, the following material indices were derived, which were used to choose the most suitable material.

The non-uniformly distributed load leads to the bending of the blades. In this case the performance of the material is driven by the yield strength (σ_y) of the material, however to keep the material as light as possible, the density of the material (ρ_{material}) also has to be taken into account, leading to the material index given by Equation (9.9a), which needs to be maximised for best performance [45]. The material also needs to be able to resist any deflections that result from the bending. For the analysis of the tip deflection, it can be assumed that the distributed loading on the blades is uniform, as this has no impact on the material index itself, but only on the design of the shape and structure of the blade. Doing so leads to material index M_2, which is given by Equation (9.9b) and is a function of the Young's Modulus(E) of the material [45].

Assuming that the fan blades follow the equation of a centre cracked plate with a very large width, the material index for a lightweight structure is given by Equation (9.9c), which is a function of the fracture toughness (K_{1C}) [46]. This means that, to increase the resistance to fracture of the material, M_3 needs to be maximised.

$$M_1 = \frac{\sigma_y^{\frac{2}{3}}}{\rho_{\text{material}}} \qquad M_2 = \frac{E_{\text{material}}^{0.5}}{\rho_{\text{material}}} \qquad M_3 = \frac{K_{1C}}{\rho_{\text{material}}} \tag{9.9a,9.9b,9.9c}$$

To maximise the fatigue resistance of a material, it's endurance limit (σ_e), which defines the material's stress amplitude needed for failure at 10^7 cycles at zero mean stress, has to be maximised [45]. While also taking into account the weight of the structure, the material index given by Equation (9.10a) can be derived, which needs to be maximised for best performance.

The resistance to resonance is increased, by increasing the natural frequency of the structure. Using the cantilever beam model for the fan blades, material index M_5 as shown in Equation (9.10b), which also tries to minimise the mass [45].

$$M_4 = \frac{\sigma_e}{\rho_{\text{material}}} \qquad M_5 = \left(\frac{E_{\text{material}}}{\rho_{\text{material}}}\right)^2 \tag{9.10a,9.10b}$$

Using all of the material indices and giving them equal importance, it was possible to choose the best material for the fan blade structure. It was found that low-density steel alloys, Nickel based super-alloys, stainless steel and titanium perform best for the given material indices [46]. For high pressure compressors which go up to a temperature of approximately 700 ° C, nickel based super alloys and titanium are preferred, due to their high service temperatures [46]. The fan for the BLI compressor, however, acts as a low pressure compressor and thus, does not have such high service temperature requirements. On the other hand, due to the fact that titanium has the lowest density and also performs well for all the other material properties, it is the best choice for a low weight fan. That is why titanium was chosen as the material for the fan blades of the BLI propulsor.

9.7. Turbofan Nacelle Design

The sizing of the engine in terms of dimensions is based on literature about engine nacelle sizing [**?**]. This gives a size estimation based on the mass flow required during take-off and the BPR. Estimating the engine fan diameter works very well for low bypass ratio engines, however, not for high bypass ratio engines. This method shows that there is a deviation for high bypass ratio engines. A linear trend line was applied to estimate the increase in fan diameter for a bypass ratio of 15. A linear trend line was chosen such that the increase in size for higher than 12 BPR engines could be done. This returned a 35% increase in fan diameter, for a BPR of 15, compared to the initial nacelle size estimation. Initially the fan diameter, with a BPR of 15, was estimated to be 1.5 metres, with the 35% increase due to the high bypass ratio it is 2.1 metres in diameter. The diameters of the engine in Table 9.8 all depend on the inlet diameter, which meant that they scale according to this diameter. The increase was therefore applied to the inlet diameter only, the rest of the dimensions followed accordingly. Table 9.8 shows the final dimensions of the engine and the nacelle. The UHBR engine results in a larger engine compared to lower BPR engines for the same amount of thrust. This is the disadvantage that UHBR engines have, larger weight and size for better fuel consumption.

Table 9.8: UHBR Albatros Embracer Nacelle dimensions

Dimension	Value
Inlet Diameter [m]	2.1
Engine Length [m]	4.4
Fan Cowl length [m]	3.0
Maximum Diameter [m]	2.3
Exit Fan Diameter [m]	1.9
Exposed Length Core [m]	1.3
Gas Generator Fan Exit Diameter [m]	1.4
Gas Generator Exit Diameter [m]	0.8

9.8. Fuel System

A thorough description of the fuel system architecture is required due to the unconventional lifting surfaces and therefore fuel storage of the CNA. Only the wing will be storing fuel, which means there are a total of two fuel tanks in the aircraft. These fuel tanks are interconnected through the use of pumps and valves to make it possible to transfer fuel from one tank to the other tank, while the engines remain operational. This interconnection between the tanks also helps with reliability. If one of the tanks leaks it means that the fuel can be moved to the other tank. The fuel system architecture can be seen in Figure 9.6. The estimated volume within the wing tank is 11.3 m^3. This gives a total volume of 23.2 m^3. However, these tank sizes are underestimated in a certain aspect and overestimated in another. They are underestimated, because the tanks are based on the size of the wingbox. These current wingboxes do not follow the shape of the airfoil, so more fuel volume is expected. The tanks are overestimated, because the volume is calculated by splitting the wing in parts with constant cross-section and calculating this volume. Therefore it was estimated that the actual fuel storage volume is close to the 23.2 m^3. The required volume for the design range is 14.7 m^3, based on a fuel weight of 11.9 tons. This means that no extra tanks have to be added somewhere else in the fuselage for extra fuel storage.

In total there are four pumps, two for each tank. The second pump of each wing is to add redundancy, such that if a pump fails the fuel tank is still usable. Each pump has a maximum flow rate of 1.39 kg/s and one engine uses a maximum of 0.43 kg/s, which means that one pump should be able to provide all the fuel flow necessary [47]. This means that three of the four upper pumps can fail during flight without the loss of fuel pressure at the engines. This is the same pump used in the Airbus A320, which makes it flight ready.

With this fuel system, it is possible to transfer fuel from one tank to the other tank, by closing and opening valves and turning pumps on and off. Valves can also limit the fuel flow into a certain section. Which means that even with fuel transfers going on, the engines will always get the right amount of fuel. The APU valve will remain closed during normal operation, since it will only be used when both engines fail. It is desired that fuel only flows to the locations required, which is another function the valves provide. The one way valves make sure that no fuel will exit the fuel tanks when it is not desired, for example during extreme flight manoeuvres. The valve between the APU and right engine makes fuel transfer from one wing to the other wing possible.

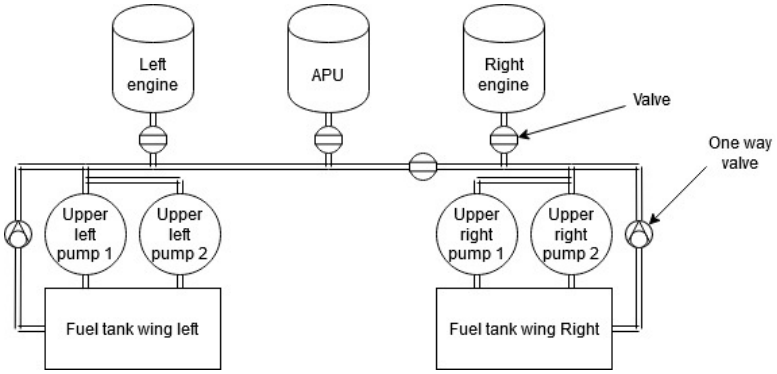

Figure 9.6: The fuel system architecture of the Albatross Embracer

9.9. Emissions

The CNA had a to meet the requirement of 10% reduction in emissions compared to similar existing aircraft. This includes not only carbon dioxide emissions but the trace emissions as well, particularly the NO_x and CO emissions were estimated. CO2 emissions are directly proportional to the amount of fuel being burnt, while NO_x and CO emissions are more difficult to predict as they are influenced by many factors. Since NO_x emissions could not be analysed directly, a statistical database [3] was used to predict how much NO_x and CO is expected to be emitted by a turbofan of BPR 15. Figure 9.7 and Figure 9.8 show trends for emissions vs BPR for engines within rated thrusts of 80 kN to 120 kN.

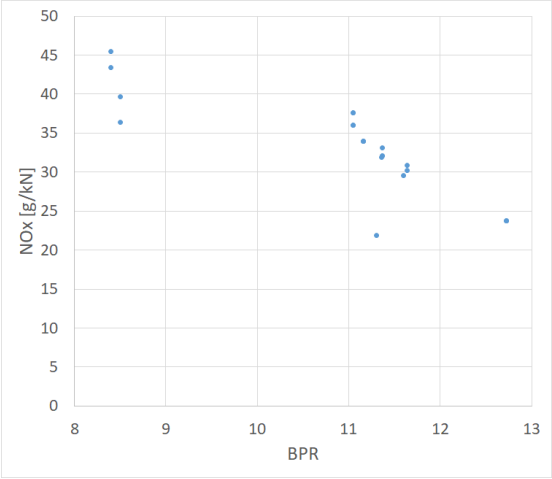

Figure 9.7: NO_x vs BPR

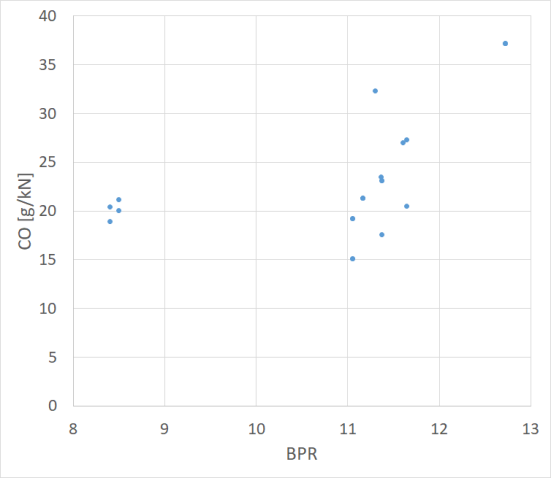

Figure 9.8: CO vs BPR

The y-axis depicts grams of pollutants emitted during reference landing and take-off conditions, divided by the total engine thrust. It can be seen that high BPRs trend towards lower NO_x emissions while CO emissions show a slightly

[3] URL `https://www.easa.europa.eu/domains/environment/icao-aircraft-engine-emissions-databank` cited [16. June 2020]

positive trend. Using these trends the NO_x emissions can be conservatively estimated to be in the range of 15 to 20 g/kN. Given that the equivalence ratio of the engine is between 0.29-0.35 and the TIT is less than 1750K, the NO_x emissions are expected to be low for this engine compared to other high bypass turbofans [41]. It is true that the CO emissions might be higher at around 50 g/kN, yet still, the reduction in NO_x plays a significant role as it is a more potent greenhouse gas and also causes more severe health effects over long term exposure [4].

Overall, the thrust produced by the CNA is on the lower side when compared to the airbus A320neo, 165 kN vs up to 220 kN [48]. This results in lower absolute emissions of NO_x and possibly equivalent CO. The engine powering the A320 NEO (PW1000G) is represented by the point at a BPR of 12.5 in Figure 9.7 and Figure 9.8. Using the thrusts mentioned earlier, the absolute CO emissions for both the CNA and A320neo lie at around 8 kg for the reference take-off and landing conditions. While the NO_x emissions for the CNA are around 2 kg, around 38% lower than the A320neo.

9.10. Synthetic Kerosene

Synthetic kerosene will be the carbon neutral fuel used after conversion. Synthetic kerosene is chemically the same as fossil fuel kerosene. This means that the engines will not have to be replaced or altered to achieve the same performance as with fossil fuel kerosene [49]. No other parts of the aircraft have to be replaced either, to convert to carbon neutral. However, there is a difference between them. Synthetic kerosene is purer than it's fossil fuel counterpart, due to it's "clean" micro-structure. This means that there will be reduced emissions in soot, sulphur, and aromatic parts [50]. There is no significant change in the other emissions, like CO and NO_x, due to the chemical similarity between the carbon neutral fuel and fossil fuel [51].

9.11. Propulsion System Mass Estimates

In this section, the mass estimation for the turbofans and the BLI propulsor is discussed. The mass estimation for the turbofan is discussed in Section 9.11.1, followed by the mass estimation of the BLI propulsor which is discussed in Section 9.11.2.

9.11.1. Turbofan Mass

Multiple statistical methods were used for engine weight estimation: Torenbeek, Svoboda, Jenkinson, and Kuz'michev [52]. Torenbeek and Jenkinson have a limit on the maximum bypass ratio. The weights that resulted from these limited weight estimation methods are increased by 49.5% for Torenbeek and 9.0% for Jenkinson, based on a more detailed ultra high bypass ratio paper [53]. Figure 9.9[53] shows the relation between the bypass ratio and the weight of the engine. GTF stands for geared turbofan and DDTF stands for direct drive turbofan. A geared turbofan is used by the Albatross Embracer, therefore the solid lines are used to estimate the increase in weight due to high bypass ratios. The turbofan will also be running at 1700 K, therefore a line of best fit between those temperatures and the relevant BPR's was made to make the estimation more accurate.

The Torenbeek method is normally valid until a BPR of 8 and Jenkinson is normally valid until a BPR of 14. The weight of these two methods was, therefore, increased by the use of Figure 9.9. The increase in weight from a BPR of 8 to a BPR of 15 is 43.3% and the increase of weight from a BPR of 14 to 15 is 4.5%. These percentages were applied to Torenbeek and Jenkinson respectively. The 4 weight estimations and the average are in Table 9.9. The average weight can be overestimated by 9.8% and underestimated by 23.7%, according to these weight estimation methods. The goal of calculating the average is to limit the limitations of each method by combining them with other methods. Torenbeek is a statistical relation based on older engines and is, therefore, less relevant, but it takes BPR, mass flow, overall pressure ratio and thrust into account. Svoboda uses a lot more modern engines in its weight estimation, but the only variable it uses is take-off thrust. Jenkinson uses take-off thrust and BPR to estimate engine mass and it is valid until a BPR of 14. Lastly, there is Kuz'michev, Kuz'michev uses a lot more variables than Torenbeek and is a bit more modern, but it is still based on old data. Kuz'michev did not give a limit on BPR, so no increase in weight was added based on Figure 9.9.

9.11.2. BLI Propulsor Weight

As mentioned in Section 9.2, the BLI propulsor consists of a fan, a duct and a motor-generator system, which powers the fan. The mass of the motor-generator system that powers the BLI propulsor was already discussed in Section 9.13.

[4] URL `https://www.epa.gov/no2-pollution/basic-information-about-no2#Effects` cited [20. June 2020]

Table 9.9: Turbofan engine weight estimation methods and the average

Method	Weight [kg]
Torenbeek	1557
Svoboda	1592
Jenkinson	2136
Kuz'michev	1621
Average	**1726**

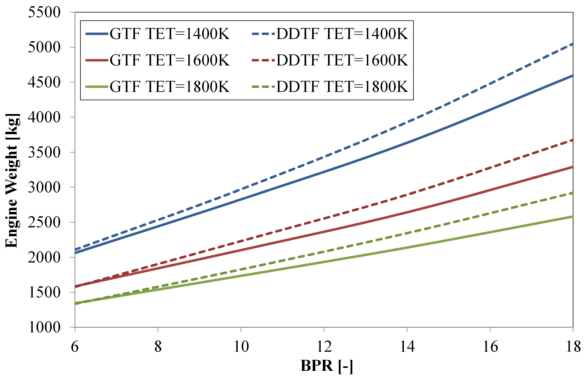

Figure 9.9: Bypass ratio versus weight for geared and direct drive turbofans

From Literature it was found that the mass of the fan for a specific ducted fan that produces 6.8 kN of thrust and requires 2.1 MW of power, is 430 kg [54]. Since the fan of the BLI propulsor produces a thrust of approximately 5.9 kN and requires a power of approximately 1.6 MW, the mass of the fan of the BLI propulsor can also be estimated to be 430 kg. The reason for this is that the thrust generated by and the power required for a ducted fan is heavily dependent on the mass flow through the fan, which is dependent on the diameter of the fan. Since the literature value has a higher value for the thrust and the power required, it can be assumed that this specific ducted fan has a higher mass flow through the fan and thus the diameter of the fan is also higher than that of the BLI propulsor. This means that the mass of 430 kg for the fan is an overestimate.

9.12. Electrical Power Systems

The electrical power system (EPS) design is discussed in this section. The system provides power to various electronic components on the CNA. The power sizing is discussed in Section 9.12.1, the architecture chosen is discussed in Section 9.12.2, the APU selection is explained in Section 9.12.3 and the mass is estimated in Section 9.12.4.

9.12.1. Power Sizing

The EPS of the CNA is similar to that of existing aircraft. The Boeing 787 was taken as a reference aircraft when it came to the EPS, due to the fact that it is highly electric, meaning that it is more dependent on electrical power and less dependent on hydraulic and pneumatic power. The CNA, was chosen to follow a similar level of electric power, as this has potential to reducing the OEW of the aircraft and thus also has the potential to help towards the sustainability goal of the CNA. From an analysis of the Boeing 787 aircraft, it can be seen that the highest electric loads come from the Environmental Control System (ECS), the Wing anti-icing systems and the electrical motor pumps which are used to power the hydraulic system of the aircraft [55].

The Power requirements for these previously mentioned systems for the Boeing 787 Aircraft are shown in Table 9.10. These power requirements for the Boeing 787 have also been scaled for the CNA, as can be seen in Table 9.10. For the ECS it was assumed that the power required can be scaled by the volume of the cabin, since the main objective of the ECS is to pressurise, supply air and provide thermal control for the cabin and cockpit. This means that a larger volume requires more power. Since the volume of the cabin is larger than that of the cockpit, it can be assumed that the scaling of the ECS power requirement happens only with respect to the cabin volume and that the cockpit volume does not need to be taken into account. The power requirement of the wing anti-icing system was calculated by scaling the Boeing 787's wing anti-icing system's power requirement by the wing area. A larger wing area requires a larger amount of heat to melt or prevent the build-up of any ice. Finally, the Boeing 787 has 4 electrical motor pumps, where each pump requires 100 kVA. For the CNA it was chosen that there would be a total of 3 electrical pumps, however only a maximum of 2 of these would be operative simultaneously at any point in time during the flight, meaning that the third pump is there just for redundancy, in case one of the pumps fail. This preliminary method leads to a total Power requirement of 400 kVA. Furthermore, it is assumed that the power factor is 1, so that the maximum power requirements is 400 kW. This assumption was made so that the power requirements would be slightly overestimated as the power conversion factor is dependent on the system and its components.

Table 9.10: Table showing the required power for the main electric components

Component	Boeing 787 Power Requirement (kVA)	CNA Power Requirement (kVA)
Environmental Control System	500	160
Wing Anti-Icing System	100	40
Electrical Motor Pumps	400	200
Total	**1000**	**400**

The previously determined power requirement is the maximum power requirement for the whole flight. However, since the cruise phase of the flight is the longest part, it is also important to analyse the power requirements during cruise. The Power requirement for the ECS stays the same. This is also true for the wing anti-icing system, however it is important to note that this system is turned on only when there is ice build up and turned off again when this is not the case. Furthermore, during cruise only 10% of the total hydraulic power is needed, which means that the electrical motor only needs to be supplied with 20 kVA during cruise [56]. This means that during cruise the total power requirement is 220 kVA (220 kW with a power conversion factor of 1).

9.12.2. Architecture

The architecture of the EPS of the aircraft is shown in Figure 9.10. The architecture is very general and also very similar to current aircraft. As can be seen by Figure 9.10, the primary power sources are the turbofan engines. These engines power the generator motor system for the BLI Propulsor as well as the generators for the on-board power appliances of the aircraft. In Figure 9.10, the black lines show the power transmission paths for normal flight, whereas the red lines show the power transmission paths for emergency situations.

As shown in Figure 9.10, the turbofans power generators, which produce the power and deliver these to the AC (alternating current) buses. From these AC buses the power is delivered to the electrical components that run on AC power and to the transformer-rectifier units (TRU), which convert the AC to DC (direct current). From the TRUs, the power is transmitted to the DC busses, which transmit the necessary power to the components which run on DC. While the power is transmitted from the AC buses to all of the AC and DC components, power is also transmitted through the battery chargers to a single battery. This battery stores energy for emergency cases where one or both of the turbofan engines fail or there is a failure in one or both of the AC buses.

One of the reasons why several main busses were chosen to power single components was due to the EasyJet A320 incident which occurred in 2006, where a failure of the general control unit led to the loss of a lot of electrical equipment including all communications electronics[5]. To prevent the loss of certain electrical components, a design choice was made, such that several buses are used to power each component, so that in the case of failure, a spare bus is still available to provide the power.

For emergency cases, where either a turbofan/generator or a bus fails, the APU is started up using the battery. The APU provides the power to the main buses, while also charging the battery that powers the APU again, in case the APU shuts off and needs to be restarted again. In the case where one or more of the main buses fails, the APU also starts up, but in this case the power from the APU is transmitted to the emergency AC bus. From this the power is transmitted to the emergency DC bus, after the current passes through the emergency TRU. However, it is still possible that the APU also fails, as leaks in the fuel piping or similar problems could arise. Then it becomes necessary to deploy the ram air turbine (RAT), which uses the energy from the airflow around the aircraft and transmits it to the Emergency generator which produces the power in the case that the APU does fail.

9.12.3. APU Selection

The APU is used primarily for emergency situations where all engines have failed, it is not operational during flight at any other time. The APU can also be used on the ground to start up the engines, however, once the engines are started, they provide all the electrical power to all subsystems for the entire duration of the flight. The reason that the APU does not operate in flight is that the hot exhaust gases would be entering the BLI propulsor inlet and causing undesirable effects for both the performance of the propulsor but also the fatigue life of the propulsor. The APU selected for the CNA is the Honeywell 131-9A. This APU has a power output of 447 kW and is also used on the Airbus A320 aircraft.

[5]URL `https://www.flightglobal.com/airbus-faces-demands-for-a320-series-electrical-systems-improvement-following-easyjet-report/88606.article` cited [16. June 2020]

Since the APU is capable of starting engines requiring more powerful than the CNAs, it will be able to provide the power required to start the CNA turbofans as well. The mass of the selected APU is 145 kg.

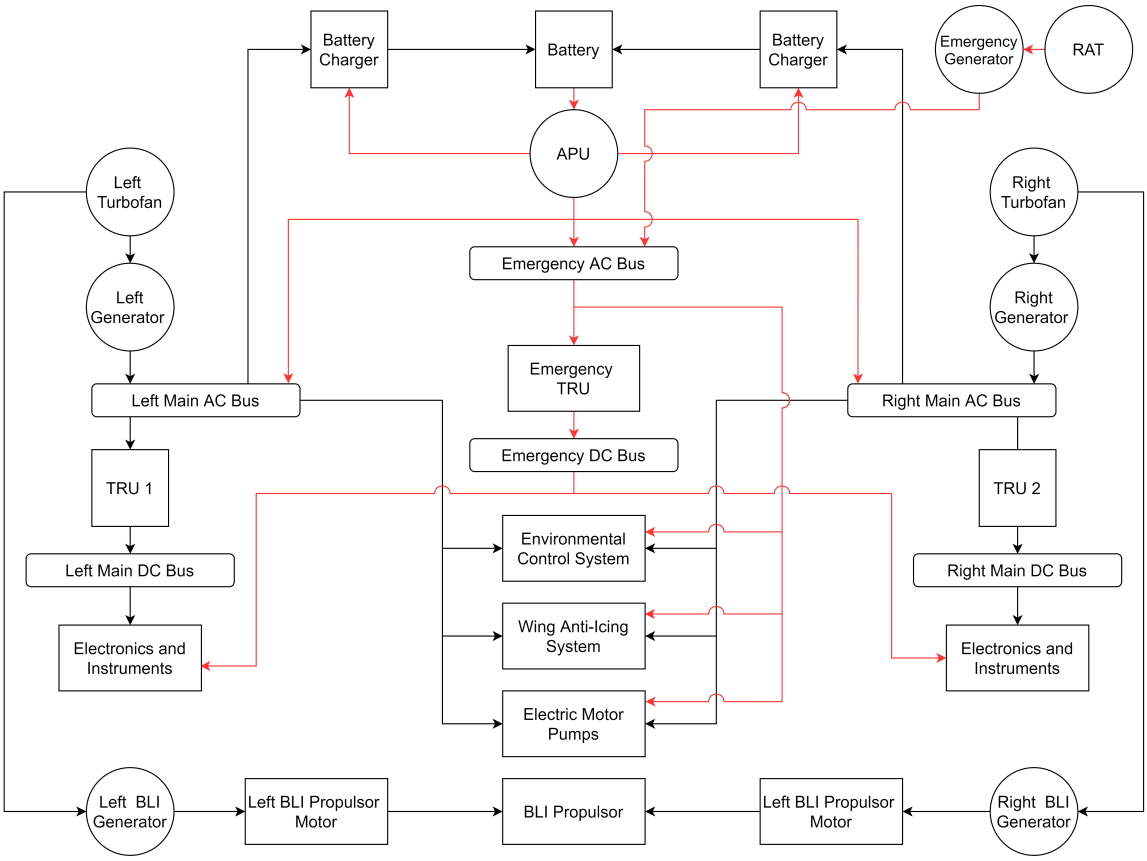

Figure 9.10: The architecture of the Electrical Power System

9.12.4. Mass Sizing

The EPS can be broken down into the electrical power generation group and the instruments and electronics group. Using Torenbeek's method for Class II weight estimations, the mass of the instruments and electronics group was found to be approximately 1060 kg and the mass of the electrical power generation group was found to be approximately 2220 kg [13]. This means that the total EPS mass is estimated to be 3280 kg. However, it is important to be very critical of Torenbeek's method because this uses empirical relationships that were derived using aircraft from before 1982. On the one hand there have been improvements in the technology behind power generation systems, which means that specific power of these systems have increased, meaning that the mass given by Torenbeek's methods are overestimates. However on the other hand it is also important to note that current aircraft also have more instrumentation and electronics onboard, due to the shift towards more electrical aircraft compared to the time when Torenbeek's methods were derived, meaning that this shift towards more electrical aircraft is not accounted for. Overall, however, the mass estimate made for the whole EPS can be seen as an overestimate, as a larger fraction of the total EPS mass is dependent on the electrical power generation group then on the instruments and electronics group.

9.13. BLI Power Distribution System

The BLI propulsor is powered via an electric motor. This motor is powered by generators in each turbofan which harvest power from the low pressure spool. The system architecture chosen for distributing electric power is discussed in Section 9.13.1 and the sizing of each component is discussed in Section 9.13.2.

9.13.1. General Architecture

The power distribution system had to be designed to handle power in the order of one to two megawatts. The high power means that considerations have to be made regarding the use of novel technologies such as high temperature superconducting (HTS) motors and generators. These technologies are currently under development and have very

high potential for aerospace applications. Using HTS components provided a prospect of high efficiency and low weight, however they were compared to conventional non-super conducting components in a qualitative trade-off to see if they provide enough advantages to justify their use.

The trade-off was performed using three criteria; efficiency, specific power and TRL9 time. These were given weights of three, two and five respectively. The TRL9 time criterion was given the highest weight because its entry into service in 2030 is a driving requirement for the aircraft. Efficiency scores were close for both systems while specific powers for HTS systems can be up to two times higher. However, the TRL9 time for conventional electric motors is essentially zero, as they are already used in smaller aircraft. The trade-off is summarised in Table 9.11.

Table 9.11: BLI electrical system trade-off

	Efficiency	**Mass**	**TRL9 time**	
Weight	**3**	**4**	**5**	
HTS	5	5	1	**2.08**
Non - HTS	4	3	5	**2.92**

It was found that using conventional non-HTS system would be a better design option because of the much higher TRL9 time. The efficiency difference is not very high either between the two systems because conventional electric motors can achieve between 90-95% efficiency while HTS motors are above 98% efficient. The only winning criterion for the HTS system is the specific power; conventional motors and generators can have peak power densities up to 9 kW/kg while HTS machines are predicted to achieve up to 20 kW/kg.

The power distribution system layout is depicted in Figure 9.11. The main ideology followed in this layout is to reduce the use of unnecessary and heavy electrical components. In addition to this, safety and reliability were also considered. The system consists of two isolated motor-generator pairs which are electrically isolated from each other. Each turbofan supplies mechanical power to a generator which converts it to electrical power, which is sent to a motor using alternating current. It was assumed that the generators generate power at 800 V. This voltage has been chosen as it is already in use in electric vehicles [6]. Increasing the voltage results in problems with electric arcing, especially in the motors.

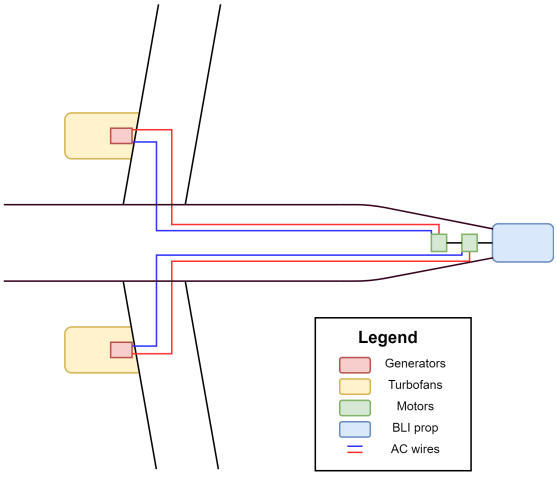

Figure 9.11: BLI power distribution system layout

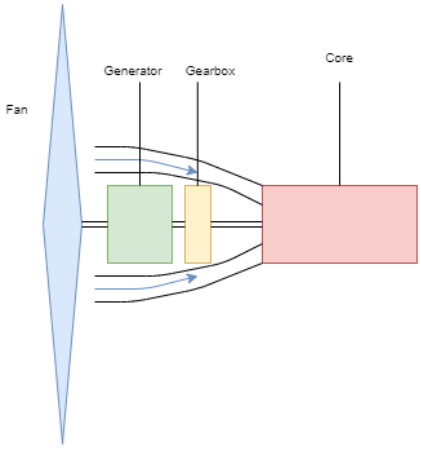

Figure 9.12: Generator packaging (not to scale)

It was decided to keep the motor generator system from each turbofan separate for a few reasons. For one, this would decreases the complexity of the system as power would not have to be cross-fed and managed between the two generators, which would also reduce system weight. The second reason is that in the event of an engine failure, the second engine can still provide half the operating power to the BLI propulsor without being affected. This increases the reliability of the system.

The only connection between the motor-generator pairs is the shaft connecting the motors. The two motors use a common shaft to power the BLI fan, however if one of these motors were to stop working either due to failure of the motor or the generator powering it, the shaft from the working motor would be adding energy into the failed motor, which could cause overheating issues and increase the risk of a fire. This is avoided by using co-axial concentric shafts

[6] URL `https://newsroom.porsche.com/en/products/taycan/battery-18557.html` cited [21. June 2020]

which are connected to each other via a one-way clutch. This way, even if one of the motors stop working, the shaft from the working motor will not be wasting mechanical power into the failed motor.

9.13.2. Component Sizing

To size the electrical components, the most important parameters were the specific power and efficiency of the components. The three primary electrical components are the motors, generators and transmission wires. Since motors can be used as generators, the sizing techniques were essentially the same for these components. The system was sized in a chain, starting at the electrical motors and ending at the generators.

The electrical wires were sized such that they would have a high transmission efficiency but at the same time, not add too much weight to the system. Two materials were explored for the wiring, namely Copper and Aluminium. The properties for these materials are shown in Table 9.12. It can be seen that copper has a significantly lower resistivity, however a much higher density. It was found that copper wiring would have to be significantly heavier than aluminium wiring for the same transmission efficiency. Hence aluminium wiring was chosen.

Table 9.12: Material properties[7]

	Aluminium	**Copper**	**Units**
Resistivity	2.65e-08	1.68e-8	$[\Omega m]$
Density	2.70	8.96	$[g/cm^3]$

A target linear mass density (ρ_l) for the wires was chosen. Then the corresponding cross-sectional area (A) of the wire was found by dividing the ρ_l with the density (σ) of the material as shown in Equation (9.11a), then the resistance was found using Equation (9.11b), where l is the length of the wire. In this case, the length of wires for one of the motor-generator pairs is 80 m which is found geometrically with a 20% margin to account for routing. Then, the power lost as heat can be calculated using Equation (9.11c), where V is the voltage. Finally the efficiency of the wire can be found by dividing the power coming out of the wire with the power coming into the wire. Upon simplification, the equation for efficiency is given by Equation (9.11d).

$$A = \frac{\rho_l}{\sigma} \qquad R = \frac{\rho \cdot l}{A} \qquad P_{lost} = \left(\frac{P}{V}\right)^2 \cdot R \qquad \eta = 1 - \frac{P \cdot R}{V^2} \qquad \text{(9.11a,9.11b,9.11c,9.11d)}$$

It was found that a higher efficiency results in a higher linear mass density for the wiring, however there is a trend of diminishing returns. The linear mass density selected was 1.3 kg/m which resulted in a wire transmission efficiency of 98.8%. Now the sizing of the motors and generators is discussed.

The motors and generators were sized based on the values of specific power and efficiency. The output power required from the motors ($P_{f_{motor}}$) was an input from the BLI fan. This power was then divided by the motor efficiency to find the motor input power ($P_{i_{motor}}$). This input power for the motors was used to estimate the mass of the motors. A similar procedure was used to size the generators, where the output power for the generators ($P_{f_{gen}}$) was found based on the transmission losses in the wires and the input power ($P_{i_{gen}}$) was found from the generator efficiency.

The motor/generator found with the highest continuous power density was the Emrax 268 unit [8], with a power density of 5.22 kW/kg. The efficiency range was between 92% and 98%. This machine also has a volumetric power density of around 19 MW/m^3. These numbers were used to size a theoretical motor/generator based on the power requirements of the BLI propulsion system. Using such a motor, the final system masses and efficiencies achieved are shown in Table 9.13.

Table 9.13: BLI electrical system mass and efficiency

Component	**Output Power [MW]**	**Mass [kg]**	**Efficiency**
Motors	1.611	308.6	0.950
Wires	1.729	234.0	0.988
Generators	1.750	371.5	0.930
Overall	**-**	**914.2**	**0.872**

[7] URL `http://hyperphysics.phy-astr.gsu.edu/hbase/Tables/rstiv.html` cited [19. June 2020]
[8] URL `https://emrax.com/e-motors/emrax-268/` cited [16. June 2020]

The motor and generator volume was found from the calculated mass and volumetric density. This resulted in a volume of 0.0423 m^3 per motor and 0.046 m^3 per generator. Assuming the motors and generators to be cylindrical, The motor is approximately 30 cm in diameter and 60 cm long. While the generator is 30 cm in diameter and 65 cm long. Accounting for extra volume due to the cooling system (pipes) the diameters were increased to 40 cm.

The generators are packaged inside the turbofan engines. Specifically they are contained within the engine core of each turbofan engine near the intake. The generators are placed between the LPC and Fan (Figure 9.12). The gearbox converts the shaft speed of the low pressure spool as required and sends power to both the fan and the generator. The generator includes a clutch that can disengage from the main shaft in the event that the generator fails, to avoid a situation where power is being put into the generator which would induce currents and generate a lot of heat. The motors are placed in the tail cone, in the location usually occupied by the auxiliary power unit. The shaft from the motors exits from the rear of the fuselage and connects to the BLI fan. The APU was then moved more forwards by approximately 1.5 m. The exhaust of the APU is located at the bottom of the tail.

The motors and generators though efficient, generate a significant amount of heat. Based on the efficiencies and power flow, each generator makes 85.5 kW of heat and the two motors together generate 86.5 kW of heat. With simplified thermodynamic analysis, it is determined that these components would need around 0.65 kg/s of air flow (at 216 K) each during cruise to keep their temperatures below 355 K (80 ° C). This is very small and thus it is not considered a design killing aspect which needs extensive analysis to prove feasibility. For the generators, the heat is managed by taking bleed air from the turbofan bypass flow. For the motors, air is taken from the APU inlets located at the top of the tail and exits between the BLI inlet and trailing edge of the vertical tail.

9.14. Verification and Validation

One of the CNA's novel features is the ultra high bypass ratio engine. The model used to predict the performance of this novel engine must be correct, to prove that the CNA is a viable aircraft for a carbon neutral future. To ensure that the predictions of the model are correct, validation and verification on the model are performed. This section discusses the verification of the model through four unit test and five system test. This section also validates the model with a GEnx-1B-70 engine performance analysis.

9.14.1. Verification

Multiple unit test and system test were performed to verify the turbofan model. First are the unit tests, multiple were performed to see if the model does what it is expected to do. First is the temperature and pressure relation. The total pressure ratio is directly related to the total temperature ratio. If the pressure ratio increases it should also increase the change in temperature. The model shows this behaviour, which can be seen in Table 9.14. This was performed on the pressure ratio of the fan. Looking at the thrust of every component is also very useful. The decrease in pressure ratio of the fan, decreased the thrust of the fan. However, it also means that less power has to be absorbed from the flow, which means that the core thrust has gone up. This effect can also be seen in Table 9.14.

Table 9.14: Change in temperature due to changing the pressure ratio of the fan

Pressure ratio [-]	**Change in temperature [K]**	**Fan thrust [N]**	**Core thrust [N]**	**BLI thrust [N]**	**Total thrust [N]**
1.4	27.4	10385	3047	1995	15507
1.3	21.1	8161	4194	1995	14472

The second unit test performed, is related to the effect of polytropic efficiencies of the fans, compressors, and turbines. A decrease in polytropic efficiency in fans and compressors means that more energy is being lost to heat for the same change in total pressure ratio. Which means that there must be an increase in total temperature after these components when the efficiency decreases. For turbines, it works a bit differently. When the efficiency of a turbine is decreased the temperature jump does not change, because a certain amount of energy has to be extracted from the flow to power the fans and compressors. Which means that a larger pressure drop occurs for a lower efficiency even if the change in temperature is the same. This behaviour can be seen in Table 9.15.

Table 9.15: Change in temperature and pressure due to change in polytropic efficiency

	Efficiency	Total Temperature Before Component [K]	Total Temperature After Component [K]	Total Pressure Before Component [Pa]	Total Pressure After Component [Pa]
Fan	0.9	243.01	270.41	33699	47178
	0.8	243.01	274.04	33699	47178
HPT	0.94	1690.00	1260.83	1863591	530694
	0.84	1690.00	1260.83	1863591	456986

The second to last unit test is about checking the calculation of the exhaust velocity. The exhaust velocity is directly related to the thrust generated, which makes this an important unit test. The exit velocity condition changes if the velocity of the exhaust flow reaches Mach 1, also called choked flow. If it reaches Mach 1 Equation (9.12a) is used, if it does not reach Mach 1 Equation (9.12b) is used. These were calculated by hand with the following parameters; $\Delta T = 100K$, $c_p = 1000\frac{J}{kgK}$, $k = 1.4$, and $T = 600K$. The hand calculations and the calculations of the model are exactly the same which means this part of the model is also verified. The results of this unit test are in Table 9.16.

$$V_e = \sqrt{2c_p\Delta T} \qquad V_e = \sqrt{(k-1)c_p T} \tag{9.12a,9.12b}$$

Table 9.16: Exhaust velocity unit test for choked and unchoked flow

Exhaust velocity	Hand calculation V_e [m/s]	Turbofan model V_e [m/s]
M = 1	489.9	489.9
M <1	447.2	447.2

Changing the freestream pressure was the last unit test performed. The pressure was changed to 0 Pa. If the freestream pressure changes to zero it would mean that total pressure at all of the stations is also equal to zero, because something times 0 equals zero. A check is performed, to check if the exhaust flow is choked. This check divides internal total pressure by freestream total pressure and compares it to the critical pressure ratio. The freestream pressure is zero, which means that it should result in a divide by zero error. Both the zeros at the stations and the divide by zero error happen in the model.

The system tests can be performed, now that the unit tests have been completed. Research into turbofans concluded that high bypass ratio engines produce thrust more efficiently and therefore should reduce in TSFC. The model should reflect that behaviour to show that the increase in BPR has a positive effect on fuel consumption. A decrease in BPR reduces the total mass flow through the engine, which leads to a reduction in engine thrust. To achieve the same amount of thrust was the mass flow increased. The results are in Table 9.17, which shows an increase in TSFC for a lower bypass ratio engine and the same amount of thrust.

Research into the BLI system showed that the introduction of a BLI system into a turbofan aircraft should reduce TSFC. A check was performed to see if that is the case. Again due to the removal of the BLI system has the total thrust of the system reduced, so the mass flow through the core was increased to match the total thrust. The results can be seen in Table 9.17 and it shows the expected increase in TSFC without BLI.

Increasing the freestream velocity should decrease the total thrust the turbofan produces, due to the smaller difference in inlet jet velocity and exhaust jet velocity. The results of this system test are in Table 9.17 and does show a decrease in thrust at higher freestream velocity. The freestream velocity is given in Mach number.

Table 9.17: The result of BLI and BPR on TSFC

BPR	BLI	Freestream mach number [-]	Total thrust [kN]	TSFC [g/kNs]	Core mass flow [kg/s]
15	yes	0.78	15527	11.83	7.9
8	yes	0.78	15499	14.55	9.7
15	no	0.78	15544	12.79	8.55
15	yes	0.9	14228	12.46	7.9

The second to last system test of the turbofan tool was checking power requirements and making sure that more power is generated by the turbines than is being consumed by the fan, compressors, and BLI. The results of this test can be seen in Table 9.18 . This table shows that the turbines do generate more power than is consumed by the other components, which means that the model follows the basic laws of physics.

Table 9.18: Power requirements and delivered by the different parts of the turbofan

Power required [W]					Power delivered [W]	
Fan	**LPC**	**BLI**	**Fan + LPC + BLI**	**HPC**	**LPT**	**HPT**
3.23E+06	4.62E+05	6.05E+05	4.30E+06	3.97E+06	4.76E+06	3.99E+06

The last system test is verifying that the BLI produces the same results as the fan of the turbofan if the inputs are the same. This has to be the case, because both use the same thermodynamic theory for the fan. Testing this gave the exact same results. The temperatures and pressures at the stations, the exit velocity, and the thrust were exactly equal, if the freestream conditions are the same and the mass flow through the BLI is the same as the mass flow through the bypass of the turbofan.

9.14.2. Validation

The validation of the tool was performed with a performance analysis of the GEnx-1B-70 [57]. The results from the model and the validation model are shown in Table 9.19 and Table 9.20. Table 9.19 shows the total pressures and temperatures at every station. Table 9.20 shows the final thrust and TSFC value of both the model and the validation model. It shows that the temperatures and pressures are very close until the combustion chamber. After the combustion chamber, there is a deviation in both temperature and pressure. This deviation results in a change in the total thrust of the aircraft. However, the thrust values are not that different and are only 7.5% higher than the validation model. The deviations after the combustion chamber can be attributed to the c_p value. A constant c_p value was assumed for after the combustion chamber. However, this is not the case in reality. A more detailed flow analysis could give more accurate values. Some of the efficiencies were also assumed. The research paper does not specify what the efficiencies of the LPT and HPT are, the same efficiencies as for the LPC and HPC have been chosen for the turbines. The paper also does not specify anything about the combustion chamber or the mechanical efficiencies, for these was an efficiency of 99% chosen. Overall does this validation show that the model is representing reality fairly well, especially everything that happens before the combustion chamber. Because everything before the combustion chamber is so accurate it means that the intake, fan, and exhaust of the BLI have been validated as well. Since it uses the same theory as the fan of the turbofan.

Table 9.19: Total pressures and temperatures at every station for the model and the GEnx-1B-70 validation model

Station	**Total pressure**		**Total temperature**	
	Model	**Validation**	**Model**	**Validation**
0	101325	101325	288.00	288.00
2	101325	101325	288.00	288.00
13	151988	151988	327.10	326.87
24	197584	197584	355.19	354.83
3	4406118	4407638	912.59	911.70
4	4362056	4319485	1790.00	1790.00
45	1004007	758412	1284.72	1212.7
5	227309	146055	918.65	838.39

Table 9.20: Thrust and TSFC validation of the model compared to GEnx-1B-70 validation

Parameter	**Model**	**Validation**
$V_{e,fan}$ [m/s]	262.63	262.67
$V_{e,core}$ [m/s]	547.04	401.92
Core Thrust [kN]	273.405	-
Fan Thrust [kN]	71.339	-
Total Thrust [kN]	344.744	320.48
TSFC [kg/(kNs)]	0.00769	0.01

9.15. Sensitivity Analysis

In order to asses the impact of changes in uncertain assumptions used in design tools, a sensitivity analysis is performed. The tool being analysed here is the integrated turbofan-BLI design tool which was used to design the turbofans and BLI system together. The more uncertain assumptions made during the design were on efficiency values of the various components, the assumed pressure ratio of the BLI fan, and properties of the air/gas. The changes analysed are summarised in Table 9.21.

The changes observed in thrust and TSFC due to the changes mentioned are summarised in Section 9.15. It can be seen that for the most part, small changes in certain values only cause proportional changes to the values of thrust and TSFC. The specific heat values do have a large effect on engine performance, for example the thrust produced goes up when the specific heat of the gas is increased, while TSFC is not affected that much. The reason for this is likely because the power that can be extracted across the turbine stages increases with gas specific heat and hence so does the thrust, but the TSFC remains approximately the same because only values after the combustion chamber

Table 9.21: Sensitivity Analysis

Parameter	Original	Changed	Parameter	Original	Changed
Fan Isentropic Efficiency	0.9	0.92	BLI Fan Pressure Ratio	1.6	1.4
Polytropic Efficiencies (All Turbines and Compressors)	0.94	0.92	Ratio of Specific Heats (Gas)	1.33	1.3
BLI Fan Isentropic Efficiency	0.9	0.92	Specific Heat (Air)	1150	1250
BLI Power Transmission Efficiency	0.87	0.8	Specific Heat (Gas)	1000	1100

are affected. Changing the specific heat of the incoming air has a negative effect on the engines performance, this is due the fact that more power is needed to drive the compressors with a higher $c_{p_{air}}$. For the analysis of the engine, the specific heats were kept constant, however this is not true in reality. Higher temperature generally increase the specific heat, hence as the air goes through the compressor stages, its c_p value increases meaning that more power is required to compress it further. At the same time, the c_p of the gas leaving the CC is also higher than the constant value (of 1150 J/kg/K) assumed earlier, resulting in more power being extracted across the turbines. Overall, the two effects work to cancel each other out and the assumption of constant specific heats is still valid for this level of design. The sensitivity analysis finds that the uncertain assumptions do not cause large changes in the final result, leading to the conclusion that the engine performance analysis is robust.

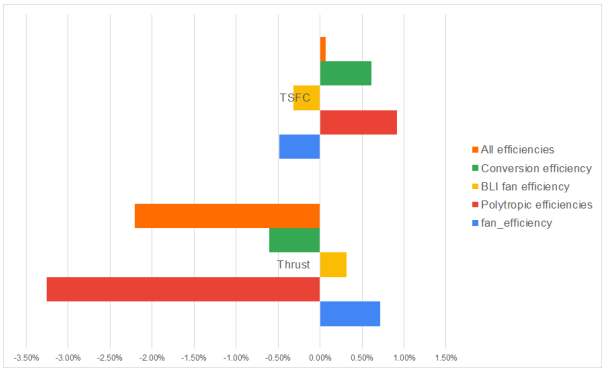

Figure 9.13: Sensitivity analysis on efficiencies

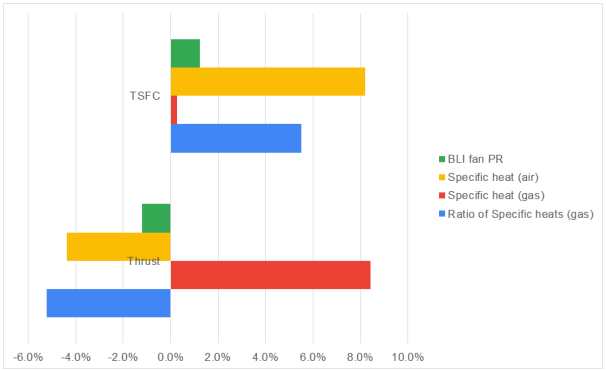

Figure 9.14: Sensitivity analysis on pressure ratio and specific heat

9.16. Recommendations

The propulsion and power systems were designed with limited time and thus could not be fully optimised. Some simplifying assumptions were made which can be removed and a more detailed analysis can be performed for the sizing of the turbofans and BLI system. Some recommendations for future design are presented here.

The turbofan can be modelled with variable specific heat values. This will result in more accurate values for thrust and TSFC. Lower BPRs should also be explored, the reason for this is that even though the efficiency of the engine will be worse with lower BPRs, the weight also reduces thus reducing the OEW of the aircraft. An analysis can be performed on the impact on fuel burn due to these opposing factors to find out the optimal BPR. Another recommendation for turbofan design is to use a programmed optimisation algorithm rather than using qualitative reasoning to converge at the optimum combination of design parameters.

The BLI power distribution system can be made lighter if higher power density motors/generators become available. There are companies that currently claim power densities up to 7.5 kW/kg [9]. Finally, a more detailed boundary layer analysis can be performed using CFD. The analysis performed at this stage was mostly empirical and did not take into account the exact geometry of the CNA fuselage and wings, it can be improved in these areas via CFD anlysis or wind tunnel testing.

[9] URL `https://www.magnax.com/magnax-blog/magnax-prepares-to-manufacture-radically-high-powered-compact-axial-flux-electric-motor` cited [20. June 2020]

10
Empennage design

The empennage design is correlated with the stability and controllability of the aircraft, therefore it is important that these are fully assessed before starting the tail sizing. In this chapter, the objectives and the driving requirements for the tail sizing are listed in Section 10.1. The sections from Section 10.2 to Section 10.6 deal with the sizing of the horizontal and vertical tail. Section 10.7, Section 10.8 and Section 10.9 deal with control surfaces actuation, structural integration and mass estimation respectively. Finally, Section 10.10 describes the necessary flight control system for the CNA.

10.1. Objective and Requirements

The stability and controllability of the aircraft is provided by the tail, which is split into the horizontal tail and the vertical tail. The horizontal tail ensures longitudinal stability and control, while the vertical tail deals with these aspects in the lateral direction. Therefore the sizing procedure of the tail is such that stability and controllability are ensured during the whole flight, for which the requirements in Table 10.1 have to be met.

Table 10.1: Driving requirements for tail sizing

Identitifer	Requirement	Source
REQ-CN-PERF-30	The CNA shall be controllable during take-off, climb, level flight, descent, approach and go-around, approach and landing.	CS 25.143
REQ-CN-SAFE-5	The CNA shall possess static stability during flight.	Own
REQ-CN-CTRL-7	Ranges of weights and CG where the airplane is safely operable shall be determined.	CS 25.23

10.2. Design Choice on the Tail Configuration

There are various tail configuration options the CNA can feature, hence a trade-off process was carried out to choose the best configuration. Candidates included conventional tail, T-tail, cruciform tail, and other unconventional configurations such as V-tail, Y-tail, H-tail, U-tail and the canard configuration. Notable characteristics of the CNA when choosing a tail configuration are the high-wing configuration, two wing-podded engines and the BLI propulsor attached at the rear of the fuselage. Tail configuration with less interference with the engine exhausts, the wake from the main wing, and the intake flow of the BLI propulsor were favoured. From this perspective, the conventional configuration, with both vertical tail and horizontal tail attached to the fuselage, was discarded. The horizontal tail must be positioned in such a way that it avoids any jet exhaust which spreads out forming a cone shape. The exhaust typically has an angle of 6° from the engine centre line [13]. The CNA has the engines integrated on its high-wing and their exhausts cover the areas next to the fuselage, where the horizontal tail is positioned according the conventional tail configuration.

The V-tail, Y-tail, H-tail and U-tail configurations and their variations (for example inverse V-tail) were quickly stashed, as they do not offer enough advantages compared to their disadvantages. The V-tail combines the rudder and the elevator, which highly increases the complexity of the control interfaces. The Y-tail extends its vertical tail below the fuselage which can restrict the rotation during take-off and landing [58]. For this, longer landing gear legs are required, which increases the total mass and also negatively affects ground stability. The H-tail and U-tail are more vulnerable to flutter, which needs to be counteracted with much heavier structures [58].

The configuration with a canard and vertical stabilisers positioned at the wingtips is a favourable configuration when considering the interference with the BLI system. This is because there is no surface in front of the BLI propulsor, so the propulsor can ingest the boundary layer in the most effective manner. However, the disadvantages in this configuration outweighs the improved effectiveness of the BLI propulsor. The main disadvantage being that the canards tend to have a shorter moment arm leading to a larger surface, increasing the structural mass [58]. Furthermore, the canard configuration requires a higher take-off airspeed, increasing the take-off distance [58]. The vertical stabilisers located at the wingtips are unfavourable for the CNA which has foldable wingtips. The stabilisers and the control surfaces added on the wingtips will require the hinges to be extremely strong, also making the folding procedure more energy

intensive. Furthermore, the control surfaces need to be placed on a mechanism that have a chance to fail, making it relatively less reliable than other configurations.

The T-tail configuration was selected as the tail layout of the CNA. It allows the horizontal tail to be placed at a sufficiently high position, free from the wing wake and the engine exhaust. The T-tail also allows the horizontal tail to have a relatively smaller area, due to its increased moment arm with the sweep of the vertical tail. One of the challenges in designing a T-tail is its decreased torsional rigidity, which requires the structures to be stronger and thus heavier. Furthermore, the higher position of the tail makes it vulnerable to "deep-stall". This is the phenomenon where the horizontal tail lies inside the wing wake during stall and post stall, which severely diminishes the elevator's ability to recover from stall. This risk can be mitigated, however, by adopting "stick-shakers" or "stick-limiters", as most commercial transport aircraft with T-tails feature today [58].

10.3. Determination of CG range

The main function of the horizontal and vertical tail is to provide stability and control. Hence the driving factor in the design of the empennage structure is the location of the centre of gravity (CG) of the aircraft and how much it moves during its normal operations. The CG can move in multiple directions, but especially in the longitudinal direction. The main contributors of the CG movement are the decreasing fuel mass throughout the flight, the arrangement of the passenger seats and the mass distributions in two cargo holds inside the fuselage. The aircraft mass can be broken down into 3 components, the OEW, the payload mass, and the fuel mass.

10.3.1. Determination of the CG of OEW

In all flight conditions, the OEW and its CG location stay the same. The CG of the OEW was determined by breaking down the OEW into smaller weight components, and estimating their CG locations. The OEW can be broken down into the airframe structure group, propulsion group, airframe services and equipment group, and the operational items. Torenbeek offers a preliminary estimation method and a more detailed weight estimation method for each of the 4 components listed above [13]. The airframe structure group mass and the operational items mass were estimated with detailed sets of estimation methods, while the other 2 groups' masses were estimated using the more preliminary methods which often involve semi-empirical relations with a very few input parameters to estimate the entire group mass. There are weight groups that cannot be estimated using Torenbeek methods, as they are meant for aircraft with conventional configurations. The BLI system mass, which consists of the generators, the propulsor fan, the nacelle and the motors, was estimated separately in Section 9.11. The total masses and the approximate masses of all the components of the final design of the CNA can be found in Table 10.2.

The airframe structure group can be divided into 6 sub-components. The wing, the empennage, the fuselage body, the undercarriage, surface control group and the engine integration such as nacelles and pylons. The masses of the fuselage body (W_f), the wing (W_W), the empennage (W_h and W_v), and the undercarriages (W_{uc}) can be found in Section 6.6, Section 8.7, Section 10.9, and Section 11.5 respectively. For the first few iterations, not all detailed dimensions of the components were known, for example the tail planform. For such components, initial estimates were made, which were adapted through iterations. The CG position of the components were estimated as follows: the braced wing at its quarter chord of the mean aerodynamic chord (MAC), empennage at 37.1 m from the nose where the quar-

Table 10.2: Weight components and their CG locations measured from the nose

Component Name	**Mass [kg]**	**CG Location Measured From the Nose [m]**
Braced Wing	9236	19.3
Empennage	534	37.1
Fuselage Body	8948	21.3
Main Undercarriage	2523	24
Nose Undercarriage	452	3
Surface Control	1131	2
Engine Pylons and Nacelles	983	13.6
Propulsion Group	4342	13.6
BLI System	914	42.6
Airframe Services and Equipment	9955	21.3
Operational Items	2251	21.3
OEW [kg]	**41270**	**19.9**

ter chord of the vertical tail is positioned, fuselage body at half the fuselage length from the nose, and the nose and the main landing gears at 3 m and 24 m respectively from the nose.

The mass of the surface control group (W_{sc}) can be estimated with a very simple expression $W_{sc} = k_{sc} \cdot \text{MTOW}^{2/3}$, where k_{sc} is a factor of proportionality which is 0.6636. This mass estimation combines the control systems for manoeuvring, trailing edge flaps, leading edge flaps and spoilers. This does not include, however, the control surfaces themselves. The CG of W_{sc} was assumed to be at the centre of the cockpit, hence 2 m from the nose. The mass of the engine nacelles and the pylons (W_n) for aircraft with high bypass turbo fans can be estimated using a simple relation $W_n = 0.65 \cdot T_{TO}$ where both W_n and T_{TO} are denoted in N. The CG was estimated to be at the centre of the nacelle, which was located 6.64 m forward of the leading edge of the MAC. The weight components explained above are part of the airframe structure group (W_s), which can be expressed as $W_s = W_W + W_h + W_v + W_f + W_{uc} + W_{sc} + W_n$.

The propulsion group mass (W_{pg}) of a jet aircraft can be approximated with $W_{pg} = k_{pg} \cdot k_{thr} \cdot N_e \cdot W_e$ where N_e denotes the number of engines, and W_e denotes the mass per engine installed. There are two factors of proportionality, k_{pg} is 1.15 for jet transports with podded engines, and k_{thr} is 1.0 for aircraft that do not have thrust reversers. With the mass estimation of the engine in Section 9.11, W_{pg} was estimated to be 3970 kg, which includes the masses of the engines, gear boxes, power controls, and the fuel system. However, this does not include the mass of the BLI system, which is estimated in Section 9.11. So on top of 3970 kg, 372 kg to account for the BLI generators is added to the propulsion group around the engines. The CG of the propulsion group was assumed to coincide with the CG of the nacelle, while the CG location of the BLI system was assumed to be at the tip of the tail of the fuselage.

The airframe services and equipment mass (W_{se}) are estimated by using a typical average of medium range transport aircraft, which is 11% of the MTOW. This mass includes APU system, navigation instruments, hydraulics, EPS, electronics, and furnishings. The method of Torenbeek underestimates the furnishing weight by approximately 2/3 of reported weights [14]. Therefore, the furnishing mass W_{fur} was calculated with $W_{fur} = 0.196 \cdot W_{ZF}{}^{0.91}$, where W_{ZF} is the zero fuel weight, and half of that mass was added on top of the estimated W_{se}. Hence, the airframe services and equipment mass was estimated with $W_{se} = 0.11 \cdot \text{MTOW} + 0.5 \cdot W_{fur}$. The CG of this mass group was assumed to be at the middle of the fuselage.

W_s, W_{pg}, and W_{se} together form the empty weight mass. The OEW can be found by adding the operational items which consists of crew provisions, passenger cabin supplies, potable water and toilet chemicals, safety equipment and trapped fuel. These masses were estimated using Torenbeek's method, and were calculated to be 2251 kg in total. In the calculation, it was assumed that the numbers of flight crews, cabin crews and passengers were 2, 4, and 194 respectively. The CG of this mass group was assumed to be at the middle of the fuselage, since most of these items are spread around the cockpit and the cabin. Summing all these mass components results in an estimated OEW of 41270 kg.

10.3.2. Shift in CG with Payload and Fuel

Once the CG of the OEW was established, the CG range of the aircraft in its various flight conditions was determined. To compute and illustrate the shift in the CG, a loading diagram was produced shown in Figure 10.1. The aircraft with OEW is loaded with cargo, passengers on window seats, aisle seats, middle seats, and the fuel in that order, while the shift in CG is tracked every step. The CG shift from the fuel mass was considered at the last stage of producing the loading diagram, which is because the fuel mass is the only mass component that changes during flight. This allowed this loading diagram to depict the extreme CG positions at any condition of the flight. The CG of range of the aircraft was determined to be 18.9 m to 20.3 m from the nose, including a safety margin of 2% MAC to account for CG shifts on board. The forward CG position is the limiting constraint for sizing the tail for controllability, while the most aft CG position is the limiting case for stability.

10.4. Horizontal Tail Sizing

The horizontal tail provides longitudinal stability and controllability. The longitudinal stability can be achieved when the gradient of the pitching moment coefficient with respect to the angle attack (C_{m_α}) is negative. The limiting location of the CG (x_{cg}) from the nose can be expressed as Equation (10.1a). When x_{cg} is greater than this, C_{m_α} is positive and therefore the aircraft is unstable [**?**]. $C_{L_{\alpha_{A-h}}}$ and $C_{L\alpha_h}$ denote the lift coefficient derivatives of the aircraft less-tail and of the tail respectively. The subscript ac denotes the aerodynamic centre. The symbol l_t denotes the moment arm of the horizontal tail, $\bar{c}$ denotes the MAC, $\frac{d\epsilon}{d\alpha}$ is the downwash effect on the tail from the wing, and $\left(\frac{V_h}{V}\right)^2$ is the ratio between the velocities experienced by the horizontal tail and the wing. The CNA has a T-tail, hence $\left(\frac{V_h}{V}\right)^2$

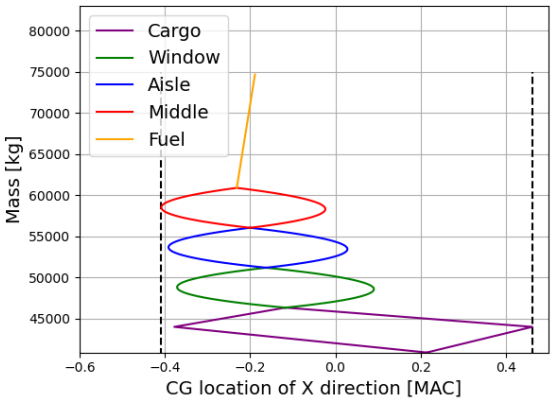

Figure 10.1: Loading diagram of the CNA

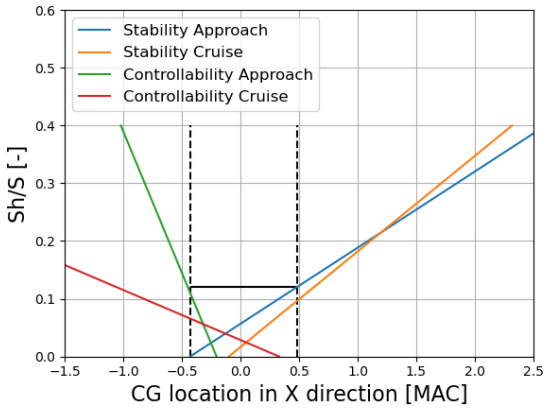

Figure 10.2: Scissor plot of the CNA

was determined to be 1 [**?**]. The term -0.05 accounts the safety margin of 5% of the MAC. The aircraft needs to be trimmable, meaning that the aircraft is adjusted in such a way that the lift forces correct themselves to maintain the set attitude without control inputs. This is achieved when the pitching moment coefficient (C_m) is zero. Similarly to stability, the limiting x_{cg} for controllability can be expressed as Equation (10.1b) [**?**]. $C_{m_{ac}}$ is the pitching moment coefficient around the aerodynamic centre, $C_{L_{A-h}}$ and C_{L_h} denote the lift coefficients of the aircraft less-tail and of the horizontal tail respectively.

$$\frac{x_{cg}}{\bar{c}} = \frac{x_{ac}}{\bar{c}} + \frac{C_{L_{\alpha_h}}}{C_{L_{\alpha_{A-h}}}} \cdot \left(1 - \frac{d\epsilon}{d\alpha}\right) \cdot \frac{S_h \cdot l_t}{S \cdot \bar{c}} \cdot \left(\frac{V_h}{V}\right)^2 - 0.05 \qquad \frac{x_{cg}}{\bar{c}} = \frac{x_{ac}}{\bar{c}} - \frac{C_{m_{ac}}}{C_{L_{A-h}}} \cdot \frac{S_h \cdot l_t}{S \cdot \bar{c}} \cdot \left(\frac{V_h}{V}\right)^2 \tag{10.1a,10.1b}$$

In both these equations, the area ratio between the horizontal tail and the wing ($\frac{S_h}{S}$) is the only variable that can be changed with design choice. Other parameters are set for each specific flight condition. These equations can be regarded as functions of $\frac{S_h}{S}$, and be plotted together to form a scissor plot. The generated scissor plot is shown in Figure 10.2, showing two sets of curves, one during cruise and another during approach.

There are several parameters that needed to be determined to create the scissor plot. The location x_{ac} was found by adding the contributions from the fuselage and the nacelles to the aerodynamic centre of the wing, which were all found using semi-empirical methods [13]. The method approximates the aerodynamic centre of the wing with AR, taper ratio, Mach number and sweep angle. The ratio $\frac{x_{ac}}{\bar{c}}$ during cruise was found to be approximately 0.4. However, the method was not compatible with low speed flight condition with an AR of 17, hence the $\frac{x_{ac}}{\bar{c}}$ during approach was approximated to be 0.3. This is slightly aft of the quarter chord, which is the approximate location of the aerodynamic centre for an airfoil at low speed, and adding slight contribution from the taper ratio and the sweep. The summation of the contributions on the $\frac{x_{ac}}{\bar{c}}$ from the fuselage and the nacelles were found to be -0.417 during cruise and -0.668 during approach. Adding these contributions to the aerodynamic centre of the wing yields the $\frac{x_{ac}}{\bar{c}}$ during approach and cruise to be -0.328 and -0.017 respectively. So the aerodynamic centre is always in front of the leading edge of MAC, and shifts slightly aft during cruise.

The $C_{m_{ac}}$, similarly to the x_{ac}, consists of contributions from different components of the aircraft. Namely from the wing, the struts, the fuselage, and additionally from the flaps only during approach, which were all found again using semi-empirical methods [**?**]. $C_{m_{ac}}$ was found to be -0.510 and -0.189 for approach and cruise respectively. Next parameter is $\frac{d\epsilon}{d\alpha}$. Typically, aircraft configurations with relatively high position of the horizontal tail, such as T-tail and cruciform, suffer less or do sometimes not have any influence from downwash. For the case of the CNA, however, it is a high-wing configuration meaning that the relative height difference between two surfaces are comparable to the downwash effect on a conventional tail on a low-wing aircraft. The $\frac{d\epsilon}{d\alpha}$ was found to be 0.186 through semi-empirical relations, involving the aerodynamic characteristics of the wing, and the relative position of the horizontal tail and the wing [**?**]. In reality, the downwash effect may be so small that it can be neglected, however by taking this into account the design becomes more conservative and hence safer.

The parameters $C_{L_{\alpha_{A-h}}}$ and $C_{L_{\alpha_h}}$ were determined using the DATCOM method as discussed in Section 7.3.2, according to the selected airfoils. Finally, the maximum C_{L_h} of the horizontal tail was estimated using $-0.35 \cdot \text{AR}_h{}^{1/3}$, where AR_h is the AR of the horizontal tail, and the maximum C_{L_h} was determined to be -0.505. During approach, which is the limiting case for controllability, the horizontal tail is likely to create more negative C_{L_h} to counteract the very high C_L. From this, $C_{L_{A-h}}$ during approach was found by subtracting C_{L_h} from the $C_{L_{\text{land}}}$. During cruise, it was assumed that the C_{L_h} was a relatively small negative number, so $C_{L_{A-h}}$ was assumed to be $1.1 \cdot C_{L_{\text{cruise}}}$. Using these parameters, the

scissor plot was drawn shown in Figure 10.2.

A smaller horizontal tail is favourable for the CNA. One reason is that generally smaller surface results in less mass, and therefore a lighter aircraft. Although the contribution of the tail mass to the OEW is relatively smaller to for example the fuselage, it still has approximately 15 kg per 1 m^2 according to the class II estimation from Torenbeek. Furthermore, the CNA employs a horizontal tail that is mounted on the vertical tail. This means that larger horizontal tail surface can lead to larger structure required on the vertical tail to maintain a sufficient torsional stiffness. In order to achieve smallest possible $\frac{S_h}{S}$, the wing position was shifted in such a way that the CG range comes around the intersection of the stability and the controllability curves. For the CG range determined with the loading diagram, this optimal position was found to be where the leading edge of the root chord was 13.2 m from the nose. With this wing position, the minimum $\frac{S_h}{S}$ ratio of 12% was achieved. This corresponds to S_h of 18.1 m^2, given the total lifting surface area to be 151.2 m^2. With this tail surface area and the location of CG during flight, the average C_{L_h} required during cruise was found to be -0.11. This was found using Equation (10.1b) with x_{cg} as the average average CG location in the range.

10.4.1. Verification, Validation and Sensitivity Analysis

Two Python codes and one Excel spreadsheet were used in the design of the horizontal tail. One code to draw the loading diagram and to identify the CG range, another code to draw the scissor plot, and the spreadsheet to perform the Class II weight estimation. All these tools were verified using unit tests and system tests. The loading diagram and scissor plot codes were verified by comparison with hand calculations, since they do not involve complex calculation. The class II weight estimation tool was verified also through hand calculations, as well as system tests by changing the input parameter and checking that the OEW increases or decreases correspondingly. Validation was carried out on the class II weight estimation by inputting the aircraft dimensions of the Boeing 737-200, assuming the same Mach number of 0.78. By plugging in aircraft data from a data base, and for some values computed or assumed, the OEW of the Boeing 737-200 estimated by the method was 27920 kg, while the OEW from the same data base is 27646 kg [59]. The relative difference is about 1%, which is the border line to assess if the iteration has converged or not. However, it was not possible to validate the braced wing mass estimation method, as there were no reference aircraft to validate its data with. The validity of the 70% weight reduction for a strut braced wing was not proved, since this method is most likely for smaller aircraft like the Cessna which may not accurately resemble the strut braced wing of the CNA. This can be validated by performing a detailed structural analysis on a larger strut braced wing, and another analysis on the same wing without the braces providing the structural support and compare the weights of those.

A sensitivity analysis was performed on all the tools that were used. There are variables that are likely to alter from reality, for example the gross shell area of the fuselage and the mass of an engine. Former because of its methodology of calculation, and latter because there may be a need to purchase engines off the shelf, that are lighter or heavier than calculated. When the gross shell area is increased from 512 m^2 by 2%, the OEW grows by 0.5%. Increasing the engine weight by 5% also increases the OEW by 0.5%. They may have a large impact on the convergence of the OEW, as it is said that the iteration converges when the OEW from the Class II weight estimation differs at most 1% from the input OEW. For the scissor plot, a change in the safety factor was considered. The maximum CG range accounts for 2% of MAC in both directions, and the stability curve has 5% of MAC as a safety margin. However the CNA has a relatively smaller MAC compared to other competitor aircraft, while having a similar overall size. For this sake, the scissor plot was produced with double the safety margins, which resulted in a 1% increase in $\frac{S_h}{S}$. This corresponds to an increase in 1.5 m^2 of horizontal surface, which can add approximately 23 kg more weight according to Equation (10.3), on top of the current size of the horizontal tail. From this analysis, it was discovered that the horizontal tail surface is sensitive to the safety margin of the CG range, which was calculated using multiple assumptions. The horizontal tail size may need to be increased to fulfil better reliability.

10.5. Vertical Tail Sizing

The vertical tail is the lifting surface responsible of the aircraft's yaw. It provides yaw control by the deflection of the rudder. In order to provide lateral stability and controllability, the vertical tail has to be sized for the worst case scenario during flight. Section 10.5.1 describes how the vertical tail is sized. Section 10.5.2 describes the verification and validation.

10.5.1. Sizing methodology

It is very complex at this stage of the design to make an accurate sizing of the vertical tail. Conversely to the horizontal tail sizing, the lateral stability and controllability of the aircraft cannot be decoupled. They are very dependent on each other, and detailed analysis requires aerodynamic derivatives which are difficult to estimate. However, for aircraft with wing-mounted engines, the critical design case for the vertical tail is the control after one engine failure at the minimum control speed in the air V_{MCA}, which is 1.2 times the stall speed at MTOW in clean configuration [13]. If the vertical tail is sized for this condition, then the lateral controllability and the stability of the aircraft are ensured. At the same time, the vertical tail size and mass have to be minimised in order to have a light design. A fast and reliable sizing procedure of the vertical tail is given by Torenbeek, which relies on Figure 10.3:

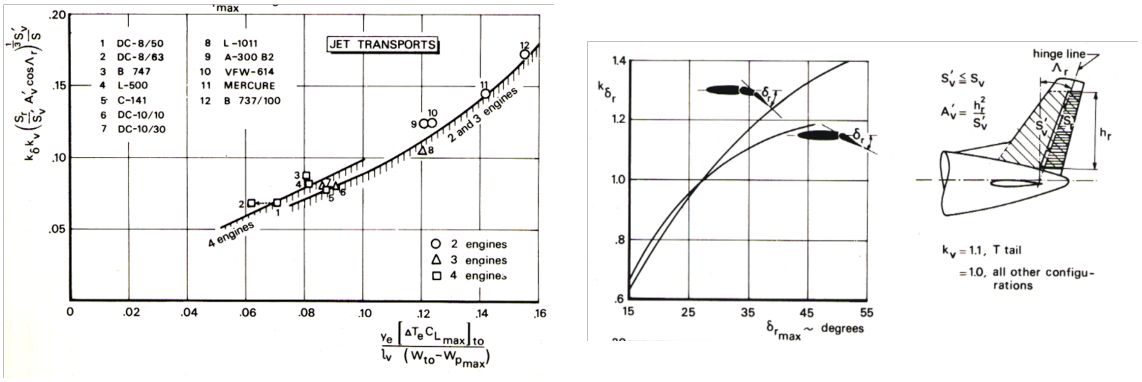

Figure 10.3: Rapid estimation of tail size for aircraft with wing-mounted jet engines [13]

On the left of Figure 10.3, Δy_e is the moment arm of the operative jet engine, which produces ΔT_e amount of thrust at take-off. Since a larger arm increases the thrust moment and so the required vertical tail surface area and weight, it was decided to keep the engine as close as possible to the fuselage. Moreover, l_v is the vertical tail arm length which is multiplied by the difference between the maximum take-off mass W_{to} and the maximum payload weight $W_{p_{max}}$. The y-axis shows constants which can be taken from the graph on the right. The constant k_{δ_r} depends on the maximum rudder deflection, which is typically 25° hence $k_{\delta_r} = 0.95$. The constant k_v depends on the tail configuration: since the configuration is the T-tail, $k_v = 1.1$. The aspect ratio A'_v and the vertical tail sweep angle are defined in Section 10.6.2. With all the values given, it is possible to get the vertical tail surface area S'_v.

The calculation of S'_v is of primary importance to understand whether the selected airfoil in Section 10.6.1 is able to provide the necessary lift coefficient for the one engine inoperative case scenario (Figure 10.4), where the vertical tail has to counteract the thrust moment at zero sideslip angle. Rudder deflection is assumed to be zero. From Figure 10.4, the equation of motion can be derived, where N_{cg} is the moment around the z-axis, L_v the vertical tail lift, T_R and Y_T the thrust arm and level, ρ the sea level density and C_{L_V} the vertical tail lift coefficient. By solving the equation of motion for L_V, it is possible to know the required C_{L_V} for the given surface area. Table 10.3 shows the results of the sizing process.

$$\sum N_{cg} = 0 \qquad T_R \cdot Y_T + L_V \cdot l_v = 0 \qquad L_V = \frac{1}{2}\rho V_{MCA}^2 S_V C_{L_V} \qquad \text{(10.2a,10.2b,10.2c)}$$

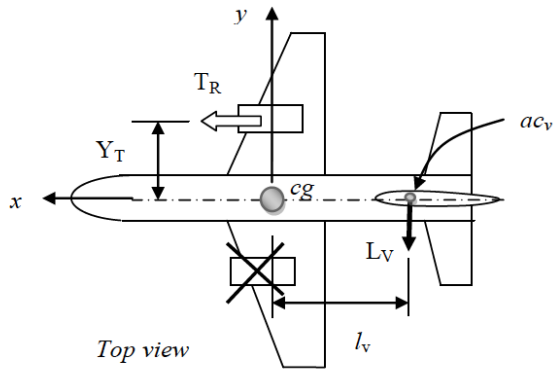

Figure 10.4: One engine inoperative case [60]

Table 10.3: Results for Vertical tail design

Parameter	Symbol	Value	Unit
Vertical Tail Arm	L_v	18.1	[-]
Rudder Surface to Vertical Tail Surface Ratio	$\frac{S_r}{S_v}$	0.4	[-]
Rudder Chord to Vertical Tail Chord Ratio	$\frac{C_r}{C_v}$	0.3	[-]
Thrust of One Engine at V_{MCA}	ΔT_e	63,341	[N]
Thrust Arm	y_e	6.39	[m]
Surface Area	S_v	16.57	[m^2]
Lift coefficient in OEI case	C_{L_V}	0.177	[-]

10.5.2. Verification and Validation

The sizing process of the aircraft was carried out with a python program where the analytical calculations from the Torenbeek method were applied. On the other hand, it was not possible to reproduce a formula for the left graph of Figure 10.3, therefore the value on the y-axis was found by inspection. For verification, unit tests were performed as well as hand calculations to check whether the program outputs were correct.

For validation, the dimensions of the vertical tail with respect to the aircraft were compared to reference aircraft which are chosen based on payload. The reference aircraft are shown in Table 10.4. As it can be seen, the vertical tail arm is comparable to the other aircraft, however the overall dimensions of the tail are significantly smaller than the competitors', as the other values show. One reason could be that the aircraft has a very large wing surface area compared to the overall dimensions of the aircraft. Furthermore, the engine lateral placement plays a big role in the vertical surface area; if the engines are placed further from the fuselage, then the thrust moment is larger hence the required vertical tail surface area increases.

Table 10.4: Results for validation of vertical tail

Aircraft	$\mathbf{L_v/L_f}$	$\mathbf{S_v}$ **[m^2]**	$\mathbf{(S_v \cdot L_v)/(S \cdot b)}$	$\mathbf{S_v/S}$
CNA	0.43	16.57	0.039	0.11
E195-E2	N.A.	16.2	N.A.	0.16
A320-200	0.34	21.5	0.065	0.18
B737-800	0.47	23.13	0.096	0.19
B757-200	0.40	34.37	0.093	0.19
Tu-204-120	0.47	34.2	0.101	0.19

10.6. Aerodynamic Design

The aerodynamic design of both the horizontal and vertical tail is critical for their respective performance. Along with that, the tail also adds toward the wetted area of the aircraft, hence drag. Thus, it is important to minimise the drag contribution from the empennage, while achieving the required performance. This section gives detailed descriptions about the different design choices made for the aerodynamic design of the tail.

10.6.1. Airfoil Selection

The horizontal and vertical tail surfaces are lifting surfaces. Thus, special consideration is required regarding the airfoil selection for the tail sections. Before selecting a suitable airfoil, all the desired features for both the tail sections were identified. First is the high lift curve slope ($C_{L_{\alpha_h}}$), which allows for a smaller tail to achieve a required C_L. Second is the low zero lift drag (C_{D_0}), as it contributes towards overall efficiency of the whole aircraft. Third is the high stall angle, as it ensures that the aircraft is controllable even if the main wing is stalled. And finally, the tail should be free of compressibility effects, as these effects contribute significantly towards the drag and effectiveness of control surfaces. Since both tail sections have control surfaces, they need to produce both positive as well as negative lift. Thus, only symmetrical airfoils were considered for the design, as they are most optimal when lift is required in both positive and negative direction. After identifying all the required features and applying the constraint of symmetric sections, a trade off was conducted for both tail sections, to select the most effective airfoil. The methodology of the trade-off followed was the same as the one for the main wing, described in Section 7.3.1. As a result of the trade off, the NACA0009 airfoil was found best suited for horizontal tail, whereas for vertical tail NACA63012 was chosen. The main reason that the two airfoils are different is due to the structural integration. The vertical tail needs to support the horizontal tail and the corresponding actuation lines for the elevator, thus a higher thickness is requires as compared to the horizontal tail.

10.6.2. Planform Design

The planform area of both the tails are governed by the stability and controllability constraint for the aircraft, as shown in previous sections. However, other planform parameters such as the aspect ratio, taper ratio, sweep angle and incidence angle, are design choices. The main governing factors driving these design choices were minimum drag and minimum weight. The different design choices made for both the tails are explained as follows.

The first parameter is the aspect ratio. The aspect ratio for the tail is defined in a similar way as for the main wing, described in Section 7.4. The aspect ratio directly affects the lift slope of the tail in a positive manner. However, since the selected tail configuration is a T-tail, high aspect ratio for horizontal tail (AR_h) implies higher weight for the vertical tail and empennage, since higher loads need to sustained. On the same hand, the vertical tail aspect ratio (AR_v) should be selected such that the horizontal tail can easily be mounted on it. Thus, in order to select the feasible design choices, initially, data from aircraft with similar configuration was retrieved [12] [13]. Further, doing iterative calculations between aerodynamic performance and structural performance, the final values for both the tails were selected.

The second parameter is the taper ratio. The taper ratio is mainly implemented to achieve an elliptical lift distribution and to minimise the structural weight. For tail, the elliptical lift distribution is not necessary, however, the weight effect is important, especially since the tail configuration is a T-tail. For vertical tail, the taper ratio is selected such that the weight is minimised, given the constraint that the horizontal tail can still be mounted at the tip end. Similarly, for the horizontal tail, the minimum weight was the main driving factor for the taper ratio value. For both the tails, multiple iterations were performed to ensure that the required area for the control surfaces (elevator and rudder) is still sufficient after changing the respective taper ratio values. Consequently, the final choices were made for both the tails.

The third parameter is the sweep angle. The sweep is implemented to ensure that the compressibility effects, mainly wave drag , do not occur. As a general rule, it was found out from literature that the critical mach number of tail should be slightly higher than the main wing, to ensure that aircraft is completely controllable [61]. In order to find the required sweep angle, the critical mach number of the airfoil was evaluated using XFLR5 [1] and the required sweep was found using the relation shown in Equation (7.6).

The final parameter is the incidence angle. For the horizontal tail, this angle ensures that no elevator deflection is required to have stability at trim conditions during cruise. Thus, it is directly based on the required lift coefficient from the horizontal tail during cruise (C_{L_h}). For the vertical tail, this angle was set to zero. This was done to maintain the symmetry across the x-z plane of aircraft (looking at the aircraft from the top view). This ensures that the vertical tail is not required to produce any lift to maintain directional trim in nominal flight. The final results for all the different planform parameters chosen for both the tails are shown in Table 10.5.

Table 10.5: Final results for planform design of both tails

	Aspect Ratio	**Taper Ratio**	**Leading Edge Sweep [deg]**	**Incidence Angle [deg]**
Horizontal Tail	3	0.85	35	-1.9
Vertical Tail	1.1	0.8	30	0

10.6.3. Other Aerodynamic Considerations

The tail configuration of CNA is a T-tail, as mentioned earlier. This configuration comes with a number of additional aerodynamic effects, compared to conventional tail configuration. Some of these effects are beneficial for the aircraft's overall performance whereas others have a negative impact. Therefore, it is important to consider these additional effects to eliminate any potential limitation of the design.

The first effect is the effect of the wing downwash. Since the horizontal tail is placed considerably above the wing plane, the downwash from the wing does not affect the horizontal tail's performance, making it more effective. On the other hand, at very high angle of attack (near or above stall angle), the situation is opposite. At these conditions, the horizontal tail intersects with the wake from the main wing, making the aircraft uncontrollable with respect to the elevator. This phenomenon is known as deep stall. It is often considered very critical for T-tail designs, as it can lead to potential safety concerns. Therefore, the tail configuration of the CNA was analysed to have an estimation of when this effect happens over the tail.

The design was studied using an OpenVSP simulation, as explained in Section 12.1. It was found out that the tail is only affected by the downwash around an angle of attack of 14° as shown in Figure 10.5. This angle is lower than the stall angle of the main wing. Therefore, there is a risk that the aircraft can get into a deep stall. However, since 14° is a very steep angle for the flight, there is a lower chance this will occur. Moreover, in order to further mitigate this risk, different pilot alert systems such as stick shakers or audio warning systems can be added to avoid the aircraft reaching

[1] URL `http://www.xflr5.tech/xflr5.htm` cited [29. May 2020]

near stall attitudes. It is thus recommended to further look into these systems and to determine the tail interaction in downwash using more advanced simulations, for the upcoming phases of the project. Nevertheless, the results of the analysis performed at this stage ensures that this will not lead to a potential limitation for the design.

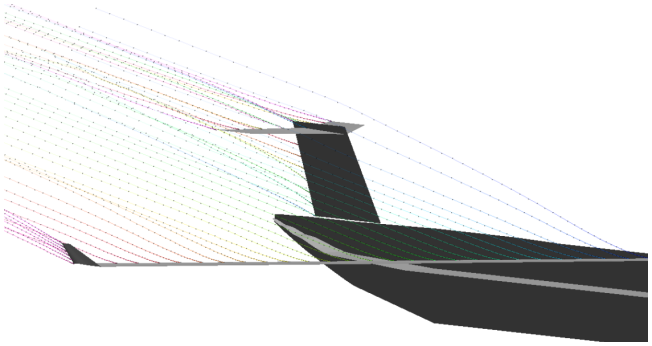

Figure 10.5: Downwash effect on tail at 14° angle of attack

The second important effect is the end plate effect. It is known that an end plate, present on a lifting surface, improves the lifting surface characteristics due to the reduction of tip vortices [32]. Winglets are an example of such effect. For the vertical tail, which is a lifting surface during manoeuvre, the horizontal tail acts as an end plate. Thus, in order to produce the same lift force, smaller area is needed. In order to take this effect into account, accurate flow simulations are needed. Hence, this effect is not considered during the design of vertical tail. However, this will not influence the performance of vertical tail, but in fact will ensure an additional margin due to slight overestimation.

10.7. Control Surfaces and Actuation

The CNA has various movable surfaces for manipulating the aerodynamic forces acting on the lifting surfaces. These include the high lift devices and the control surfaces. These surfaces will be actuated using electrohydraulic actuators powered by electrical motor pumps, similar to the Boeing 787[2]. As mentioned in Section 9.12, the CNA is installed with 3 electrical motor pumps, while only 2 of them are needed to have a full control over the aircraft. The redundant pump increases the reliability of the aircraft, since a complete loss of control of the aircraft that can lead to a catastrophic failure requires two motors to fail simultaneously. For the current stage of the design, the hydraulic circuits are laid out so that there is one circuit that controls the movable surfaces on the right side of the aircraft, and another that controls the left side. Both of them are connected to the rudder in a parallel manner. Lastly, one redundant pump circuit connects to all the control surfaces on the CNA and takes over the control in case one pump fails. The circuit scheme is visualised in Figure 10.6.

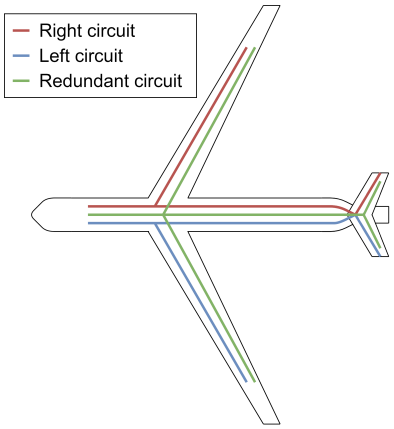

Figure 10.6: The hydraulic circuit layout of the CNA

There may be a more weight efficient scheme with shorter circuit lengths, or a more redundant scheme that allows the aircraft to be safely controllable with only one of the three pumps like the A320. This is achieved by independently connecting all three circuits to the surfaces to control the aircraft in all three axes [62]. However, that requires more details about the movable surfaces themselves such as the power required or the control derivative (such as p_{δ_e} for

[2]URL `https://janes.ihs.com/Janes/Display/jawa5814-jawa` cited [27. June 2020]

ailerons) per section of that control surface. These have not yet been designed, and it is recommended in the further design processes to size the remaining movable surfaces, such as the elevators, the spoilers, and the horizontal stabiliser if it is later decided to adopt an adjustable stabiliser. Then, with the knowledge of the required torque and power, a more weight efficient architecture of the hydraulic circuits can be designed that allows more redundancy.

10.8. Structural Integration

The T-tail is one of the popular tail configurations employed by commercial aircraft, thus the integration to the fuselage can be considered as safe-and-tried. However for the case of the CNA there are notable changes around the tail, namely the BLI propulsor at the back. These components do not have any physical interference, but the loads from these two components on the fuselage integration must be considered at the same time.

The total mass of the BLI system attached at the aft of the fuselage is approximately 1000 kg. Normally, the tail cone will only experience load through the horizontal tail or the vertical tail. For example the horizontal tail produces a lift force of about 24 kN during approach. With the weight of the BLI system, this load increases to about 34 kN which is 40% more than the aircraft without a BLI system. On top of that the tailcone is loaded by the weight of the BLI system, which is about 10 kN. The structure of the tailcone needs to be significantly stronger than average T-tail aircraft. Furthermore, with the BLI system integrated at the rear of the fuselage, there may be need for extra cutouts inside and outside of the fuselage structure for maintenance accessibility. These cutouts act as weak points of the structure, which is loaded by the weight of the BLI. When there is a cutout present on the bottom side of the fuselage near the tail, the surface can experience serious compressive load and become more vulnerable to buckling. The BLI propulsor also produces a thrust force, compressing the tailcone structure even more. When further developing this concept, extra attention is required in the placements of the cutouts and reinforcement of the tailcone.

10.9. Mass estimation

The tail group mass can be divided into two masses. Horizontal tail mass can be estimated using Equation (10.3) [13]. The subscript h denotes the horizontal tail. The same equation can be used to estimate the vertical tail mass by replacing the subscript h with v. The tail surface weight (W_h or W_v) can be estimated using the factor of proportionality (k_h or k_v), tail surface area (S_h or S_v), dive velocity in EAS m/s (V_D), and the sweep of the tail surface (Λ_h or Λ_v). The parameter k_h is 1.0 assuming a fixed stabiliser and k_v is $1+0.15\cdot\frac{S_h\cdot h_h}{S_v\cdot b_v}$ for vertical tail mounted horizontal tail (T-tails and cruciform tails). The rest of the right hand side can be found graphically, using Figure 10.7. The tail sizes were not yet determined, which requires the range of CG of the aircraft. Therefore, at the very early stage of iteration, S_h and S_v were assumed to be approximately 30 m^2 and 20 m^2 respectively. Through iterations, S_h, S_v, Λ_h, Λ_v, and V_D were designed to be 18.1 m^2, 16.6 m^2, 35°, 30° and 156.7 m/s respectively. This resulted in the horizontal and the vertical tail masses of 262 kg and 272 kg respectively. The CG of the tail group was estimated to be 37.1 m, leaving sufficient space for the BLI propulsor at the back.

$$\frac{W_h}{S_h} = k_h \cdot f\left(\frac{S_h^{0.2}\cdot V_D}{\sqrt{\cos\Lambda_h}}\right) \tag{10.3}$$

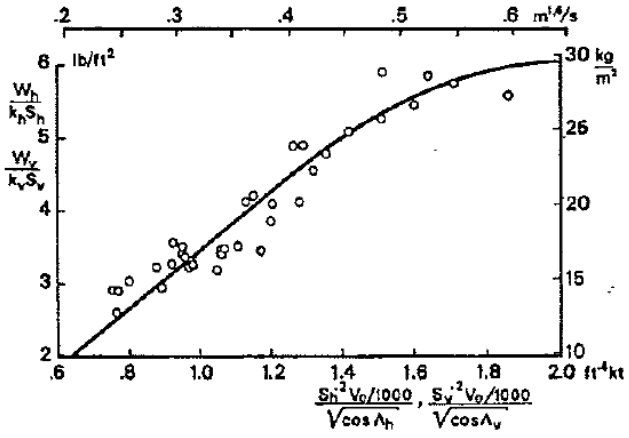

Figure 10.7: A semi-empirical relation between the horizontal tail planform and its mass [13]

10.10. Flight Control Systems

In order to guarantee a safe and efficient flight, the CNA has to be equipped with flight control systems, which enable the pilot to interact with the aircraft subsystems. The control of the aircraft attitude, the flight trajectory and the mission profile can be done by means of the FBW (Fly-By-Wire, or primary flight control), the AFDS (Autopilot Flight Director System) and the FMS (Flight Management System). Figure 10.8 provides a schematic overview of the flight systems architecture.

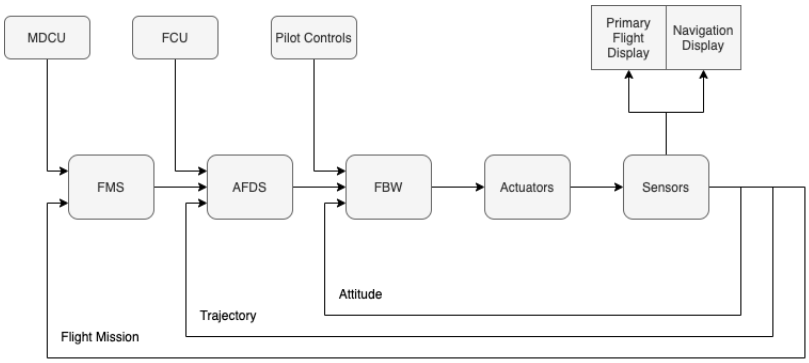

Figure 10.8: Flight control systems architecture

The FBW is concerned with the control of the attitude of the aircraft. It takes as inputs the pilot controls and, via aircraft dynamics, determines the aircraft response to the manoeuvre throught the flight envelope. To ensure harmonic control of the aircraft, sensors are used to measure the aircraft response, which then send the measurements back to the FBW. The aircraft attitude is also shown in the primary flight display and the navigation display.

The ADFS performs additional control loop closure to control the aircraft trajectory. It controls the speed, the heading and the altitude at which the aircraft flies. Depending on the flight phases, several flight modes are presented. For example, during the landing phase the ILS (Instrument Landing System) and MLS (Microwave Landing System) can be used. The control and indication associated with these multiple autopilot modes is provided by a Flight Control Unit (FCU) which allows the selection of the flight mode and also provides information on whether the selected flight mode is operated correctly. The final outer loop closure is controlled by the FMS. It performs the operations regarding navigation, ensuring that the FBW and AFDS systems are positioning the aircraft at the correct point in the sky which should coincide with one of the multiple waypoints that characterise the aircraft route. The pilot interfaces with the FMS via a Multifunction Control and Display Unit (MCDU).

Regarding the CNA, the mass of the flight control system was implicitly taken into account during the Class II weight estimation in the surface control group (W_{sc}). However, further analysis is necessary. In particular, the mission profile has to be analysed further in order to better estimate the avionics architecture and subsequently the power required from the EPS.

11
Landing Gear Design

This chapter describes the design choices made and the outcomes of the processes in designing the landing gears of the CNA. The objectives and requirements are discussed in Section 11.1, the design choices on the positioning are discussed in Section 11.2, the structural design is reported in Section 11.3, and the retraction scheme of the gears are explained in Section 11.4. The mass estimation is performed in Section 11.5, and finally the recommendations for further designs are discussed in Section 11.6.

11.1. Objective and Requirements

The CNA's landing gear has been designed to fulfil ground stability and controllability requirements, as well as to withstand structural load during landing. As the design of the other components of the aircraft were drawn out in more detail, it was seen that the conventional tricycle landing gear configuration is not the best configuration to make the most out of the BLI system of the CNA. The CNA employs 1 nose landing gear with 2 tires, 2 main landing gears and 2 supporting landing gears attached on the struts as shown in Figure 11.1. The motivation of adopting this configuration is explained in Section 11.2.

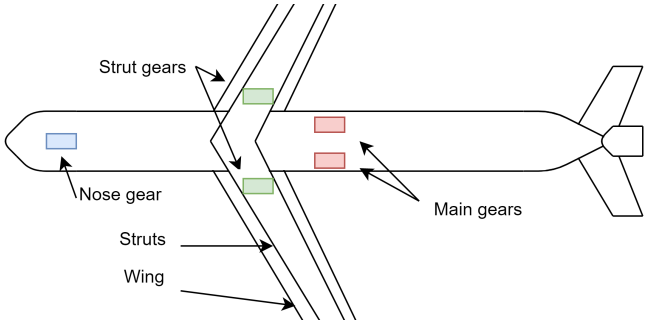

Figure 11.1: The positions of the nose landing gear, the main landing gears and the strut landing gears of the CNA

11.2. Positioning of the Landing Gear

There are three main constraints when positioning the landing gears in a conventional tricycle configuration, which some of them were difficult to meet for the case of CNA without affecting its performance. First, the nose landing gear shall carry a specific range of load to allow for steering force while not overloading it. Typically, a nose landing gear carries 8% to 15% of the MTOW [13]. Next to that the landing gears shall have lateral stability on the ground during sharp turns. Lastly, the main landing gears need to have a sufficient height so that the aircraft fuselage does not touch the ground during take-off and landing.

One special feature of the CNA that hinders the landing gear position is the BLI propulsor located at the aft tip of the fuselage. The maximum angle the aircraft can pitch during take-off without scraping the body of the aircraft is the scrape angle, and the lift-off pitch angle (θ_{LOF}) must not exceed the scrape angle. θ_{LOF} can be found for an aircraft using Equation (11.1), where the first term is the angle of attack needed for take-off and the second term is a correction term to account for the rotation of the fuselage right after lift-off [13]. $\frac{d\theta}{dt}$ is the rate of rotation of the aircraft during lift-off, which is about 3-4°sec for large transports and 4-5°sec for small transports [13]. For the case of CNA which is not as large as a Boeing 747, for example, 4°sec was used. The sum of ℓ_1 and ℓ_2 is the shortest distance between the bottom of the main landing gear and the point of ground contact, while the ℓ_1 accounts for the change in this length caused by deflection of the tire and the gear strokes when in standstill. ℓ_1 was assumed to be zero in Equation (11.1), since this length was found to be an order of magnitude smaller than $\ell_1 + \ell_2$ even when considering the maximum deflection of the tire during hard landing. Ideally, the landing gears are positioned such that the scrape angle is just slightly larger than θ_{LOF}. This allows maximum use of the volume of the fuselage around its tail. This means that θ_{LOF} is dependent on ℓ_2, which is also dependent on θ_{LOF}. So θ_{LOF} was found iteratively every time the main landing gear position was adjusted. Finally, the θ_{LOF} of the CNA was calculated to be 12°

$$\theta_{\text{LOF}} = \alpha_{\text{LOF}} + \frac{d\theta}{d\text{t}} \cdot \left(\frac{2 \cdot \ell_1}{V_{\text{LOF}}} + \sqrt{\frac{\ell_2 \cdot C_{L_{\text{LOF}}}}{g C_{L_\alpha}}} \right) \qquad \text{where} \quad \alpha_{\text{LOF}} = \frac{1}{C_{L_\alpha}} \left(C_{L_{\max}} - C_{L_{\text{cruise}}} - p \cdot C_{L_{\text{TO}}} \right) \tag{11.1}$$

A problem arose here, which is that the scrape angle of the CNA cannot be changed. Aircraft without a BLI propulsor can adjust its scrape angle easily by modifying the fuselage tail shape. However, this was not a viable option as the scrape angle of the CNA was defined by the BLI propulsor fixed in one place, which effectively elongates the fuselage. This requires the gear legs to be relatively longer, which would most likely require fairings when retracted. The fairings will disturb the flow around the fuselage ingested by the BLI, diminishing its effectiveness. This was solved by adding another set of landing gears on the struts. The main function of them is to provide lateral stability during landing and while stationary. This enabled the main gears to be positioned closer to the fuselage centre line, that does not require large fairings.

During landing, the main gears and the supporting gears need to touch the ground simultaneously to also provide better lateral stability. Hence, telescopic landing gears were employed on the strut gears allowing them to extend so that all four gears touch down at the same time. The supporting gears are positioned inside the inboard portion of the struts, which extends horizontally out from the bottom of the fuselage. The longitudinal position of the strut gears is 16 m from the nose. In order to minimise the required extension of the strut gears, the main gears were positioned as forward as possible, at 20.5 m from the nose. This landing gear position still allowed the CG to be always forward of the main gear with respect to the ground, even when the aircraft is at θ_{LOF} during take-off. With these positions, the strut gears need to extend their legs by about 0.73 m, when assuming the pitch angle during touch down is about 8° similar to the A320 family [63]. This means that the minimum required length of the cylinder of the telescopic strut gears is 0.73 m. The extensions of the strut gears may also be used during take-off to aid the aircraft to pitch up and lift off. However, this requires much more energy than when extending the leg during landing, as the gears need to lift up the entire aircraft weight. This may rise a need to increase the power budget, since electrical power is also used by the control surfaces such as the HLDs and elevators. At this stage of the design, the strut gears are not designed to extend their legs during take-off, but only during landing.

Due to the introduction of the support from the gears, the load carried by each gear cannot be controlled with only their positions, since this is a statically indeterminate system. However, the nose landing gear still needs a specific range of loads to carry as mentioned previously. This can be solved by adjusting the stiffness of all the gears, such that when all gears have the same lengths of 2 m from the bottom of the fuselage, desirable load is carried by the nose gear. In the further design stage, it is recommended to adjust the relative stiffnesses, or consider employing hydraulic springs that are able to control their stiffnesses on either of the legs.

11.3. Structural Design

The critical load case of the main landing gears is hard landing, where they must absorb the shock from the impact. The CNA has a MTOW of 70 tonnes, for similar weight class aircraft such as A320 and Boeing 737, the main landing gears typically consist of 2 legs with 2 tires on each leg. The CNA will have 2 main landing gears with 2 tires on each leg, which are relatively positioned close to each other to allow for more space efficient shorter legs.

Aircraft main landing gears are typically compatible with different types of tires, adjusted depending on the condition of the runway of the airports. For example, A320-200 with the configuration of maximum ramp weight of 75900 kg has 4 different compatible tires, varying in both their pressure and their dimensions. The CNA is designed to also be compatible with different tires, but for the sake of simplicity the main landing gear was designed with one specific type of tire available off the shelf. The selected tire has a size 46x17-20 (46 inch diameter, 17 inch wide, and the centre hole with 20 inch diameter) and a pressure of 13.8 bar, identical to the tires of the A320-200 with a ramp weight of 75900 kg, operating with the highest tire pressure [9]. Higher pressure would mean that the tire deflections are smaller, meaning that with this tire the largest required shock absorber stroke can be determined using Equation (11.2).

$$E = \frac{\text{MLW}}{2} \cdot w^2 = N_{sa} \cdot P_{sa} \cdot \lambda_{\text{LG}} \cdot (\eta_t \cdot S_t + \eta_{sa} \cdot S_{sa}) \qquad \text{where} \quad S_t = \frac{\lambda_{\text{LG}} \cdot L_{\text{wheel}}}{p \cdot \sqrt{D_t \cdot b_t}} \tag{11.2}$$

E denotes the energy absorbed by the shock absorbers simply derived from $E = \frac{m \cdot V^2}{2}$. w is the ultimate descent velocity which can be approximated with $w = 0.9 \cdot (W/S)^{0.25}$ where W/S is the wing loading in kg/m^2, N_{sa} is the number of shock absorbers per leg, P_{sa} is the static load per leg, λ_{LG} is the ratio of maximum load to static load per leg, η_t and η_{sa} are the energy absorbance efficiency factors of the tires and the shock absorbers respectively [13]. As the CNA is em-

ploying oleo-pneumatic shock absorbers, η_t and η_{sa} are taken to be 0.47 and 0.8 respectively [13]. Oleo-pneumatic shock absorbers allow for a shorter minimum required leg length, resulting from their high shock absorbance efficiency. S_t and S_{sa} are the maximum tire deflection and the minimum required shock absorber stroke in m respectively. S_t can be approximated with the expression on the right [13]. L_{wheel} is the maximum static load in N on each tire, p is the pressure of the tire in Pa, D_t and b_t are the diameter and the width of the tires in m respectively. λ_{LG} was assumed to be 2.0, which is the lowest value of the typical range of 2.0 to 2.5, in order to compute the maximum possible deflection required [13]. S_t was approximated as 0.32 m, assuming 4 main gear wheels are supporting about 92% of the aircraft mass on the ground hence L_{wheel} of $0.23 \cdot \text{MTOW} \cdot g$. w was calculated to be 4.2 m/s, N_{sa} is 1, and P_{sa} of 92% of MLW, assuming a touch down with only one leg. Finally, S_{sa} was found to be 0.42 m.

The diameter of the cylinder (D) of the main landing gear legs, which will employ a telescopic landing gear that allows to be shortened while it is retracted, can be calculated using a semi-empirical relation of $D = 1.3 + 0.11 \cdot \sqrt{P_s}$ where P_s is the maximum static vertical load per leg [13]. The landing gear cylinder diameters of the main landing gears was determined to be 21 cm, assuming the maximum static load per leg of 46% of the MTOW. The dimensions of the main gears discussed above are based on the case when the main landing gears are the only gears to touch down. However, the CNA also touches down with the strut gears that eases the load carried per leg. Therefore, these dimensions can serve as the upper limits, meaning that the main gears can be sized relatively smaller than presented above. More detailed design of both the strut gears and the main gears is recommended, which first requires a study of the load cases when the aircraft lands with the strut gears and the main gears simultaneously.

Landing gears are safe life components, they need to be replaced during maintenance after a certain number of flights. This also means that they need to have a high safety factor, compared to other aircraft components. For the landing gears of the CNA, the selected material is steel. Steel has a high ultimate strength that allows for a more space efficient gear, which is beneficial in eliminating the need for fairings. Steel is also a cheap material, compared to for example titanium. Furthermore, titanium is a very hard material that is difficult to shape and form, which makes the production more energy intensive.

11.4. Retraction and Extension

There are several ways the landing gears can be retracted into the fuselage. Typically for a high-wing aircraft, they rotate around an axis parallel to the fuselage. This is to extend the landing gear further to achieve a better lateral stability. This retraction scheme comes at a cost of requiring large lateral space inside the fuselage, which often requires fairings. If same scheme was to be employed by the CNA, fitting landing gear legs that can extend to 2 m out of the fuselage centre line, inside a 3.9 m wide space under the cabin is challenging without the use of fairings. Therefore, the main landing gears of the CNA are rotated around the axis perpendicular to the fuselage, like the nose landing gear, as shown in Figure 11.2. The red arrows indicate the direction the actuators are pulled, and how the main landing gears retract into the fuselage. This is feasible for the CNA, since there is no need to extend the legs so far from the fuselage centre line, as the supporting gears provide lateral stability. Furthermore, the fuselage has sufficient volume under the cabin where the main landing gears are retracted, which has enough clearance in the longitudinal direction.

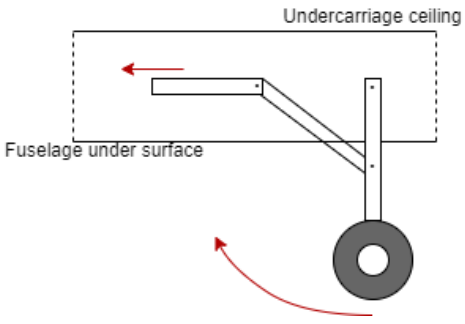

Figure 11.2: Sketch of the retraction mechanism of the main landing gear

The nose landing gear is retracted below the cockpit. The positioning of it in the longitudinal direction may be adjusted to fit its leg, which is slightly longer than that of similar aircraft. This shift in position does not influence the scrape angle, which is dominated by the height and the positioning of the main landing gear. However, this does affect the loads required to be held by the supporting gears to keep the load on the nose gear to be in the range of 8% to 15% of the aircraft mass. The supporting gears are retracted inside the struts, while the tire can be stored inside the fairing around the fuselage where the struts are attached.

11.5. Mass Estimation

Torenbeek's class II weight estimation method is used to estimate the mass of the undercarriage (W_{uc}). It can be estimated using the factor of proportionality (k_{uc}), the MTOW, and 4 empirically found coefficients (A, B, C, and D) [13]. k_{uc} is 1.08 for a high-wing configuration aircraft. The coefficients for the nose and the main undercarriages can be found in Table 11.1, which are typical values for a civil aircraft with retractable undercarriages. Given the MTOW of 70337 kg, the nose and the main undercarriages were estimated to have the masses of 452 kg and 2523 kg.

Table 11.1: Coefficients for undercarriage sizing [13]

Coefficients	Main Undercarriage	Nose Undercarriage
A	18.1	9.1
B	0.131	0.082
C	0.019	0
D	$2.23 \cdot 10^{-5}$	$2.97 \cdot 10^{-6}$

$$W_{uc} = k_{uc} \cdot \left(A + B \cdot \text{MTOW}^{0.75} + C \cdot \text{MTOW} + D \cdot \text{MTOW}^{1.5}\right) \tag{11.3}$$

However, the CNA has more landing gears than discussed above. The sizing method of the strut gears is not established, and the detailed functions of the supporting gears are still not completely designed. The nose landing gear and the main landing gears will need to carry relatively less loads than the conventional configuration, which might reduce structural components leading to a reduction in weight. Combining with the uncertainties of the details of the strut landing gears themselves, their masses were omitted in the weight estimation that was considered when assessing the performance of the aircraft. Hence the total mass of the undercarriage group was estimated to be 2975 kg. This assumption may lead to an underestimation in the OEW, which may affect the performance the whole aircraft. The most extreme expected increase is about 2500 kg, when assuming the main gears and strut gears have identical masses, while the main gears are sized without the strut gears in the design. This uncertainty, which could have been accounted for by for example assuming the strut gears to have the same masses as the nose gears, was only identified at the very late stage due to the time constraints. It is recommended to perform another set of iterations with a more conservative estimation of the undercarriage mass.

11.6. Recommendations

The landing gear is one of the many novel components of the CNA, which is at an especially young stage of development. One very important recommendation is to analyse the effect of the fairing on the boundary layer ingested by the aft propulsor, for example with a CFD analysis. If the main gear fairings have only a small effect on the performance on the BLI, then there is no need to opt for this novel configuration. The tricycle configuration is a safe-and-tried configuration, which may significantly cut down on the research and development cost. Once it has been confirmed that the fairings indeed disturb the boundary layer around the fuselage too much, then the design of this novel landing may be resumed. The landing scheme of the CNA with various conditions need to be first identified. This includes the level landing as considered in this design, as well as the lateral drift landing. Once that is established the strut gears and the main gears may be sized. The sizing procedure includes the adjustments in the stiffness of all the gears for the nose gear to carry the favourable amount of load for every scenario while on the ground. Then, the dimensions of the gears and the shock absorber stroke lengths of the main gears and the strut gears may be sized, based on the dimensions described in Section 11.3.

There are several aspects that could disprove the feasibility of this landing gear scheme, which needs more detailed design or analysis. The supporting struts were added to provide lateral stability, however this is not explicitly calculated for the CNA. It was assumed that having two pairs of legs at different positions from the nose provides enough stability that it will not tip over during sharp turns. However, there may be a need to further shorten the legs or to shift the supporting landing gear more outwards into the struts to improve the lateral stability. Lastly, the struts are not explicitly designed to take into account the loads from the supporting gears. The struts' main load case was the load induced by the lift force on the main wing, but the load case on the ground may be more critical with this configuration. The weight of the wing combined with the load carried by the struts can have large compression loads, which can cause buckling on such slender structures.

12
Aerodynamic Modelling and Noise

This chapter describes the final aircraft design and its characteristics. It describes models and the aerodynamic performance of the final design in Section 12.1. It then describes the final design's noise effects in Section 12.2.

12.1. Aerodynamic Performance Modelling

The various sub-systems of the aircraft, such as the wings, fuselage and empennage, have an influence on the aerodynamic characteristics of the entire aircraft. Thus, in order to assess the aerodynamic performance of the final design, aerodynamic models were used to estimate the crucial aerodynamic parameters. These aerodynamic parameters were the C_L, C_{D_i}, C_D and the $\frac{L}{D}$. The estimation of these parameters can be obtained using various methods depending on the required level of accuracy. For instance high-fidelity Computational Fluid Dynamics (CFD) software are capable of providing the highest level of accuracy, however, it comes with a significant cost of computational time and resources. This deems it "inefficient" to be used within a design loop where a fast computational time is desired. For relatively faster computations with reasonable accuracy, a more suited option was employed which was to make use of solvers based on the linear aerodynamic theory (Potential Flow). For this purpose the chosen software was OpenVSP which is an open-source code developed by NASA that utilises linear solvers in the form of the Vortex Lattice Method (VLM) or the Panel Method. The use of such methods is suitable for low Mach number flows, however, predictions for (transonic) compressible flows are still possible provided the assumption that no shock waves are present in the flow field. The chosen method to carry out the aerodynamic analysis was the VLM, which, as opposed to the panel method, can also provide the distributed lift loads on the wing which is very valuable for assessing the lift distribution and for structural calculations. The VLM was also used during the planform design, as addressed in Section 7.4, in order to assess the changes in the wing performance due to changing planform parameters. Figure 12.1 shows the model of the entire aircraft generated within OpenVSP. One thing to be noted for the OpenVSP model is that the BLI propulsor was not included. This was due to the fact that the BLI system was not finalised at the point when the aerodynamic modelling process was being carried out. However, in order to include the effect of BLI in the drag calculations, the effective area of the tail cone was increased. This led to an overestimation of the skin friction drag, which implicitly accounted for the drag of the BLI propulsor.

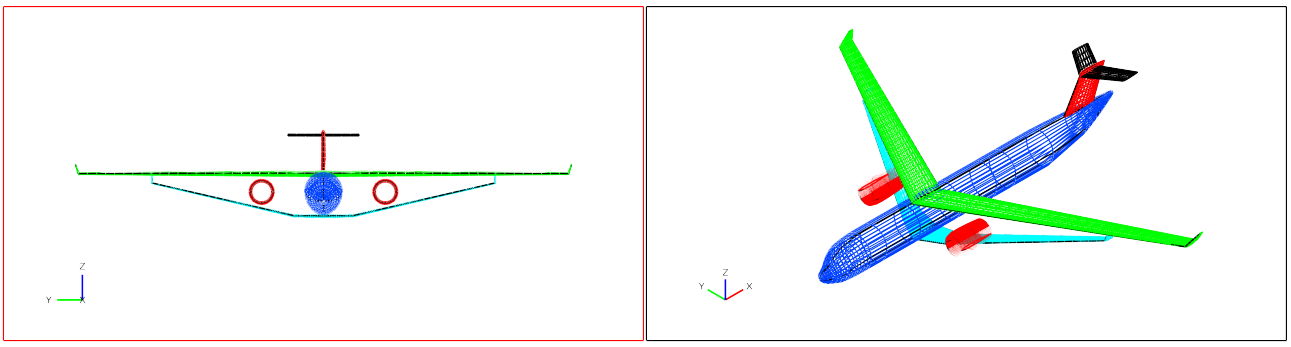

Figure 12.1: Model of the aircraft generated in OpenVSP

The generated model was fed into the VLM simulation in order to obtain the aerodynamic parameters. During this process it was however noted that the skin friction drag was very poorly represented by the VLM. In order to achieve a better estimate for the drag, another function called Parasite Drag was used, which is a function inside OpenVSP itself. The Parasite drag function uses the wetted area ratios of the defined geometry and statistical relations for laminar and turbulent boundary layers to predict the skin friction coefficient, C_f, for a given Reynolds Number. For laminar boundary layers, there is only one function that is used which is the Blasius equation given by Equation (12.1a) [1]. For turbulent boundary layers however, there are numerous relations available of which the most relevant for this design, given the high Reynolds numbers during flight, would be the High Reynolds Number Prandtl Power Law relation as shown in Equation (12.1b) [1].

$$C_f = \frac{1.32824}{\sqrt{Re}} \qquad C_f = \frac{0.0725}{Re^{1/5}} \tag{12.1a,12.1b}$$

[1] URL `http://openvsp.org/wiki/doku.php?id=parasitedrag` cited [12. June 2020]

The aerodynamic modelling first started by analysing the baseline aircraft. With the outputs of the baseline, the iterative design process was then initiated. As the design iteration progressed, the iteration changes were implemented into the OpenVSP model, and by using the VLM and the Parasite Drag calculator, the aerodynamic parameters were then estimated. The exact details of the iterations are explained in Chapter 4. After the convergence of the iterations, the aerodynamic characteristics of the final design are shown in Figure 12.2.

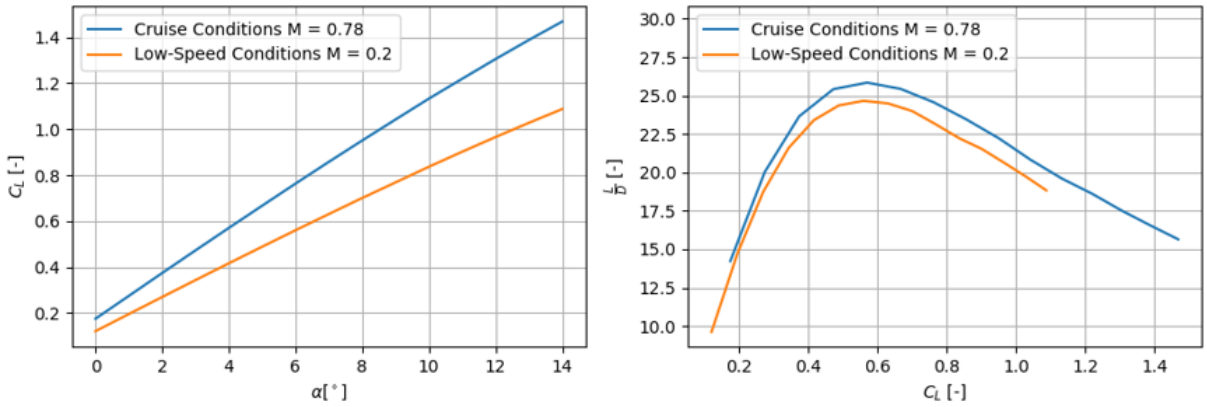

Figure 12.2: Aerodynamic polars of the entire aircraft simulated through OpenVSP

As seen through Figure 12.2, the simulation results show the lift and drag characteristics at low speed and cruise conditions. The most intriguing characteristic of the final design, is arguably the enormous lift to drag ratio ($\frac{L}{D}$) of around 26. This considerably higher $\frac{L}{D}$ is achieved due to the very high aspect ratio which minimises the induced drag. Furthermore, these results do not include the effect of the BLI, meaning that an even higher value for $\frac{L}{D}$ can be achieved with the inclusion of BLI. With the results of the aerodynamic parameters finalised, the next step was to assess the validity of the results.

As mentioned earlier, the VLM is a linear method, and thus cannot account for non-linear effects such as shock waves and flow separation. If these shocks are present in the flow field and cause the boundary layer to separate, then the VLM results would overestimate the lift and underestimate the drag. The results of a study on the aerodynamic design of a winglet showed the comparison between wind tunnel measurements and VLM predictions [64]. Figure 12.3 and Figure 12.4 show some of the results of that study where VLM results (obtained using VLAERO) are compared with wind tunnel data at a Mach number of 0.8. As seen through the figures, VLM is able to accurately model both the lift and the drag for the range of angles of attack between -2° and 6°. Beyond 6° however, there is a large discrepancy between the two data sets. The cause of this discrepancy came from the fact that there were shocks being formed over the wings, thus causing the flow to separate, a phenomenon that the VLM cannot handle.

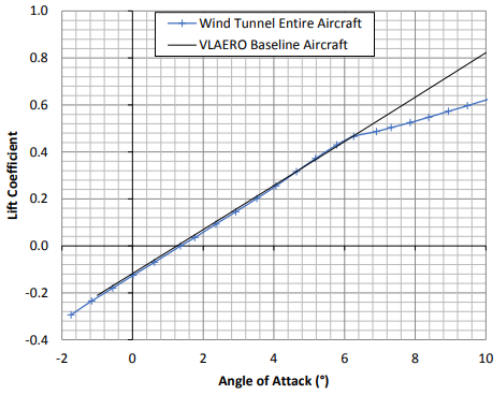

Figure 12.3: Comparison of lift curve predicted by VLM with the wind tunnel measurements at M = 0.8

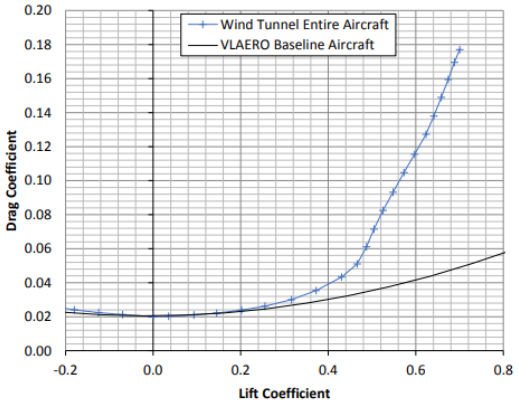

Figure 12.4: Comparison of the drag predicted by VLM with the wind tunnel measurements at M = 0.8

Figure 12.5: Comparision of the VLM results with wind tunnel measurements [64]

The aerodynamic modelling process for this project had been heavily dependent on VLM. Since the aircraft is to be designed to fly at transonic speeds where shocks are prone to occur, it was necessary to assess the validity of the VLM results. In order to do so, it had to be confirmed that there are no significant shocks forming on the wing at cruise conditions.

Since there was very limited literature found dedicated to the aerodynamic performance of the chosen airfoil under transonic flow conditions, it was very difficult to predict whether or not shocks are present. Therefore, in order to resolve this, it was decided to carry out a 2D CFD simulation for the NASA 02-0414 airfoil in the flow conditions it would experience when integrated in a wing at cruise conditions.

The CFD simulation of the NASA 2-0414 airfoil was done using Ansys Fluent. For the simulation, an angle of attack of 1° was considered. The reason being that the required angle of attack of the wing to achieve the cruise C_L of 0.454 is around 2°, and accounting for the induced angle, the effective angle of attack seen by the airfoil would be approximately 1°. The geometry of the physical domain is as follows, the fluid domain is rectangular section with a height of 10m and a length of 15m, and LE of the airfoil is placed 5m from the inlet, halfway along the height of the rectangle and has a chord length of 1m. Thus the airfoil is placed far away from the boundary such that the wall boundary conditions do not interfere with the solution. The meshing process involved refining the mesh over the entire domain and particularly over the boundary of the airfoil. In order to test for convergence, two different levels of refined meshes were generated where each mesh consists of triangular elements. The first mesh was the baseline mesh and was the coarsest, having a maximum face size of 0.1m with an edge sizing and an inflation layer at the boundary of the airfoil surface. The following mesh was just the baseline mesh with a mesh refinement factor over the whole domain of 2. Figure 12.6 depicts the finest mesh used for the calculations.

In terms of the setup of the solver and the model, a density based steady state solver was used, with a $k-\omega$ transition SST turbulence model. This turbulence model was chosen for this particular case as the Reynolds number of the flow is between the order of $Re \sim \mathcal{O}(10^5)$ and $Re \sim \mathcal{O}(10^6)$, which would typically result in the flow starting off as being laminar at the LE and transiting to turbulent before reaching the TE. For the fluid model itself, the ideal gas model was used for the density and the Sutherland model for the viscosity. For the boundary conditions, the walls and the airfoil surface had a no slip boundary condition, the outlet was a pressure outlet and the inlet was set as Pressure Far-Field with a freestream Mach number of 0.6754, which is the Mach number experienced by the airfoil in a 30° swept wing ($0.78 \cdot cos(30) = 0.6754$). Lastly for the operating conditions, the ambient atmospheric conditions for an altitude of 11000m (International Standard Atmosphere, altitude 11000m) was used. The simulation was then carried out for different meshes to check for convergence, using an implicit second order upwind scheme with a maximum of 1000 iterations. Figure 12.8 shows the results for the CFD simulation for the NASA SC 2-0414 airfoil at an angle of attack of 1°.

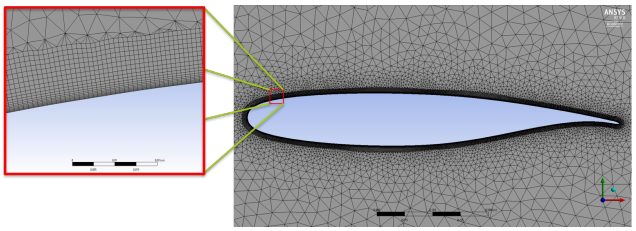

Figure 12.6: Finite Volume Mesh for the NASA SC 2-0414 airfoil at an angle of attack of 1°

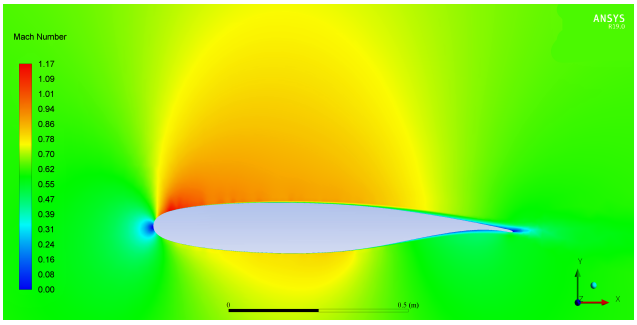

Figure 12.7: Mach number contours over the NASA SC 2-0414 at an angle of attack of 1°

Figure 12.8: CFD simulation of the NASA SC 2-0414 airfoil at a freestream mach number of $0.78 \cdot \cos 30°$

As evident through Figure 12.7, the flow field is free of any shock waves at the operating condition. Through the results of this simulation it was confirmed that the predictions made using VLM for the cruise conditions are valid, and thus reflect the actual nature of the aerodynamics of the designed aircraft.

12.2. Noise

This section describes the noise generated by the CNA. Section 12.2.1 describes the airframe noise and Section 12.2.2 describes the turbofan noise generated by the CNA. Section 12.2.3 describes the Dutch Aircraft Noise Model (NRM) and the conclusions made with the use of this model.

12.2.1. Airframe Noise

Airframe noise arises from the interaction between the aircraft structure and the flow field. It can therefore be scaled according to several geometrical properties. Airframe noise is the prominent noise source during approach and landing, and with improved turbofan noise reduction, airframe noise may be responsible for the lower bound on the noise produced by aircraft. The airframe noise is predicted by NASA's Aircraft Noise Prediction Program as described in Equation (12.2) [65].

$$p_e^2(f,\theta,\phi) = \frac{\rho_\infty \cdot c \cdot P \cdot D(\theta,\phi) \cdot F(S)}{4 \cdot \pi \cdot r^2 \cdot (1 - M \cdot \cos\theta)^4} \tag{12.2}$$

Here, p_e^2 is the effective pressure in Pascal distributed in 1/3-octave bands with f as their centre frequencies. θ and ϕ are the polar and the azimuthal directivity angles respectively, $D(\theta,\phi)$ is the directivity function and $F(S)$ is the dimensionless empirical spectral function. Furthermore, P is the power function in Watts, M is Mach number and r is the distance from the source to observer in metres. The effective pressures for each airframe component with all geometrical inputs for each component are listed in Table 12.1. Furthermore, sea level reference conditions were used.

In Table 12.1, A is surface area (m^2) and b is span (m), where the subscripts w, s, and f indicate wing, strut, and flaps respectively. Also, δ_f is the deflection angle of the flaps (degrees), d is the diameter of the wheels (m), and n is the number of wheels, where the subscripts *main* and *aux* stand for main landing gear and auxiliary landing gear respectively. The equations used to relate the aforementioned geometrical parameters to Equation (12.2) are described by NASA's Aircraft Noise Prediction Program and can be found in the TU Delft MSc. course 'Introduction to Aircraft Noise' [65].

Table 12.1: Geometrical Inputs to Equation (12.2)

Clean Wing	Strut	Leading Edge HLD	Trailing Edge HLD	Main Landing Gear	Auxiliary Landing Gear
A_w	A_s	A_w	A_f	d_{main}	d_{aux}
b_w	b_s	b_w	b_w	b_w	b_w
			b_f	n_{main}	n_{aux}
			δ_f		

After having determined the squared effective pressure for all components they were summed up. This included one wing, the strut, LE HLD and TE HLD, next to 2 main landing gears with two tires each and 3 auxiliary landing gear with two tires each. Then, the overall A-weighted sound pressure level in dBA was calculated using Equation (12.3a). Where SPL is the Sound Pressure Level in dB defined by Equation (12.3b) with the reference effective pressure p_{e_0} equal to $2 \cdot 10^{-5}$, and where the subscript i stands for each of the 43 1/3-octave centre frequencies used by all aforementioned equations and tools. Furthermore, ΔL_A is the A-weighted function defined by Equation (12.4), with f the 43 1/3-octave centre frequencies.

$$L_A = 10 \cdot \log \sum_i 10^{\frac{\text{SPL}(i)+\Delta L_A(i)}{10}} \qquad \text{SPL} = 10 \cdot \log\left(\frac{p_e^2}{p_{e_0}^2}\right) \tag{12.3a,12.3b}$$

$$\Delta L_A = -145.528 + 98.262 \cdot \log f - 19.509 \cdot (\log f)^2 + 0.975 \cdot (\log f)^3 \tag{12.4}$$

The tool described here for the design of low airframe noise emissions is used in Section 12.2.3 to draw meaningful conclusions. It can be noted already, however, that at one meter distance, the airframe noise is in the order of L_A = 99dBA. To put this in perspective, the airframe noise of the A320neo calculated with the same model is L_A = 95dBA at one meter distance.

12.2.2. Turbofan Noise

The noise of a turbofan depends on a lot of different aspects, which can not be determined at this stage in the design, like the shape of the fan blades. This meant the approach for the noise analysis had to change compared to what was expected. The noise is estimated by looking at the noise produced by an equivalent aircraft (Airbus A320), with engines that exist today (PW1100G), during take-off. This was done in take-off conditions, because that is when the

engine produces the largest amount of noise. The PW1100G engine performance was estimated with the turbofan design tool developed during the design of the CNA to find the exhaust velocity of the fan and the core. Once the exhaust velocity is known, the kinetic energy of this flow can be determined. This is done with Equation (12.5a). Since this is at take-off, V_0 equals to 0 and V_j is the exhaust velocity with $\dot{m}$ the mass flow. The energy of the core and bypass flow was summed and the average velocity was calculated by rewriting Equation (12.5a). Equation (12.5b) shows that acoustic power scales with velocity, to the power eight, and diameter to the power two. ρ is the freestream density and c is the speed of sound, these do not change between the two engines. With this estimation and the expected noise generation during take-off for a similar lower BPR engine, the expected change in noise can be found.

$$E_k = \frac{1}{2}\dot{m} \cdot (V_j^2 - V_0^2) \qquad W \sim \frac{\rho \cdot V^8 \cdot D^2}{c^5} \tag{12.5a,12.5b}$$

In Table 12.2 the estimations of the exhaust velocities of the PW1100G and the UHBR engine of the Albatross Embracer can be found. The overall pressure ratios, fan area, and total thrust were taken from the ICAO engine emission database [2]. These values and the same TIT for both engines were used to estimate the mass flow and the exhaust velocity of the PW1100G. The noise of an A320 with a PW1100G engine is taken from the EASA noise database for jet engines [3]. This noise was converted to acoustic power, which was then scaled for the CNA with Equation (12.5b). Table 12.2 shows that the UHBR engine reduces the noise caused by the exhaust of the engine compared to the engines on the A320. However, this does not take into account the increase in noise from the larger fan blades and other noise sources in the engine. Therefore it can be expected that this engine does not reduce noise production significantly compared to current state-of-the-art engines. However, the engines of the CNA require less thrust than the A320neo and, therefore, it can be assumed that the noise of the engine will be lower.

Table 12.2: Noise comparison PW1100G and the Albatross Embracer UHBR engine

Parameter	PW1100G	UHBR
Exhaust velocity fan [m/s]	265.6	240.5
Exhaust velocity core [m/s]	284.3	156.2
Mass flow fan [kg/s]	371.5	326.7
Mass flow core [kg/s]	29.5	22.0
Total energy in flow [J]	1.43E+07	9.72E+06
Average exhaust velocity [m/s]	267.0	236.1
Diameter fan [m]	2.06	2.07
Noise [dB]	85.6	81.4
Noise Power [W]	3.63E+08	1.37E+08

12.2.3. Dutch Aircraft Noise Model: NRM

The NRM (Nederlands Rekenmodel), or the Dutch Calculation Model, is a model used for predicting aircraft noise in the Netherlands, in particular for Schiphol Airport. The tool for this NRM is not public, and was provided to the CNA aerodynamics department by Prof. Dr. Simons, chairholder of the Aircraft Noise and Climate Effects department at the faculty of Aerospace Engineering at TU Delft. It uses as input:

- Classification of aircraft types into classes;
- Flight profiles for each class;
- Noise data for each class in the form of noise-power-distance (NPD) tables.

As none of these inputs are available for the CNA, they needed to be computed. First of all, the CNA needs to be put into a weight and noise class. The MTOW of approximately 70 tons puts the CNA in weight category 4: MTOW range of 60-100 tons. The noise class is determined from measurements by the ICAO, which are not available as the aircraft is not yet built nor tested. According to empirical trends, noise levels for new aircraft types are generally lower than the representative aircraft within the same weight class. To be conservative, the CNA is assumed to be in the same noise class as the Boeing 737-300 with HardWall Forward Acoustic Panels (HWFAP). Although this class is represented by this old aircraft, it includes the newer models of the aircraft A319, A320, A321, Boeing 734, 736, 737, 738 and 739. This puts the CNA in noise class 3; a reduction ΔEPNdB between 9 and 18.

[2] URL `https://www.easa.europa.eu/domains/environment/icao-aircraft-engine-emissions-databank` cited [16. June 2020]
[3] URL `https://www.easa.europa.eu/domains/environment/easa-certification-noise-levels` cited [16. June 2020]

Based on class 4/3 (weight/noise), flight profiles are selected. These are dependent on the chosen procedure and the distance of the flight. The profiles give the height, flight speed and thrust setting for ideal situations. The real profile will most likely differ, as it is dependent on pilot inputs, engine transients, actual aircraft configurations and external factors such as the weather. Based on regular, ICAO, and airport specific procedures, the CNA will adapt one of nine take-off codes and four take-off classes or one of three landing codes and three landing classes. Together with the weight/noise class, this provides any flight of the CNA with a noise code; e.g. if KLM were to fly from Schiphol to Munchen (a flight of 680km) with the CNA, it would make use of a NADP2 departure procedure (Noise Abatement Departure Procedure) with climb to 1500 ft, and the administration number for noise calculations would be 4690600.

The third input to the NRM is the noise data for the CNA class in the form of NPD tables. These tables summarise the overall A-weighted sound pressure levels in dBA for pre-determined source-receiver distances and thrust settings. All distances and thrust settings that are not listed in the NPD tables are linearly interpolated from the NPD tables. Furthermore, in the NPD tables it is assumed that the aircraft is an omnidirectional point source. For the weight/noise class 4/3 of the CNA, the NPD table used had the code 469, and represents varying competitor aircraft such as the A320 and the Boeing 737. After having determined the A-weighted sound pressure levels from the NPD tables, they are corrected for lateral sound attenuation.

For the example given before, a flight of KLM from Schiphol (AMS) to Munchen (EDDM) with the CNA, the flight profile is shown in Figure 12.9. For this flight profile, the L_A is calculated. To correct for the time dependency of L_A, however, the Sound Exposure Level (SEL) is plotted in Figure 12.10. The two graphs depict the situation for the first 20 km of the flight.

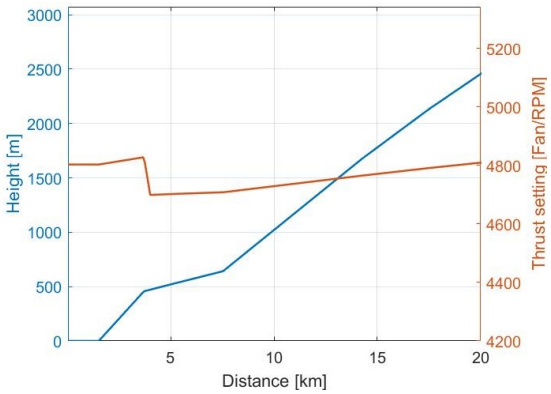

Figure 12.9: Flight profile for take-off 4690600

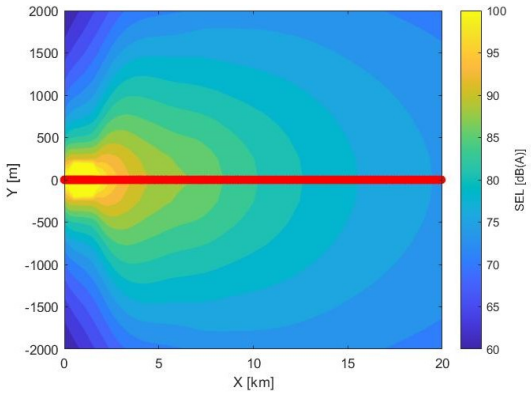

Figure 12.10: Sound Exposure Level for take-off 4690600

For the same example, but for landing, a 3° glide angle with reduced flap setting is used. Furthermore, a descent procedure with an initial approach altitude of 3000 ft is used. This procedure is administrated as 4691201. For landing 4691201, only the last 30 km of the flight is shown in Figure 12.11, Figure 12.12, and Figure 12.13.

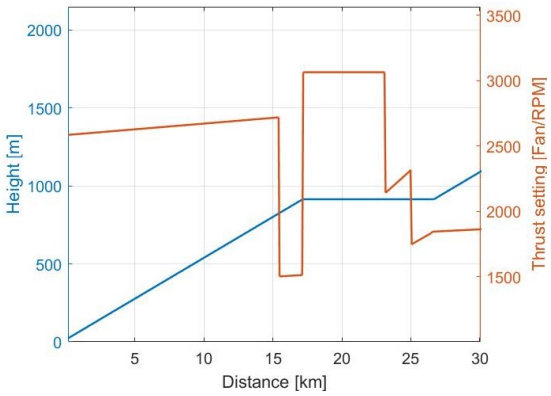

Figure 12.11: Flight profile for landing 4691201

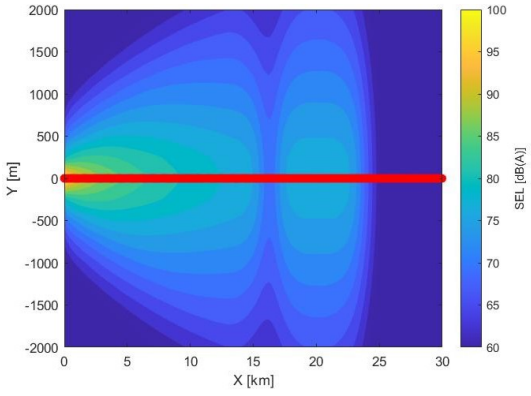

Figure 12.12: Sound Exposure Level for landing 4691201

To validate the assumptions used in the calculation of these results, the results from Section 12.2.1 and Table 12.2 can be used. Since the airframe noise is the most accurate prediction, its results are primarily useful. The airframe noise is calculated as L_A. To validate the NRM, the maximum L_A is plotted in the vicinity of the airport (radius of 2000m) in Figure 12.13. The maximum is taken, since L_A varies with time.

Since the prediction made in Section 12.2.1 is based on both azimuthal and polar angle, a zero degree azimuthal

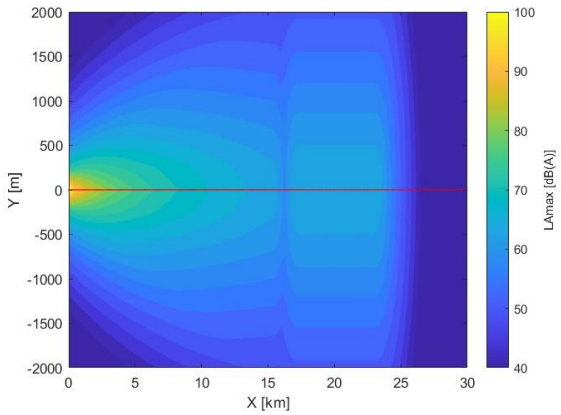

Figure 12.13: Maximum L_A for landing 4691201

directivity angle is assumed. Furthermore, no assumption on the polar angle is made, but the maximum values of L_A are taken to be conservative. The maximum L_A of the airframe at 1m distance is 99dBA. This corresponds with the landing plots for L_A where at close proximity the aircraft produces up to 100 dBA. Furthermore, when comparing with landing 4691201, it can be seen that around 800 m height the thrust settings are low and the airframe noise is dominant. With the tools described in Section 12.2.1, the airframe noise at 800 m distance is 41dBA which corresponds with Figure 12.13 and Figure 12.12 where a dip in the graph is seen at ~17 km between 40 and 50 dBA. This validates the assumptions on the weight/noise class, the class dependent flight profiles, and the NPD values and therefore justifies all plots visualised in this section for the CNA.

As described in Section 12.2.1, the airframe noise of the CNA is 4 dBA louder than an A320neo at 1 meter distance. At 800 m height the airframe noise of an A320neo is 37 dBA, which makes the CNA 4 dBA louder at this distance as well. This increase in noise is most significantly due to the struts, which effectively create the noise of a second smaller wing. The reason that the aircraft is not producing significantly more noise, is that the flaps and slats are the main source of noise. Due to the struts not having those, the order of airframe noise increase is low. It is important to note that the extra landing gears in the strut increase the noise with less than 1 dBA, which is undetectable by human ears. In Section 12.2.2, the noise of the CNA dominated by turbofans is 4 dB less than the A320neo with PW1100G. As dBA scales directly with dB, the noise of the CNA dominated by turbofans are also 4 dBA less than the A320neo with PW1100G. The conclusion is that despite all extra components of the CNA contributing to noise, the CNA has its noise in the same order of magnitude as the A320neo.

This means that the CNA satisfies the requirement of fly-over noise stated by the customer, as the A320neo is well withing this requirement. Also, it can be concluded that the CNA satisfies the current standards of the ICAO. The last update of the ICAO took 12 years, and decreased the maximum noise level with 7 EPNdB in 2013. Extrapolating, the next reduction of maximum noise with 7 EPNdB will be around 2025. In order to fullfill the ICAO standards by then, the aircraft needs to be tested and certified by the ICAO before 2025. To mitigate the risk of not being able to certify before 2025, it is recommended that airframe noise reduction techniques and materials shall be researched. To decrease the noise even more, it is recommended that research is done in sound absorbing materials in the engine nacelles and to research design of nacelle and flaps geometry with the aim of noise reduction.

13
Flight Performance

This chapter covers the assessment of the performance of the aircraft during take-off, climb and landing. Several requirements set by the customer and airworthiness regulations concerning the aircraft performance have to be met. The chapter is structured as follows. Section 13.1 describes the take-off performance of the CNA, Section 13.2 describes the climb performance, Section 13.3 describes about the landing performance and finally Section 13.4 lists recommendations for later design phases.

13.1. Take-Off Performance

The objective of the take-off analysis is to calculate the required take-off distance, which is the distance from the point where the aircraft is at stand still to the point where the aircraft has cleared the obstacle height h_{obst} of 35 ft (11 m) [66]. REQ-CN-PERF-19 asserts that the total take-off distance at sea level should not be greater than 1800m .

The chosen method to calculate the take-off distance, which is valid for jet transport aircraft, splits the take-off distance into ground roll distance S_G, rotation distance S_R and the climb over obstacle distance S_{obst}, as shown in Figure 13.1 [66]. During the analysis, it was assumed that the aircraft weight does not change during take-off, hence the MTOW is constant during the whole path. This assumption has the effect of slightly overestimating the take-off distance. The following subsections describe how each segment of the take-off distance is calculated at sea level.

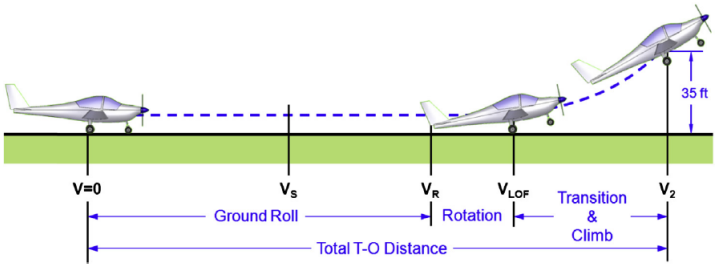

Figure 13.1: Take-off distance [66]

13.1.1. Ground Roll

The first phase to be assessed in the take-off performance is the ground roll distance. In Figure 13.2, the forces are acting on an aircraft during the ground roll on a flat surface. The forces acting in the vertical direction are the lift L and the weight W, whereas the forces in the horizontal direction are the thrust T, the drag D and the friction force dependent on the friction ground coefficient μ and the net normal force $R_M = W - L$. The equation of motion is then showed in (Equation (13.1a)). The general solution for the equation of motion leads to the ground run distance S_G, which is shown in Equation (13.1b)

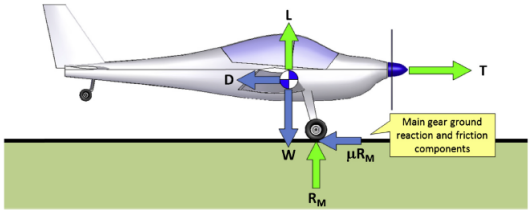

Figure 13.2: Forces diagram for the take-off run [66]

$$\frac{dV}{dt} = \frac{g}{W}[T - D - \mu \cdot (W - L)] \qquad S_G = \frac{V_{LOF}^2 \cdot W}{2 \cdot g \cdot [T - D - \mu \cdot (W - L)]_{at \frac{V_{LOF}}{\sqrt{2}}}} \qquad \text{(13.1a,13.1b)}$$

In Equation (13.1b), V_{LOF} is the lift-off speed, which is 1.1 times the stall speed in take-off configuration. As shown in Figure 9.3, the thrust is a function of speed and altitude, whereas the drag coefficient is calculated with the following general method, where C_{D_0} is the zero lift drag coefficient and C_{D_i} the induced drag coefficient:

$$C_D = C_{D_0} + C_{D_i} \qquad C_{D_i} = k \cdot C_L^2 \qquad k = \frac{1}{\pi \cdot A \cdot e} \qquad \text{(13.2a,13.2b,13.2c)}$$

During take-off and landing the aircraft is subject to the ground effect, which is a reduction in induced drag due to the fact that the wing pushes air down. Subsequently, the ground pushes the air up, generating further lift on the wing. CS-25 regulations state that the ground effect should be taken into account when the wing height from the ground is less than twice the wingspan, hence in both take-off and landing (Section 13.3) the ground effect was considered. Equation (13.3a) was used to calculate the induced drag coefficient that accounts for ground effect $(C_{D_i})_{IGE}$. This was done by multiplying the induced drag without ground effect $(C_{D_i})_{OGE}$ (calculated as in Equation (13.2b)) with the ground influence coefficient Φ. This is dependent on the ratio between the wing span b and the wing height h, which in turn is assumed to be the sum of the main landing gear height h_{lg} and the fuselage height h_f (Equation (13.3b)). Since the ratio is approximately 0.13, the Wieselberger method to calculate Φ was used (Equation (13.3c)), as it is valid for h/b ranging from 0.033 to 0.25 [66].

$$(C_{D_i})_{IGE} = \Phi \cdot (C_{D_i})_{OGE} \qquad h = h_{lg} + h_f \qquad \Phi = 1 - \frac{1 - 1.32 \cdot (h/b)}{1.05 + 7.4 \cdot (h/b)} \qquad \text{(13.3a,13.3b,13.3c)}$$

The final step was to calculate the lift, the drag and the thrust at $V = V_{LOF}/\sqrt{2}$, where the C_L is the zero lift coefficient at take-off. Finally, the ground coefficient was estimated to be between 0.03 and 0.05, assuming the aircraft is not going to brake. Since μ also depends on the type of the ground, the value was set to 0.05 for a conservative estimation. With this information, it was possible to calculate the ground roll distance. Results are shown in Table 13.1.

13.1.2. Rotation and Transition

The rotation is a transient phase of the take-off, where the pilot starts to pull up and, within the rotation distance, the aircraft starts to rotate and lift-off. For large aircraft, this phase can last between 2 to 5 seconds. It was assumed that this phase is 3 seconds and carried out at rotation velocity $V_R = V_{LOF}$ [66]. The rotation distance is $S_R = 3 \cdot | V_{LOF} |$.

The transition phase follows the rotation, and it is the phase that starts with the aircraft lift-off and ends when the aircraft has completed a rotation θ_{climb} and starts the climb with this climb angle. There are two possible scenarios: either the aircraft finishes the rotation at a transition height h_{tr} lower than the 35 ft obstacle height h_{obst}, or the obstacle height gets overcome before the transition phase is finished (h_{obst}<h_{tr}), as shown in Figure 13.3.

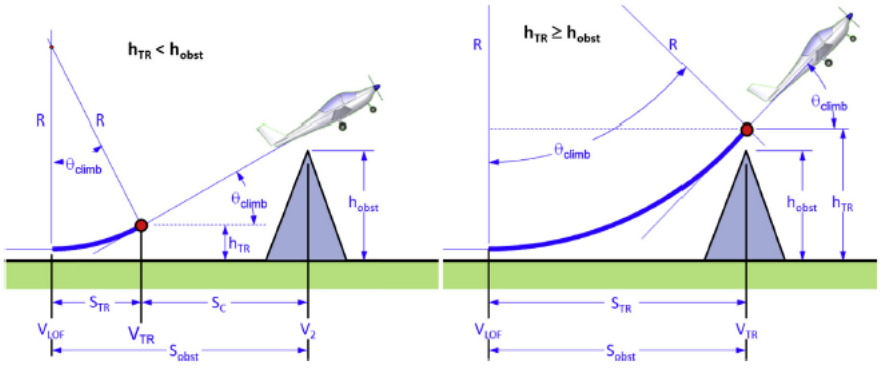

Figure 13.3: Left figure shows the aircraft perform transition and straight climb before the obstacle height is reached, whereas the right figure shows the obstacle height reached before finishing the transition phase [66]

The transition phase starts at V_{LOF} and ends at V_2, which is 1.1 the minimum control speed in air V_{MCA}, hence 1.32 times $V_{S_{take-off}}$. Therefore the transition speed V_{tr} is the average between the lift-off speed and V_2 ($V_{tr} = 1.16 V_{S_{take-off}}$). With the lift coefficient assumed to be 0.9 times the maximum lift coefficient at take-off, the load factor n could be

estimated along with the radius of transition R (Equation (13.4a) and Equation (13.4b))[66].

$$n = \frac{L}{W} = \frac{\frac{1}{2}\cdot\rho\cdot\left(1.16\cdot V_{S_{take-off}}\right)^2\cdot S\cdot\left(0.9\cdot C_{L_{max_{take-off}}}\right)}{\frac{1}{2}\cdot\rho\cdot V^2_{S_{take-off}}\cdot S\cdot C_{L_{max_{take-off}}}} = 1.211 \qquad R = \frac{{V_{tr}}^2}{g\cdot(n-1)} \tag{13.4a,13.4b}$$

The climb angle was found with Equation (13.5a) where thrust and drag refer to the final condition where the aircraft flies at V_2. It was then possible to use Equation (13.5b) to calculate the transition height and, based on whether it is higher or lower than the obstacle height, it was known whether the take-off includes the climb segment.

$$\sin(\theta_{climb}) = \frac{T-D}{W} \qquad h_{tr} = R\cdot(1-\cos(\theta_{climb})) \tag{13.5a,13.5b}$$

Assuming the scenario on the left of Figure 13.3, the obstacle distance can be calculated as follows:

$$S_{obst} = S_{TR} + S_C \qquad S_{TR} = R\cdot\sin(\theta_{climb}) \qquad S_C = \frac{h_{obst}-h_{TR}}{\tan(\theta_{climb})} \tag{13.6a,13.6b,13.6c}$$

Table 13.1 shows the results and characteristic parameters of the take-off analysis. The parameters $C_{D_{0_{take-off}}}$ and $k_{take-off}$ are retrieved from simulation. It can be seen that the transition height is smaller than the obstacle height, hence the situation analysed above pertains to this analysis. Furthermore, the take-off distance is smaller than 1800m, hence REQ-CN-PERF-19 is met.

Table 13.1: Result for take-off performance

Parameter	Symbol	Value	Unit
Zero Lift Drag Coefficient at Take-off	$C_{D_{0_{take-off}}}$	0.01204	[-]
Induced Drag Factor at Take-off	$k_{take-off}$	0.039648	[-]
Thrust at $V_{LOF}\cdot\sqrt{(2)}$	$T_{V_{LOF}\cdot\sqrt{(2)}}$	140,720	[N]
Thrust at V_2	T_{V_2}	122942	[N]
Transition Altitude	h_{TR}	8.69	[m]
Climb Angle	θ_{climb}	7.16	[deg]
Ground Run Distance	S_g	1354	[m]
Rotation Distance	S_R	194	[m]
Transition Distance	S_{TR}	139	[m]
Climb Distance	S_C	18	[m]
Take-off Distance	S_{TO}	1706	[m]

13.1.3. Verification and Validation

The tool was verified by means of unit tests and hand calculations. For example, increasing the parasite drag and the mass of the aircraft should have resulted in a longer take-off path, which was the case.

For validation, several parameters of the take-off performance of the CNA were compared with reference aircraft, as shown in Table 13.2. It can be seen that the aircraft has a lower MTOW than the A320-200 and B757-200, which already suggests that the take-off distance should be shorter. In addition to this, the achievable V_2 is again in favour of the CNA, which is another indication of a shorter take-off distance. Finally, the expected outcome shows the take-off distance to be shorter and in a reasonable range.

Table 13.2: Results for take-off validation

Aircraft	MTOW [kg]	V_2 [kts]	S_{TO} [m]
CNA	68711	151	1706
A320-200	73500	143	2180
B757-200	115900	150	2226

13.2. Climb Performance

The climb performance analysis was done to assess whether the aircraft is capable of satisfying the requirements shown in Table 13.3. In addition to this, the service ceiling of the aircraft needed to be found, as well as verifying

whether the climb phase can be performed with the range and fuel weight consumption assumed in Class I.

Table 13.3: Driving requirements for cruise performance

Identifier	Requirement	Source
REQ-CN-PERF-24	The CNA shall have a rate of climb of 1800 ft/min in clean configuration, at sea-level conditions.	Own
REQ-CN-FLTPRF-14	The steady climb gradient shall not be less than 2.4% for two-engined aeroplanes at V_2 with the critical engine inoperative and the aircraft in take-off configuration with retracted landing gear.	CS 25.121b

13.2.1. Climb with One Engine Inoperative

Airworthiness regulations state that the aircraft should be able to perform the climb after the final take-off path with one engine inoperative (REQ-CN-FLTPRF-14). The forces that act on the aircraft during climb are presented in Figure 13.4.

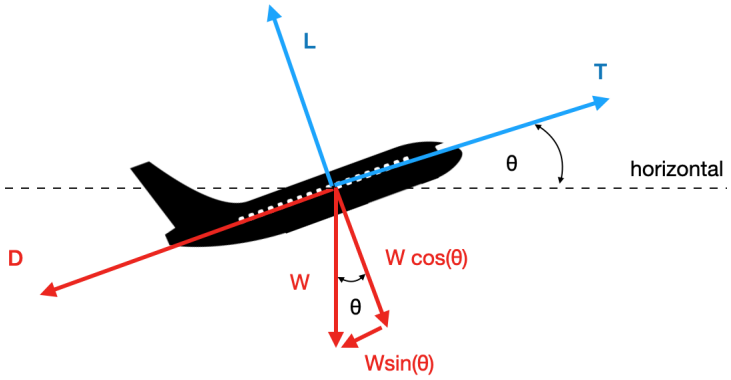

Figure 13.4: Forces during climb

From Figure 13.4, Equation (13.7a) and Equation (13.7b) are derived, where θ is the climb gradient:

$$T - D - W\sin(\theta) = \frac{W}{g}\frac{dV}{dt} \qquad L - W\cos(\theta) = \frac{W}{g}\cdot V\frac{d\theta}{dt} \tag{13.7a,13.7b}$$

To simplify the analysis, the small angle approximation was used, and it was assumed that the aircraft is flying steady. In real life this would not be the case, however it can be assumed for the climb phase after take-off transition, since this phase has a small change in altitude and the effect of the assumption is negligible. Hence Equation (13.8a) and Equation (13.8b) are obtained:

$$T - D - W\sin(\theta) = 0 \qquad L = W \tag{13.8a,13.8b}$$

By multiplying Equation (13.8a) with velocity V the power available $P_a = T \cdot V$, the power required $P_r = D \cdot V$ and the steady rate of climb $ROC_{st} = V \cdot sin(\theta)$ were found (Equation (13.9)). For clarity, the velocity V is the true airspeed V_{TAS}.

$$ROC_{st} = V \cdot sin(\theta) = \frac{T \cdot V - D \cdot V}{W} \tag{13.9}$$

For the one engine inoperative case, the weight was assumed to be equal to the MTOW, as the fuel consumed in take-off has a very small effect on the climb performance. The velocity is equal to V_2, which determines the available thrust from Table 13.1 and the drag. The zero lift drag coefficient and the induced drag factor were taken from simulation for clean take-off configuration (flaps and landing gear retracted). With all the values known, it was found that the climb gradient at one engine inoperative is 3.13%, hence REQ-CN-FLTPRF-14 is satisfied.

13.2.2. Service Ceiling

In order to find the ceiling of the aircraft, the climb range and the fuel consumed during this phase, a numerical simulation was performed. The climb strategy is to climb at a standard constant indicated airspeed V_{IAS} of 150 m/s, which is indicated by the anemometer. However, as the air density decreases with increasing altitude, the mach number increases, and when the aircraft reaches M=0.78 the pilot has to fly at a constant Mach number, which is indicated by the Machmeter. This means that the en route climb procedure is not performed at constant true airspeed V_{TAS}, therefore Equation (13.9) is not valid for this procedure and the correction for unsteady flight had to be implemented. The implementation of the unsteady condition starts by multiplying V with Equation (13.7a), which results into Equation (13.10a). Furthermore, the left term can be multiplied by $\frac{dh}{dh}$, and by observing that $\frac{dh}{dt} = V \cdot sin(\theta) = ROC$, it is possible to arrive at Equation (13.10b) and Equation (13.11).

$$T \cdot V - D \cdot V - W \cdot V \cdot \sin(\theta) = \frac{W}{g} \cdot V \frac{dV}{dh} \frac{dh}{dt} \qquad ROC \left[1 + \frac{V}{g} \frac{dV}{dh} \right] = \frac{P_a - P_r}{W} \tag{13.10a,13.10b}$$

$$\frac{ROC}{ROC_{st}} = \frac{1}{1 + \frac{V}{g} \frac{dV}{dH}} \tag{13.11}$$

Next, $\frac{dV}{dH}$ can be interpreted as in Equation (13.12a), where V_{EAS} is the equivalent airspeed, which is the speed independent of the altitude (Equation (13.12b)). $\frac{d\sqrt{\frac{\rho}{\rho_0}}}{dH}$ is evaluated by taking the local density and the step size in the simulation as dH, which is kept to 100 ft for a good accuracy. Furthermore, after Mach 0.3 the compressibility effects cannot be neglected, hence Equation (13.13) is used to calculate the true velocity, where V_{IAS} is assumed to be approximately equal to the calibrated airspeed V_{CAS} (hence no errors deriving from instruments installation errors):

$$\frac{dV}{dH} = V_{EAS} \cdot \frac{d(\sqrt{\frac{\rho_0}{\rho}})}{dH} \qquad V_{EAS} = V_{TAS} \cdot \sqrt{\frac{\rho}{\rho_0}} \tag{13.12a,13.12b}$$

$$V_{TAS} = \sqrt{\frac{2\gamma}{\gamma - 1} \cdot \frac{p}{\rho} \cdot \left[\left[1 + \frac{p_0}{p} \cdot \left[\left(1 + \frac{\gamma - 1}{2\gamma} \cdot \frac{\rho_0}{p_0} \cdot V_{CAS}^2 \right)^{\frac{\gamma}{\gamma - 1}} - 1 \right] \right]^{\frac{\gamma - 1}{\gamma}} - 1 \right]} \tag{13.13}$$

The numerical simulation assumed that the aircraft starts its climb procedure from sea level with the weight equal to the MTOW minus the Class I fuel weight estimated for the take-off procedure. It then computed the rate of climb for all velocities at sea level, and computed the fuel weight necessary to climb to the next level. It also computed the ground distance covered as well, given the constant indicated airspeed and related rate of climb. The calculated fuel weight was then subtracted from the aircraft weight for the next altitude calculation, and the process continued until the altitude where the maximum rate of climb equals 500 ft/min was found. This value is important as it gives the service ceiling, which is defined as the altitude where the maximum achievable rate of climb is 500 ft/min (CS-25). In addition to this, the thrust and the total thrust specific fuel consumption are dependent on speed and altitude. However, there are no empirical estimation methods for these parameters, as the UHBPR concept is very recent and no database containing data of similar engines is available. Therefore, in order to have representative values of ROC and fuel weight reduction, a numerical interpolation method was used to approximate the variation of thrust and the TSFC with speed and altitude.

The results of the simulation are shown in Figure 13.5. The lines show the variation in rate of climb with true airspeed for the same altitude. For low altitudes especially, a kink is noticeable at around Mach 0.5, and this is due to the fact that the TSFC gets worse when the air density is high and the true airspeed is high, which is something that was expected as the engines are not designed to be efficient at high speeds and low altitudes. It could be seen that the ceiling was 33800 ft, which is lower than the cruise altitude of 36000 ft. This means that the aircraft iss not able to reach the optimum cruise height with the given take-off conditions. During this phase however, the horizontal distance covered during climb is approximately 300 km and the fuel consumed is 821 kg. The ground distance calculated with the numerical simulation was then different from the empirically estimated value in Section 5.3. Indeed, the estimated ground distance for the climb phase was 200 km, and fuel consumed during this phase is 1565 kg. Therefore 100 km of the range is already covered during climb and also the fuel consumed is lower. It would then be necessary to carry out a small cruise phase at a lower altitude, therefore the weight of the aircraft lowers and the optimum cruise altitude can be reached. For example, it is assumed that the aircraft carries the cruise phase at 33800 ft once this altitude is

reached. The remaining cruise range to be covered is of 3491 km. From the simulation, it is found that the aircraft can cover 4110 km of range at this constant altitude. Since flying at a higher altitude reduces the fuel consumption, it is very likely that the aircraft will be able to climb a further 2200 ft and perform the mission profile as planned.

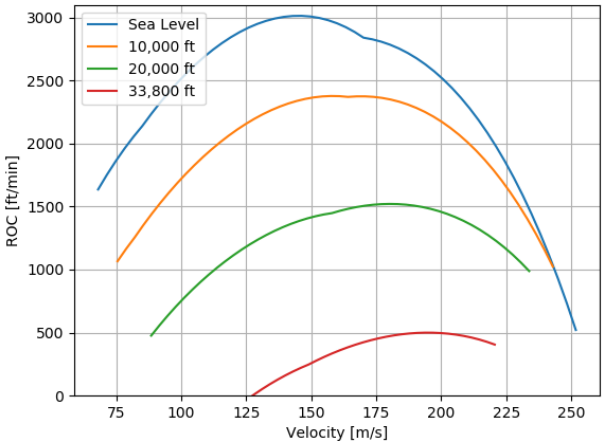

Figure 13.5: Climb Performance

13.2.3. Verification and Validation

For verification, unit tests were performed on the simulation tool in order to check whether the given results were correct. For example, increasing the MTOW or increasing the induced drag should have resulted in a lower ceiling of the aircraft, and this was the case.

For validation, the MTOW as well as the ceiling and the maximum thrust at sea level were compared with data from reference aircraft, as shown in Table 13.4. It is possible to notice that the service ceiling is lower than the reference aircraft. The reason for this is that the high lift-over-drag ratio of the CNA in the Class I leads to a low MTOW, which subsequently lowers the thrust required at sea level, which is much lower than that of the reference aircraft, even though the MTOWs are in the same range. This means that the thrust available is lower, which lowers also the rate of climb and thus the ceiling of the aircraft. However, it must be considered that the calculated service ceiling of the CNA is the ceiling straight after the climb is finished: during cruise it gets higher and is very likely to reach similar values of the reference aircraft, which instead are the maximum service ceilings during cruise. Further analysis is needed to assess what is the exact maximum ceiling of the aircraft during cruise.

Table 13.4: Results for climb performance validation

Aircraft	MTOW [kg]	Thrust sea level [kN]	Service Ceiling [ft]
CNA	70337	165	33800
Boeing 737-800	78220	214	39000
E195-E2	61500	190	41000
MD 90-30	70760	222	37000

13.3. Landing Performance

The landing performance analysis aimed to calculate the required landing distance, which is the distance from the runway threshold until the point of complete stop of the aircraft. The CNA design must meet the top-level requirements and CS-25 rules, which are shown in Table 13.5.

Table 13.5: Driving requirements for landing performance

Identifier	Requirement	Source
REQ-CN-PERF-20	The CNA shall land within 1800 m, measured from 15m above the runway until standstill, on a paved runway at sea-level conditions and maximum landing weight.	Own
REQ-CN-FLTPRF-6	The landing distance shall be determined.	CS 25.125
REQ-CN-FLTPRF-7	Reference stall speed is a calibrated airspeed defined by the applicant. It may not be less than a 1-g stall speed.	CS 25.103

The analysis procedure, taken from literature, splits the landing distance into the approach distance S_A, the flare distance S_F, the free-roll distance S_{FR} and the braking distance S_{BR}, shown in Figure 13.6[58] . The following subsections describe the methodologies used in the analysis, followed by the results.

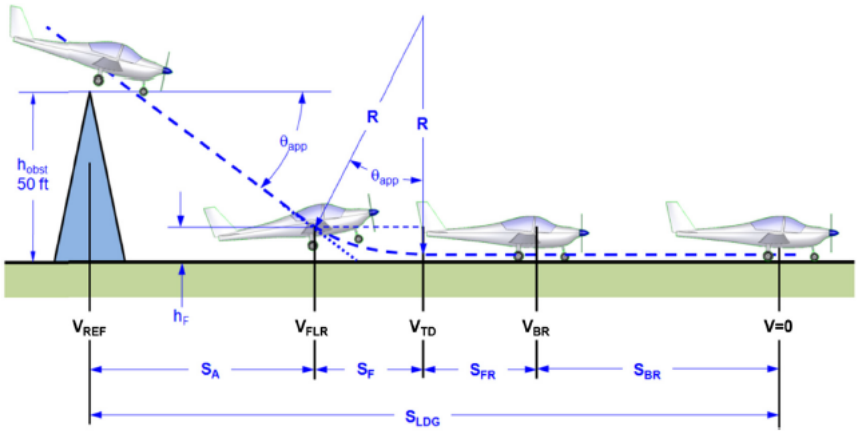

Figure 13.6: Components of landing distance [58]

13.3.1. Approach and Flare

The approach phase is the phase from the point where the aircraft is 50 ft above the runway threshold until the point where the aircraft starts to rotate. As shown in Figure 13.6, the parameters that define the approach distance are the flare height h_f, the screen height h_{scr} and the approach angle θ_{app}, which can be assumed to be 3° [58]. This phase is conducted at constant reference speed V_{REF} (also called approach speed V_{app}) which is 1.3 times the stall speed in landing configuration. The landing stall speed is specifically dependent on the maximum lift coefficient during landing $C_{L_{maxland}}$ and the maximum landing weight MLW. By taking the average of the ratio MLW/MTOW of the competitor aircraft, it was found that the MLW corresponds to 86% of the MTOW. The procedure to calculate the approach distance is similar in structure as the transition distance for take off mentioned in Section 13.1.2, where the load factor and radius are calculated as in Equation (13.4a) and Equation (13.4b), with the lift coefficient assumed to be 0.9 times the maximum for landing [66]. Once the rotation radius and load factor are known, the flare height, the approach distance and the flare distance can be calculated as in Equation (13.14a), Equation (13.14b) and Equation (13.14c):

$$h_F = R \cdot (1 - cos(\theta_{app})) \qquad S_A = \frac{h_{obst} - h_F}{tan(\theta_{app})} \qquad S_F = R \cdot sin(\theta_{app}) \qquad \text{(13.14a,13.14b,13.14c)}$$

13.3.2. Roll Free and Brake

The roll free phase is the phase where the aircraft, once in touch with the ground, is rolling free before applying the brakes. Typically this phase has a duration of 3 seconds for transport aircraft [66]. Since this phase is short, the aircraft touchdown velocity V_{TD} is assumed to be the same as the velocity during braking V_{BR}, which is 1.1 times the $V_{S_{land}}$. Therefore, the free roll distance is $S_{FR} = 3 \cdot V_{TD}$.

The braking distance is the distance from where the pilot applies the brakes until complete stop. As a design choice the aircraft does not use thrust reversers but uses other braking systems simultaneously [58]. Hence the approach to find the braking distance was the same as in Section 13.1.1 for ground roll distance, with $V = V_{BR}$ and $T = 0$ as the aircraft does not use reversers. Hence the equation for braking distance is Equation (13.15a), where the induced drag was computed as in Section 13.1.1. Moreover the drag contribution from the flap had to be taken into consideration. This was done by using the polynomial approximations shown in Equation (13.15b) to Equation (13.17), which are specific for double slotted flaps and rely on a database of flaps used in jet aircraft [58]. The polynomial Δ_1 accounts for the flap chord contribution to the drag, whereas Δ_2 takes into account the drag contribution of the flap deflection; other parameters are the wing chord R_f, the aileron deflection δ_f (in degrees), and $\frac{S_{flap}}{S_{ref}}$, the ratio between the flap surface area and the wing surface area. The ground coefficient μ is usually between 0.3 and 0.5 when braking: 0.3 was chosen for a more conservative analysis [58]. The results of the landing performance analysis are shown in Table 13.6. The total landing distance is 1719 m, which means that both requirements REQ-CN-PERF-24 and REQ-CN-FLTPRF-14

are met. $S_{BR} = -\frac{V_{BR}^2 \cdot MLW}{2 \cdot g\left[T - D_{ldg} - \mu \cdot (MLW - L)\right]_{at\,\frac{V_{BR}}{\sqrt{2}}}}$) $\Delta C_{D_{fap}} = \Delta_1 \cdot \Delta_2 \cdot \left(\frac{S_{flap}}{S_{ref}}\right)$

(13.15a,13.15b)

$$\Delta_1 = -21.090 \cdot R_f^3 + 14.091 \cdot R_f^2 + 3.165 \cdot R_f - 0.00103 \tag{13.16}$$

$$\begin{aligned}\Delta_2 = &-3.9877 \cdot 10^{-12} \cdot \delta_f^6 + 1.1685 \cdot 10^{-9} \cdot \delta_f^5 - 1.2846 \cdot 10^{-7} \cdot \delta_f^4 + 6.1742 \cdot 10^{-6} \cdot \delta_f^3 + \\ &- 9.89444 \cdot 10^{-5} \cdot \delta_f^2 + 6.8324 \cdot 10^{-4} \cdot \delta_f - 3.892 \cdot 10^{-4}\end{aligned} \tag{13.17}$$

Table 13.6: Result for landing performance

Parameter	Symbol	Value	Unit
Zero Lift Drag Coefficient in Landing	$C_{D_{0_{land}}}$	0.01204	[-]
Induced Drag Factor in Landing	k_{land}	0.039648	[-]
Flare Height	h_F	1.56	[m]
Flap Chord to Wing Chord	R_f	0.25	[-]
Flap Area to Wing Area	$\frac{S_{flap}}{S_{ref}}$	0.1625	[-]
Flap Deflection	δ_f	50	[°]
Approach Distance	S_A	268	[m]
Flare Distance	S_F	45	[m]
Free Roll Distance	S_{FR}	169	[m]
Brake Distance	S_{BR}	913	[m]
Landing Distance	S_{land}	1395	[m]

13.3.3. Verification and Validation

The landing performance was assessed by using a Python program. The program was verified with hand calculations in order to check that all parameters were calculated correctly, hence the methodology has been verified. For validation, the landing performance of the aircraft was compared with reference aircraft in Table 13.7. It can be noticed that the landing distance of the CNA is lower than the reference aircraft. This is due to the lower MLW and approach speed. The ratio MLW/MTOW also appears to be in the same range, hence the results are valid.

Table 13.7: Comparison of landing performances

Aircraft	MLW [kg]	MLW/MTOW	V_{app} [kts]	Landing distance [m]
CNA	59092	0.86	129	1395
A320-200	64500	0.88	134	1440
B757-200	95450	0.82	137	1564

13.4. Recommendations on Performance Design

The simulation for the climb performance demonstrated that it is not possible to perform a straight climb to the optimum cruise altitude after take-off at sea level with the MTOW. The recommendation is thus to analyse quantitatively what cruise distance in this altitude is needed to lower the aircraft weight such that the service ceiling goes above the optimum cruise altitude. In addition to this, a quantitative analysis on the ground distance and fuel consumed during all the flight phases shown in Figure 5.1 is suggested for a better estimate of the overall aircraft performance.

14
Manufacturing, Assembly, and Integration Plan

The Manufacturing, Assembly, and Integration Plan (MAI plan) shows how different parts of the aircraft will be manufactured, assembled and integrated into the final aircraft. The aircraft itself is fairly conventional with a couple of novel features that will change the assembly and integration process compared to conventional aircraft. This chapter discusses how the CNA will be manufactured (Section 14.1), followed by the conversion process of the aircraft (Section 14.2).

14.1. Initial Manufacturing

The MAI plan can be seen in Figure 14.1. The different colours represent the different assembly groups. Some parts and assemblies are manufactured and assembled in parallel, in order to reduce production time and therefore cost. The first parts being produced are the lifting surfaces. The lifting surfaces on the CNA consist of the main wing, the horizontal stabiliser and the vertical stabiliser. The assembly of these are then separated into multiple parts. The most important of which is the wing box, which is also the part where all of the parts in the lifting surface assembly attach to. It will be manufactured at the same time as the leading edge of the wing and the trailing edge of the wing. The main wing of the aircraft also has a folding mechanism and engine pylons. The folding mechanism is included in the outer wing of the aircraft. The outer wing assembly also includes the wingtip. This will be assembled separately from the main wing and integrated into the main wing at the next step in the MAI plan. The outer wing does not need any hydraulic parts or lines since all of the control surfaces are on the inner wing.

The wing box, leading edge, trailing edge, and engine pylon are assembled into a pre-wing once they are manufactured. This assembly comprises of one half of a wing, without control surfaces, where the control surfaces will be manufactured in parallel with the centre wing box. These and the outer wing will be combined to form the full 50 meters long wing span. At this point in the assembly, the wing still misses it's hydraulic, electrical, and fuel lines. These are then added in the next step to complete the wing assembly. The same steps will be taken for the vertical and horizontal stabiliser, however in a simpler manner as they don't have a centre wingbox nor folding wingtips, and they do not need to store fuel or attach engines.

The manufacturing of the fuselage will start in parallel with the manufacturing of the wings. The centre fuselage is one of the largest parts of the aircraft and therefore starts production earlier than the cockpit and tail-cone. The cockpit and the tail-cone will have all the structural attachments ready for landing gear, instruments, and stabilisers. The cockpit and the tail-cone also have bulkheads to keep the pressure difference with the passenger compartment and outside air constant. Once all three are done they are combined into one fuselage. This is just a bare structural tube, none of the electrical lines and other details have been added to the fuselage. The electrical motors for the BLI system are added at this point as well. It is important to add these early on, since these are positioned deep in the tail cone. Most aircraft already have maintenance doors in the aft of the tail-cone for the APU, which means maintenance would be obstructed by the APU alone. Therefore maintenance is only slowed down for the electrical motors.

Now that the fuselage and the main wing are done, they can be integrated. However, an important part is still missing, which is the strut. Since the strut is not a lifting device, the shape is fairly simple. It does not need control surfaces, further simplifying its manufacturing process. However, it does have landing gears attached to it and therefore needs hydraulic lines for operation. With the strut, main wing, and fuselage complete, they can be integrated.

Now that the largest parts are connected, the electrical and hydraulic lines through the fuselage can be attached. The environmental control system is integrated during this stage as well. Access to the structure is important such that the ducts from the engine can be integrated into the rest of the fuselage. These ducts have to go all the way to the tail, such that the APU can also provide the air in case of an emergency. The EPS bus will be integrated while the electrical lines are integrated into the fuselage. While these are being attached the vertical tail is also integrated. Since the aircraft has a T-tail configuration it is important to attach the vertical tail first. The horizontal tail can then be attached. While that is going on the avionics are added to the cockpit.

The aircraft is mostly complete at this point. However, some very important things still need to be added. The first of which are the landing gear and the APU. There are five landing gears to be attached, one in each strut, the nose

landing gear, and two main landing gear below the fuselage. Since the hydraulic system is already in place they can be attached to that directly. The APU is added to the tail while the landing gear is installed. Both of these integration are not in contact with the passenger compartment, meaning that work on the passenger compartment can be done simultaneously. The components such as wall panels, overhead storage, seats, etc. are integrated into the fuselage.

The propulsion system is installed last as it is the most expensive part. First the BLI propulsor will be installed. The electrical motors and the shafts were already installed in the tail-cone, thus only the BLI fan and nacelle are yet to be attached. The doors of the fuselage are installed while the BLI is being installed. This is an appropriate time to do so as the doors are not in the way after this moment, because constant access to the fuselage is no longer required. The last and most expensive element of the aircraft are the turbofan engines. These will be attached to the pylons on the wing. The BLI and engines are manufactured by another company that specialises in turbofan engines. Turbofan engines itself are very complex and complicated and, therefore, take a long time to design and manufacture.

Sustainability is an important aspect to the manufacturing of aircraft. This can be in terms of social, economic or environmental sustainability. An aspect of social sustainability is having high safety standards for the factory workers. Economic sustainability of the manufacturer could come in the form of not outsourcing part production. If parts are build in-house, it results in a higher investment cost in facilities and equipment, but lower part cost due to no transport costs. However, this is not certain. It could be that a different company could produce and transport the parts at a lower cost than what the Albatross Embracer company can provide. The transport of the parts also effects environmental sustainability, due to emissions produced during transport. This transport effect also relates to producing parts in different locations. Therefore, it is beneficial, from a sustainability point of view, to not outsource parts and to produce them in the same factory.

14.2. Conversion

The aircraft also needs to convert from fossil fuels to a carbon-neutral fuel. The fossil fuel in this case is kerosene and the carbon-neutral fuel is synthetic kerosene. These fuels have the same properties and therefore the aircraft does not need to swap any parts for its conversion. The fuel tanks and fuel lines of the aircraft will be cleaned such that no residue of the fossil fuel is left in the aircraft. This conversion will happen during one of the C-checks or D-check that the aircraft will undergo. These checks perform multiple tests on the aircraft to see if certain components need to be replaced. During these checks, it is easy to fit in a fuel tank cleaning without extra delay in returning to service.

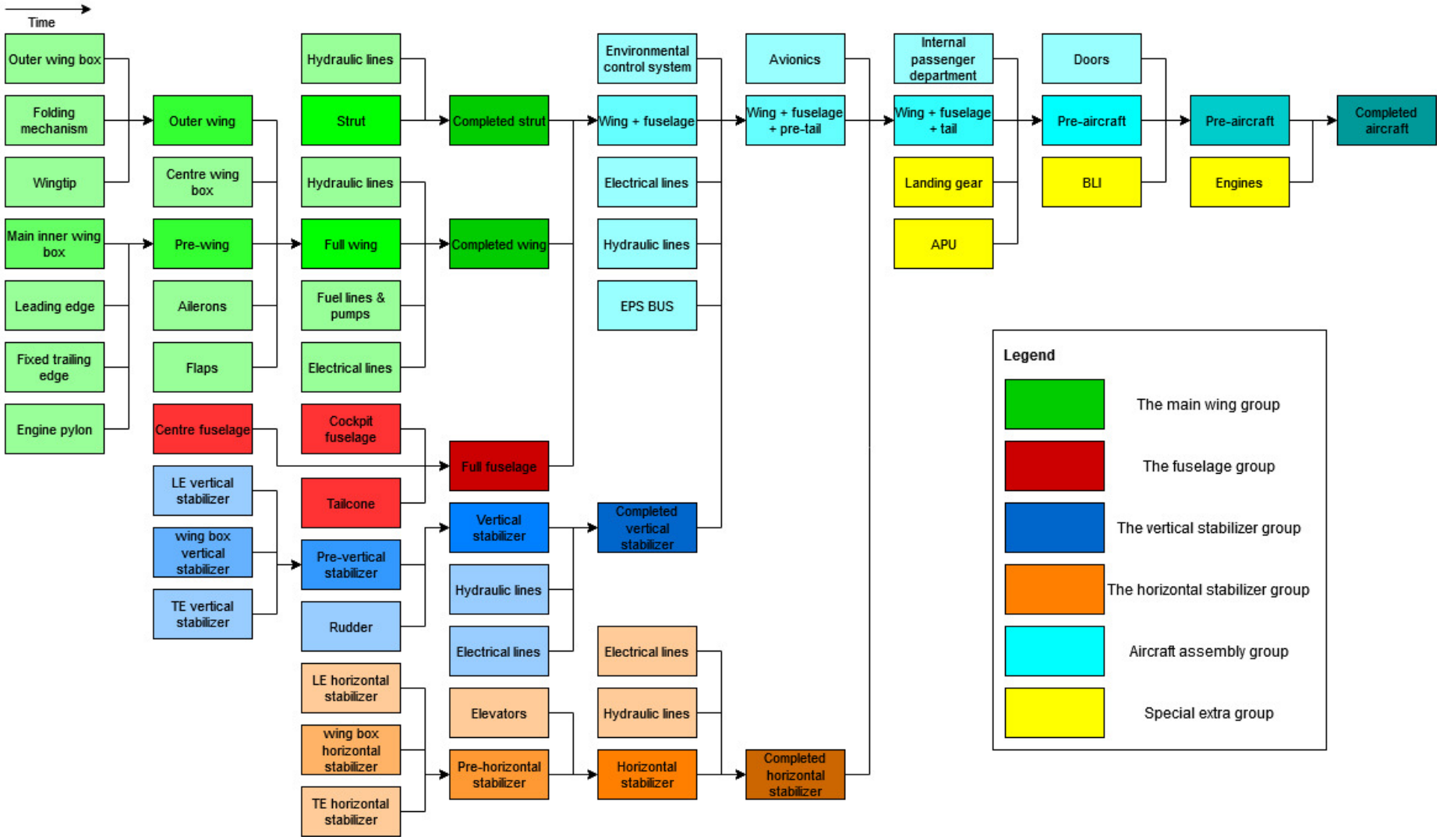

Figure 14.1: Manufacturing, Assembly and Integration plan of the Albatross Embracer

15
Logistics and Operations

In this chapter, the operations and logistics of the CNA are introduced. From the operations point of view, the CNA configuration is similar to conventional configurations, allowing for standard operational procedures to be applicable. However, due to the presence of some unconventional subsystems, there are special operational procedures that have to be implemented. The three main operations considered here are ground Operations, flight Operations and end of life operations, as explained in Section 15.1. In terms of logistics, the focus is on the conversion aspect and the fuel availability, since these two aspects are unique compared to conventional aircraft. The detailed description of these logistics aspects is given in Section 15.2.

15.1. Operations

This section describes the operational aspects of the CNA. The three main operations related to CNA are described , namely, ground operations in Section 15.1.1, flight operations in Section 15.1.2 and end of life operations in Section 15.1.3.

15.1.1. Ground Operations

The ground operations include all the different activities, starting from the aircraft's landing on the runway from previous flight, and leading to the aircraft's next take-off. A brief overview of these operational activities is shown in Figure 15.1. In Figure 15.1, the ground operations are divided into three main categories, arrival , handling and departure. After landing on the runway, the aircraft needs to taxi to the gate. During taxing, additional operations need to be carried out for the CNA, to fold the outboard section of the wing. This activity is crucial from airport operations point of view, since the type of parking gate required will change if the folding mechanism does not work. This is also illustrated in Figure 15.1. However, the risk of malfunction of the folding mechanism is already mitigated to a certain extent using redundancies and safety factors as described in Section 8.6. Thus, this should not be an issue for ground handling. If the malfunction still occurs, the aircraft will need to taxi to a different gate, suited for larger aircraft.

Once the CNA reaches the gate, the parking brakes are applied and the engines are shut down. The BLI propulsor is already set to zero thrust condition during the approach, and will be completely shut down along with the engines after parking at the gates. Once the engines are shut off, the APU can handle the electricity supply for cabin systems. However, the ground power supply should be connected as soon as possible to avoid additional emissions during unloading. This can be done by using either a direct connection to the airport‘s central grid or using a mobile unit. It is advisable for the airport authorities to use sustainable means of power generation, if mobile units are used. This will help cut down the emissions even further. Afterwards, the passengers, luggage and the cargo can be unloaded. Along with it, the servicing of the cabin such as refilling or cleaning can also be done. The configuration of the CNA is conventional in this regard and thus all these operations can be carried out using standard procedures. In terms of refuelling, the logistics of fuel supply for the airports is important for the CNA, which is discussed in detail later in Section 15.2.1.

Once the refuelling of the aircraft is complete, the payload can be loaded and the aircraft can be made ready for pushback. The APU can be used for the engine startup and will be turned off once the engines are started. It is advised for the aircraft authorities to use the sustainable pushback vehicles for CNA taxing, so that the engines are started later, only near the runway. Many of these vehicles are already being tested at different airports [1]. By using these type of vehicles, the vehicle's ground sustainability will be increased and overall airport emissions can also be decreased. The CNA design will be able to comply with such vehicles as long as their design is made with respect to conventional commercial aircraft. Further,the wing folding procedure will be initiated.

[1] URL https://simpleflying.com/schiphol-reduced-aircraft-emissions/ cited [19. June 2020]

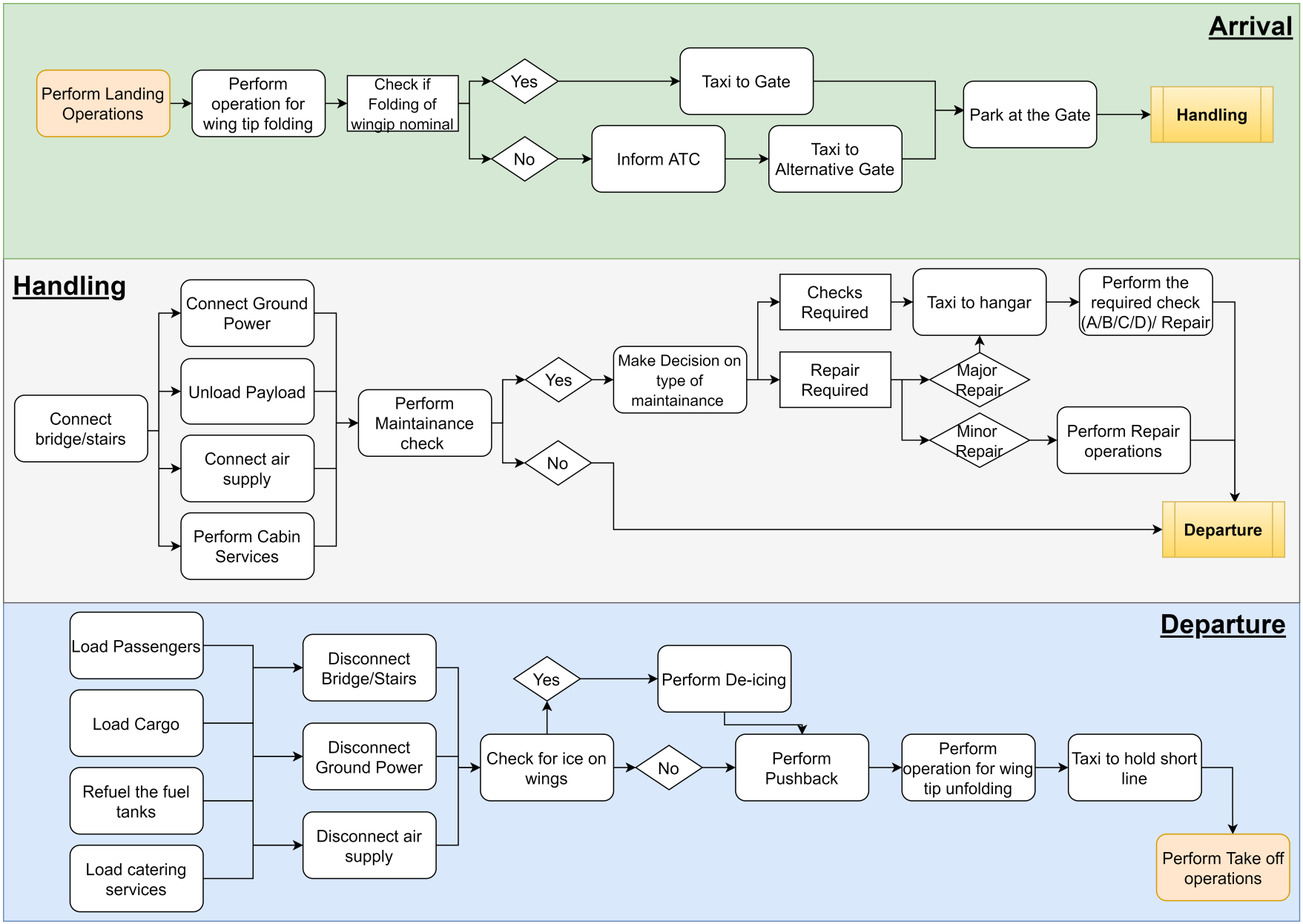

Figure 15.1: Ground Operations Concept Diagram

The time constraint on folding is fixed based on conventional time for taxiing, with a certain safety factor. Thus, this additional operation will not hinder the ground operational performance of the CNA. Another important operational aspect shown in the Figure 15.1 is related to maintenance. If the aircraft needs some maintenance, the aircraft should be able to fit in the maintenance hangar. For the CNA, this should not be a problem as the folding part is folded up to 120 deg, resulting in a vertical height of the aircraft comparable to conventional aircraft.

15.1.2. Flight Operations

The flight operations for the aircraft relate to the operations once the aircraft starts its take off roll, and continues till it lands on a runway. The main flight operations for the CNA are similar to the conventional aircraft as the flight path and the flight systems are similar. The BLI propulsor requires additional operations. But these operations only include different strategies to use the BLI propulsor effectively, so it does not induce any additional operational loads on the flight crew. The BLI is only activated in the cruise phase and during all the other phases of the flight it is turned off. However, this strategy might change in the future detailed design stages, with the increased accuracy of boundary layer data and propulsor design. In conclusion, the main flight operations for the CNA follow directly from its functional flow, as shown in the Figure 2.2.

15.1.3. End of Life Operations

The end of life operations of the CNA are important, especially considering the recyclability and sustainability requirements. The overview of the required operations is given in Figure 15.2. Once the CNA has surpassed its operation time, it will then be retired. The first phase of the retirement is the disassembly phase. In this phase, all the valuable components from the aircraft will be disassembled. Depending on the quality of the components, they will be either sent to be reused by the airline or to the certified repair shops to be inspected and get repaired. After this phase, the airworthiness of the aircraft will be lost and it will become business waste instead. The next phase is the dismantling phase. Some of the parts after dismantling will be sent for reuse in the non-aerospace application and the rest of waste will be sent for recycling. For the CNA, more than 90 % of the primary structure will be recyclable, as will be described Section 17.3. Thus, the required disposal activities will be considerably lower.

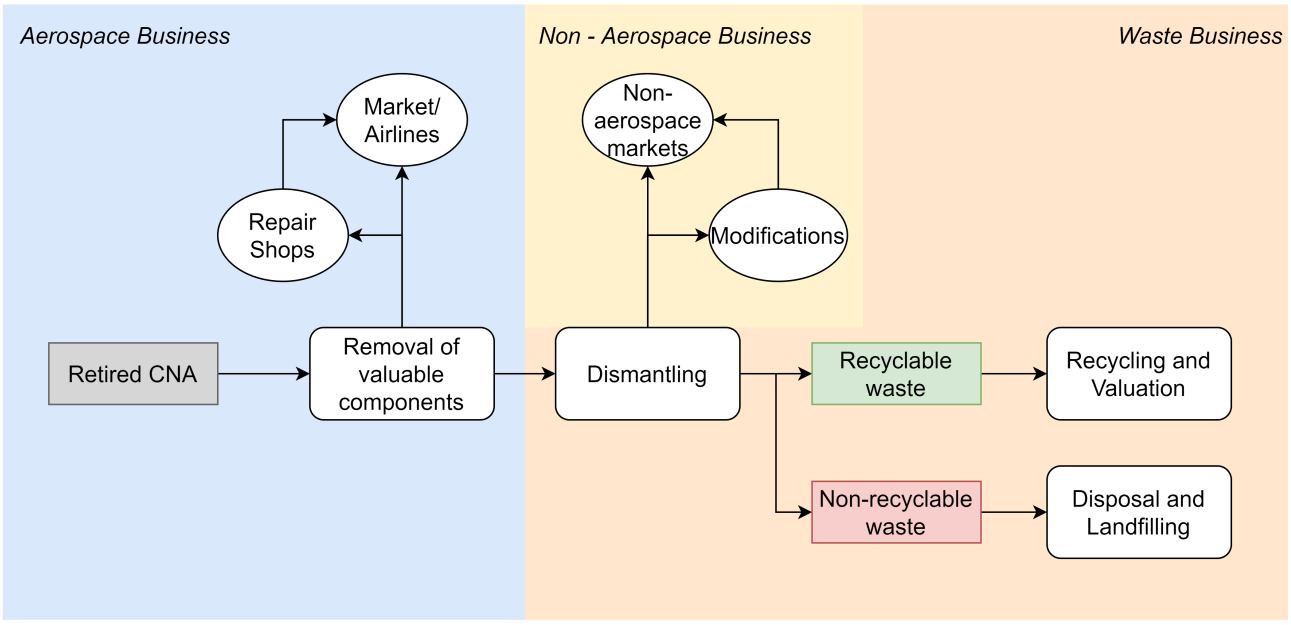

Figure 15.2: End of life operations

15.2. Logistics

The logistics concept of the CNA design is similar to that of conventional aircraft. However, there are two special aspects which need to be specifically addressed for the CNA design, as these are unique for this design. These two aspects are the fuel production and availability and conversion of the aircraft to the synthetic kerosene based propulsion. Both of these aspects are described in detail in Section 15.2.1 and Section 15.2.2 respectively.

15.2.1. Fuel

As mentioned earlier, the CNA uses synthetic kerosene as the post conversion energy source. Thus it requires special attention towards its production and availability at the airports and the logistics associated with it. The initial challenge is associated with the logistics involved in the production of the synthetic kerosene. The production of the synthetic kerosene can be broken down into into three main steps. The first step is the capturing of the carbon from air or a carbon rich source. The second step is to capture hydrogen from demineralised water. The final step is to combine the carbon and hydrogen using energy from renewable electrical energy sources. Thus, the carbon emissions produced from the aircraft feeds back towards the production of fuel, making synthetic kerosene carbon neutral as well as contributing towards a circular economy. The production of synthetic kerosene is at its infant stages at the current time, if compared with the total kerosene demand [50] [2]. However, with the increasing interest in the sustainability goals and the synthetic kerosene itself, it can be expected that the production scale will increase substantially. Especially, since other sectors such as automotive are also considering the use of synthetic kerosene [3]. Thus, the logistics involved with the production process of the fuel is expected to be feasible, considering the entry into service period of the aircraft.

The next logistic challenge is the supply of the synthetic kerosene from the plant to the airports. This can be managed mainly through two possible scenarios. First scenario is the centralised production. In this scenario, a large scale production plant is installed and the fuel is distributed from this central hub to different branches. The second scenario is the distributed production, where production is done on-site near the airports and then fuel is supplied using pipe lines. This second scenario is the promising strategy for the initial phases, since it requires smaller investments from the authorities. However, it will have a drawback considering the long term economic benefits due to small scale production. Therefore, for long term, a centralised production will be an economically favourable approach.

The biggest advantage of the synthetic kerosene, in terms of logistics, in both the scenarios is the required storage and handling infrastructure. Since its similar to the conventional kerosene, little to no changes in the infrastructure are needed. This gives further incentive to airport authorities and the airlines to invest in the synthetic kerosene. Thus, it can be concluded that the logistics involved with the fuel handling at the airport will not require additional investment, since the existing infrastructure is compatible with synthetic kerosene. Furthermore, no major drawbacks are foreseen with respect to the logistics required from the production point of view.

15.2.2. Conversion

One of the features of the design is its ability to convert from conventional jet fuel to a carbon neutral energy source. For the CNA, the post conversion energy source is synthetic kerosene. The use of synthetic kerosene allows for a realistic, yet sustainable and efficient design. Along with design benefits, it also allows advantages in terms of logistics of the conversion. Synthetic kerosene has a similar chemical structure as regular kerosene. Thus, no major modifications are needed for the propulsion system and fuel system. Only the fuel tanks will need to cleaned before using synthetic kerosene. This will ensure that no mixing with the impurities or with earlier used kerosene would happen. In terms of time required for the conversion, since only the wing tanks need to cleaned, it will definitely fulfil the one month time requirement. In order to have an exact estimate and to avoid additional ground time for the aircraft, this conversion procedure will be conducted as a part of aircraft's regular C check. The C check is a regular maintenance check which is conducted every 3000 flight hours. It involves detailed inspection of airframe, engines, heavy lubrication, and a small part of the corrosion prevention program [67]. A regular C check takes about average of 5 days of ground time [67]. After adding the conversion process, the new expected ground time is one week. This conversion process is thus economically feasible from the perspective of both time and cost. Furthermore, it satisfies the customer's requirement for the conversion time of one month.

[2] URL https://newmobility.news/2019/02/11/biokerosene-is-not-booming-yet/ cited [25. June 2020]
[3] URL https://www.bosch.com/stories/synthetic-fuels/ cited [25. June 2020]

16
RAMS Characteristics

RAMS stands for reliability, availability, maintainability and safety. Throughout the design process, numerous design choices were made to improve the RAMS characteristics. Since the aircraft sees use in a commercial environment, a good operational availability is of paramount importance to the commercial success of the aircraft. Availability is affected by both the aircraft's reliability and maintainability as documented in Section 16.1 and Section 16.2 respectively. The design choices that lead to an improved availability and safety can be found in Section 16.3 and Section 16.4.

16.1. Reliability

The reliability is the probability of system failure during the operational life of the CNA. Section 16.1.1 explains the reliability of the propulsion system, whereas Section 16.1.2 shows the overall reliability of the aircraft.

16.1.1. Propulsion System Reliability

To assess the reliability of the novel propulsion system of the CNA, it is important to first look into whether there are any additional risks that are introduced which could lead to partial or catastrophic failure of the aircraft. If there are any additional risks it is crucial to make sure that there are possible ways to mitigate the risk. If this is not possible then the introduced risk becomes a design killer as the aircraft can then not meet the top level safety requirements.

Looking into the UHBPR turbofan engine, it can be seen that this is just a normal turbofan engine. The only difference between the UHBPR turbofan engine and other engines used on current aircraft, is the fact that the UHBPR turbofan engine has a higher BPR, which just means that a greater proportion of the total thrust of the engine comes from the bypass flow. This means that the turbofan engines and their novel UHBPR do not lead to any additional risks. The same can be said for the fuel storage and distribution system, which follow conventional methods that are used on current aircraft.

The main risk introducing part of the propulsion system is the inclusion of the BLI Propulsor. The inclusion of the BLI propulsor adds the additional risk of the BLI propulsor failing. However, this has no effect on the overall reliability of the propulsion systems as the BLI propulsor is not a critical thrust producer as the BLI propulsor is only used during the cruise phase. This means that the turbofan engines have the capability of providing all of the thrust in case the BLI propulsor does fail. However, on the other hand the fan blades of the BLI propulsor can break or burst, meaning that they become projectiles that have large velocities due to the high rotational velocity of the fan. This leads to the risk of the fan blades penetrating the duct of the BLI propulsor and thus damaging either the tail or other parts of the fuselage structure. This could lead to problems in controllability and stability of the aircraft. However, the risk of this can be reduced by further strengthening of the duct, such that it would not be possible for the fan blades of the BLI propulsor to pass through the duct of the BLI propulsor and damage any other parts of the aircraft's fuselage. This means that there are various ways the risk of tail-strike or fuselage-strike can be mitigated, meaning that it does not affect the overall reliability of the propulsion system significantly and thus, the propulsion system should meet the top level reliability requirements. However, it is important to note that this does lead to an increased mass of the system. Due to this it is important that in the later stages of the design of the BLI propulsor an analysis is carried out on where the parts of the bursted fan blades are most likely to penetrate the duct or hit the tail, such that only these specific parts are structurally reinforced. Doing so will minimise the additional mass of the system.

16.1.2. Reliability of the Overall Aircraft

The CNA features many aspects linked to current operating conventional aircraft, which are proven to be reliable thanks to the numerous flights which are operated every day. The focus of reliability is then centred on the unconventional aspects of the design, followed by a qualitative analysis of the probability of a catastrophic failure

An unconventional aspect of the aircraft is the wing tip folding mechanism. As mentioned in Section 8.6.3, each folding mechanism is equipped with two actuators, where one actuator is operating and the other is actuated in case the main one fails. The reliability of the mechanism is further enhanced by the structural lightness of the folding parts of the wings, which are not meant to carry fuel, hence the required load on motors is lower. Furthermore, the ailerons

are not placed in the folding part of the wings, which means that roll control is independent of folding mechanism failure, thereby providing more reliability on the roll performance.

For the BLI electric power system, the electrical non-moving elements (such as wires) are proven to have a very high reliability, however the motors provide the shaft power to the BLI propulsor by means of a common shaft. In case one motor fails, it has to be ensured that the second motor can operate independently of the other, so power can be delivered without losses due to the shaft being slowed down by the other motor. As mentioned in Section 9.13.1, the use of co-axial shafts prevents this issue, thus increasing the overall reliability of the system.

Regarding the risk of catastrophic failure, a top level requirements is that the aircraft should have a risk of catastrophic failure due to the carbon neutral propulsion system which is lower than 10^{-9} per flight hour. This is also mentioned in the CS-25 regulations (AMC 25.19 6.c.3) . As this requirement is also valid for currently flying aircraft such as the A320neo, a qualitative comparison of the propulsion systems was performed to assess whether the CNA has the same probability of catastrophic failure.

From the reliability analysis, it can be noticed that the propulsion system differs from the conventional jet propulsion system only by the UHBPR engines and the BLI propulsor. As having a higher bypass-ratio only results in a higher mass flow of cold air, this does not cause any relevant increase or decrease of probability of catastrophic failure with respect to the A320neo engines.

Besides that, the BLI propulsor has a reliability comparable to propellers. Even in the case of failure during the flight, the aircraft is still able to perform an emergency landing with the two turbofans. Furthermore, in the event that a titanium blade spins off, the structure of the duct is strong enough to contain the impact and leave the tail unharmed. Considering that the conversion from normal kerosene to synthetic kerosene does not change the propulsion system reliability, it can be qualitatively concluded that the risk of catastrophic failure of the CNA is less than 10^{-9} per flight hour, hence the top-level requirement is met.

16.2. Maintainability

For any airline, an aircraft that is easy to maintain is desired. "Maintainability pertains to the ease, accuracy, safety, and economy in the performance of maintenance actions." [68, p 87]. Maintainability is taken into account in the design process directly, by a series of maintainability requirements that are formulated for each subsystem. The main requirements are formulated in Table 16.1 where REQ-CN-SAFE-8 is the top level requirement. Additionally, the structure should consist of parts that can be removed relatively easily such that they can be replaced. Easily in this context relates to the fact that not many other parts must be removed before reaching the broken part. How parts are connected exactly is beyond the level addressed in this report, so assessing the aircraft maintainability is difficult. However, two main design choices were made to improve maintainability. First and foremost, the aircraft engines are mounted below the wing, which improves its accessibility drastically. Secondly, the folding wingtip rotates by more than 90° in order to lower the aircraft total height such that it fits in standard maintenance hangars used by the industry today. Further assessment of the maintainability is recommended in next design phases.

Table 16.1: Main requirements with respect to maintainability

Identifier	Requirement	Source
REQ-CN-SAFE-8	Means must be provided to allow inspection (including inspection of principal structural elements and control systems), replacement of parts normally requiring replacement, adjustment, and lubrication as necessary for continued airworthiness.	CS 25.611
REQ-CN-WING-6	The wing structure shall consist of different subassemblies in order to speed up the manufacturing and maintenance processes.	Design
REQ-CN-WING-7	Each wingbox section shall have an access hatch for maintanance and inspection purposes.	Design
REQ-CN-CABIN-9	The interior linings shall consist of different parts that can be easily removable by one technician, to allow inspection of the fuselage structure.	Design
REQ-AE-PROP-19	The engine nacelles shall have easy access hatches to provide access to engine components for inspection and maintainance.	CS 25.901

16.3. Availability

Airlines can only turn a profit with an aircraft when it is in the air. The more and the longer the aircraft is grounded for a certain reason, the less profitable it becomes. Especially for low cost airlines, fast turn-around times and a high availability are critical to their operations. Since they operate a very tight schedule, one small malfunction that reduces the availability for only a small amount of time is enough to have a huge impact on the flight scheduling of that airline. This can have devastating effects in terms of reactionary costs, especially when losing slots at airports[69].

Availability is the conjunction between reliability and maintainability. It is defined as "the probability that the system will be in an operational state when called upon at a random point in time"[68, p 90]. A system with a high availability is ready to be deployed when needed because it is both reliable and maintainable. When designing for availability, the objective is to reduce the aircraft's downtime as much as possible and there are certain means to do that. By preventive maintenance, problems can be identified and alleviated before they can have a severe impact on the operations. Longer service intervals (for example by choosing materials with low crack propagation rates) and a small probability of failure (for example by putting novel aircraft parts through extensive testing) further reduce downtime. If failure does occur, a redundancy in systems can help to keep the aircraft operational for a short period of time, before requiring a repair. This can be done if the number of components that are allowed to fail are documented, as well as the limits of operating with a reduced amount of redundancy.

Availability is integrated in the design process whenever possible in the current design phase. Two examples where availability had an impact on design choices are highlighted. In the first example, the aircraft is designed such that it can fly without the BLI in case there would be any malfunction in the BLI system. This means the airline's scheduling is not affected that day and the aircraft remains operational. However, the airline prefers to operate with the BLI running in order to decrease fuel burn. In the second example, the folding wingtip mechanism houses two actuators that rotate the wingtip. The system is specifically designed in such way that the mechanism can function with only one actuator. This is extremely important, since the aircraft would remain immobilised at an airport after touchdown or would be prevented from take-off if the mechanism would not work. This would have a profound impact on the availability of that aircraft.

16.4. Safety

The CNA was designed according to safety requirements to comply as much as possible with the airworthiness regulations. For example REQ-CN-SAFE-1 is satisfied with the cabin layout that is designed for all passengers to be able to evacuate within 90 seconds with half the exits blocked. Furthermore, the vertical tail was designed to ensure controllability in the case of one engine inoperative, satisfying REQ-CN-SAFE-7. The CNA has several novel features that may pose higher safety risks compared to conventional aircraft. These are for example the very slender main wing, the use of synthetic kerosene, the BLI propulsor aft of the fuselage, and the folding wingtips.

The slender wing was designed with a safety factor of 1.5, and the torsional rigidity of it was increased to avoid flutter inside the flight envelope. The CNA is equipped with fire extinguishing system to in case of fire, which synthetic kerosene is expected to have equivalent flammability as jet fuel as the chemical compositions are almost identical [50]. The duct of the BLI propulsor is able to prevent blades from bursting out. For the folding wingtip, the control scheme was established that does not allow the aircraft to take-off with its wingtips retracted. Furthermore, the mechanisms are designed to withstand the design ultimate flight load with one malfunctioning pin, and the limit flight load with two malfunctioning pins.

As discussed above, the safety of the aircraft was always considered throughout the design process of the CNA. This shows that the novel features of the CNA do not pose serious safety flaws at this stage of the design. In order for the CNA to be certified, there are still numerous safety aspects that needs to be investigated. These include the damage tolerance from for example bird strikes, its crashworthiness, and the ditching characteristics unique to the CNA.

17
Design Summary

The results of the design process are summarised in this chapter. First off, the configuration of the aircraft is described in Section 17.1 and its mass and cost estimations are discussed in Section 17.2. The design's improvements compared to existing aircraft are summarised in Section 17.4 and its compliance with requirements is described in Section 17.5. Finally, the different iterations and their results are summarised in Section 17.6.

17.1. Aircraft Configuration

In this section, the final aircraft configuration is summarised along with the differences in layout from the conceptual design phase. A major change to the propulsion system was the addition of the BLI propulsor after the initial conceptual design phase. In this phase, the winning concept was the braced wing aircraft[3]. The second best concept featured a BLI propulsor. It was found that including this propulsor on the winning concept would result in a more efficient aircraft. Hence, these concepts were combined to form the configuration that was designed in the detailed design phase.

The wingspan was increased slightly from 49.6 m to 50.6 m, to improve aerodynamic efficiency. This meant that the folding section of the wing would have to be slightly longer as well. This proved to be possible and hence was adopted for the final design. In addition to this, the strut braces were made to have roughly the same sweep as the main wing because it was found that this would decrease the structural weight.

The fuselage was decreased in width from 4.2 m to 3.9 m. This was done because it was found that the previous version of the fuselage was slightly larger than needed. However at the same time, the height of the fuselage was also increased from 4.2 to 4.3 m, giving it a double-bubble cross-section. This was done to accommodate the central wing-box inside the body of the aircraft since a fairing would affect the boundary layer reaching the aft BLI propulsor. This increase in fuselage height also has the benefit of increased passenger comfort due to the cathedral like ceilings at 2.34 m.

The landing gear had to go through quite a few changes because of issues with the allowed tip-back angle. The nacelle of the BLI propulsor caused the angle to become smaller than needed if a conventional landing gear was used. Keeping a tri-cycle configuration would result in very tall landing gear, also resulting in an unrealistic large wheel-span. This would be a problem for two reasons, for one it would add more weight to the landing gear and second, large fairings would probably be required and these would interfere with the boundary layer causing undesirable interference for the BLI propulsor. Hence, it was chosen to move the main landing gear backwards such that their height remained low (similar to competing aircraft). Extra landing gears were added to the wing struts for two reasons, one was to compensate for the increased load on the nose gear and the second was to provide lateral stability.

17.2. Aircraft Mass and Cost Estimation

Through careful budgeting over the course of the design process as described in Section 4.6, the two crucial resources of mass and cost available to the different departments were subjected to an iterative process. This process allowed for tight integration between the departments allowing each one to limit and estimate their resource usage according to the latest aircraft-wide values. Each department worked with an overall limit within which they could freely move resources. The specific resource allocation within the department is discusses within the respective chapters. With these latest estimations fixed, an overall picture of both the aircraft mass and cost could be sketched. The aircraft itself was estimated with a MTOW of 70459 kg. Splitting this up into departments, the department-wide masses of 5809 kg for the propulsion group, 10274 kg for the aerodynamic group, 12017 kg for the structure group and 1176 kg for the control group was estimated. The remaining mass was grouped in an "other" department which contains all additional masses that could not be estimated in the different groups. This breakdown can be seen in Figure 17.1. At this point in the design process, the actual values were assessed to potentially end up 5% higher due to contingencies. The production cost was taken into account in a qualitative manner by all departments by trying to actively reduce costly elements and taking into account financial effects of design choices. The quantitative estimation from the different components was performed in Section 18.2 and led to an estimated 58.4 M$ production cost and 1.3 M$ development cost per aircraft. The total cost per aircraft was thus estimated at 59.7 M$ (in the case of either Airbus or Boeing buying up the design) and the cost breakdown per aircraft can be seen in Figure 17.2.

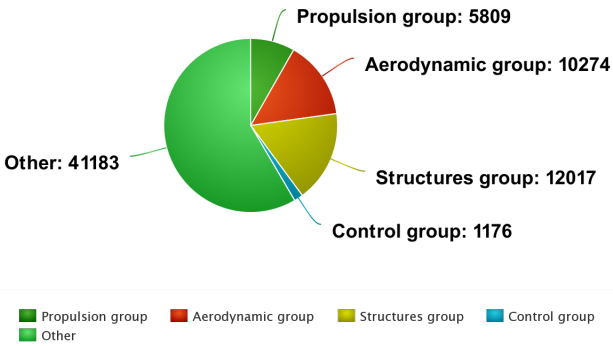

Figure 17.1: Mass budget breakdown for the MTOW in kg

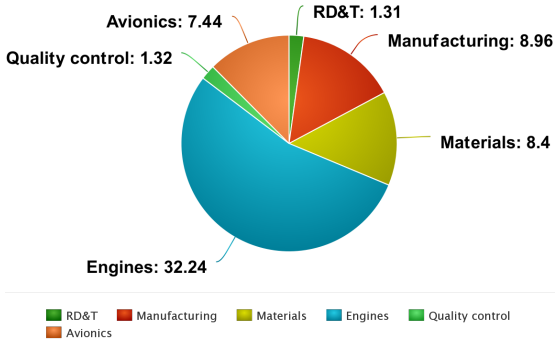

Figure 17.2: Cost budget breakdown for the total cost per aircraft in M$

17.3. Aircraft Material Breakdown

One of the CNA's top level requirements was to have 75% of its primary structure be recyclable by mass (REQ-CN-SUS 1). In order to meet this requirement, many parts of the aircraft were designed with materials that are easier to recycle. For example, aluminium was preferred compared to steel, titanium or carbon fibre composites. In addition to this, aluminium alloys were also analysed to find the alloys that were more sustainable in the sense that they are easier to manufacture parts with (lower energy required) and also more recyclable. Although a large amount of the aircraft is composed of aluminium allows, some components required different properties, such as the landing gear. The landing gear are manufactured using steel, which is also very recyclable compared to carbon composites [1].

The primary structure of the aircraft is defined as the fuselage structure, the wing structure, the empenage and the landing gear. The masses of these components along with their material and recyclability are presented in Table 17.1.

Table 17.1: Primary structure material breakdown

Components	Mass [kg]	% Primary Structure Mass	Material	Recyclable
Wing Group	9235.8	40.7	Aluminium 2014-T6	Yes
Fuselage Group	8948.5	39.5	Aluminium 2014-T6	Yes
Landing Gear	2975.4	13.1	Steel	Yes
Engine integration	983.4	4.3	Aluminium 2014-T6	Yes
Tail Group	534.1	2.4	Aluminium 2014-T6	Yes
Total	22677.2	100	[-]	100%

It can be seen that the primary structure is actually 100% recyclable. However, some parts like windows, epoxy adhesive, etc will reduce this number but it will be at least 90%. It must be noted however, that the primary structure only consists of 55% of the OEW. The remaining OEW mass is taken up by the components not part of the primary structure such as the hydraulic systems, control surfaces, the engines, electrical cables, and furnishings. Hence, a 90% recyclability of the primary structure does not mean 90% recyclability of the entire aircraft. However, the primary requirement (REQ-CN-SUS 1) given by the customer is still met and surpassed, which also improves the sustainability of the CNA.

17.4. Improvements Compared to Existing Aircraft

The CNA combines various novel technologies to improve structural, aerodynamic and propulsive performance. These technologies culminate in to a very efficient aircraft with improved characteristics compared to the competing aircraft such as the Airbus A320neo.

The CNA offers a significant improvement in the lift to drag ratio and a lowered TSFC compared to the A320neo. This results in an improvement of 17% fuel burn in terms of kilograms of fuel burnt per passenger kilometre. Apart from reducing carbon emissions (during the pre-conversion phase) the reduced fuel will greatly reduce the operating costs of customer airlines.

The CNA has smaller engines because of its decreased thrust requirement, owing to the improved L/D. Conserva-

[1] URL `https://www.steelsustainability.org/recycling` cited [30. June 2020]

tive analysis shows that the noise is either similar or only slightly lower than the A320neo. However, it is predicted that more detailed analyses would show that the CNA is quieter, due to the fact that it produces 75% of the thrust of A320neo. Apart from this, the CNA also cuts down on emissions of NOx emissions by up to 38%.

17.5. Requirement Compliance

The CNA was developed based on a set of customer, user, and legal requirements. These requirements are presented along with their compliance status in Table 17.2. The sections explaining the compliance of each requirements is also present. The requirement which has been complied with is marked with (✓), requirements which have been partially complied with are marked with ( ) while requirements which have not been complied with are marked with (X). The requirements that are partially met or not met are discussed after the compliance matrix.

Table 17.2: Requirement compliance matrix

Requirement ID	Description	Source	Verf.	Relevant Sections
REQ-CN-PERF-1	The CNA shall have a cruise speed of Mach 0.78.	Customer	✓	Section 9.3 and Section 12.1
REQ-CN-PERF-2	The CNA shall have a maximum range of at least 3400 nm.	Customer	✓	Section 5.3
REQ-CN-PERF-3	The CNA shall carry a payload of 20 tons.	Customer	✓	Section 5.3
REQ-CN-PERF-4	The CNA shall have a range at max payload of 2150 nm.	Customer	✓	Section 5.3
REQ-CN-PERF-5	The CNA shall be able to carry 194 pax in a high density lay-out and 7 LD3 containers underfloor at max payload.	Customer	✓	Section 6.3
REQ-CN-PERF-6	The CNA shall be able to carry 150 pax in 2 class layout and 7 LD3 containers underfloor at max payload.	Customer	✓	Section 6.3
REQ-CN-PERF-11	The CNA shall develop lift to counteract the MTOW.	CS 25.331	✓	Section 7.4
REQ-CN-PERF-17	The CNA shall be able to convert to carbon neutral within one month.	Customer	✓	section 14.2
REQ-CN-PERF-18	The CNA shall provide electrical power to all electrical subsystems.	Design	✓	Section 9.12
REQ-CN-PERF-19	The CNA shall be able to take-off within a runway length of 1800m at sea level.	Design	✓	Section 13.1
REQ-CN-PERF-20	The CNA shall land within 1800 m, measured from 15m above the runway until standstill, on a paved runway at sea-level conditions and maximum landing weight.	Design	✓	section 13.3
REQ-CN-PERF-21	The CNA shall be able to climb out with one engine inoperative with a climb gradient of 2.4%.	CS 25.121	✓	Section 13.2
REQ-CN-PERF-24	The CNA shall have a rate of climb of 1800 ft/min in clean configuration, at sea-level conditions.	Design	✓	Section 13.2
REQ-CN-PERF-28	The aircraft shall have a climb gradient of 2.4 % during take-off.	CS 25.111	✓	Section 13.2
REQ-CN-PERF-31	The CNA shall have a wingspan of less than 36 m while on ground.	User (Airport)	✓	Section 8.6
REQ-CN-SAFE-1	All passengers shall be evacuated within 90 seconds with half the exits blocked.	CS 25.803	( )	Chapter 6
REQ-CN-SAFE-2	The emergency slides shall not interfere with any parts of the airframe when deployed.	Design	✓	Chapter 6
REQ-CN-SAFE-4	The CNA shall have a 10^9/flight hour risk of catastrophic failure	Customer	( )	Chapter 16.1
REQ-CN-SAFE-5	The CNA shall possess static stability during all flight phases.	Design	✓	Section 10.4
REQ-CN-SAFE-6	The CNA shall possess dynamic stability during all flight phases.	Design	( )	Section 10.4

REQ-CN-SAFE-7	The CNA shall be designed so that it is controllable if all engines fail.	CS 25.671d	✓	Section 9.12
REQ-CN-SAFE-9	The CNA shall not be adversely affected by flutter at any point in the flight envelope.	CS 25.629	✓	Section 8.4
REQ-CN-ECON-5	The CNA shall enter into service in 2030.	Customer	✓	Section 18.1
REQ-CN-ECON-6	The list price of the CNA shall be $110 million.	Customer	✓	Section 2.4
REQ-CN-ECON-7	The CNA shall be capable of serving all airports currently served by the Airbus A320 or Boeing 737.	Customer	✓	Section 8.6 and Section 9.12
REQ-CN-SYS-SUS-1	The CNA's primary structure shall be recyclable for 75% of its mass.	Customer	✓	Chapter 6 and Section 8.3.2
REQ-CN-SYS-SUS-2	The CNA shall have a 10% emission reduction per passenger kilometre with repect to A320neo/ 737max whilst using fossil fuel.	Customer	✓	Section 9.9
REQ-CN-SYS-SUS-3	The CNA shall produce no more than 96.5 EPNdB at the lateral full-power reference noise measurement point as described by ICAO annex 16.	Customer/ Legal	( )	Section 12.2
REQ-CN-SYS-SUS-4	The CNA shall produce no more than 91.3 EPNdB at the flyover reference noise measurement point as described by ICAO annex 16.	Customer/ Legal	( )	Section 12.2

1. **REQ-CN-SAFE-1** This requirement was not quantitatively verified. However, the conventional configuration of the fuselage and the fact that the doors and emergency exits are placed in accordance with regulations, it can be concluded that this requirement would be verified when the actual evacuation test is conducted as part of the certification process.

2. **REQ-CN-SAFE-4** This requirement was not quantitatively verified, however all the novel systems on the aircraft are designed to increase reliability. And the BLI propulsor, which is novel does not cause catastrophic failure if it were to fail. Hence, it can be concluded that the CNA can be designed for this requirement during the detailed design stage of product development.

3. **REQ-CN-SAFE-6** This requirement was only partially verified. The CNA is designed to possess longitudinal static stability, however the lateral dynamic stability is not analysed because of the limited time. It is expected that lateral stability can ensured with more detailed analysis since the aircraft has a conventional tube-wing configuration.

4. **REQ-CN-SYS-SUS-3** The aircraft noise was measured in SEL and not EPNdB. However, the CNA was almost the same noise level as an A320neo using SEL. This would likely mean that the CNA also match the EPNdB requirement.

17.6. Iteration and Results

The CNA design involved building design tools, verifying, and then validating these tools. All the tools were connected by linking the outputs from one to the inputs of the other, forming a chain of data flow as explained in the Section 4.2 and depicted in Figure 4.2. In total, three complete design iterations were performed. The OEW of the class I estimate converged within 1%. The variations of the OEW and MTOW with each iteration are shown in Figure 17.3. The final percentage difference between the class I and class II OEW was 0.63%. The final values for OEW, MTOW and fuel mass are 41272 kg, 70469 kg and 9188 kg respectively.

The reason for the initial divergence in masses was due to the fact that the OEW calculated from the class I method was underestimated. Furthermore, the L/D and TSFC values also changed from the baseline values throughout the iteration process. The L/D and TSFC however were also almost converged in the third iteration; the values for TSFC and L/D did not change much between the second and third iteration.

There were also a few major design changes that occurred during the iterations. The major change was the updated landing gear configuration. This was caused by the increased lift-off angle during rotation which meant that the landing gear would have to become very big if the tricycle configuration was used. Hence the configuration was changed to the one described in Chapter 11. Once the iteration process was completed, the final aircraft was analysed in terms of performance to verify that all the performance requirements are met, as described in Chapter 13.

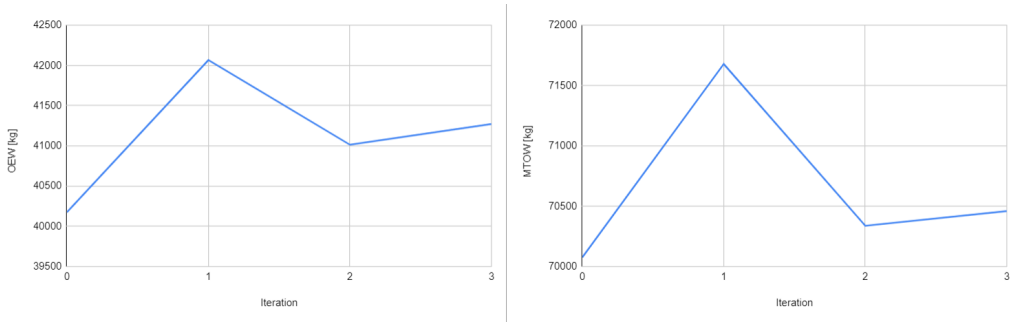

Figure 17.3: OEW and MTOW changes with iteration

17.7. Sensitivity Analysis

In order to quantify the effect of changing some of the design parameters of the CNA on its fuel efficiency, a sensitivity analysis was performed on the aircraft. This could not be done very rigorously; the most accurate way to perform a sensitivity analysis on the entire aircraft design would be to change certain values such as the L/D and then do several design iterations based on the new L/D until the OEW converged. However, this would not be possible as completing one design iteration would take about one hour, and if five iterations have to be performed for five different L/D, TSFC and OEW values, then the total time would exceed 75 hours. Instead a different approach was followed.

The sensitivity analysis was performed by changing the values of L/D and then finding the increase in fuel mass required to still meet the range requirement at a payload of 20 tons. This change in fuel weight would also change the MTOW. This would of course mean that the OEW would also have to change as parts such as the turbofans and wings would get heavier or lighter based on the MTOW. Since a full design iteration could not be performed to find the new MTOW, an empirical relationship between OEW and MTOW was used. This was done based on the data of existing aircraft earlier used for the class I estimation used in the conceptual design phase [3]. The resulting linear relationship between OEW and MTOW was adjusted to fit the CNA by increasing the y-intercept from 9204 to 10903 based on the final masses obtained in Section 17.6. Essentially, the CNA has a higher OEW for a given MTOW than the conventional aircraft used to obtain the relationship, likely due to the addition of the BLI system which adds roughly 1000 kg to the OEW.

Finally, the sensitivity analysis was performed by changing the L/D, TSFC and OEW by 10% in each direction. The results are presented in Figure 17.4 where each line shows the effect of changing a different parameter. It can be seen that the CNA can meet the fuel efficiency (or emissions reduction) requirement (REQ-CN-SUS-2) even in the case that the OEW, TSFC or L/D values are 10% worse than predicted. A 10% change in either of the three parameters results in a 8% change in fuel burn. It was found in Section 10.4.1 that the OEW predicted using the class II estimation was within 1% of the reference aircraft, hence it is predicted that this parameter will remain close to the value predicted. The L/D and TSFC were also found to be accurate via validation, both these values can get 6% worse in conjunction and the CNA will still meet the requirement for 10% emissions reduction.

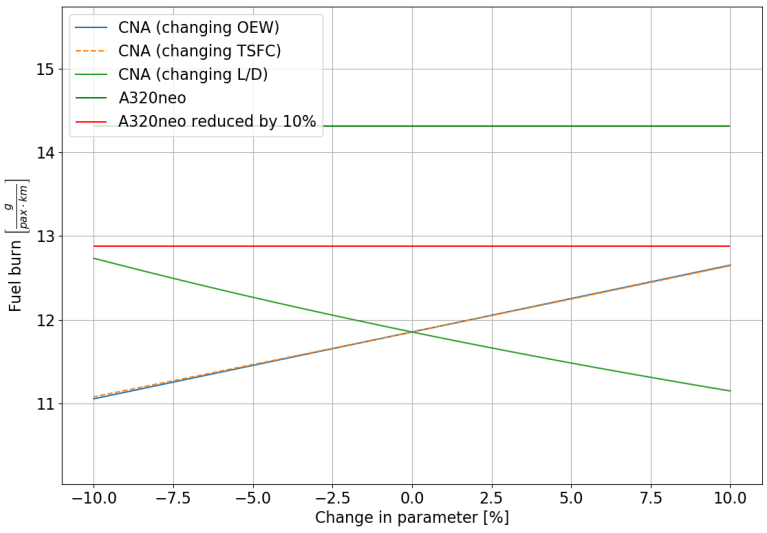

Figure 17.4: Effect of various parameters on fuel burn

18
Financial Analysis

This chapter analyses and describes the financial aspects of the design and evaluates the financial feasibility and profitability for both aircraft manufacturer and user. This is achieved through an analysis of the development cost of the design in Section 18.1 and of its production cost in Section 18.2 which are specifically relevant to the manufacturer. The direct operational cost is then analysed in Section 18.3 which is of importance to the end user. Finally, the return on investment is evaluated in Section 18.4, which reveals the overall profitability of the design for a potential client manufacturer.

18.1. Development Cost

Before the production of the aircraft begins, large effort is put into the research, development and testing (RD&T) of the aircraft design. This of course also leads to a RD&T cost, which is then also part of the total cost of the aircraft. This can be estimated using the DAPCA IV cost estimation method. The DAPCA IV cost estimation method is a preliminary cost estimation method and was also chosen for this reason, since the design of the CNA is still in its initial stages. In the DAPCA IV method, the RD&T cost is broken down into the Engineering cost, Tooling cost, Development Support cost and Flight test costs which are all dependent on the maximum velocity of the aircraft ($V_{\max}$) in knots, the empty weight of the aircraft (EW) in lbs, the production Quantity (Q) and the number of aircraft that are used for flight testing (FTA).

The engineering cost accounts for the time that is spent on airframe design and analysis, test engineering, configuration control and systems engineering. Most of the engineering hours are in fact spent during the development stage, however it is also possible that a small proportion of the engineering time is also spent on the production phase, but this proportion of the engineering time is accounted for in the RD&T stage. The total number of engineering hours is calculated using Equation (18.1a) and to calculate the engineering cost, the total number of engineering hours can be multiplied by the hourly rate. The tooling cost is dependent on the tooling hours, which is the time spent on preparing the production phase. The tooling hours account for the time spent on designing and manufacturing of tools, moulds and dies and the preparation of the numerically controlled production. The tooling hours can be calculated using Equation (18.1b) and can be converted to tooling costs, by multiplying by the hourly cost of this phase. The Development Support cost includes nonrecurring costs that come from making models and test pieces during the development phase of the aircraft's design process. Furthermore, costs of simulation tools for development are also included in the development support costs, which can be calculated using Equation (18.2a). The flight test cost can be calculated using Equation (18.2b). This includes all of the costs which come from the tests to show that the aircraft meets all airworthiness requirements.

$$H_E = 4.86 \cdot EW^{0.777} \cdot {V_{max}}^{0.894} \cdot Q^{0.163} \qquad H_T = 5.99 \cdot EW^{0.777} \cdot V_{max}^{0.696} \cdot Q^{0.263} \tag{18.1a,18.1b}$$

$$C_{Dev} = 45.42 \cdot EW^{0.630} \cdot V_{max}^{1.3} \qquad C_F = 1243.03 \cdot EW^{0.325} \cdot V_{max}^{0.822} \cdot \mathrm{FTA}^{1.21} \tag{18.2a,18.2b}$$

From the Class II weight estimation the EW of the aircraft was found to be 39000 kg (86000 lbs). From the performance analysis was known that the maximum velocity of the aircraft in its normal operation is 235 m/s (458 knots). Most aircraft use 2 to 6 prototypes for test flights. The CNA will have 6 such prototypes, as it was assumed that more testing of the BLI propulsor, the landing gears and the braced wings would be necessary to prove compliance with airworthiness requirements. Additionally, the market analysis in Chapter 3 showed that there could be two different scenarios, leading to two different production quantities. These scenarios depend on whether Airbus or Boeing would buy the CNA concept and thus replace their own aircraft, or whether the CNA would cover a third of the market as a direct competitor to Airbus and Boeing. This means that the production quantity of the CNA can either be 10400 or 6940 over 20 years. The RD&T cost were calculated in 1986 $ (as given by the DAPCA IV method) and by accounting for inflation, the RD&T cost could be calculated in 2030 $ leading to the results in Table 18.1 [1].

It is very important to be critical of the results in Table 18.1 for multiple reasons. Firstly, the method heavily depends on the estimation of the future inflation rates, however, this is something difficult to predict, as unexpected events can easily affect inflation. Secondly, the DAPCA IV method is not aircraft class specific, and can be used for transport, fighter and bomber aircraft. Since it is such a generic estimation method, it is most likely also very inaccurate. This

[1] URL `https://data.oecd.org/price/inflation-cpi.htm#indicator-chart` cited [22. June 2020]

Table 18.1: Breakdown of the RD&T cost of the Aircraft

Component	Cost for Q=6940 (2030 M$)	Cost for Q=10400 (2030 M$)
Engineering Cost	6173.0	6593.8
Tooling Cost	5625.7	6257.2
Development Support Cost	522.8	522.8
Flight Testing Cost	209.0	209.0
Total Cost	**12530.5**	**13582.8**
Development Cost per Aircraft	**1.8**	**1.3**

was already known in the beginning, but the DAPCA IV method was still chosen as it is the only method that was found that could be applied to the CNA at this preliminary stage of the design. Furthermore, the DAPCA IV model does not account for the extra RD&T costs that arise from the novel subsystems, due to the fact that these are most likely unknown concepts for a cost model that makes estimations for 1986. The cost model does not account for the extra engineering and testing or creation of models that will be necessary in the development stage of the CNA. This means that the engineering cost and the development support cost are most likely underestimated and that the real cost of the development stage is bound to be higher.

18.2. Production Cost

The production cost of an aircraft accounts for a majority of the cost of the aircraft. The production cost can also be estimated using the DAPCA IV estimation model, which was the case for the RD&T cost. The DAPCA IV estimation method accounts for the manufacturing cost, the manufacturing materials cost, the engine cost and the quality control cost.

The manufacturing cost of the aircraft includes the cost of all manufacturing processes. The manufacturing hours are calculated using Equation (18.3a). Again the manufacturing cost can be calculated using the hourly cost. The manufacturing materials cost accounts for all of the raw materials, hardware and equipment that are purchased to manufacture the aircraft. This cost is estimated using Equation (18.3b). The DAPCA IV cost estimation model, assumes that the cost of the engine is already known. This is mainly because engines are usually bought from engine manufacturers and not designed and manufactured by the aircraft designers. Since, engines with a UHBPR of 15 are not yet available on the market, it is assumed that the cost of these will be the same as the P&W1124G, which is a turbofan engine with a BPR of 12.5, the highest available BPR today. This means that the unit cost of the engines is assumed to be 12 Million $ (2020) [2]. However, it is important to note that this also accounts the cost for the engine development, so since the development of the engine is carried out by the engine manufacturers, this cost is added to the production cost of the aircraft. The DAPCA IV cost estimation method, regards quality control as a part of the production phase of the aircraft. The quality control cost includes the cost of all inspections on tools, parts, assemblies and the final aircraft. The amount of hours spent on quality control are directly related to the manufacturing hours ($H_{\text{manufacturing}}$) and given by $H_{QC} = 0.133 \cdot H_{\text{manufacturing}}$.

$$H_{\text{Manufacturing}} = 7.37 \cdot EW^{0.82} \cdot V_{max}^{0.484} \cdot Q^{0.641} \qquad C_{\text{Materials}} = 11 \cdot EW^{0.921} \cdot V_{max}^{0.621} \cdot Q^{0.799} \qquad \text{(18.3a,18.3b)}$$

The same values for the EW, V_{max} and the production quantity were used for the calculation of the production cost as was done for the calculation of the RD&T cost. Furthermore, according to the DAPCA IV estimation method, the cost of the avionics is in the range between 5-25 % of the total production cost. The exact percentage depends on the sophistication level of the avionics of the aircraft. As the avionics of the CNA is not very sophisticated and not very simple, the middle value is taken, meaning that it is assumed that the avionics cost is 15% of the total production cost. Accounting for inflation, the results in 2030 $ shown in Table 18.2 can be obtained.

As was the case for the RD&T, the DAPCA IV method also has some inaccuracies for the production cost. Firstly, the DAPCA cost method does not account for the BLI propulsor that is located in the tail, meaning that the cost of this is not represented in the engine cost. Furthermore, due to the BLI propulsor being placed in the aft of the fuselage, the fuselage of the CNA needs to be structurally stronger in the aft than for conventional aircraft. This requires more manufacturing time due to the additional strength, and it also requires more manufacturing time due to the increased complexity of the aft fuselage design. This means that the materials cost for the fuselage are also underestimated. Furthermore, the DAPCA IV model also does not account for the strut and the additional structural strength that the wing requires, meaning that again the cost of manufacturing and materials are underestimated by the DAPCA method. Furthermore, due to the increased complexity of the design of the CNA compared to a conventional aircraft, the CNA

[2] URL `https://www.bloomberg.com/news/articles/2011-12-14/jetblue-to-buy-pratt-whitney-engines` cited [18. June 2020]

Table 18.2: Breakdown of the Production cost of the Aircraft

Component	Cost for Q=6940 (M$)	Cost for Q=10400 (M$)
Manufacturing	71942.3	93237.6
Materials	63232.5	87358.3
Engines	223765.0	335325.1
Quality Control	10580.5	13712.4
Avionics	53841.0	77388.1
Total Cost	**423361.3**	**607021.5**
Production Cost per Aircraft	**61.3**	**58.4**

also requires a greater amount of quality control, meaning that the cost of this is also underestimated by the DAPCA IV model. All in all, this means that the additional complexity of the design is not accounted for by the DAPCA IV method, which means that the production costs estimated in Table 18.2 are underestimated and that in reality the costs will be higher.

18.2.1. Cost Breakdown Structure

Figure 18.1 and Figure 18.2 show the cost breakdown structures for production quantities of 6940 and 10400 aircraft respectively. Both cost breakdown structures show that more than 95 % of the cost of the aircraft comes from the production phase of the aircraft, which is expected. For both cases it can be seen that in the production cost, the engine cost is dominant, meaning that cheaper engines could lead to a large decrease in the cost of the aircraft, however as already discussed, the cost of the engines is relatively high compared to conventional aircraft, mainly due to the development cost that has to go into developing a high BPR turbofan engine.

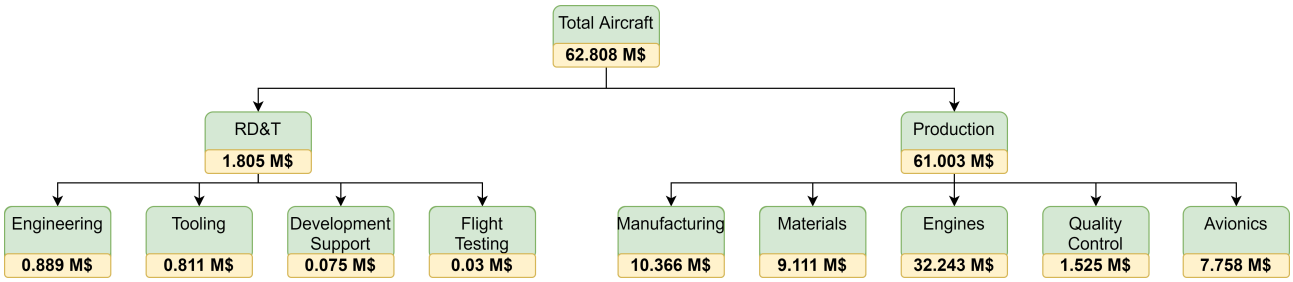

Figure 18.1: Cost Breakdown Structure for a Production Quantity of 6940 Aircraft

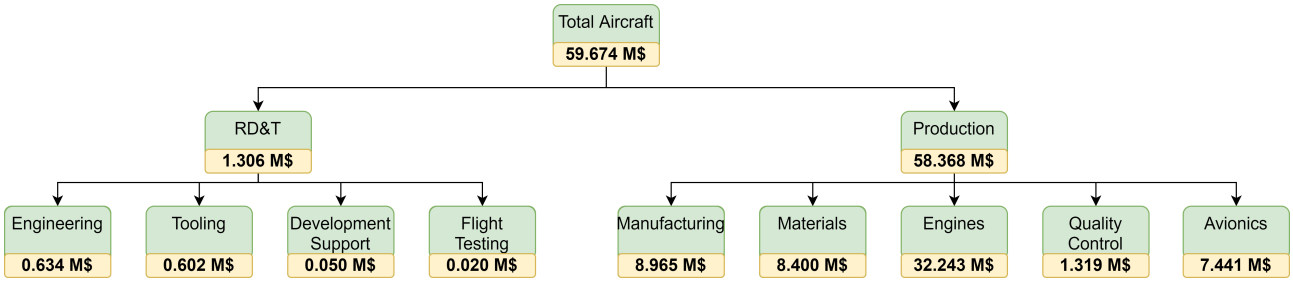

Figure 18.2: Cost Breakdown Structure for a Production Quantity of 10400 Aircraft

18.3. Direct Operating Cost

In order to compare the financial competitiveness of aircraft during their operations, one must look at its operating cost. With the indirect operating costs relying on services provided by the airlines themselves, a real comparison can only be made using the direct operational cost of the aircraft. This was done by estimating costs such as depreciation and fuel costs per flight, and taking the summation of those elements. An effective method for this is the estimation method known as DOC+I developed by NASA based on costs made in a deregulated and thus more realistic environment compared to a simulated environment [70]. This method relies on an initial aircraft cost C_{AC} estimation using the operational empty weight as seen in Equation (18.4a) and on an initial estimate of the engine cost C_{eng} as seen in

Equation (18.4b). For consistency's sake, this cost was estimated using formulas from the same method. All estimated costs are given in 2010 $.

$$C_{AC} = 10^6 \cdot \left(1.18 \cdot m_{oe}^{0.48} - 116\right) \qquad C_{eng} = 1.76 \cdot 82.5 \cdot T_{eng} \tag{18.4a,18.4b}$$

As discussed, the direct operating cost can be estimated by adding up the variety of elements directly incurring the cost during operations. The method relies on a multitude of variables leading to Equation (18.5) and the value was computed in $s per flight. These variables are listed as being: the residual airframe value R; the airframe cost C_{AF}; the airframe life P_{af} given as 15 years; the airframe spares S_{af} given as equal to $0.06 \cdot C_{AF}$; the engine spares given as equal to $0.23 \cdot C_{eng}$; the engine life P_{eng} given as 15 years; the aircraft utilisation U given as 625 hours a year; the interest rate R_{int} assumed at 2%; the block time t_B taken as 3 hours for this design's usage; the number of flight crew N_{fc} taken as 2 pilots; the international salary premium F_i given as 1.1 for international flights; the take off mass m_{to}; the number of cabin crew N_{cc} taken as 4 for this type of flight; the base cost per cabin crew C_{cc_b} given as 77 $ per hour; the fuel mass used for the aircraft's range m_{fuel}; the fuel density ρ_{fuel} and its cost C_{fuel} found to be 1.14$ a litre [3]; the mass of the airframe m_{af} and the variable C_{Lr} given as 25.

$$(DOC/\text{flight})_{NASA} = C_{dp} + C_{ins} + C_{fc} + C_{fuel} + C_{maint} + C_{int} + C_{cc} + C_{lf} + C_{nav} \tag{18.5}$$

The different variables of Equation (18.5) are as follows: The Depreciation cost comes from the capital value of an aircraft that is effectively depreciating each day due to the wear and tear of its parts. This value could be estimated in $/flight using Equation (18.6) and was found to equal 3331 $/flight. The insurance cost stems from the fact that the aircraft has to be insured against a variety of events in order to protect itself against unexpected financial losses. Through this the aircraft's operator hedges itself against potential financial risks. This value was estimated using Equation (18.7) and found to equal 432 $/flight. The interest cost is important because, in the current financial environment, aircraft purchases are almost exclusively made through loans leading to long-term debt down payments on these loans. These down payments could be approximated using Equation (18.8) and were found to equal 2636 $/flight.

$$\mathrm{C}_{dp\,\text{year}} = (1-R) \cdot \left(\frac{C_{AF}}{P_{af}}\right) + S_{af} \cdot \left(\frac{C_{AF}}{P_{af}}\right) + \frac{C_{eng}}{P_{af}} + S_{eng} \cdot \left(\frac{C_{eng}}{P_{eng}}\right) \tag{18.6}$$

$$C_{ins} = \frac{0.0035 \cdot C_{AC}}{U} \tag{18.7}$$

$$C_{\text{int}} = \frac{R_{\text{int}} \cdot \left(C_{AC} + 0.06 \cdot C_{AF} + 0.23 \cdot C_{\text{eng}}\right)}{U} \tag{18.8}$$

The flight crew that operates the aircraft have to be compensated for their work according to their relatively high skill and the intense training followed to obtain the job. This cost was estimated using Equation (18.9a) and found to equal 3151 $/flight. The cabin crew that work within the cabin have to be compensated for their work in assisting passengers and operating all cabin and cargo areas of the aircraft. Their cost was estimated through Equation (18.9b) and found to equal 1170 $/flight. The fuel cost per flight of the aircraft remains the biggest contribution to overall operating costs. This is more so the case with the CNA using a more expensive synthetic kerosene. Its cost per flight could be approximated using Equation (18.10) and using the values mentioned in the variables list above. The fuel cost was found to equal 11960 $/flight.

$$C_{fc} = t_B \cdot N_{fc} \cdot F_i \cdot \left(440 + \frac{0.532 \cdot m_{to}}{1000}\right) \qquad C_{cc} = t_B \cdot N_{cc} \cdot C_{cc_b} \tag{18.9a,18.9b}$$

$$C_{cfuel} = m_{fuel} \cdot \rho_{fuel} \cdot C_{fuel} \tag{18.10}$$

The maintenance cost contributes to the costs because, over the course of its lifetime, the aircraft will suffer both wear and damages from its everyday use and more serious and irregular damage. It furthermore needs regular checks and parts have to be replaced on a periodic basis. This entire process leads to further costs that could be approximated to a per flight basis using Equation (18.11) and was found to equal 2811 $/flight. Finally, with aircraft operating across the globe on a variety of airports, the landing and navigation fees are of importance because, during its usage, the aircraft makes use of the facilities and infrastructure of these airports. This has its price through landing and navigation fees that could be estimated using both Equation (18.12a) and Equation (18.12b) and the total was found to equal 1004 $/flight.

[3] URL `https://kalavasta.com/pages/projects/aviation.html` cited [18. June 2020]

$$(C_{al})_{NASA} = \left(\left(1.26 + 1.774 \cdot \left(\frac{m_{af}}{10^5}\right) - 0.1071 \cdot \left(\frac{m_{af}}{10^5}\right)^2\right) \cdot t_B + \left(1.614 + \quad 0.7227 \cdot \left(\frac{m_{af}}{10^5}\right) + 0.1204 \cdot \left(\frac{m_{af}}{10^5}\right)^2\right)\right) \cdot C_{Lr} \tag{18.11}$$

$$\left(C_{lf}\right)_{NASA} = 6.25 \cdot \frac{m_{to}}{1000} \qquad (C_{\text{nav}})_{NASA} = 0.2 \cdot 500 \cdot \sqrt{\frac{m_{\text{to}}}{1000}} \tag{18.12a,18.12b}$$

Using these values and plugging them back into Equation (18.5) allowed for the direct operational cost to be estimated at 26495 $/flight. With a range of 3981 km and 194 passengers, this cost could be estimated at 0.03414 $/km/pax. This value allows for a clearer financial comparison between operating aircraft and is crucial to airliners when estimating their return on investment when investing in the purchase of a new aircraft. This method remains based on empirical data and thus only serves as an initial estimate, further and more detailed estimations can be made by the client themselves to fit their specific use cases.

18.4. Return on Investment

In order to evaluate the financial potential and feasibility of the aircraft's market positioning as discussed in Chapter 3, it was crucial to evaluate the programme's return on investment (ROI). This value is given by the difference of the total programme revenue with the total programme cost which is then divided by the total programme cost, as seen in Equation (18.13), and with all costs in 2030 $s. In the case of the CNA, being bought out by either Airbus or Boeing and as advised in Section 3.4, a total of 10407 aircraft can be produced and sold at a list price of 55 M$ over the course of 20 years. In the case of the client of the CNA entering the market as a competitor to Airbus or Boeing, a total of 6940 aircraft can be produced at a list price of 55 M$ over the same time period. Having estimated the development costs of the programme in Section 18.1 and the total production cost in Section 18.2, the total programme cost could be estimated by summing the two. This was found to equal 620603 M$ for the buying out case and 437478 M$ for the competitor entry case. The total programme revenue on the other hand could be estimated by multiplying the total amount of aircraft produced and sold with their list price. This equals 572385 M$ for the buying out case and 381700 M$ for the competitor entry case. Plugging these values into Equation (18.13) gave a return on investment of negative 7.77% for the buying out case and negative 12.75% for the competitor entry case.

$$\text{ROI} = \frac{\text{Total programme revenue} - \text{Total programme cost}}{\text{Total programme cost}} \cdot 100 \tag{18.13}$$

The aircraft, with its current development and production costs together with its required competitive market listing can not be profitable, even in the optimum case of successfully producing and selling the aimed amount (which is a very optimistic assumption in the current market). However, as discussed in Section 3.3, financial benefits through government subsidies among others will reduce the overall costs by up to 50%. In this optimum case, the return on investment could be turned positive to up to 84.46% in the buying out case and 74.50% in the competitor entry case. It is again concluded that the financial benefits of carbon neutral flight are essential to financial feasibility and profitability of the design.

19
Project Development

The design phases of an aircraft are split up into conceptual design, preliminary design and detailed design. The extent of product development performed during the DSE is considered to be at a conceptual level. This work only assessed the feasibility of the CNA, however the actual journey to the first delivery will involve many more steps and milestones. The road map for further product development is presented in Figure 19.1. The top level flow of processes is shown by the green, arrow shaped boxes. These are broken down into more detail by the blue boxes. The steps to be taken for the design of the aircraft and the certification to follow are discussed in Section 19.1 and Section 19.2 respectively.

19.1. Design

The first design phase after the conceptual phase is the preliminary design. In this phase, detailed wind tunnel and CFD analysis is used to determine the aerodynamic characteristics of the entire aircraft. Minor changes to the layout are made if needed, and detailed structural and control systems design is performed. At the end of this phase, the overall design configuration is frozen [32]. The CNA preliminary design will include a detailed analysis of the novel systems; strut brace and slender wing structure, the aerodynamic effect of the BLI system, folding wing tips and unconventional landing gear structure. These systems will likely add time to the preliminary design phase. After preliminary design, a critical decision is made whether to commence with the detailed design phase. The detailed design phase involves the design of every structural component; ribs, spars, stringer, etc. The location and size of every bolt and rivet is determined, and the manufacturing tools and assembly jigs are designed [32]. It is important to note here that the first certification step actually takes place before detailed design is commenced as shown in Figure 19.1.

19.2. Certification

Next the certification process is commenced. The major stages of certification are shown in Figure 19.1 which are derived from EASA [1]. Certification is expected to take longer for the CNA due to the introduction of the novel systems which will require more certification considerations. The two longest certification phases will be building the prototype and demonstrating compliance. If there are certain areas of non compliance, the related components will have to go through a redesign. This is a very unfavourable situation as it leads to large amounts of time and money being lost. Once the aircraft is certified, large scale manufacturing and assembly can begin, soon followed by deliveries to customer airlines. The preliminary timeline for the different project activities is shown in the form of Gantt chart in Figure 19.2.

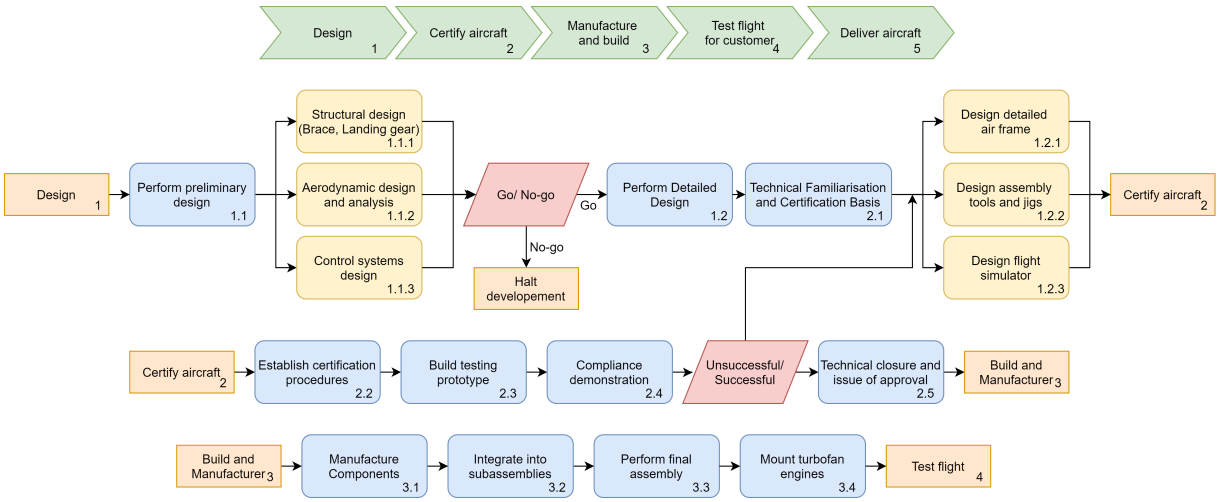

Figure 19.1: Product Design and Development Logic

[1] URL `https://www.easa.europa.eu/domains/aircraft-products/aircraft-certification` cited [18. June 2020]

ID	Task Mode	Task Name	Duration	Start	Finish
1		**Design**	**72,05 mons**	**Mon 6-7-20**	**Mon 12-1-26**
2		**Perform Preliminary Design**	**12 mons**	**Mon 6-7-20**	**Fri 4-6-21**
3		Perform Structural Design	12 mons	Mon 6-7-20	Fri 4-6-21
4		Perform Aerodynamic Design	12 mons	Mon 6-7-20	Fri 4-6-21
5		Perform Control System Design	12 mons	Mon 6-7-20	Fri 4-6-21
6		Go/No Go decision	0,05 mons	Mon 7-6-21	Mon 7-6-21
7		**Perform Detailed Design**	**60 mons**	**Tue 8-6-21**	**Mon 12-1-26**
8		Develop certification	6 mons	Tue 8-6-21	Mon 22-11-21
9		Design Detailed Air fram	30 mons	Tue 23-11-21	Mon 11-3-24
10		Design Assembly tools and jigs	24 mons	Tue 12-3-24	Mon 12-1-26
11		Design flight simulator	30 mons	Tue 23-11-21	Mon 11-3-24
12		**Certify Aircraft**	**55 mons**	**Tue 12-3-24**	**Mon 29-5-28**
13		Establish Certification procedures	6 mons	Tue 12-3-24	Mon 26-8-24
14		Build testing prototypes	12 mons	Tue 27-8-24	Mon 28-7-25
15		Perform compliance demonstration activities	36 mons	Tue 29-7-25	Mon 1-5-28
16		Perform technical closure	1 mon	Tue 2-5-28	Mon 29-5-28
17		**Manufacturing**	**17 mons**	**Tue 30-5-28**	**Mon 17-9-29**
18		Manufacture different components	12 mons	Tue 30-5-28	Mon 30-4-29
19		Integrate into sub assemblies	2 mons	Tue 1-5-29	Mon 25-6-29
20		Perform final assembly	3 mons	Tue 26-6-29	Mon 17-9-29
21		Deliver Aircraft	0 mons	Mon 17-9-29	Mon 17-9-29

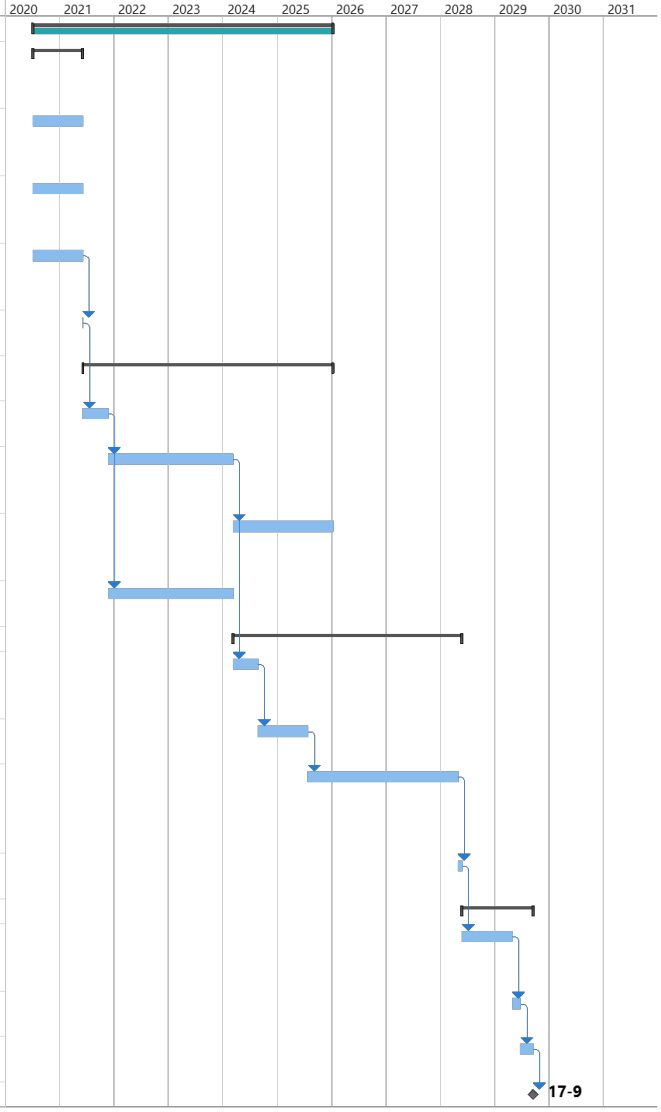

Figure 19.2: Gantt Chart for upcoming Project Phases

20 Risk Assessment

Throughout the previous reports, over 130 organisational, system and subsystem risks were presented [2][3]. In this final report, the focus is put on the risk assessment of the final product after the time period of the DSE. The main risks assessed are listed in Table 20.1. Risks R132, R133, R138, and R143 originate from the current world situation (Covid-19 crisis), where many aspects are uncertain. These aspects are dependent on the world and local politics, and will only be determined when the current crisis is overcome. These unsure aspects include, amongst others, new social and working standards, financing of bankrupt airlines, and the general opinion on the risks of globalisation. The risk scoring system is shown in Table 20.3 and Table 20.2. The risk map is displayed in Figure 20.1 with the risk level description explained in Table 20.4.

Table 20.1: Risk Assessment; SYS refers to the System Engineering department, PRD refers to the Production department, MKT refers to the Market and PR department, PERF refers to the Performance department, and OPR refers to the Operation department

Risk ID	Dep.	Risk Description	Probability	Impact	Risk Factor
R132	PRD	A delay in production occurs	3	4	12
R133	MKT	The market shrinks	3	5	15
R134	MKT	A CNA crashes	1	5	5
R135	PERF	Synthetic kerosene proves to be unfeasible	2	4	8
R136	OPR	Handling of the aircraft during landing proves to be too difficult	2	3	6
R137	MKT	A competitor aircraft with better performance is launched after EIS	2	4	8
R138	MKT	Airlines do not want or are not to renew their fleet when EIS is planned	3	4	12
R139	PRD	Production and R&D cost rise greatly above the foreseen budget	2	4	8
R140	OPR	Parts are difficult to acquire when needed in a remote location	3	2	6
R141	OPR	Maintenance grounds the CNA longer than competitors	3	2	6
R142	PRD	At EOL, not the required 75% of the aircraft can be recycled	2	3	6
R143	MKT	World travel gets reformed	3	3	9
R144	SYS	The CNA does not pass certification procedures	2	4	8
R145	SYS	The testing of the CNA proves that systems are underdeveloped	2	4	8
R146	SYS	The CNA is not profitable to sell as a standalone aircraft	2	5	10

Table 20.2: Risk scoring system on probability

Score	Description	Probability (occurance)
1	Rare: very small chance of happening	Less than once
2	Unlikely: small chance of happening	Once
3	Occasionally: even chance of happening	One to two times
4	Likely: high chance of happening	Two to three times
5	Almost Certain: very high chance of happening; expected	Three to four times

Table 20.3: Risk scoring system on impact

Score	Description	Impact (time)	Impact (quality)
1	Low: very small impact	Hours to days	Minor confusion
2	Medium: small impact, small changes necessary	Days to a week	Inaccuracies
3	High: part of the design needs to be redone, fixed and/or overtime is needed	One or multiple weeks	Serious oversights
4	Very High: significant setback, a big part of the design needs to be (re)done in order to solve the problem	One or multiple months	Sever shortcomings
5	Extreme: major setback, very hard to recover, if not impossible	Months to a year	Unacceptable design

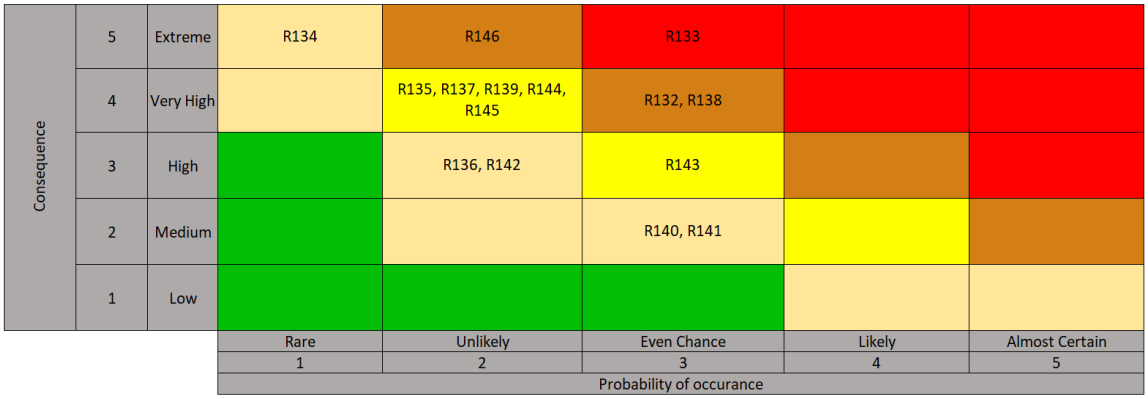

Figure 20.1: Risk map

Table 20.4: Risk level description

Risk Factor	Risk Level Catagory	Description
1 to 3	Negligible Risk	Manage by routine procedures; Reviewed at least every 5 weeks
4 to 6	Moderate Risk	Manage by engineering departments; Reviewed at least every 3 weeks
7 to 9	Significant Risk	Manage by Risk Manager; Reviewed at least every 2 weeks
10 to 14	High Risk	Manage by Systems Engineers and Risk Manager; Reviewed at least every week
15 to 25	Severe Risk	Manage by Team Leader and Risk Manager; Reviewed on a daily basis

The aim for the main overall risks is to mitigate them to be within the risk level category "Moderate" or "Negligible", shown in Table 20.4. As can be seen in Figure 20.1, almost all risks had to be mitigated. The most dangerous risk is R146 shown in Table 20.1. The design is performed to the best of the team's capabilities and all risks responsible for the cancellation as described in previous reports have been mitigated. Therefore, the focus of mitigating this risk is put on the impact. To lower the impact, it is important that certain novel systems or subsystems are developed further after cancellation of the project. In this way not a full CNA aircraft will be the product, but certain systems such as the BLI system, the landing gear system or the strut-braced wing structure will be able to represent the CNA. By organising departments during R&D as individual groups that act as their own 'companies', this risk is mitigated from impact 5 to impact 3.

The risks associated with the current world situation as described before, are mitigated with respect to both impact and probability. Risk R132 is mitigated by structuring the workplace such that decisions and regulations from the government are accounted for in advance. This includes, amongst more, organising the production as a '1.5 m society', strict cleaning rules and well ventilated areas. Furthermore, to reduce the impact there will be more time allocated for the production in the time-budget. This mitigated the risk to a probability of 2 and an impact of 3. Risk R133 is

mitigated by reducing the impact, as a possible market shrink is an external factor. To reduce the impact, the target market will be expanded when the initial target market proves to be shrinking. This can be done by, for example, selling techniques or components to use synthetic kerosene to other sectors such as the automotive or the seafaring market. Also, this can be done in combination with the mitigation action taken for R146, which is establishing the ability to sell aircraft components on their own. This will expand the market from only the airlines, to both airlines and aircraft manufacturers.

In addition, risk R138 and risk R143 are mitigated by reducing the impact. This is done by a well timed release of the CNA, anticipating the market. Next to that, the CNA must be presented as "the solution" to the problems causing these risks. In order to do so, an extra team in the PR section will be created focusing solely on this. These actions will reduce the impact of risk R138 to 3 and risk R143 to 2. Moreover, risk R138 is mitigated by presenting great deals for airlines when the CNA is bought in bulk. This is possible in the case that government and other carbon neutral subsidies reduce the overall cost, as explained in Section 18.4. This reduces the probability of this risk to 2.

The risks associated with parts and maintenance are mitigated with respect to probability, since the impact can not be changed (it costs money every second the aircraft is grounded). Risk R140 is mitigated by setting up a new branch of the CNA-company with physical offices at every airport the CNA uses. Together with the well set up supply-routes between these offices and the factories, the probability is reduced to 2. Risk R141 is mitigated by increasing the maintenance skill of the maintenance departments of the airlines. This is done by setting up courses, training and structured manuals on the new and novel maintenance aspects of the CNA for the customer airlines. This reduces the probability of R141 to 2. Risk R136 is mitigated in the same manner as risk R141. It is done by giving extra training, courses and manuals on how to handle the aircraft during landing. This reduces the probability to 1.

Risk R137 is mitigated by reducing the impact. This is done in the same manner as risk R138 and R143: by presenting the CNA as "the solution" to the world problems such as environmental sustainability. With putting the focus on the conversion to be carbon neutral, the impact of the risk is mitigated to 3. Risks R144 and R145 are mitigated with respect to impact. To do so, extra time is taken in the planning that accounts for these risks, making the risk of not making the EIS lower. In this case, when the risks do happen, there will be less or no delay in schedule, therefore reducing the impact on the EIS. This action reduces the impact from 4 to 3.

The last risk that was mitigated was risk R135. The impact is lowered by designing the CNA to also use bio-kerosene and a blend of bio-kerosene and synthetic kerosene. As both are effectively kerosene, only minor adaptions need to be made. Next to that, if the management team predicts that synthetic kerosene will become unfeasible, part of the profit from the CNA will be put into the development of synthetic kerosene. As this investment will result in more sales, the investment is justified. This action lowers the possibility to 1.

The mitigation action described move all risks to "Negligible" and "Moderate", except for risk R133 as can be seen in Figure 20.2. As this is a "Significant" risk, it needs to be monitored in regular intervals by the risk manager, preferably every two weeks. This will reduce the chance that the design will fail to a minimal level.

Consequence							
	5	Extreme	R134				
	4	Very High					
	3	High	R135, R136	R132, R137, R138, R139, R144, R145, R146	R133		
	2	Medium		R140, R141	R143		
	1	Low					
			Rare	Unlikely	Even Chance	Likely	Almost Certain
			1	2	3	4	5
			Probability of occurance				

Figure 20.2: Mitigated risk map

21
Conclusion

Sustainability has become an increasingly important topic and several different governments across the world have been pushing towards more environmentally sustainable approaches throughout different industries. This has led to policies such as the European Green Deal, which aims to make Europe climate neutral by 2050. However, for the aviation industry this aim leads to a so called circular causality problem, as there may be limited investment into scaling up the production of alternative energy sources due to the limited availability of aircraft that employ these, while on the other hand, airlines may be reluctant to buy such aircraft due to the limited availability of the fuel. To resolve this problem the carbon neutral ready aircraft was proposed.

The aim of this project was to design an aircraft that can initially be powered using fossil fuels and then be converted to use a carbon neutral source. The aim of this report was to present the conceptual design of the carbon neutral airliner, while showing that it meets its requirements and can help Europe become climate neutral. The carbon neutral aircraft features a braced high aspect ratio wing which can be folded up and has a propulsion system which consists of two ultra high bypass ratio turbofan engines and a boundary layer ingesting propulsor at the aft of the fuselage. The aircraft is presented in fig. 21.1. To summarise, the designed carbon neutral aircraft meets its top level requirements which are given in Section 2.2. Furthermore, at least 90 % by mass of the primary structure of the aircraft is recyclable and compared to the A320neo, the carbon neutral aircraft has 17% less fuel while it is still powered on fossil fuel. Additionally the CNA has a 38% reduction in NO_x and a 17% in CO_2. The aircraft has a financial profitability, however this is heavily dependent on government action and subsidies. This means that the carbon neutral aircraft provides a solution to the aforementioned "chicken-and-egg" scenario, by being an aircraft that is environmentally sustainable, financially feasible and comparable in terms of payload and range to the A320 baseline. From the recommendations however, it is clear that a lot still needs to be done before the carbon neutral aircraft can enter into service in 2030.

Figure 21.1: The Carbon Neutral Ready Airliner

Bibliography

[1] John-Alan Pascoe. *Project Guide: Carbon Neutral Airliner*. TU Delft, 2020.

[2] Y Farah, K Kaneko, A van Meenen, S van Reen, B Saify, S Shrestha, S Singh, M Swart, F Vassen, S Vermani, and M van Vliet. Design of a Carbon Neutral Aircraft: Project Plan. Technical report, TU Delft, 2020.

[3] Y Farah, K Kaneko, A van Meenen, S van Reen, B Saify, S Shrestha, S Singh, M Swart, F Vassen, S Vermani, and M van Vliet. Design of a Carbon Neutral Aircraft: Baseline Report. Technical report, TU Delft, 2020.

[4] Y Farah, K Kaneko, A van Meenen, S van Reen, B Saify, S Shrestha, S Singh, M Swart, F Vassen, S Vermani, and M van Vliet. Design of a Carbon Neutral Aircraft: Midterm Report. Technical report, TU Delft, Delft, 2020.

[5] Global Market Forecast 2019. Technical report, Airbus, .

[6] Global Market Forecast 2018. Technical report, Airbus, .

[7] Boeing Commercial Airplanes. The Boeing Next-Generation 737 Family – Productive, Progressive, Flexible, Familiar. *Backgrounder*, pages 1–6, 2015.

[8] Yongxiang Yang, Rob Boom, Brijan Irion, Derk Jan van Heerden, Pieter Kuiper, and Hans de Wit. Recycling of composite materials. *Chemical Engineering and Processing: Process Intensification*, 51:53–68, 2012. ISSN 02552701. doi: 10.1016/j.cep.2011.09.007.

[9] A320 Aircraft Characteristics: Airport and Maintenance Planning. Technical report, Aibus S.A.S, Blagnac Cedex, 2005.

[10] Wouter Van Der Wal. AE3212-II - Simulation , Verification and Validation, 2020.

[11] J Roskam. *Part V: Component weight estimation*. 1985. ISBN 1884885551.

[12] D P Raymer. *Aircraft design: A conceptual approach*. 1992.

[13] E Torenbeek. *Synthesis of Subsonic Airplane Design: An Introduction to the Preliminary Design of Subsonic General Aviation and Transport Aircraft, with Emphasis on Layout, Aerodynamic Design, Propulsion and Performance*. Delft University Press, Delft, 1976. ISBN 9789029825054.

[14] Brandon Basgall, Wanbo Liu, Truman Cassady, and Willem A. Anemaat. Aircraft Design Weight Methods Comparison and Improvement. (January):1–15, 2020. doi: 10.2514/6.2020-1259.

[15] Michael Chun-Yung Niu. Airframe Structural Design: Practical Design Information and Data on Aircraft Structures, 1988.

[16] Tipps DO, Skinn DA, Rustenburg JW, T Jones, and Harris DA. Statistical loads data for the Airbus A-320 aircraft in commercial operations. DOT/FAA/AR(April):1–104, 2006.

[17] P. Balakrishnan, M.J. John, L. Pothen, M.S. Sreekala, and S. Thomas. *Natural fibre and polymer matrix composites and their applications in aerospace engineering*. Elsevier Ltd, 2016. ISBN 9780081000373. doi: 10.1016/b978-0-08-100037-3.00012-2.

[18] Peter Haase and Zoltan Mikulik. Composite Damage Metrics and Inspection. Technical report, Bishop GmbH, Hamburg, 2012.

[19] C. Lynch, A. Murphy, M. Price, and A. Gibson. The computational post buckling analysis of fuselage stiffened panels loaded in compression. *Thin-Walled Structures*, 42(10): 1445–1464, 2004. ISSN 02638231. doi: 10.1016/j.tws.2004.04.002.

[20] Linda Werfelman. Thin Skinned. *Flight Safety Foundation*, (October):18–20, 2004.

[21] M. Nita and D. Scholz. Estimating the Oswald Factor from Basic Aircraft Geometrical Parameters. *Deutscher Luft- und Raumfahrtkongress*, 281424:1–19, 2012.

[22] Jan Roskam. *Airplane Design – Part VI: Preliminary Calculation of Aerodynamic, Thrust and Power Characteristics*. 1987.

[23] Ira H Abbott, Albert E von Doenhoff, and Louis S. Stivers. Summary of Airfoil Data. Technical Report 1, National Advisory Committee for Aeronautics, 1945.

[24] Charles D. Harris. NASA supercritical airfoils. *NASA Technical Paper*, (2969):1–76, 1990.

[25] Pasquale Sforza. *Commercial Airplane Design Principles*. Butterworth-Heinemann, Boston, 2014. ISBN 978-0-12-419953-8.

[26] John F. Gundlach IV, Philippe André Tétrault, Frank H. Gern, Amir H. Nagshineh-Pour, Andy Ko, Joseph A. Schetz, William H. Mason, Rakesh K. Kapania, Bernard Grossman, and Raphael T. Haftka. Conceptual design studies of a strut-braced wing transonic transport. *Journal of Aircraft*, 37(6):976–983, 2000. ISSN 00218669. doi: 10.2514/2.2724.

[27] Wrik Mallik, Rakesh K. Kapania, and Joseph A. Schetz. Multidisciplinary design optimization of medium-range transonic truss-braced wing aircraft with flutter constraint. *54th AIAA/ASME/ASCE/AHS/ASC Structures, Structural Dynamics, and Materials Conference*, pages 1–11, 2013. doi: 10.2514/6.2013-1454.

[28] G. Carrier, O. Atinault, S. Dequand, J. L. Hantrais-Gervois, C. Liauzun, B. Paluch, A. M. Rodde, and C. Toussaint. Investigation of a Strut-braced wing configuration for future commercial transport. *28th Congress of the International Council of the Aeronautical Sciences 2012*, 1:104–119, 2012.

[29] Ohad Gur, Manav Bhatia, Joseph A. Schetz, William H. Mason, Rakesh K. Kapania, and Dimitri N. Mavris. Design optimization of a truss-braced-wing transonic transport aircraft. *Journal of Aircraft*, 47(6):1907–1917, 2010. ISSN 00218669. doi: 10.2514/1.47546.

[30] Manav Bhatia, Rakesh K. Kapania, and Raphael T. Haftka. Structural and aeroelastic characteristics of truss-braced wings: A parametric study. *Journal of Aircraft*, 49(1):302–310, 2012. ISSN 00218669. doi: 10.2514/1.C031556.

[31] Andy Ko, William H. Mason, and Bernard Grossman. Transonic aerodynamics of a wing/pylon/strut juncture. *21st AIAA Applied Aerodynamics Conference*, (June):1–10, 2003. doi: 10.2514/6.2003-4062.

[32] J D Anderson. *Fundamentals of Aerodynamics*. McGraw-Hill series in aeronautical and aerospace engineering. McGraw-Hill Education, 2016. ISBN 9781259251344.

[33] J M Corum, R L Battiste, K C Liu, and M B Ruggles. Basic Properties of Reference Crossply Carbon-Fiber Composite. Technical report, Oak Ridge National Laboratory, 2000.

[34] Adelina Vanessa Benedict. An Experimental Investigation of GLARE and Restructured Fiber An Experimental Investigation of GLARE and Restructured Fiber Metal Laminates Metal Laminates Scholarly Commons Citation Scholarly Commons Citation. 2012.

[35] James Ainsworth, Craig Collier, Phil Yarrington, Ryan Lucking, and James Locke. Airframe wingbox preliminary design and weight prediction. *69th International Conference on Mass Properties 2010*, pages 155–195, 2010.

[36] Jan R Wright and Jonathan E T A T T Cooper. Introduction to Aircraft Aeroelasticity and Loads. LK - https://tudelft.on.worldcat.org/oclc/898769287, 2014.

[37] Dewey H Hodges and G Alvin. T A T T Pierce. Introduction to structural dynamics and aeroelasticity, 2011.

[38] Mayuresh J. Patil, Dewey H. Hodges, and Carlos E.S. Cesnik. Nonlinear aeroelasticity and flight dynamics of high-altitude long-endurance aircraft. *Journal of Aircraft*, 38(1): 88–94, 2001. ISSN 00218669. doi: 10.2514/2.2738.

[39] Influence of Body Geometry and Flow Conditions on Axisymmetric Boundary Layers At Subcritical Mach Numbers. Technical Report September 1979, ESDU, 1979.

[40] Geometrical characteristics of typical bodies. Technical Report July, ESDU, 2017.

[41] Jos P. van Buijtenen, Wilfried P.J. Visser, Savad Shakariyants, and Francesco Montella. *Propulsion and Power AE2203: Gas Turbines*. Number FEBRUARY. TU Delft, 2011.

[42] Arvind Gangoli Rao. Engine Design Trends, 2020.

[43] Rainer Schnell, Dirk Schönweitz, Marius Theune, and Johakim Corroyer. Integration- and Intake-Induced Flow Distortions and Their Impact on Aerodynamic Fan Performance. In Rolf Radespiel, Reinhard Niehuis, Norbert Kroll, and Kathrin Behrends, editors, *Advances in Simulation of Wing and Nacelle Stall*, pages 251–269, Cham, 2016. Springer International Publishing. ISBN 978-3-319-21127-5.

[44] Jason R. Welstead and James L. Felder. Conceptual design of a single-aisle turboelectric commercial transport with fuselage boundary layer ingestion. Technical report, American Institute of Aeronautics and Astronautics, 2016.

[45] Michael Ashby and Kara Johnson. *Materials and Design*. 2010. ISBN 9781856174978. doi: 10.1016/C2009-0-26530-5.

[46] Ikpe Aniekan, Owunna Ikechukwu, P O Ebunilo, and Ememobong Ikpe. Material Selection for High Pressure (HP) Compressor Blade of an Aircraft Engine. *International Journal of Advanced Materials Research*, 2(4):59–65, 2016. ISSN 2381-6813.

[47] Fuel Boost Pump Type 8410 and Canister Type 8411.

[48] PW1100G-JM Product Card, 2019.

[49] Margaret Kilpatrick. The Investigation of Noise, Vibrations and Emissions of Aero-Gas Turbine Combustion with Synthetic Kerosene Fuels. Technical report, Georgia Southern University, Statesboro, 2019.

[50] Rob Terwel and John Kerkhoven. *Carbon neutral aviation with current engine technology*. Stichting Sangeest, 2018.

[51] Bernard Gerard, Barbara Herbschleb, Remco Kistemaker, and Remo Snijder. De potentie van synthetische kerosine als alternatieve brandstof voor de luchtvaart. Technical report.

[52] Venedikt Kuz'Michev, Ilia Krupenich, Evgeny Filinov, and Yaroslav Ostapyuk. Comparative Analysis of Mathematical Models for Turbofan Engine Weight Estimation. *MATEC Web of Conferences*, 220:1–7, 2018. ISSN 2261236X. doi: 10.1051/matecconf/201822003012.

[53] Periklis Lolis. Development of a Preliminary Weight Estimation Method for Advanced Turbofan Engines. Technical Report July, University of Cranfield, 2014.

[54] Patrick C. Vratny and Mirko Hornung. Sizing Considerations of an Electric Ducted Fan for Hybrid Energy Aircraft. *Transportation Research Procedia*, 29(2017):410–426, 2018. ISSN 23521465. doi: 10.1016/j.trpro.2018.02.037.

[55] Ian Moir, Allan Seabridge, and Malcolm Jukes. *Civil Avionics Systems*. 2013. ISBN 9781118536704. doi: 10.1002/9781118536704.

[56] O Biedermann, J Engelhardt, and G Geerling. More Efficient Fluid Power Systems Using Variable Displacement Hydraulic Motors. *International Council of the Aereonautical Sciences*, 1998.

[57] Ahmed F. El-sayed. Performance Analysis of Cold Sections of High BYPASS Ratio Turbofan Aeroengine. *Journal of Robotics and Mechanical Engineering Research*, 2(1):18–27, 2017. doi: 10.24218/jrmer.2017.23.

[58] Snorri Gudmundsson. *The Anatomy of the Tail*. 2014. ISBN 9780123973085. doi: 10.1016/b978-0-12-397308-5.00011-8.

[59] Lloyd Jenkinson, Paul Simpkin, and Darren Rhodes. *Civil Jet Aircraft Design*. 1999. doi: 10.2514/4.473500.

[60] Mohammad H. Sadraey. *Aircraft Design: Systems Engineering Approach*. John Wiley & Sons Ltd, 2012. ISBN 9781119953401. doi: 10.1002/9781118352700.ch2.

[61] E Obert, R Slingerland, D J W Leusink, T van den Berg, J H Koning, M J L van Tooren, and Technische Hogeschool Delft. Afdeling der Luchtvaart-en Ruimtevaarttechniek. *Aerodynamic Design of Transport Aircraft*. Ios Press, 2009. ISBN 9781586039707.

[62] B. Aigner, F. Peter, E. Stumpf, B. Hauber, and D. Metzler. Assessment of Electromechanical Flight Control Actuators with Regard to Direct Operating Costs. *Deutscher Luft- und Raumfahrtkongress 2016*, 66(17 2):1–11, 2016.

[63] A318/A319/A320/A321 Flight Crew Training Manual. Technical Report Suppl. 5, Airbus, 2008.

[64] Nicolas El Haddad. *Aerodynamic and Structural Design of a Winglet for Enhanced Aerodynamic and Structural Design of a Winglet for Enhanced Performance of a Business Jet*. PhD thesis, Embry-Riddle Aeronautical University, 2015.

[65] Dick G Simons. *Introduction to Aircraft Noise*. Delft University Press, Delft, 2018.

[66] Snorri Gudmundsson. *General Aviation Aircraft Design: Applied Methods and Procedures*. 2013. ISBN 9780123973085. doi: 10.1016/C2011-0-06824-2.

[67] Remzi Saltoglu, Nazmia Humaira, and Gökhan Inalhan. Aircraft Scheduled Airframe Maintenance and Downtime Integrated Cost Model. *Advances in Operations Research*, 2016, 2016. ISSN 16879155. doi: 10.1155/2016/2576825.

[68] van Tooren M.J.L. Hamann, R.J. *Systems Engineering & Technical Management Techniques Part II Lecture Notes*. Number 2. 2006.

[69] Andrew Cook, Graham Tanner, and Philippe Enaud. Quantifying Airline Delay Costs - The Balance Between Strategic and Tactical Costs. *14th Air Transport Research Society World Conference*, 2010.

[70] By Rashid Ali, Omran Al-shamma, Rashid Ali, and Omran Al-shamma. A comparative study of cost estimation models used for preliminary aircraft design. *Global Journal of Research In Engineering*, 14(4), 2014.